Nonlinear Model Order Reduction and Control of Very Flexible Aircraft

Thesis submitted in accordance with the requirements of
the University of Liverpool for the degree of Doctor in Philosophy
by
Nikolaos D. Tantaroudas (M.Sc Electrical Engineering and Computer Science)

March 2015

"Give me a lever long enough and a fulcrum on which to place it, and I shall move the world."

Archimedes, 287-212 BC

Acknowledgements

First of all, I would like to acknowledge my supervisor Professor Kenneth Badcock for giving me this interesting subject, his trust, and together his support and ideas to investigate.

I would also like to thank Dr. Andrea Da Ronch from the University of Southampton for introducing me to the Linux world, and for providing direction and guidance related to this work. Of course my second supervisor Professor George Barakos shall not be forgotten, for the advices he has given, for creating the stimulating working environment, and for solving several technical difficulties for the CFD lab.

Moreover I need to acknowledge Dr. Evangelos Papatheou and Dr. George Vasdravellis from the University of Sheffield and the University of Heriot–Watt respectively, for the discussions we had related to the active control in experimental problems.

Special thanks should go to Professor John Mottershead and Dr. Shakir Jiffri for the great collaboration we had, and for giving me the chance to take part in the active vibration control project.

Furthermore, I would like to thank Dr. Rafael Palacios and Dr. Andrew Wynn from Imperial College London, and Dr. Henrik Hesse now in ETH Zurich, for their overall collaboration and their help during my visits there.

Thanks should go to all the members of the CFD lab, but in particular to name some, past (Dr. Andrew McCracken, Dr. Jacobo Angulo, Dr. David Kennett) and present (Vasilis Pastrikakis, Vladimir Leble, Guanqun Gai, George Hoholis, Dr. George Zografakis, and Dr. Sebastian Timme) for the fruitful discussions we had so far and for making the last three years quite enjoyable.

In addition, I would like to further express my gratitude to Dr. Vincenzo Muscarello from the Politecnico di Milano for being a good friend and for the intense discussions we had during the first year of my introduction to aeroelasticity.

Lastly, special thanks go to my family and friends. With your presence, or sometimes even with your absence, you made this work possible.

This research has been supported by the Engineering and Physical Sciences Research Council (EPSRC) through Grant.

Abstract

In the presence of aerodynamic turbulence, very flexible aircraft exhibit large deformations and as a result their behaviour is characterised as intrinsically nonlinear. These nonlinear effects become significant when the coupling of rigid–body motion with nonlinear structural dynamics occurs and needs to be taken into account for flight control system design. However, control design of large–order nonlinear systems is challenging and normally, is limited by the size of the system. Herein, nonlinear model order reduction techniques are used to make feasible a variety of linear and nonlinear control designs for large–order nonlinear coupled systems. A series of two–dimensional and three–dimensional test cases coupled with strip aerodynamics and Computational–Fluid–Dynamics is presented. A systematic approach to the model order reduction of coupled fluid–structure–flight dynamics models of arbitrary fidelity is developed. It uses information on the eigenspectrum of the coupled-system Jacobian matrix and projects the system through a Taylor series expansion, retaining terms up to third order, onto a small basis of eigenvectors representative of the full–model dynamics. The nonlinear reduced–order model representative of the dynamics of the nonlinear full–order model is then exploited for parametric worst–case gust studies and a variety of control design for gust load alleviation and flutter suppression. The control approaches were based on the robust $\mathcal{H}_\infty$ controller and a nonlinear adaptive controller based on the model reference adaptive control scheme via a Lyapunov stability approach. A two degree–of–freedom aerofoil model coupled with strip theory and with Computational–Fluid–Dynamics is used to evaluate the model order reduction technique. The nonlinear effects are efficiently captured by the nonlinear model order reduction method. The derived reduced models are then used for control synthesis by the $\mathcal{H}_\infty$ and the model reference adaptive control. Furthermore, the numerical models developed in this thesis are used for the description of the physics of a wind–tunnel model at the University of Liverpool and become the benchmark to design linear and nonlinear controllers. The need for nonlinear control design was demonstrated for the wind–tunnel model in simulation. It was found that for a wind–tunnel model with a cubic structural nonlinearity in the plunge degree–of–freedom, conventional linear control designs were inadequate for flutter suppression. However, a nonlinear controller was found suitable to increase the flight envelope and suppress the flutter. A large body of work dealt with the development

of a numerical framework for the simulation of the flight dynamics of very flexible aircraft. Geometrically–exact nonlinear beam structural models were coupled with the rigid–body, the flight dynamics degrees–of–freedom and the strip theory aerodynamics, for the description of the nonlinear physics of free–flying aircraft. The flexibility effects of these vehicles on the flight dynamic response is quantified. It is found that different angle of attack and control input rotation is needed to trim a flexible aircraft and that a rigid analysis is not appropriate. Furthermore, it is shown that the aircraft flexibility has an impact on the flight dynamic response and needs to be included. The fully coupled models are consequently reduced in size by the nonlinear model reduction technique for a cheaper and a simpler computation of a variety of linear and nonlinear automatic control designs that are applied on the full–order nonlinear models inside the developed framework for gust load alleviation. The approach is tested on a Global Hawk type unmanned aerial vehicle developed by DSTL, on a HALE full aircraft configuration, and on a very large flexible free–flying wing. A comparison of the developed control algorithms is carefully addressed with the adaptive controller achieving better gust loads alleviation in some cases. Finally, future possible implementations and ideas related to the nonlinear model order reduction and the control design of flexible aircraft are discussed.

Declaration

I confirm that the thesis is my own work, that I have not presented anyone else's work as my own and that full and appropriate acknowledgement has been given where reference has been made to the work of others.

Nikolaos D. Tantaroudas
February 2015

List of Publications

Tantaroudas, N.D., Da Ronch, A., Badcock, K.J., and Palacios, R., "Nonlinear Reduced Order Model for Rapid Gust Loads Analysis of Flexible Manoeuvring Aircraft", submitted to the Journal of Aircraft.

Tantaroudas, N.D., Da Ronch, A., Gai, G., Badcock, K.J., and Palacios, R., "On Active Control Strategies for Flexible Aircraft Gust Loads Alleviation", submitted to the AIAA Journal.

Tantaroudas, N.D. and Da Ronch, A., "Nonlinear Reduced Order Aeroservoelastic Analysis of Very Flexible Aircraft", Book Chapter in Unmanned Vehicles, John Wiley & Sons, Ltd (accepted for publication).

Tantaroudas, N.D., Da Ronch, A., Badcock, K.J., and Palacios, R., "Model Order Reduction for Control Design of Flexible Free–Flying Aircraft", AIAA Atmospheric Flight Mechanics Conference, Scitech 2015, AIAA Paper 2015–0240, Kissimmee, FL., Jan. 2015

Tantaroudas, N.D., "PySharp: A Python Computational Toolbox to Simulate the Flight Dynamics of Flexible Aircraft with Full and Reduced Order Models", Technical Report, University of Liverpool, 2015.

Tantaroudas, N.D., "A Famous Example on the Model Reference Adaptive Control Step-by-Step", Technical Report, University of Liverpool, 2015.

Tantaroudas, N.D., "Control Design based on the Nonlinear Model Order Reduction Technique", Technical Report, University of Liverpool, 2015.

Tantaroudas, N.D., " A series of Aeroelastic Models to be used for the Analysis and the Design of Very Flexible Aircraft", Technical Report, University of Liverpool, 2014.

Tantaroudas, N.D., Da Ronch, A., Gai, G., Badcock, K.J., Palacios, R., "An adaptive Aeroelastic Control Approach using Nonlinear Reduced Order Models", 14th AIAA Aviation Technology, Integration, and Operations Conference, AIAA Paper 2014–2590, Atlanta, Georgia, June 2014.

Fichera, S., Jiffri, S., Wei, X., Da Ronch, A., Tantaroudas, N.D., Mottershead, J.E., "Experimental and Numerical Study of Nonlinear Dynamic Behaviour of an Aerofoil", ISMA2014 conference on Noise and Vibration Engineering, Leuven, Belgium, Sept., 2014.

Da Ronch, A., McCracken, A.J., Tantaroudas, N.D., Badcock, K.J., Hesse, H., and Palacios, R., "Assessing the Impact of Aerodynamic Modelling on Manoeuvring Aircraft", AIAA Atmospheric Flight Mechanics Conference, Scitech 2014, AIAA Paper 2014–0732, 13-17 January 2014, National Harbor, M.D.

Da Ronch, A., Tantaroudas, N.D., Jiffri, S. and Mottershead, J.E., "A Nonlinear Controller for Flutter Suppression:from Simulation to Wind Tunnel Testing",55th AIAA/ASME/ASCE/AHS/SC Structures, Structural Dynamics, and Materials Conference, Scitech 2014, AIAA Paper 2014–0345, 13-17 January 2014, National Harbor, MD.

Papatheou, E., Tantaroudas, N.D., Da Ronch, A., Cooper, J.E., and Mottershead,J.E., "Active Control for Flutter Suppression:An Experimental Investigation", IFASD 2013, Bristol, UK.

Da Ronch, A., Tantaroudas, N.D., Timme, S., and Badcock, K.J., "Model Reduction for Linear and Nonlinear Gust Loads Analysis", 54th AIAA/ASME/ASCE/AHS/ASC Structures, Structural Dynamics and Material Conference, AIAA Paper 2013–1492, Boston, Massachusetts.

Da Ronch, A., Tantaroudas, N.D., and Badcock, K.J., "Reduction of Nonlinear Models for Control Applications", 54th AIAA/ASME/ASCE/AHS/ASC Structures, Structural Dynamics and Material Conference, AIAA Paper 2013–1491, Boston, Massachusetts.

Contents

List of Figures

List of Tables

List of Symbols

$ar_{a1}, ar_{a2}, ar_{a3}$	=	Rigid–body angular acceleration in x, y, z
$ar_{v1}, ar_{v2}, ar_{v3}$	=	Rigid–body angular velocities in x, y, z
$ar_{d1}, ar_{d2}, ar_{d3}$	=	Rigid–body rotation in x, y, z
$ad_{a1}, ad_{a2}, ad_{a3}$	=	Aerofoil section angular acceleration in x, y, z
$ad_{v1}, ad_{v2}, ad_{v3}$	=	Aerofoil section angular velocity in x, y, z
$ad_{d1}, ad_{d2}, ad_{d2}$	=	Aerofoil section rotation in x, y, z
α_h	=	Centre of gravity to midchord distance nondimensional distance
$\boldsymbol{A}$	=	Jacobian matrix of the residual $\boldsymbol{R}$ with respect to the states $\boldsymbol{w}$
b	=	Semichord
$\boldsymbol{B}$, $\boldsymbol{C}$	=	Second and third order operators in the Taylor expansion
c	=	Vector of location of aerofoil sections with respect to the wing span
c_h	=	Nondimensional distance from the midchord to the flap hinge
C_ξ^c	=	Critical damping in plunge, $2\sqrt{m\,K_\xi}$
C_α^c	=	Critical damping in pitch, $2\sqrt{I_\alpha\,K_\alpha}$
C_ξ, C_α	=	Viscous damping in plunge and pitch, respectively
C_L, C_m	=	Lift and pitch moment coefficients
cx, cy, cx	=	Location of aerofoil section with respect to the wing span
d_{a1}	=	Aerofoil section acceleration in x
d_{a2}	=	Aerofoil section acceleration in y
d_{a3}	=	Aerofoil section acceleration in z
d_{v1}	=	Aerofoil section velocity in x
d_{v2}	=	Aerofoil section velocity in y
d_{v3}	=	Aerofoil section velocity in z
d_{d1}	=	Aerofoil section deformation in x
d_{d2}	=	Aerofoil section deformation in y
d_{d3}	=	Aerofoil section deformation in z
e_0, e_1, e_2, e_3	=	Quaternions from global frame to body frame

h	=	Timestep
I_α	=	Second moment of inertia of aerofoil about elastic axis
$\boldsymbol{K}_\xi$, $\boldsymbol{K}_\alpha$	=	Plunge stiffness and torsional stiffness about elastic axis
L, M	=	Lift and pitch moment
m	=	Aerofoil sectional mass
P_a, P_v, P_d	=	Acceleration,velocity and displacement vector
Pa_{GB}	=	Vector of rigid–body accelerations in x, y, z
Pa_{BA}	=	Vector of aerofoil accelerations in x, y, z
Pd_{GB}	=	Vector of rigid–body displacements in x, y, z
Pd_{BA}	=	Vector of aerofoil deformations in x, y, z
Pv_{GB}	=	Vector of rigid–body velocities in x, y, z
Pv_{BA}	=	Vector of aerofoil velocities in x, y, z
r_{a1}	=	Rigid–body acceleration in x
r_{a2}	=	Rigid–body acceleration in y
r_{a3}	=	Rigid–body acceleration in z
r_a	=	Radius of gyration of aerofoil about elastic axis, $r_a^2 = I_\alpha / m\, b^2$
r_{v1}	=	Rigid–body velocity in x
r_{v2}	=	Rigid–body velocity in y
r_{v3}	=	Rigid–body velocity in z
r_{d1}	=	Rigid–body displacement in x
r_{d2}	=	Rigid–body displacement in y
r_{d3}	=	Rigid–body displacement in z
$\boldsymbol{R}$	=	Residual vector
R_t	=	Rotation matrix of quaternions
S_α	=	First moment of inertia of aerofoil about elastic axis
S_k, S_{kd}	=	Rotation matrix to body frame and its derivative
t	=	Physical time
U_∞	=	Freestream velocity
U_L	=	Linear flutter speed
U^*	=	Reduced velocity, $U/b\,\omega_\alpha$
U_{eff}	=	Effective freestream speed
$\boldsymbol{w}$	=	Vector of unknowns
w_g	=	Gust vertical velocity
w_0	=	Intensity of gust vertical velocity
$\boldsymbol{w}_f$	=	Augmented aerodynamic states
x_α	=	Aerofoil static unbalance, $S_\alpha / m\, b$
x_α	=	Aerofoil static unbalance, S_α / mb
x_δ	=	Reduced centre of gravity distance from flap hinge

Greek

α	= Angle of attack
β_{ξ_3}, β_{ξ_5}, β_{α_3}, β_{α_5}	= Nonlinear cubic and quintic aerofoil spring constants in plunge and pitch
β, γ	= Newmark integration parameters
ζ_ξ	= Damping ratio in plunge, C_ξ/C_ξ^c
ζ_α	= Damping ratio in pitch,C_α/C_α^c
λ_i	= i–th eigenvalue of $\boldsymbol{A}$
μ	= Mass ratio, $m/\pi\,\rho\,b^2$
ρ	= Freestream density
τ	= Nondimensional time, $t\,U/b$
τ_g	= Gust gradient
$\boldsymbol{\phi}_i$, $\boldsymbol{\psi}_i$	= i-th right and left eigenvectors of $\boldsymbol{A}$
ξ	= Nondimensional displacement in plunge, h/b
$\bar{\omega}$	= Ratio of ω_ξ/ω_α
ω_α	= Uncoupled pitching mode natural frequency about elastic axis, $\sqrt{K_\alpha/I_\alpha}$
ω_ξ	= Uncoupled plunging mode natural frequency, $\sqrt{K_\xi/m}$

Symbol

$\dot{(\,)}$	= Differentiation with respect to t, $d(\,)/dt$
$(\,)'$	= Differentiation with respect to τ, $d(\,)/d\tau$
$\bar{(\,)}$	= Complex conjugation

Acronyms

2-DOF	=	Two degree–of–freedom
3-DOF	=	Three degree–of–freedom
CFD	=	Computational fluid dynamics
CSD	=	Computational structural dynamics
CSM	=	Computational structural mechanics
UVLM	=	Unsteady–vortex–lattice method
DLM	=	Double–lattice–method
MPI	=	Message passing interface
PML	=	Parallel meshless
RANS	=	Reynolds–averaged Navier–Stokes
SVD	=	Singular value decomposition
HSV	=	Hankel singular values
FOM	=	Full–order model
NFOM	=	Nonlinear full–order model
ROM	=	Reduced–order model
NROM	=	Nonlinear reduced–order model
MRAC	=	Model reference adaptive control
LQR	=	Linear quadratic regulator
LQG	=	Linear quadratic Gaussian
MPC	=	Model predictive control
FL	=	Feedback linearisation
SOS	=	Sum–of–squares
UAV	=	Unmanned aerial vehicle
HALE	=	High–altitude long–endurance
FCS	=	Flight control system
HBM	=	Harmonic balance method
POD	=	Proper orthogonal decomposition
LCO	=	Limit cycle oscillations

Chapter 1

Introduction

The interest behind high–altitude long–endurance (HALE) vehicles has increased in recent years because they provide low–cost efficient platforms for a variety of applications. The low structural mass and high aerodynamic efficiency enable flight at high–altitudes and low–speeds with minimal energy consumption. The range of applications of HALE aircraft varies from monitoring and collecting data of the atmospheric environment, to rescue missions in bio-hazard poisonous environments. The advantage of unmanned HALE aircraft is their ability to operate at extreme conditions for long duration times without putting at risk human life.

The analysis and design of HALE aircraft, however, presents some unique challenges that are not critical for more rigid (and stiff) aircraft. The dynamic interaction between the structural deformation of wings, the aerodynamics, and flight mechanics may cause structural failure as occurred in 2003 on the NASA's Helios prototype shown in Figure 1.1. Following this accident, there was an increased interest in the aerodynamic–structural–flight response that occurs in light, very flexible and high–aspect–ratio wings [1]. The first detailed investigations into the dynamics of a very flex-

Figure 1.1: NASA Helios unmanned aerial vehicle as in Ref. [1]

ible aircraft predate this, and were carried out by the Daedalus Project, in 1989 [2, 3].

Prior to the Daedalus Project the longest distance record by a human powered plane was set at 23 miles and took place in 1979 with a flight across the English Channel [4]. This record was broken during the initiation of the Daedalus project and as a result in 1988 Daedalus flew 73 miles over the Aegean Sea from Iraklion Air Force Base on Crete to Santorini island.

Helios was developed under the Environmental Research Aircraft and Sensor Technology (ERAST) NASA program, as a HALE class vehicle. Two configurations were produced. The first one was tailored to achieve high–altitude and the second one was expected to achieve long–endurance flight. As expected, the first Helios configuration broke another altitude record on August 13^{th} 2001 with a flight at 96863 feet. However, the second configuration that was designed for long–endurance flight did not have the same success and on June 26^{th} 2003 broke apart mid–flight during testing. Helios encountered low–level turbulence during flight. After approximately 30 minutes of flight time a larger than expected wing dihedral formed because of the turbulence and the aircraft began a slowly diverging pitch oscillation. The wing dihedral remained high and the oscillations never subsided. Instead, they grew with each period and this led to the destruction of the aircraft (Figure 1.2).

Figure 1.2: NASA Helios flight accident as in [1]

One of the reasons for the Helios flight accident was the limited understanding of the fluid–structure coupling that occurs in these aircraft, and the absence of computational tools to simulate their flight behaviour under turbulence. The main aim of this thesis is the development of a multidisciplinary framework that addresses all the above issues in the analysis and design of highly flexible aircraft [5].

A systematic approach to flight control system (FCS) design is developed for very flexible and very large aircraft, of the type being considered for low–environmental–impact air transport and for long–endurance unmanned operations. A virtual flight test environment that supports the design of advanced nonlinear flight control systems (FCS) that fully accounts for the vehicle structural flexibility is created. To model the flight dynamics of flexible aircraft, a nonlinear structural code is coupled with a variety of aerodynamic models, and the flight response is examined. However, the coupled full–order model nonlinear equations are too expensive to solve for the full range of flow

conditions and atmospheric turbulence of interest and are too large to be used for a careful control design.

Parametric searches are performed to estimate the critical loads that the aircraft will encounter during the expected life cycle and these are used for structural sizing. Inaccuracies in the load estimates can result in a very conservative (and inefficient) design. Thus, methods for generating reduced–order models (ROMs) via reduction of the full–order nonlinear equations of motion are needed in such a way that the essential nonlinear behaviour is preserved. The usual separation of flight dynamics and aeroelasticity is not appropriate for flight control when very low structural frequencies (which are also often associated with large amplitude motions) are present. Modelling and design methods based on a fully coupled system analysis are therefore necessary. The use of high–fidelity fluid–structure–flight models results in large order systems which are incompatible with control design as the bulk of control theory was developed for systems of relatively low–order. This introduces the question of how to reduce the dimension of the large–order nonlinear system while retaining the ability to predict nonlinear effects.

Hence, the development of a nonlinear ROM is considered in this thesis for control applications of very flexible aircraft in particular. From a simulation standpoint, the challenges to be overcome in the analysis and design of HALE aircraft are:

1. The development of a multidisciplinary framework to realistically model the nonlinear interactions in the fluid, structure, flight dynamics, and control fields.

2. The lack of an approach to systematically reduce large computational models to a smaller system for faster simulation times and for control synthesis design.

3. The exploitation of advanced control design strategies to improve the effectiveness of the closed–loop response to gusts.

Several technical and scientific challenges are overcome which includes the simulation of significant aerodynamic and structural nonlinearities in the full aircraft dynamics through the systematic development of a hierarchy of fully coupled large–order models. In specific, this thesis deals with the reduction of these models to small–order nonlinear systems suitable for control development and the design of robust control laws based on these reduced nonlinear models for gust load alleviation, trajectory control and stability augmentation.

1.1 Aeroelastic Modelling of Very Flexible Aircraft

Initial work in nonlinear aeroelasticity for very flexible aircraft has been published in [5], where it was found that the inclusion of aircraft structural dynamics when analysing the flight dynamic characteristics of a very flexible aircraft (VFA) is very important.

As the flexibility increases the wing deformation increases and there are additional contributions from the rigid body motion in the aerodynamics. Patil et al. [6] developed a formulation for the complete modelling of a HALE-type aerial vehicle. Drela [7] developed an analysis tool which was implemented in ASWING, a numerical toolbox for flexible aircraft. Its formulation was based on a geometrically–exact nonlinear isotropic beam, and could provide fast analysis for flight dynamic characteristics. Other researchers also followed a similar approach in modelling nonlinear aeroelasticity. Cesnik and Brown designed a nonlinear structural analysis toolbox [8,9] for modelling a flexible aircraft using a strain–based approach. For example, the work presented in [9] examined a HALE–type aircraft which was modelled with a rigid fuselage and highly flexible, high–aspect–ratio composite wing representative of a very flexible aircraft (VFA). Palacios et al. [10] developed a nonlinear aeroelastic toolbox which used the three–dimensional Euler equations to model the flow, and the structural deformations were modelled using 1–D and a 2–D beam elements. Su et al. [11] presented a study on coupled aeroelasticity and results related to the dynamic stability and the open–loop gust responses of a blended wing–body aircraft. In that case, the wing was modelled by a low–order aeroelastic formulation that was capable of capturing the important structural nonlinear effects, and the coupling with the flight dynamics degrees–of–freedom. Aeroelastic stability was assessed and compared with flutter results when all, or some of the rigid–body degrees–of–freedom were constrained.

Several researchers demonstrated the process of flexible aircraft configuration design in the past [12,13]. These investigations presented the challenges in the design of HALE type vehicles that can operate in the thin atmosphere. In particular, it was shown that the lack of methods to allow predictions of HALE structural mass, engine performance at high altitudes, and low Reynolds numbers for high–aspect–ratio configurations were challenging problems. Some of these challenges were addressed by Drela [7] who developed an integrated model for aerodynamic, structural, and control simulation of flexible aircraft in extreme flight situations. The structural model was considered by including joined nonlinear beams which allowed arbitrarily large deformations.

Very flexible aircraft (VFA) modelling has received increased attention since the Helios flight accident. Analysis based on nonlinear structural dynamics can be indicative of the stability of flexible aircraft. However, rigid–body motion introduces a significant aerodynamic contribution, and for that reason open–loop responses with coupled rigid–body and structural dynamics were extensively examined [6, 14–16]. Patil et al. [6] studied the open–loop dynamics of a flying–wing structure similar to that of Helios and found that flap positions used to trim the flexible aircraft differ greatly from those used to trim the rigid aircraft. The authors also captured the instability in the phugoid mode which was present during large dihedral angles which was the main reason for the Helios structural failure. Similar studies by Raghavan et al. [14] and Su et al. [15] confirmed this result. In an attempt to validate their modelling approach and their

developed numerical toolboxes, Su et al. built a very flexible UAV called the X–HALE and performed flight test [17, 18].

Palacios et al. [19] studied different type of structural dynamic models and aerodynamics in the nonlinear flight mechanics of very flexible aircraft. The structural dynamic models included displacement based, strain–based and intrinsic geometrically nonlinear beams. It was demonstrated that all the different beam finite element models could be obtained from a single set of equations. This investigation extended strain–based structural dynamic models to include shear effects. More importantly, the intrinsic first–order description of the nonlinear beam equations was found to be several times faster than conventional ones traditionally applied in the field of aeroelasticity.

In conclusion, composite beam models provide a reliable and efficient way to capture the structural dynamics of high–aspect–ratio wings. Most commonly found in the literature, is the displacement and rotation–based beam formulation followed by the strain–based beam element formulation. Some work has also been published with hybrid intrinsic geometrically nonlinear composite beams. Herein, a geometrically–exact composite beam model is used to represent the dynamics of very flexible free-flying aircraft [20]. Results are obtained using two–node displacement–based elements. In a displacement–based formulation, nonlinearities arising from large deformations are cubic terms, as opposed to an intrinsic description where they appear up to second order. This thesis addresses the nonlinear model order reduction of the developed coupled fluid–structure models using a high–fidelity structural modelling and low–order unsteady aerodynamics.

1.2 Unsteady Aerodynamic Model

A large variety of lower and higher–fidelity aerodynamic modelling techniques has been applied in nonlinear aeroelasticity, In multidisciplinary problems such as nonlinear aeroelasticity and very flexible aircraft (VFA) modelling, it is important to distinguish the difference between analysis methods for prediction as opposed to simulation. In a *simulation*, there is an increased need for a well–defined configuration for an accurate characterisation of the phenomenon in question and in these cases higher–fidelity flow modelling techniques are required. For example in aeroelasticity, a simulation may be performed in order to understand a particular fluid–structure interaction mechanism, or to establish the amplitude of a limit cycle oscillation (LCO).

In contrast, *prediction* methods are meant to support the design process by providing fast answers to important questions such as "Is this configuration aeroelastically stable at this particular flight condition?". Hence, prediction methods should require small computational cost which translates to lower–fidelity aerodynamic modelling and they should be practical for parametric studies (i.e. worst–case gust searches).

The aerodynamic models range from the typical two–dimensional strip theory which is low–cost and low–fidelity, towards medium–fidelity aerodynamic models with Doublet–Lattice Method (DLM) and Unsteady Vortex–Lattice Method (UVLM) that offer relatively cheap calculations. The computational cost however increases dramatically with Computational–Fluid–Dynamics and this is an area that still needs advances. In this thesis, the low–fidelity aerodynamic models come from the two–dimensional

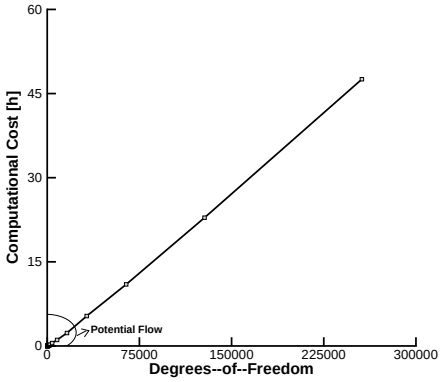

Figure 1.3: Computational cost with respect to the degrees–of–freedom to capture 1 s of an unsteady flight dynamic calculation with strip aerodynamics and CFD

strip theory, while the higher–fidelity aerodynamics come from Computational–Fluid–Dynamics. Figure 1.3 shows the computational cost required to capture 1 s of an unsteady flight dynamic simulation with respect to the number of degrees–of–freedom with potential flow assumption and with CFD.

1.2.1 Typical Section and Strip Theory

Several analysis methods for the classical aeroelastic stability problems, divergence and flutter are available [21] since the 1930s. Of course, simplifying assumptions are made in order to reduce the complexity and the computational cost of the systems. Most simplifications address the aerodynamic part of the problem.

In the most simple case, only a representative two-dimensional section of the aeroelastic lifting surface (typical section) is considered reducing a three–dimensional into a two–dimensional problem which can even be analytically treated up to a certain degree. The unsteady flow is modelled in this approach by a frequency domain expression for the incompressible two–dimensional potential flow over a flat plate in harmonic motion, originally found by Theodorsen [22].

An extension of this approach, called strip theory, adapts the same two–dimensional unsteady flow model for a three–dimensional aeroelastic system by combining section aerodynamics with a beam model for the wing structure. Although simple and computationally inexpensive, strip theory can provide fairly reliable (and usually conservative)

results for divergence speed, critical flutter velocity and aileron reversal. However, it requires that the physical characteristics of the configuration under investigation can be properly reduced to a beam–type structure and that three–dimensional aerodynamic effects do not have a significant impact on aeroelasticity. Moreover, for high–aspect–ratio aircraft, such as very flexible aircraft flying at low cruise velocities, the two–dimensional, inviscid and incompressible unsteady aerodynamic model have been shown to predict the behaviour well. Tang et al. [23] constructed an experimental high–aspect–ratio wing aeroelastic model with a slender body at the tip. Time–domain responses due to flutter and limit cycle oscillations (LCO) were measured in a wind–tunnel test. A theoretical model was developed to cross validate the experimental data. For the structural equations of motion, nonlinear beam theory was combined with the aerodynamic stall model. The theory and the experiment were in good agreement for static aeroelastic computations, flutter speed, dynamic LCO amplitude and frequency.

For the description of the non–circulatory part of the unsteady aerodynamic forces generated due to wing motion, a contribution from a gust disturbance or a control surface rotation, the idea of finite–state modelling was introduced. Wagner [24] was the first to calculate the indicial function to obtain the lift response of a two–dimensional flat plate in incompressible inviscid flow [24]. Following Wagner's work, Jones [25] suggested the use of the Laplace transform, and also obtained an approximate expression of the Wagner function. However, there was an increased interest in the time–domain methods for the unsteady aerodynamic modelling and as a result many new modelling methods were introduced. Vepa [26] and Dowell [27] used the method of Padé approximations to give a finite–state representation of any aerodynamic frequency lift function. The newest finite–state modelling was introduced by Peters [28] who offered a new type of finite–state aerodynamic model in 1995. This model offers the finite–state equations for the induced flowfield. These equations are derived directly from the potential flow. The induced flow expansion satisfies the condition that few states will be needed in the frequency range of interest. This number of states was compared to other aerodynamic modelling techniques based on Wagner and Theodorsen functions.

One of the biggest advantages of finite–state models is that they can be cast as a small system of first–order differential equations which allows the application of control theory. Furthermore, the time evolution of the aerodynamic states is known explicitly and these can be written both in the frequency and in the time–domain.

Peters' finite–state aerodynamic modelling is well known among researchers in the field of nonlinear aeroelasticity and several have coupled this inflow theory with their structural solvers for the description of the nonlinear flight dynamics of high–aspect–ratio wings [8, 11, 29]. Su et al. [15] presented a method to model the coupled nonlinear flight dynamics and the aeroelasticity of highly flexible flying wings. A low–order nonlinear strain–based finite element 1–D beam model framework, coupled with Peters' inflow theory, was used to analyse their nonlinear flight dynamic characteristics dur-

ing a gust response. Patil et al. [6, 30] coupled the geometrically–exact, intrinsic beam equations with Peters' aerodynamics, and studied the flexibility effects on the stability of highly flexible wings with large dihedral. He concluded that their impact on the stability analysis of flexible vehicles was very important.

Very few researchers have coupled their structural solvers based on older concepts and the exponential approximations of the Wagner and Küssner functions. The Wagner and Küssner functions that are used in this thesis for the unsteady aerodynamic modelling, as presented in Leishman [31], have been used for the modelling of flexible free–flying aircraft with flight dynamic degrees–of–freedom [32]. Herein, additional contributions to the aerodynamic forces arising from the velocity and the acceleration of the control surface rotation were taken into account.

1.2.2 Doublet–Lattice Method

A large body of work has been published on the aerodynamic modelling with the Doublet–Lattice Method (DLM). DLM is based on the linearised potential flow model, solves the Laplace's equation for the incompressible flow, and is formulated in the frequency domain. Moreover, it is based on the assumption of harmonic motion of lifting surfaces, which are approximated as flat plates of infinitesimal thickness. This method is combined with a structural model, usually a linear finite element model and most times an interpolation is used to define a relationship between the structural deformations and the motion of the aerodynamic surfaces. DLM has been extensively used throughout the years. Blair et al. [33] provided the theoretical development of the DLM in the past 40 years. Albano et al. [34] assumed the aerodynamic surface as a set of lifting elements which were short line segments of acceleration–potential doublets. The normal velocity induced by an element of unit strength was given by an integral of the subsonic kernel function. The loads applied on each individual element were determined by assuming that they satisfied the normal velocity and the boundary conditions at a set of points on the surface. In this way he demonstrated that the DLM can be used for the calculation of lift distributions on oscillating surfaces at low speed.

Kier [35], compared results from a quasi–steady Vortex–Lattice Method (VLM), strip theory and unsteady DLM. An example of the panelling scheme used for the DLM is shown in Figure 1.4. Baldelli et al. [36] used a rational function approximation of the DLM to model the flight dynamic behaviour of the General Atomics–Aeronautical Systems (GA–ASI) Predator UAV. Elastic modes were not included in the aeroelastic model. In Baldelli et al. [37] the modelling and control characteristics of an aeroelastic morphing vehicle were investigated. Patil et al. [38] analysed the importance of the aerodynamic and structural nonlinearities in the aeroelastic behaviour of high–aspect–ratio wings. It was found that the static structural geometric nonlinearities were not

very important within the range of the flight operation, and three–dimensional effects arising from the aerodynamics were minimal.

DLM underwent significant improvements during the years. Rodden et al. [39, 40] extended the aerodynamic method for applicability at higher frequencies and for flutter analysis, aeroservoelastic analysis of control surfaces, and short wavelength dynamic gust responses. A further refinement by Rodden et al. [40] accounted for wing tip corrections in the aerodynamics which resulted in an overall improvement of the convergence of the method.

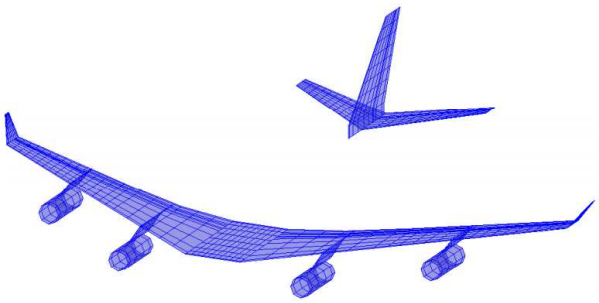

Figure 1.4: Panelling scheme for an aircraft for DLM, as in [35]

The DLM is computationally inexpensive. It can model small control surface rotations by modifying the flow tangency boundary condition on their corresponding panels. However, the control surface aerodynamic effects obtained in this manner depend on the discretisation and usually exceed experimentally observed results, requiring empirical corrections.

1.2.3 Unsteady Vortex-Lattice Method

The Unsteady Vortex–Lattice Method (UVLM) has its origins in the Vortex–Lattice Method (VLM) and is used to obtain a medium–fidelity three–dimensional solution of the unsteady aerodynamics. Hedman et al. [41] introduced the VLM for the calculation of quasi–steady state loadings on thin elastic wings in subsonic flow. The surfaces were divided into panels in both chordwise and spanwise directions. Lan et al. [42] developed a quasi VLM method for application in thin wing aeroelastic problems. He presented two–dimensional results for aerofoils without flap deflection and calculated the lift and pitching moment coefficients. VLM gradually improved and Mook et al. [43] applied it to high angle of attack test cases for unsteady flow calculations for a variety of geometries such as rectangular and delta wings. Furthermore, Konstadinopoulos et al. [44] presented a general method for computing unsteady incompressible three–dimensional flows around arbitrary geometries.

Katz et al. [45] was one of the first to introduce the UVLM method for the calculation of the aerodynamic forces acting on lifting surfaces undergoing random three–dimensional motion. A Delta wing was considered and numerical results for high angle of attack and sideslip condition were presented. A detailed description of the method has been presented in many textbooks related to low–speed aerodynamics [46]. This technique of aerodynamic modelling makes feasible the solution of a three–dimensional potential flow based on a vortex–ring discretisation of the domain, about lifting surfaces. These vortex–ring quadrilateral elements are used to discretise the lifting surfaces and wakes. The vorticity distribution of all vortex elements is determined by applying the non–penetration boundary condition over the bound vortex panels along the lifting surfaces.

The induced velocities over the normal vector of each individual vortex–ring are computed by the Biot–Savart law. All the inputs to the aerodynamic forces such as structural deformations, rigid–body motion, control surface rotation and gust velocities are introduced through non–vortical velocities applied on each surface panel. Following the calculation of this vorticity distribution, the aerodynamic pressures are computed using Bernoulli's equation. The resulting aerodynamic loads are finally converted into forces and moments at the beam nodes assuming coincident meshes and rigid cross–sections [47, 48].

The UVLM is a geometrically nonlinear method in which the shape of a force–free wake is obtained as part of the solution procedure. It therefore accurately captures the aerodynamic lags over a large range of reduced frequencies at low flight velocities which makes this method suitable for the analysis of very flexible aircraft [19].

Fritz et al. [49] used the UVLM to model the oscillating plunging, pitching, twisting and flapping motions of finite–aspect ratio wings. Moreover, the results were verified by the theory and by experimental data. Palacios et al. [19] assessed different structural and aerodynamic models for the nonlinear flight dynamics of very flexible aircraft. Strip theory and Vortex–Lattice methods were considered. It was found that strip theory indicial aerodynamics perform well in small amplitude dynamics around a large static wing deflection. However, for large amplitude wing dynamics the three–dimensional aerodynamic description of UVLM gave better predictions. Murua et al. [50] studied the coupled aeroelasticity and flight mechanics of a very flexible and light vehicle that was modelled with a geometrically–exact composite beam formulation and a general three–dimensional Unsteady Vortex–Lattice Method. The stability properties and the open–loop dynamic responses of the configuration were investigated.

A typical modelling of the panelling scheme for the UVLM is shown in Figure 1.5

UVLM offers great capabilities in the aeroelastic modelling of very large and flexible aircraft and its efficiency has been demonstrated even when flight dynamic degrees–of–freedom are included and the body undergoes large rigid body motion [52].

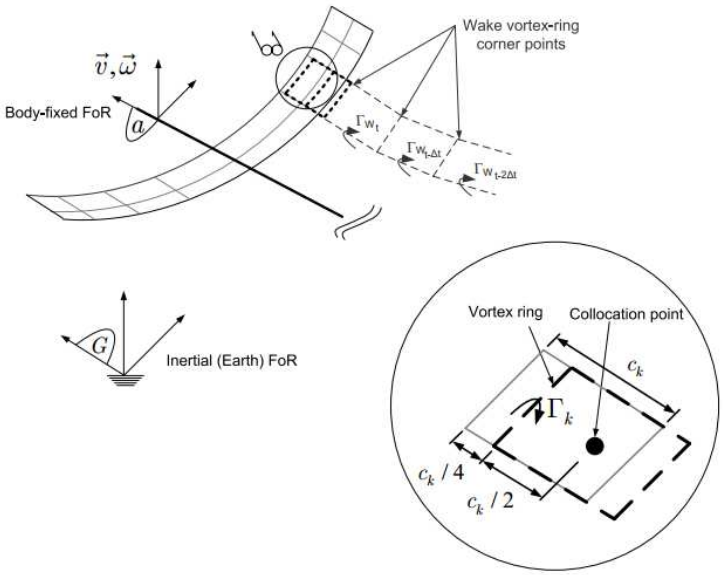

Figure 1.5: Panelling scheme for the UVLM as in [51]

1.2.4 Computational Fluid Dynamics

Computational Fluid Dynamics (CFD) is used to perform aeroelastic time–domain simulations using a general model of the flow physics. Due to the relatively high cost and the need of a precise geometry definition, such simulations for fully coupled nonlinear calculations were prohibitive and have developed the last two decades.

Since the interest lies in creating the capabilities to perform a coupled fluid–structure–flight analysis, a mesh deformation tool is needed to transfer information between the fluid and the structural solver.

Ide et al. [53] dealt with the simulation and dynamic aeroelastic response of a flexible wing that had mounted multiple control surfaces. It was demonstrated that control surfaces can suppress the flutter and perhaps various nonlinear phenomena that take place in the transonic flight regime. Pioneering work came out from Farhat et al. [54] who presented a computational methodology for the simulation of the aeroelastic behaviour of free–flying flexible aircraft during high G–maneuvers. Unstructured dynamic meshes were used with a CFD flow solver. A robust method for updating an unrestrained and unstructured fluid mesh was introduced. Heinrich et al. [55] showed that the aerodynamic loads acting on a flexible aircraft result in structural deformation which causes changes in the fluid flow and the loads. Numerical static aeroelastic calculations were presented in high Reynolds number against experimental data. The TAU CFD solver used, was coupled with commercial FEM codes such as ANSYS and NASTRAN and an interpolation module was included to transfer the aerodynamic loads onto the structural nodes between the CFD and CSM meshes. Palacios et al. [10] presented results for a slender composite wing using a high–fidelity approach. The compressible flow was

modelled using the three–dimensional Euler equations on a deformable mesh and static nonlinear aeroelastic calculations were performed.

Ludovic et al. [56] used the CFD solver ELSA, coupled with a simplified beam model, and computed aerodynamic calculations for static cases. Song et al. [57] presented results on the aerodynamic characteristics of adaptive wings with flexible trailing–edges using the FLUENT CFD solver. It was demonstrated that during the trailing–edge deformation the overall aerodynamic performance lift/drag ratio was increased compared to rigid trailing–edge configurations. Moreover, it was suggested that this dynamic deflection of the wing can potentially suppress the separating stall and increase the flutter speed. Raveh et al. [58] provided two novel approaches for gust response analysis of elastic free aircraft using CFD. Furthermore, in [59] a methodology for a more computationally efficient method for the gust response analysis of elastic aircraft in the transonic flight regime was introduced.

A body of work is developing for calculation based on CFD. Guo et al. [60] performed numerical simulations for discrete gust response analysis for a free–flying flexible aircraft. Trimming results and dynamic aeroelastic open–loop calculations were presented for rigid and elastic versions of a HALE–type vehicle. Kenway et al. [61] demonstrated a parallel code to perform very large calculations on multi processors for aerostructural analysis and optimisation purposes of flexible aircraft. Romanelli et al. [62] coupled a structural model with a CFD solver and computed the aeroelastic trim of a flexible free–flying aircraft. An illustration of the implementation of a multidisciplinary nonlinear Fluid–Structure Interaction (FSI) problems was presented. Sotoudeh et al. [63] dealt with gust response analysis and provided detailed studies for nonlinear beams, coupled with a hybrid quasi–steady CFD–inflow model that captured efficiently the unsteady induced gust velocity effect. Similar work was done by Hasselbring et al. [64] with the use of a linearised unsteady Reynolds averaged Navier–Stokes (URANS) code to the unsteady gust loads computation. Moreover, Ritter [65] described the CFD dynamic analysis with fully coupled structural dynamics and rigid–body dynamics. Following this, Guo et al. [66] presented a CFD based simulation for light elastic structures in maneuvering flight and Liu et al. [67] provided an efficient CFD stability analysis of flexible aircraft by the use of reduced–order models.

In conclusion, most of the work presented so far in nonlinear coupled CFD calculations of flexible free–flying aircraft has been incomplete in some senses. Firstly, either the flight dynamic degrees–of–freedom are not included. Secondly, in most cases only static aeroelastic or trimming calculations have been provided. Lastly, the time–domain results that have been published have not presented a detailed investigation of the aeroelastic behaviour of the flexible aircraft under gust turbulence. Nevertheless, the increase in computing power and advances in the model order reduction techniques, will eventually make feasible some or all of the above.

1.3 Model Order Reduction

Model order reduction is an active mathematical field of research that focuses on the development of low–order models to describe the dynamics of the full–order dynamic equations of a system. Reduced models can be applied in control theory [68–70], for the development of a reduced–order controller that can be implemented in a physical setup.

There is a great need for the development of reduced–order models in aeroelasticity. Firstly, they can be used in parametric studies (worst–case gust searches) and significantly speed up the computations. Secondly, because they retain the dynamics of the full–order model, they can be used directly to design a low–order controller that is applicable on the original system.

Model order reduction in structural dynamics is a well established idea. Guyan [71] provided a method to reduce the equivalent mass and stiffness matrices of large order structural dynamics systems. Han et al. [72] applied the proper orthogonal decomposition (POD) in the modal analysis of homogeneous structures. The model reduction method of POD was demonstrated on a detailed finite element beam model (FEM) and the resulting POD modes were compared to the theoretical modes of the beam. Kerschen et al. [73] used POD to examine the nonlinear normal modes of nonlinear structures.

In aeroelasticity, the development of reduced–order aeroelastic models has been an active area of research. Several approaches are available and have been reviewed. Lucia et al. [74] reviewed the development of reduced–order modelling techniques such as Volterra series, proper orthogonal decomposition (POD) and harmonic balance methods (HBM). Results from two–dimensional and three–dimensional test cases were presented. In Volterra series, time–domain calculations can be used to generate system responses to produce a small–order differential equation or an integral relation between the forces and the motion. Roy et al. [75] derived linear reduced–order models for systems with rigid–body degrees–of–freedom based on a component mode synthesis. Zhou et al. [69] presented a model reduction based on the balanced realisation for unstable systems.

Pioneering work in the field was published by Galerkin [76] where the proper orthogonal decomposition (POD) method for a general equation in fluid dynamics was presented. Proper orthogonal decomposition (POD) makes use of discrete system responses to provide a set of modes that can be used to reduce the full–order equations through projection.

Willcox et al. [77] developed a new method for performing a balanced reduction of a high–order linear system. The technique combined POD and balanced realisation concepts. It used snapshots from discrete responses to obtain a low rank approximation of the observability and controllability grammians. Results were presented for a two–

dimensional aerofoil in unsteady motion. A discussion to extend the method to nonlinear systems was provided.

Aouf et al. [78] developed a systematic model–controller order reduction method applied to a flexible aircraft test case. This method was based on a mixed μ–synthesis to determine which flexible modes are kept in the model and found the corresponding reduced–order controller that guaranteed robust closed—loop performance. Numerical examples were given for a flexible model of a B–52 bomber and for a three–mass flexible system. Penz [79] presented three algorithms based on the common approximation of the controllability and observability grammians. The first two methods were related to the square root and the Schur method, while the third one was based on a heuristic balancing–free algorithm. The POD method was also applied on a three–dimensional nonlinear aeroelastic test case with moving boundaries in transonic flow for the AGARD 445.6 wing [80].

POD achieves a reduction in the number of spatial degrees–of–freedom. Moreover, if the aeroelastic response exhibits a periodic behaviour, then a reduction based in the time–domain can be achieved through an expansion in a Fourier series. Beran et al. [81] formulated a periodic coupled space–time solution method which was then reduced through a projection onto POD modes. However, not much has been presented on the development of nonlinear reduced–order model that can retain the full–order nonlinear dynamics behaviour.

Kim et al. [82] developed a new approach to generate CFD based ROMs for fast flutter analysis at reasonable computational cost. Samples of the unsteady response due to input commands were taken to identify the low–order matrices of the reduced system. The approach was demonstrated on a representative Boeing wind–tunnel airplane modelled with a finite element method and coupled with CFD.

Woodgate et al. [83] studied time–domain aeroelastic simulations. His approach made use of Hopf bifurcation and centre manifold theory to compute the flutter speed and the amplitude of a limit cycle oscillation (LCO). It was demonstrated that if the full–order semi–discrete system of equations is available, a nonlinear reduced–order model which is parametrised can be obtained if the nonlinear residual is first expanded in a Taylor series, and secondly is then projected onto a basis. In this way a reduced model was formed including nonlinear terms arising from high–order Jacobian–vector products. The evaluation of these terms provided some numerical challenges but these were overcome, and a method for systematically reducing large–order aeroelastic systems to a small–order nonlinear model for LCO prediction was demonstrated.

The method presented in [83–85] allowed the systematic prediction of a limit cycle response at a feasible computational cost with little a–priori knowledge of the system behaviour. The first step of this method presented in [83] was to calculate the linear stability boundaries using a Schur complement eigenvalue method. Secondly the aeroelastic full–order residual was expanded in Taylor series and all the terms were

projected onto the aeroelastic critical eigenvector. In order for the projection to be completed, matrix–free products were required which were evaluated using extended order arithmetic. This resulted in a nonlinear ordinary differential equation in one complex variable. That equation could be solved with little computational cost to obtain the nonlinear response of the system for chosen parameters values. Furthermore, uncertain parameters were included in the Taylor expansion, and so non–deterministic calculations for LCO response were also possible based on the reduced model. Badcock et al. [86] demonstrated all the above on a number of large dimension aeroelastic aircraft test cases.

Amsallem et al. [87] presented an interpolation method for adapting reduced–order models in aeroelasticity. He dealt with the robustness with respect to the system parameters changes and the computational cost of the reduced–order model generation. The interpolation method was based on the Grassman manifold and its tangent space, and its applicability was demonstrated on complete fighter configurations with CFD. Moreover, in [88] he dealt with the stabilisation of linear CFD based reduced–order models without affecting their accuracy. This was applied on a linearised unsteady supersonic flow, on a structural dynamics system (CSD) and on a fully coupled CSD/CFD system in the transonic flow regime. Moreover, in [89] he studied Galerkin reduced–order models for the semi–discrete wave equation. Results related to the error estimates of the approximated reduced–order model were presented. It was found that when the approximation of the POD subspace is constructed, these errors are proportional to the sum of the neglected singular values. Furthermore, in [90] a POD projection method was presented for a F–16 configuration using CFD for the subsonic, transonic and supersonic regimes. A methodology for fast, real time CFD aeroelastic computations that lies in the off–line computation of a database of reduced–order bases associated with a discrete set of flight parameters, and their corresponding interpolation method, was detailed. Another approach by the centre manifold reduction for the flutter of aerofoils under gust loading was presented in [91]. Poussot–Vassal et al. [92] presented a reduced–order model of a flexible aircraft model using Krylov methods.

Another way of model order reduction by using an ad–hoc methodology was presented recently in [93] for a linear time–variant system (LTV) and the closed–loop stabilisation of a flexible wing. Model order reduction of linear time–invariant (LTI) systems is, in general a straight forward process where one has to limit the reduction error and select the stable states to be removed. Reduced–order model generation for LTV systems systems is more complex, but techniques based on coprime factorisation have been developed [68]. The main objective of the closed–loop control was to enlarge the allowable flight envelope by stabilising the flexible modes that became unstable after a certain airspeed was exceeded.

Wang et al. [94] applied balanced POD on a three–dimensional aircraft wing and showed that while input–output behaviour was retained, the method was able to ef-

fectively reduce the order of the system and thus the computational cost. Some other researchers used model order reduction techniques to derive low–order controllers for large–order aeroelastic systems and simplify the control design process [29, 95]. In this approach the order of the aircraft was reduced with balanced truncation. This was done by the use of the Hankel singular values which provide a measure of energy for each state in a system. These values form the basis for the balanced model reduction in which high energy states are retained while low energy states are discarded. Similar reduction techniques have been applied in [52, 96, 97] but with flight dynamics degrees–of–freedom included in the model, and potential flow assumptions.

Most of the available approaches for model order reduction deal with the derivation of linear reduced–order models. One of the main contributions of this thesis is the development of nonlinear parametrised ROMs with respect to the induced gust velocity and control surface rotation and in some cases the flow conditions that retain the nonlinearity of the coupled system. This has been demonstrated with a series of two–dimensional and three–dimensional test cases coupled with a variety of lower and higher–fidelity aerodynamic solvers whose development was part of this thesis [98–103].

1.4 Control of Flexible Aircraft

The performance of very flexible aircraft can be improved by the use of active control methodologies, which makes feasible the design of lighter and larger vehicles. The objective of such an implementation is the reduction of the gust loads, the trajectory control and the stability augmentation which are achieved through feedback control, whereby actuators apply forces to the airframe based on the structural response as measured by sensors.

Control of flexible aircraft is a multidisciplinary research topic that requires tools for aerodynamic and structural dynamics and knowledge of control theory. Due to the large–order of the coupled systems, most of the time, flight control design is very challenging. The solution to that problem can come with the development of suitable reduced–order models (ROMs), so that the control system designed on the basis of the reduced model will perform well when applied to the actual distributed system. Several control approaches exist in the literature suitable for linear and nonlinear systems.

Initial approaches on the control of flexible aircraft were published in [104]. Gregory et al. [104] studied the dynamic inversion to control these aircraft. In Ref. [105] a modified dynamic inversion controller was applied on a large, highly flexible supersonic vehicle. Theoretical work on the mathematical stability of these aircraft by using dynamic inversion control was detailed in [106]. This work built on previous results based on rigid aircraft and included the new dynamics that are introduced by the flexibility effects in the mathematical stability analysis.

Aouf et al. [78] presented a systematic model order reduction method applied to the control of a flexible aircraft. The method was based on the μ synthesis and determined which flexible modes can be truncated from the full–order model of the aircraft and found a corresponding reduced–order controller that preserved robust closed–loop performance. Numerical examples were given for a B–52 bomber and for a three–mass flexible system. Sofrony et.al [93] addressed the problem of the active mode stabilisation for an aircraft with flexible wings. The main objective of the closed–loop implementation was to enlarge the allowable flight envelope (flutter speed), and this was done by stabilising flexible modes that may become unstable after a certain speed is exceeded. In that case, the original full–order model (FOM) had a large state dimension and hence a controller was designed based on the reduced–order model (ROM).

Nonlinearities in aeroelastic systems induce pathologies such as LCO under certain circumstances, and there has been limited study of the active control of these nonlinear aeroelastic systems. A linear controller usually can stabilise the nonlinear system but empirical evidence suggests that stability is not guaranteed in strongly nonlinear regimes. Strganac et al. [107] designed a nonlinear controller based on partial feedback linearisation. The approach followed, depended on the exact cancellation of the nonlinearity. Finally, an adaptive control method was introduced in which guarantees of stability were studied both mathematically and numerically.

Nevertheless, in a physical implementation whether the system is linear or nonlinear, one needs to take into account delay effects from control surfaces and measurements of the system during the feedback loop that can potentially affect the overall stability of the system under examination. Huang et al. [108] designed a Linear Quadratic Gaussian ($\mathcal{LQG}$) control that took into account such a control input delay, and demonstrated the approach on an experimental wing–tunnel model for flutter suppression. The method presented, performed better than the classical feedback and conventional $\mathcal{LQG}$ controllers, both of which do not take into account the input time delay. The problem of the flutter suppression was also studied by Yu et al. [109] who dealt with the experimental study of the flutter control for a wind–tunnel model by using an ultrasonic motor as an actuator. The aeroservoelastic system was based on Theodorsen's potential flow, and a sub–optimal controller was derived due to the fact that the aerodynamic states could not be measured directly.

A large body of work is available on the linear control for gust load alleviation and trajectory control when rigid–body degrees–of–freedom were coupled with nonlinear structural dynamics. Shearer et al. [110] presented the trajectory control of a six degrees–of–freedom body fixed reference frame coupled with a nonlinear structural model . The aerodynamic model considered was based on an unsteady finite–state potential flow. The control problem was split in two parts. A fast inner loop for the lateral motion that was controlled by a Linear Quadratic Regulator ($\mathcal{LQR}$) and for the longitudinal motion by using a nonlinear proportional, integral and derivative approach

($\mathcal{PID}$). Dillsaver et al. [29] investigated the problem of gust load alleviation by using reduced–order models for the control design. The reduction method used the balanced truncation that is based on the Hankel singular values to derive a low–order model. Assuming stochastic continuous gust models, an $\mathcal{LQG}$ controller was designed to reduce the structural deformations. Furthermore, a command tracking control system was presented for the longitudinal flight, which tracked a pitch angle command in the presence of a gust disturbance. Other approaches for gust load alleviation by means of linear optimal control were presented in [98], and in that case, an $\mathcal{H}_\infty$ controller was efficient in alleviating the gust loads for a two degree–of–freedom aerofoil with structural nonlinearities. The controller was based on the reduced model and could stabilise the nonlinear system at the worst–case gust, under realistic amplitude of induced gust velocities. $\mathcal{H}_\infty$ control based on the linear reduced–order models for the gust load alleviation has been applied also in [96] for a very flexible aircraft with a large wing dihedral.

Cook et al. [32] presented a similar approach, where the robust linear $\mathcal{H}_\infty$ control, combined with a linear model order reduction methodology, was investigated for the gust rejection on a large and very flexible aircraft using trailing–edge control surfaces. For the worst–case gust length, the controller was able to reduce the peak root bending moments by approximately 9%. As the gust length was increased, the controller achieved better reduction in the loading of the linear system, but it became less capable of rejecting the disturbances on the nonlinear model. Theoretical development of the nonlinear state feedback H_∞ control was presented by Van der Schaft [111]. He worked on a nonlinear state–space analog, based on the Hamilton–Jacobi equations and inequalities, with unified results on the $\mathcal{L}2$ gain analysis of smooth nonlinear systems. Goman et al. [112] compared classical engineering approaches to flight control system design (FCS) with the $\mathcal{H}_\infty$ control by using the rigid–body modes as feedback and notch and lag filters for the structural dynamics modes.

The nonlinear coupling of the structural dynamics and the flow equations, sometimes yields significant modelling uncertainties. A lot of work has been done on the control of linear and nonlinear systems under parametric uncertainties. For example, Fradkov et al. [113] presented a passification based robust autopilot for the attitude control of a flexible aircraft under parametric uncertainty. The application of this control methodology lies in the fact that if a system is passive with respect to some output y then it can be asymptotically stabilised by the output feedback $u = -ky$ where $k > 0$. However, with a detailed high–fidelity or even a lower–fidelity flow model this is most of the time, not true.

Schirrer et al. [114] synthesised an optimal controller using a convex approach based on the Youla parametrisation and a linear matrix inequalities (LMI) formulation for disturbance rejection of a Blended wing body (BWB) aircraft. The same authors in [115] used a D–K iteration control synthesis via a genetic algorithm to the lateral flight control design for a flexible (BWB) aircraft configuration. Smain et al. [116] applied µ-synthesis

controller design to study the robust performance for the vertical acceleration control of a B–52 longitudinal aircraft model with flexibility. The controller synthesis is shown to minimise the effect of the induced gust velocities on the aircraft vertical acceleration and in order to achieve robust performance an μ controller is synthesised using the D-K iteration procedure. Moreover, Meng et al. [117] designed an $\mathcal{H}_\infty$ controller which was consequently reduced by a linear balanced truncation and was compared with the full–order controller. However, again, most of the derived controllers were applied on relatively simplified, and small full–order systems.

Few people have applied adaptive and nonlinear control techniques in aeroelastic systems. Recent advances in adaptive control and especially in $\mathcal{L}_1$ adaptive control theory made possible the application of adaptive control of uncertain nonlinear systems [118]. This design uses a state predictor similar to the indirect model reference adaptive control schemes, however the control input is obtained by filtering the estimated control signal which guarantees the boundness of all the signals involved. Cao et al. [119] applied the $\mathcal{L}_1$ on wing–rock control and missile control [120]. Keum et al. [121] developed an $\mathcal{L}_1$ adaptive controller for a prototypical pitch–plunge two–dimensional aeroelastic system in the presence of gust loads. Other techniques of adaptive control such as model reference adaptive control have been applied to a flexible aircraft problem by using a rigid aircraft as a reference model and a neural network adaptation to control the structural flexible modes and compensate for the effects of unmodeled dynamics [122]. Recently Chowdhary et al. [123] presented flight test results for adaptive controllers based on the model reference adaptive control ($\mathcal{MRAC}$) architecture on the Georgia Tech GT Twinstar fixed wing engine aircraft with 25% of the wing missing. The second promising recent adaptive control architecture was based on the derivative–free $\mathcal{MRAC}$ method [124]. Yucelen et al. [125] presented this high–gain adaptive controller on several simple numerical examples. Gibson et al. [126] worked on the stabilisation of an unstable phugoid mode of a very flexible aircraft. Comparisons between a Linear Quadratic Gaussian controller ($\mathcal{LQG}$) and an adaptive $\mathcal{LQR}$ were provided for a relatively simple fluid–structure aircraft model that could still capture the instability.

Model predictive control ($\mathcal{MPC}$), also known as a receding horizon control, is a discrete method that is well known in the optimal control field [127]. In this technique, the control signal is calculated by performing a constrained optimisation over a finite control horizon indicated by the number of future control steps at each sampling time. Giesseler et al. [128] presented a model predictive controller for the active gust load alleviation using a gust sensor for the incoming gust shape that took gust propagation delays into account. This controller was applied on an aeroservoelastic aircraft model. Haghighat et al. [129] designed a model predictive controller to perform gust load alleviation for a very flexible aircraft with coupled rigid–body and structural dynamics. The performance of the model predictive control was improved by introducing an additional feedback–loop to increase the accuracy of the predicted future states. The efficiency

of the control system was tested for various discrete and continuous gusts. More recently, Simpson et al. [97] presented results on the gust load alleviation for very flexible aircraft using an $\mathcal{MPC}$ controller that was derived from a linear reduced–order model based on the balanced truncation. In addition, comparisons were made between the $\mathcal{MPC}$ methodology and conventional optimal linear controllers such as $\mathcal{LQR}$. It was concluded that in physical problems with control input or state constraints, the $\mathcal{MPC}$ controller was superior.

However, not much has been done on the nonlinear aeroelastic control. Lin et al. [130] investigated the effects of nonlinearities on the dynamic response and the control performance of an aeroelastic system. A nonlinear state–dependent Riccati equation method and a state feedback sub–optimal control law was derived for the aeroelastic response and flutter suppression of a three degree–of–freedom aerofoil section. Potential nonlinear control approaches as presented in [107] involved partial or full feedback linearisation. The problem in applying this method of nonlinear control lies in the fact that for systems with ill-defined relative degree usually this method needs modification. Several examples can be found in the case when nonlinear systems fail to have a well defined relative degree. For these systems, methods for constructing approximate systems that are input–output linearisable were presented in [131] and [132]. Some recent papers proposed switched controllers for nonlinear systems with ill–defined relative degree at the exact singularity points [133]. For gust load alleviation purposes though, additional unobservable aerodynamic states are introduced to describe the gust and the flap contribution for the unsteady part of the lift and moment equation and the physical applicability of the controller is difficult.

Another method, which is different from feedback linearisation, provides good stabilisation when applied to nonlinear systems, but has not been applied to the control of flexible aeroelastic systems yet, is the sum of squares ($\mathcal{SOS}$) method. This technique ($\mathcal{SOS}$) was originally introduced by Parrilo [134]. The fundamental method behind it, is that the $\mathcal{SOS}$ problems can be converted into a convex optimisation problem, which can be solved efficiently using semi–definite programming ($\mathcal{SDP}$). $\mathcal{SOS}$ nonlinear controllers have been applied to many cases, including stability analysis of nonlinear systems [135, 136]. Additional control applications of $\mathcal{SOS}$ have also been discussed in [137, 138]. In general, in order to obtain a nonlinear optimal control, one needs to solve the Hamilton–Jacobi inequality corresponding to a given performance index [111]. $\mathcal{SOS}$ optimisation may become in the future, one potential field that aerospace engineers will look into, when designing nonlinear controllers for flexible aircraft.

1.5 Thesis Outline

The coupling of the flight dynamics degrees–of–freedom with nonlinear structural dynamics will provide novel tools for the modelling and the simulation of next generation

aircraft. The resulting free–flying geometries will be of large dimension either when coupled with low–fidelity potential models or high–fidelity CFD aerodynamics. The mathematical models that describe the general formulation of the coupled structure–fluid–flight equations are given and a variety of structural models, described by the same modelling techniques, is developed.

Several optimal linear and nonlinear control techniques exist in the literature but due to the order of the aeroelastic systems are not easily applicable. To overcome these problems, a nonlinear model order reduction technique is developed which can be used to derive small–order nonlinear systems that retain the original nonlinear full–order dynamics and are suitable for control design. Controllers based on the optimal robust $\mathcal{H}_\infty$ control are tested on a variety of aeroelastic systems.

In Chapter 2, the options for the residual evaluation and the aerodynamic models are described together with the nonlinear model order reduction technique and the control design methods. Chapter 3, presents a detailed evaluation of the reduced–order model with high–fidelity and low–fidelity aerodynamics from different aeroelastic codes. The resulting reduced–order models are used for fast parametric gust studies and it is shown that the reduction technique is independent of the aerodynamic modelling. Moreover, a validation is presented for a flexible wing and a rigid free–flying wing with CFD against lower and medium–fidelity aerodynamics.

Following this, a demonstration of the control design based on $\mathcal{H}_\infty$ control is provided in Chapter 4. The controller is applied to the worst–case gust search for a two degree–of–freedom aerofoil model. Furthermore, the aeroelastic model is validated against an experimental wind–tunnel model and it is shown that different controllers, linear and nonlinear, can be designed based on that model and that nonlinear designs sometimes are superior.

A more complex aerofoil model with additional degrees-of–freedom for the flap is developed in Chapter 5. Nonlinear reduced–order models are generated to compute a worst–case gust and the resulting model is used for a nonlinear adaptive control design. This is also shown, for an unmanned aerial vehicle, where the nonlinear reduced models are used for $\mathcal{H}_\infty$ and adaptive control design for gust loads alleviation.

Finally, the flight dynamics degrees–of–freedom are included and trimming results for a rigid and a fully elastic HALE aircraft configuration are compared. It is shown that the flexibility effects play an important role in the flight dynamics analysis and need to be included. Following this, the approach is demonstrated for a very flexible high–aspect–ratio flying–wing. The flexibility effects are quantified for a gust response. Moreover, the model reduction basis is identified and convergence studies are run to construct the basis and identify the retained modes. These reduced models are then used for fast parametric gust studies and control design based on the $\mathcal{H}_\infty$ controller.

The $\mathcal{H}_\infty$ controller, performs well at specific freestream conditions, even under stochastic disturbances. However, at other freestream conditions the same controller

might even cause instability. Thus, the development of adaptive controllers is crucial. In this way, the controller gains are tuned real time and the system remains stable as its properties change.

Chapter 2

Mathematical Formulation

2.1 Full Order Model

The general form of the fully coupled fluid–structure–flight nonlinear models of arbitrary fidelity for the description of the flight dynamics of a very flexible aircraft can be represented in state–space form. Denote by $\boldsymbol{w}$ the n–dimensional state–space vector which is conveniently partitioned into fluid, structural and rigid–body degrees–of–freedom.

$$\boldsymbol{w} = \left\{\boldsymbol{w}_f^T, \boldsymbol{w}_s^T, \boldsymbol{w}_r^T\right\}^T \tag{2.1}$$

The state–space equations describing the nonlinear dynamics are written in general vector form are

$$\frac{d\boldsymbol{w}}{dt} = \boldsymbol{R}\left(\boldsymbol{w}, \boldsymbol{u}_c, \boldsymbol{u}_d\right) \tag{2.2}$$

where $\boldsymbol{R}$ is the nonlinear residual, $\boldsymbol{u}_c$ is the input vector (e.g. control flap deflections or thrust) and $\boldsymbol{u}_d$ is the exogenous vector for the description of some form of disturbance acting on the system (e.g. gust). The homogeneous system has an equilibrium point, $\boldsymbol{w}_0$, for given constant $\boldsymbol{u}_{c0}$ and $\boldsymbol{u}_{d0}$ corresponding to a constant solution in the state–space and satisfying

$$\frac{d\boldsymbol{w}_0}{dt} = \boldsymbol{R}\left(\boldsymbol{w}_0, \boldsymbol{u}_{c0}, \boldsymbol{u}_{d0}\right) = 0 \tag{2.3}$$

The residual form in Eq. (2.3) forms the reference for the model reduction described below. The system is often parametrised in terms of an independent parameter (freestream-speed, air density, altitude, etc.) for stability analysis. The options for the residual evaluation of the aeroelastic systems under examination are described in the following Chapters.

2.2 Nonlinear Model Order Reduction

Denote $\Delta \boldsymbol{w} = \boldsymbol{w} - \boldsymbol{w}_0$ the increment in the state–space vector with respect to an equilibrium solution. The large–order nonlinear residual formulated in Eq. (2.2) is expanded in a Taylor series around the equilibrium point

$$\begin{aligned} \boldsymbol{R}(\boldsymbol{w}) \approx \boldsymbol{A}\,\Delta\boldsymbol{w} + \frac{\partial \boldsymbol{R}}{\partial \boldsymbol{u}_c}\,\Delta\boldsymbol{u}_c + \frac{\partial \boldsymbol{R}}{\partial \boldsymbol{u}_d}\,\Delta\boldsymbol{u}_d + \\ \frac{1}{2}\,\boldsymbol{B}(\Delta\boldsymbol{w},\,\Delta\boldsymbol{w}) + \frac{1}{6}\,\boldsymbol{C}(\Delta\boldsymbol{w},\,\Delta\boldsymbol{w},\,\Delta\boldsymbol{w}) + \mathcal{O}\left(|\Delta\boldsymbol{w}|^4\right) \end{aligned} \tag{2.4}$$

retaining terms up to third order in the perturbation variable. The Jacobian matrix of the system is denoted as $\boldsymbol{A}$ and the vectors $\boldsymbol{B}$ and $\boldsymbol{C}$ indicate, respectively, the second and third order operators. The elements are calculated as

$$\begin{aligned} A_{ij} &= \frac{\partial R_i(\boldsymbol{w}_0)}{\partial w_j} \\ B_i(\boldsymbol{x},\,\boldsymbol{y}) &= \sum_{j,\,k} \frac{\partial^2 R_i(\boldsymbol{w}_0)}{\partial w_j\,\partial w_k}\,x_j\,y_k \\ C_i(\boldsymbol{x},\,\boldsymbol{y},\,\boldsymbol{z}) &= \sum_{j,\,k,\,l} \frac{\partial^3 R_i(\boldsymbol{w}_0)}{\partial w_j\,\partial w_k\,\partial w_l}\,x_j\,y_k\,z_l \end{aligned} \tag{2.5}$$

The full–order system is projected onto a basis formed by a small number (denoted by m) of eigenvectors of the Jacobian matrix evaluated at the equilibrium position. A clear choice for the basis is to use eigenvectors corresponding to structural modeshapes modified by the flow at the specific equilibrium point, which are readily available when tracking frequencies and modeshapes for increasing air speed. This is equivalent to adding aerodynamic mass, damping and inertia. If required, the basis can be enhanced by including additional eigenvectors until convergence. The right and left eigenvalues and eigenvectors are complex in general. The eigenvalues of $\boldsymbol{A}$ are the same as the eigenvalues of $\boldsymbol{A}^T$, whereas the eigenvectors of $\boldsymbol{A}$ are different from the eigenvectors of $\boldsymbol{A}^T$. The set of right eigenvectors $\boldsymbol{\phi}_i$ is obtained by solving

$$\boldsymbol{A}\,\boldsymbol{\phi}_i = \lambda_i\,\boldsymbol{\phi}_i \quad \text{for } i = 1, \ldots, n \tag{2.6}$$

The set of left eigenvectors, $\boldsymbol{\psi}_i$, is obtained by solving the adjoint eigenvalue problem

$$\boldsymbol{A}^T\,\boldsymbol{\psi}_i = \lambda_i\,\boldsymbol{\psi}_i \quad \text{for } i = 1, \ldots, n \tag{2.7}$$

If all the eigenvalues are distinct, the right and left eigenvectors corresponding to different eigenvalues are biorthogonal. It is then convenient to normalise the eigenvectors

to satisfy the biorthonormality conditions, expressed by

$$< \boldsymbol{\phi}_i, \boldsymbol{\phi}_i >= 1, \quad < \boldsymbol{\psi}_j, \boldsymbol{\phi}_i >= \delta_{ij}, \quad < \boldsymbol{\psi}_j, \bar{\boldsymbol{\phi}}_i >= 0 \quad \text{for } i,j = 1,\ldots,m \tag{2.8}$$

and resulting in

$$< \boldsymbol{\psi}_j, \boldsymbol{A}\,\boldsymbol{\phi}_i >= \lambda_i\,\delta_{ij}, \quad < \boldsymbol{\psi}_j, \boldsymbol{A}\,\bar{\boldsymbol{\phi}}_i >= 0 \quad \text{for } i,j = 1,\ldots,m \tag{2.9}$$

where δ_{ij} is the Kronecker delta. Note that the Hermitian inner product is defined as $< \boldsymbol{x}, \boldsymbol{y} >= \bar{\boldsymbol{x}}^T\,\boldsymbol{y}$, with the overbar denoting complex conjugation. The $(n \times m)$ right and left modal matrices, respectively, $\boldsymbol{\Phi}$ and $\boldsymbol{\Psi}$, are formed as

$$\boldsymbol{\Phi} = [\boldsymbol{\phi}_1, \ldots, \boldsymbol{\phi}_m], \quad \boldsymbol{\Psi} = [\boldsymbol{\psi}_1, \ldots, \boldsymbol{\psi}_m] \tag{2.10}$$

The full–order model is projected onto a small basis of m representative eigenvectors using a transformation of coordinates

$$\Delta\boldsymbol{w} = \boldsymbol{\Phi}\,\boldsymbol{z} + \bar{\boldsymbol{\Phi}}\,\bar{\boldsymbol{z}} \tag{2.11}$$

where $\boldsymbol{z} \in \mathbb{C}^m$ is the state-space vector governing the dynamics of the reduced–order nonlinear system.

When nonlinear terms in the Taylor series expansion of the large–order nonlinear residual are neglected, a linear reduced model can be derived. Substituting the transformation of coordinates in Eq. (2.11) into Eq. (2.4) and premultiplying each term by the conjugate transpose of the left modal matrix yields

$$\bar{\boldsymbol{\psi}}_j^T\,\left(\boldsymbol{\phi}_i\,z_i' + \bar{\boldsymbol{\phi}}_i\,\bar{z}_i'\right) = \bar{\boldsymbol{\psi}}_j^T\,\left(\boldsymbol{A}\,\boldsymbol{\phi}_i\,z_i + \boldsymbol{A}\,\bar{\boldsymbol{\phi}}_i\,\bar{z}_i + \frac{\partial\,\boldsymbol{R}}{\partial\boldsymbol{u}_c}\,\Delta\boldsymbol{u}_c + \frac{\partial\,\boldsymbol{R}}{\partial\boldsymbol{u}_d}\,\Delta\boldsymbol{u}_d\right) \quad \text{for} \quad i,j = 1,\ldots,m \tag{2.12}$$

If the eigenvalues are distinct, which is not always the case, the properties in Eqs. (2.8) and (2.9) yield the formulation of a linear ROM

$$z_i' = \lambda_i\,z_i + \bar{\boldsymbol{\psi}}_i^T\,\left(\frac{\partial\,\boldsymbol{R}}{\partial\boldsymbol{u}_c}\,\Delta\boldsymbol{u}_c + \frac{\partial\,\boldsymbol{R}}{\partial\boldsymbol{u}_d}\,\Delta\boldsymbol{u}_d\right) \quad \text{for } i = 1,\ldots,m \tag{2.13}$$

Eq. (2.13) consists of m uncoupled ordinary differential equations (ODEs). The terms of the reduced model are calculated once and for all after the eigenvalues, eigenvectors, and equilibrium are known. For large–order coupled systems, as those arising using CFD, the solution of the eigenvalue problem is a challenging task and the use of standard routines is impractical. The Schur complement eigenvalue solver from the University of Liverpool was developed for this specific problem and was applied to realistically sized aeroelastic models in Badcock et al. [139].

Manipulation of the higher–order terms in Eq. (2.4) yields the formulation of a nonlinear ROM. In addition to the linear terms in Eq. (2.12), the two contributions from the second and third Jacobian operators are

$$\bar{\boldsymbol{\psi}}_j^T \left(\frac{1}{2} B_i \left(\Delta \boldsymbol{w},\, \Delta \boldsymbol{w} \right) + \frac{1}{6} C_i \left(\Delta \boldsymbol{w},\, \Delta \boldsymbol{w},\, \Delta \boldsymbol{w} \right) \right) \tag{2.14}$$

The terms $\boldsymbol{B}$ and $\boldsymbol{C}$ are, respectively, bilinear and trilinear functions in the argument variables. This property implies that, after substitution of the transformation of coordinates, the additional terms may be written as

$$\begin{aligned} B_i \left(\Delta \boldsymbol{w},\, \Delta \boldsymbol{w} \right) = \sum_{r=1}^{m} \sum_{s=1}^{m} \Big(& B_i \left(\boldsymbol{\phi}_r,\, \boldsymbol{\phi}_s \right) z_r\, z_s + B_i \left(\boldsymbol{\phi}_r,\, \bar{\boldsymbol{\phi}}_s \right) z_r\, \bar{z}_s + \\ & B_i \left(\bar{\boldsymbol{\phi}}_r,\, \boldsymbol{\phi}_s \right) \bar{z}_r\, z_s + B_i \left(\bar{\boldsymbol{\phi}}_r,\, \bar{\boldsymbol{\phi}}_s \right) \bar{z}_r\, \bar{z}_s \Big) \end{aligned} \tag{2.15}$$

and

$$\begin{aligned} C_i \left(\Delta \boldsymbol{w},\, \Delta \boldsymbol{w},\, \Delta \boldsymbol{w} \right) = \sum_{r=1}^{m} \sum_{s=1}^{m} \sum_{t=1}^{m} \Big(& C_i \left(\boldsymbol{\phi}_r,\, \boldsymbol{\phi}_s,\, \boldsymbol{\phi}_t \right) z_r\, z_s\, z_t + C_i \left(\boldsymbol{\phi}_r,\, \boldsymbol{\phi}_s,\, \bar{\boldsymbol{\phi}}_t \right) z_r\, z_s\, \bar{z}_t + \\ & C_i \left(\boldsymbol{\phi}_r,\, \bar{\boldsymbol{\phi}}_s,\, \boldsymbol{\phi}_t \right) z_r\, \bar{z}_s\, z_t + C_i \left(\boldsymbol{\phi}_r,\, \bar{\boldsymbol{\phi}}_s,\, \bar{\boldsymbol{\phi}}_t \right) z_r\, \bar{z}_s\, \bar{z}_t + \\ & C_i \left(\bar{\boldsymbol{\phi}}_r,\, \boldsymbol{\phi}_s,\, \boldsymbol{\phi}_t \right) \bar{z}_r\, z_s\, z_t + C_i \left(\bar{\boldsymbol{\phi}}_r,\, \boldsymbol{\phi}_s,\, \bar{\boldsymbol{\phi}}_t \right) \bar{z}_r\, z_s\, \bar{z}_t + \\ & C_i \left(\bar{\boldsymbol{\phi}}_r,\, \bar{\boldsymbol{\phi}}_s,\, \boldsymbol{\phi}_t \right) \bar{z}_r\, \bar{z}_s\, z_t + C_i \left(\bar{\boldsymbol{\phi}}_r,\, \bar{\boldsymbol{\phi}}_s,\, \bar{\boldsymbol{\phi}}_t \right) \bar{z}_r\, \bar{z}_s\, \bar{z}_t \Big) \end{aligned} \tag{2.16}$$

The second and third order operators consist, in general, of $4\,m^2$ and $8\,m^3$ contributions. However, it is possible to exploit the symmetry of the operators with respect to the arguments [1], which reduces the total number of evaluations to $2\,m^2 + m$ in the case of the bilinear function. Equation (2.15) can then be rearranged as

$$\begin{aligned} B_i \left(\Delta \boldsymbol{w},\, \Delta \boldsymbol{w} \right) = \sum_{r=1}^{m} \Big(& B_i \left(\boldsymbol{\phi}_r,\, \boldsymbol{\phi}_r \right) z_r^2 + 2\, B_i \left(\boldsymbol{\phi}_r,\, \bar{\boldsymbol{\phi}}_r \right) z_r\, \bar{z}_r + B_i \left(\bar{\boldsymbol{\phi}}_r,\, \bar{\boldsymbol{\phi}}_r \right) \bar{z}_r^2 + \\ & 2 \sum_{s=r+1}^{m} \Big(B_i \left(\boldsymbol{\phi}_r,\, \boldsymbol{\phi}_s \right) z_r\, z_s + B_i \left(\boldsymbol{\phi}_r,\, \bar{\boldsymbol{\phi}}_s \right) z_r\, \bar{z}_s + \\ & B_i \left(\bar{\boldsymbol{\phi}}_r,\, \boldsymbol{\phi}_s \right) \bar{z}_r\, z_s + B_i \left(\bar{\boldsymbol{\phi}}_r,\, \bar{\boldsymbol{\phi}}_s \right) \bar{z}_r\, \bar{z}_s \Big) \Big) \end{aligned} \tag{2.17}$$

For the third order term, the total number of evaluations may be reduced to $2/3 \left(2\,m^3 + 3\,m^2 + m \right)$. For conciseness, the corresponding formulation of $\boldsymbol{C}$ is omitted.

The high–order terms required in the model reduction are represented by the bilinear and trilinear functionals formulated in Eq. (2.5). It is possible to calculate all the

[1] Note that $B_i \left(\boldsymbol{x},\, \boldsymbol{y} \right) = B_i \left(\boldsymbol{y},\, \boldsymbol{x} \right)$ and similar properties hold for the third order operator.

contributions without having to resort to complex arithmetic, or calculating all the second and third order partial derivatives analytically [83]. Because it is only their action on vectors that is required, matrix–free products are used.

For the first order Jacobian–vector product and for the second and third order operators, the directional derivatives on any set of coinciding real vectors, $\boldsymbol{x} \in \mathbb{R}^n$, can be approximated using finite differences

$$\boldsymbol{A}\,\boldsymbol{x} \;=\; \frac{\boldsymbol{R}_1 \,-\, \boldsymbol{R}_{-1}}{2\,\epsilon} \,+\, \mathcal{O}\left(\epsilon^2\right) \tag{2.18}$$

$$\boldsymbol{B}\left(\boldsymbol{x},\,\boldsymbol{x}\right) \;=\; \frac{\boldsymbol{R}_1 \,-\, 2\,\boldsymbol{R}_0 \,+\, \boldsymbol{R}_{-1}}{\epsilon^2} \,+\, \mathcal{O}\left(\epsilon^3\right) \tag{2.19}$$

$$\boldsymbol{C}\left(\boldsymbol{x},\,\boldsymbol{x},\,\boldsymbol{x}\right) \;=\; \frac{-\boldsymbol{R}_3 \,+\, 8\,\boldsymbol{R}_2 \,-\, 13\,\boldsymbol{R}_1 \,+\, 13\,\boldsymbol{R}_{-1} \,-\, 8\,\boldsymbol{R}_{-2} \,+\, \boldsymbol{R}_{-3}}{8\,\epsilon^3} \,+\, \mathcal{O}\left(\epsilon^4\right) \tag{2.20}$$

where $\boldsymbol{R}_l \;=\; \boldsymbol{R}\left(\boldsymbol{x}_0 \,+\, l\,\epsilon\,\Delta\boldsymbol{x}\right)$. Note that the system Jacobian matrix is in general available in analytic form. To calculate all the terms in Eqs. (2.15) and (2.16), a set of identities for the manipulation of terms like $\boldsymbol{B}\left(\boldsymbol{x},\,\boldsymbol{y}\right)$ and $\boldsymbol{C}\left(\boldsymbol{x},\,\boldsymbol{y},\,\boldsymbol{z}\right)$ can be derived. The following two identities

$$\boldsymbol{B}\left(\boldsymbol{x} \,+\, \boldsymbol{y},\,\boldsymbol{x} \,+\, \boldsymbol{y}\right) \;=\; \boldsymbol{B}\left(\boldsymbol{x},\,\boldsymbol{x}\right) \,+\, 2\,\boldsymbol{B}\left(\boldsymbol{x},\,\boldsymbol{y}\right) \,+\, \boldsymbol{B}\left(\boldsymbol{y},\,\boldsymbol{y}\right) \tag{2.21}$$

$$\boldsymbol{B}\left(\boldsymbol{x} \,-\, \boldsymbol{y},\,\boldsymbol{x} \,-\, \boldsymbol{y}\right) \;=\; \boldsymbol{B}\left(\boldsymbol{x},\,\boldsymbol{x}\right) \,-\, 2\,\boldsymbol{B}\left(\boldsymbol{x},\,\boldsymbol{y}\right) \,+\, \boldsymbol{B}\left(\boldsymbol{y},\,\boldsymbol{y}\right) \tag{2.22}$$

yield the desired result for the second order term

$$\boldsymbol{B}\left(\boldsymbol{x},\,\boldsymbol{y}\right) \;=\; \frac{1}{4}\left(\boldsymbol{B}\left(\boldsymbol{x} \,+\, \boldsymbol{y},\,\boldsymbol{x} \,+\, \boldsymbol{y}\right) \,-\, \boldsymbol{B}\left(\boldsymbol{x} \,-\, \boldsymbol{y},\,\boldsymbol{x} \,-\, \boldsymbol{y}\right)\right) \tag{2.23}$$

A similar set of identities is readily derived for $\boldsymbol{C}$ which combined together results in the following general formulation for a third order term

$$\begin{aligned}\boldsymbol{C}\left(\boldsymbol{x},\,\boldsymbol{y},\,\boldsymbol{z}\right) \;=\; \frac{1}{6}\Big(&\boldsymbol{C}\left(\boldsymbol{x}+\boldsymbol{y}+\boldsymbol{z},\,\boldsymbol{x}+\boldsymbol{y}+\boldsymbol{z},\,\boldsymbol{x}+\boldsymbol{y}+\boldsymbol{z}\right) \,-\, \boldsymbol{C}\left(\boldsymbol{x}+\boldsymbol{y},\,\boldsymbol{x}+\boldsymbol{y},\,\boldsymbol{x}+\boldsymbol{y}\right) \,-\\ &\boldsymbol{C}\left(\boldsymbol{x}+\boldsymbol{z},\,\boldsymbol{x}+\boldsymbol{z},\,\boldsymbol{x}+\boldsymbol{z}\right) \,-\, \boldsymbol{C}\left(\boldsymbol{y}+\boldsymbol{z},\,\boldsymbol{y}+\boldsymbol{z},\,\boldsymbol{y}+\boldsymbol{z}\right) \,+\\ &\boldsymbol{C}\left(\boldsymbol{x},\,\boldsymbol{x},\,\boldsymbol{x}\right) \,+\, \boldsymbol{C}\left(\boldsymbol{y},\,\boldsymbol{y},\,\boldsymbol{y}\right) \,+\, \boldsymbol{C}\left(\boldsymbol{z},\,\boldsymbol{z},\,\boldsymbol{z}\right)\Big)\end{aligned} \tag{2.24}$$

Because eigenvalues are complex in general, the formulations in Eqs. (2.23) and (2.24) derived for any real vector, $\boldsymbol{x},\boldsymbol{y},\boldsymbol{z} \in \mathbb{R}^n$, can be applied to any complex vector when the real and imaginary parts are treated separately. Denoting

$$\boldsymbol{p} \;=\; \boldsymbol{p}_1 \,+\, i\,\boldsymbol{p}_2, \quad \boldsymbol{p} \in \mathbb{C}^n, \quad \boldsymbol{p}_1,\,\boldsymbol{p}_2 \in \mathbb{R}^n \tag{2.25}$$

it follows that, for example,

$$\boldsymbol{B}\left(\boldsymbol{p},\,\boldsymbol{p}\right) \;=\; \boldsymbol{B}\left(\boldsymbol{p}_1,\,\boldsymbol{p}_1\right) \,-\, \boldsymbol{B}\left(\boldsymbol{p}_2,\,\boldsymbol{p}_2\right) \,+\, 2\,i\,\boldsymbol{B}\left(\boldsymbol{p}_1,\,\boldsymbol{p}_2\right) \tag{2.26}$$

and

$$\boldsymbol{C}\left(\boldsymbol{p},\,\boldsymbol{p},\,\boldsymbol{p}\right) \,=\, \boldsymbol{C}\left(\boldsymbol{p}_1,\,\boldsymbol{p}_1,\,\boldsymbol{p}_1\right) \,-\, 3\,\boldsymbol{C}\left(\boldsymbol{p}_1,\,\boldsymbol{p}_2,\,\boldsymbol{p}_2\right) \,+\, i\left(3\,\boldsymbol{C}\left(\boldsymbol{p}_1,\,\boldsymbol{p}_1,\,\boldsymbol{p}_2\right) \,-\, \boldsymbol{C}\left(\boldsymbol{p}_2,\,\boldsymbol{p}_2,\,\boldsymbol{p}_2\right)\right) \tag{2.27}$$

The evaluation of the finite differences suffers from the truncation error for values of the step size ϵ which are too large, and from the rounding error for values which are too small. The latter effect is more significant for the coefficients that include a third order product. Woodgate et al. [83] and Badcock et al. [84] conducted convergence studies and obtained a reliable set of coefficients for the reduced model over a significant range of ϵ.

A major computational challenge arises when using CFD as the source of the aerodynamic predictions. The solution of a large sparse linear system arising from an eigenvalue problem is needed for model generation, see Eq. (2.11). To overcome this, the Schur complement eigenvalue formulation is used. The method leads to a small nonlinear eigenvalue problem that can be solved rapidly by removing the need to solve large sparse linear systems that are almost singular. The solution against the coupled system Jacobian matrix of Eq. (2.2) is most conveniently done by partitioning the matrix as

$$\boldsymbol{A} \,=\, \left[\begin{array}{cc} \frac{\partial\,\boldsymbol{R}_f}{\partial\boldsymbol{w}_f} & \frac{\partial\,\boldsymbol{R}_f}{\partial\boldsymbol{w}_s} \\ \frac{\partial\,\boldsymbol{R}_s}{\partial\boldsymbol{w}_f} & \frac{\partial\,\boldsymbol{R}_s}{\partial\boldsymbol{w}_s} \end{array}\right] \,=\, \left[\begin{array}{cc} \boldsymbol{A}_{ff} & \boldsymbol{A}_{fs} \\ \boldsymbol{A}_{sf} & \boldsymbol{A}_{ss} \end{array}\right] \tag{2.28}$$

The block $\boldsymbol{A}_{ff}$ represents the influence of the fluid unknowns on the fluid residual and has by far the largest number of non–zeros for the structural models used. The term $\boldsymbol{A}_{fs}$ arises from the dependence of the CFD residual on the mesh motion and speeds, which depend in turn on the structural solution, and is evaluated by finite difference. The term $\boldsymbol{A}_{sf}$ is due to the dependence of the generalised forces on the surface pressures. Finally, the block $\boldsymbol{A}_{ss}$ is the Jacobian of the structural equations with respect to the structural unknowns.

Write the coupled system eigenvalue problem as

$$\left[\begin{array}{cc} \boldsymbol{A}_{ff} & \boldsymbol{A}_{fs} \\ \boldsymbol{A}_{sf} & \boldsymbol{A}_{ss} \end{array}\right] \boldsymbol{p} \,=\, \lambda\,\boldsymbol{p} \tag{2.29}$$

where $\boldsymbol{p}$ and λ are the complex eigenvector and eigenvalue, respectively. Partition the eigenvector as

$$\boldsymbol{p} \,=\, \left\{\boldsymbol{p}_f^T,\,\boldsymbol{p}_s^T\right\}^T \tag{2.30}$$

By substituting $\boldsymbol{p}_f$ from the first set of equations into the second set of equations in Eq. (2.29), it can be found that the eigenvalue λ, assuming it is not an eigenvalue of

$\boldsymbol{A}_{ff}$, satisfies the nonlinear eigenvalue problem

$$\boldsymbol{S}(\lambda)\,\boldsymbol{p}_s = \lambda\,\boldsymbol{p}_s \tag{2.31}$$

where $\boldsymbol{S}(\lambda) = \boldsymbol{A}_{ss} - \boldsymbol{A}_{sf}\left(\boldsymbol{A}_{ff} - \lambda I\right)^{-1}\boldsymbol{A}_{fs}$. The matrix $\boldsymbol{S}(\lambda)$ is the sum of the structural matrix and a second term arising from the coupling of the fluid and structure. The nonlinear Eq. (2.31) is solved using Newton's method. To overcome the cost of forming the residual and its Jacobian matrix at each iteration, an approximation of $\left(\boldsymbol{A}_{ff} - \lambda I\right)^{-1}$ is used. More details on the Schur complement eigenvalue solver and its application to realistically sized aeroelastic models can be found in Badcock et al. [139]

2.2.1 Gust Treatment in the Reduced Order Models

2.2.1.1 Overview

The determination of the worst–case structural forces from an encounter with idealised atmospheric disturbances is an important problem in aircraft design [140]. Whether the atmospheric disturbance is characterised by deterministic or stochastic functions defined by a frequency power spectrum and the Gaussian distribution for the frequency content at any particular time, the turbulence is specified as a change in the freestream airflow over the aircraft. The established analysis methods are linear, using potential flow aerodynamics. This allows superposition and frequency domain calculations to be exploited. In CFD simulations the specification of the gust is more complicated. First, the frequency domain formulation is nonlinear, meaning that the calculation is likely to be done in the time–domain, implying a high computational cost and that each gust must be analysed with a new calculation. Secondly, in principle it is straightforward to apply an atmospheric disturbance as a far field boundary condition. In practice however, numerical dissipation makes it difficult to propagate this disturbance to the interaction with the aircraft. To overcome this problem a simpler simulation is formulated that applies the disturbance to the mesh velocities only. This does not allow for the gust to be modified by the interaction.

2.2.1.2 Treatment in Computational Fluid Dynamics Model

Parameswaran et al. [141] presented a method for gust calculations, the field–velocity approach which is also used in this work. The gust is introduced into the CFD solver by modification of the velocity of the grid points during the unsteady motion of the aircraft. A disadvantage of the field–velocity approach is that the gust is assumed frozen, and the influence of the structural response on the gust is neglected. The approach has received widespread use because of the lack of alternative methods.

The disturbance vector is denoted by

$$\Delta \boldsymbol{u}_d = \{u_{g\,x},\, u_{g\,y},\, u_{g\,z}\}^T \tag{2.32}$$

This vector depends on time and is applied to the mesh velocities before the calculation of the residual. Without loss of generality, the treatment in the model order reduction is illustrated for the vertical component of gust velocity, $u_{g\,z}$.

The new challenge is to calculate a term in the reduced model to represent the gust. This term corresponds to the contribution in Eq. (2.4) given by

$$\frac{\partial \boldsymbol{R}}{\partial \boldsymbol{u}_d} \Delta \boldsymbol{u}_d.$$

The derivation of this contribution should be independent of the gust allowing different gusts to be applied to the reduced model without any recalculation.

Using the chain rule, the dependence of the nonlinear full–order residual on the gust perturbation is rewritten as

$$\frac{\partial \boldsymbol{R}}{\partial u_{g\,z}} = \frac{\partial \boldsymbol{R}}{\partial \dot{\boldsymbol{z}}} \frac{\partial \dot{\boldsymbol{z}}}{\partial u_{g\,z}} \tag{2.33}$$

where $\dot{\boldsymbol{z}}$ is the mesh velocity vector. The first term on the right side depends on the point coordinates only and can be computed independent of the gust definition using finite differences or analytical differentiation.

The gust is defined as a function of space and time such as $u_{g\,z}\,(x, y, z, t)$ and as a result the second term on the right side of Eq. (2.33) depends on both spatial and temporal coordinates. The time–domain gust response using a ROM, as formulated by Da Ronch et al. [98], requires the calculation at each time step of the following contribution

$$\bar{\boldsymbol{\psi}}_i^T \frac{\partial \boldsymbol{R}}{\partial \dot{\boldsymbol{z}}} \frac{\partial \dot{\boldsymbol{z}}}{\partial u_{g\,z}} \tag{2.34}$$

where $\bar{\boldsymbol{\psi}}$ is the matrix of the eigenvectors $\boldsymbol{A}^T$. The first two terms on the left side involve a matrix–vector multiplication, and this can be done before the time–domain ROM simulation. At each time step iteration, the vector on the right side needs to be updated to account for the gust translation, and the scalar product of two vectors is then needed. Therefore, at each time step of the ROM, an inner product of two vectors of the dimension of the CFD mesh is needed, increasing the cost of calculating solutions by the ROM. However, the CFD code does not need to be accessed for this operation, which requires only the grid point coordinates, and the ROM can be applied to any definition of discrete or continuous gust.

2.3 Aerodynamic Model

Several options for the aerodynamics can be used. Using an engineering approach, an aerodynamic model being as simple as possible yet sufficiently accurate is incorporated. In the most simple case, a two–dimensional linear aerodynamic model can be used on a representative two–dimensional section of the aeroelastically most critical lifting surface. The unsteady flow is modelled in this approach by a frequency domain expression for the incompressible two–dimensional potential flow over a flat plate in harmonic motion, originally formulated by Theodorsen [22].

An extension to this approach, called strip theory, adapts the same two–dimensional unsteady flow model for a three–dimensional aeroelastic system by combining section aerodynamics with a beam model for the wing structure. Strip theory can provide fairly reliable, and usually conservative, results for divergence speed, critical flutter speed and aileron reversal. However, it requires that the physical characteristics of the aircraft configuration under analysis can be adequately reduced to a beam–type structure and that three–dimensional aerodynamic effects do not have a significant impact on the aerodynamics.

The total aerodynamic loads consist of contributions arising from the section motion, trailing–edge flap rotation, and the penetration into a gusty field as illustrated in Figure 2.1. The aerodynamic loads due to an arbitrary input time–history are obtained through convolution against a kernel function. Since the assumption is of linear aerodynamics, the effects of the various influences on the aerodynamic forces and moments are added together to find the variation of the forces and moments in time for a given motion and gust. It follows that

$$C_i = C_{i,s} + C_{i,f} + C_{i,g} \tag{2.35}$$

where the dependence on time is not shown explicitly. The sub–index i is used for denoting the lift coefficient, $i = L$, and pitch moment coefficient, $i = m$, whereas s, f, and g indicate the contributions from the section motion, flat rotation, and gust perturbation, respectively. A schematic representation of the various contributions to the aerodynamic loads is shown in Figure 2.1 . A brief description of each contribution to the total aerodynamic loads is summarised in the following three sections.

2.3.1 Section Motion

The first term on the right hand side of Eq. (2.35) indicates the increment in the aerodynamic loads caused by a generic motion of the wing section. Each structural node of the beam stick model, has six degrees–of–freedom that consist of three rotations and three translations. As the aerodynamic model here presented is two–dimensional, the resulting motion of the wing section that occurs in the three–dimensional space is

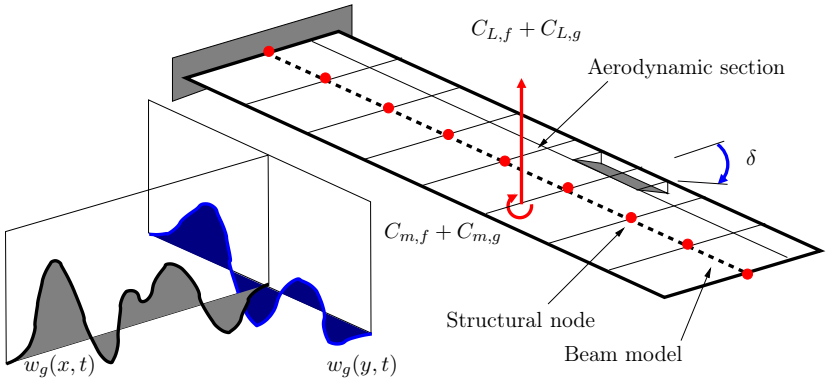

(a) Trailing–edge control surfaces and atmospheric gust u_g

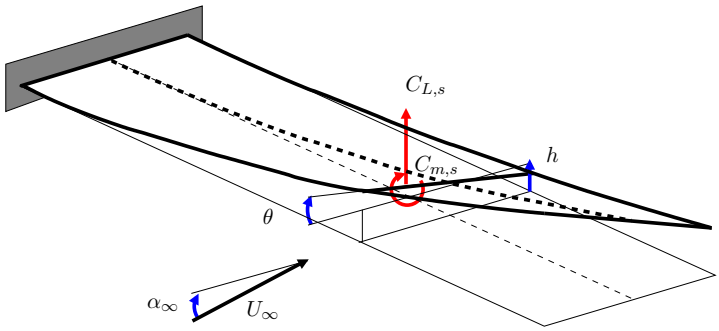

(b) Wing section structural deformations ($h, \alpha = \alpha_\infty + \theta$)

Figure 2.1: Schematic of a slender wing structure showing various contributions to the aerodynamic loads, as in Ref. [142]

projected on the plane defining the wing cross–section. Referring to Figure 2.1(b), the motion of the wing section contributing to the aerodynamic loads consists of the vertical displacement of the structural beam model, denoted by h, and a rotation around the elastic axis, denoted by θ. This information is readily available from the solution of the structural problem.

Denote by α the effective angle of incidence of the wing section which includes the freestream angle of attack, α_∞, and the wing torsional deformation, θ. Scale the vertical displacement, h, by the semichord of the wing cross section, $\xi = h/b$. The resulting force and moment coefficients for any arbitrary section motion in pitch and plunge are formulated as in [31]

$$\begin{aligned} C_{L,s}(\tau) =& \pi \left(\xi''(\tau) - a_h \alpha''(\tau) + \alpha'(\tau)\right) + \\ & 2\pi \left(\alpha_0 + \xi_0' + (1/2 - a_h)\alpha_0'\right) \phi_w(\tau) + \\ & 2\pi \int_0^\tau \phi_w(\tau - \sigma) \left(\alpha'(\sigma) + \xi''(\sigma) + (1/2 - a_h)\alpha''(\sigma)\right) d\sigma \qquad (2.36) \\ C_{m,s}(\tau) =& \pi (1/2 + a_h) \left(\alpha_0 + \xi_0' + (1/2 - a_h)\alpha_0'\right) \phi_w(\tau) + \\ & \pi (1/2 + a_h) \int_0^\tau \phi_w(\tau - \sigma) \left(\alpha'(\sigma) + \xi''(\sigma) + (1/2 - a_h)\alpha''(\sigma)\right) d\sigma + \\ & \frac{\pi}{2} a_h \left(\xi''(\tau) - a_h \alpha''(\tau)\right) - (1/2 - a_h) \frac{\pi}{2} \alpha'(\tau) - \frac{\pi}{16} \alpha''(\tau) \qquad (2.37) \end{aligned}$$

The Wagner function, ϕ_w, accounts for the influence of the shed wake, and is known exactly in terms of Bessel functions. For a practical evaluation of the integral, the exponential approximation of [143] is used

$$\phi_w(\tau) = 1 - \Psi_1 e^{-\varepsilon_1 \tau} - \Psi_2 e^{-\varepsilon_2 \tau} \qquad (2.38)$$

where the constants are $\Psi_1 = 0.165$, $\Psi_2 = 0.335$, $\varepsilon_1 = 0.0455$, and $\varepsilon_2 = 0.3$.

2.3.2 Trailing–edge Flap Rotation

The second term on the right hand side of Eq. (2.35) represents the increment in the aerodynamic loads for any arbitrary trailing–edge rotation, see Figure 2.1(a). The build–up in the loads not only depends on the instantaneous flap rotation, but also on its time derivatives (speed and acceleration). The relations between the control surface

input, δ, and the load coefficients are

$$
\begin{aligned}
C_{L,f}(\tau) = & -T_4\,\delta'(\tau) - T_1\,\delta''(\tau) + \\
& 2\,\pi\left[\left(\frac{1}{\pi}\,T_{10}\,\delta_0 + \frac{1}{2\,\pi}\,T_{11}\,\delta_0'\right)\phi_w(\tau) + \right. \\
& \left.\int_0^\tau \left(\frac{1}{\pi}\,T_{10}\,\delta' + \frac{1}{2\,\pi}\,T_{11}\,\delta''\right)\phi_w(\tau-\sigma)\,d\sigma\right] \qquad (2.39)\\
C_{m,f}(\tau) = & -\frac{(T_4+T_{10})}{2}\,\delta(\tau) - \\
& \frac{\left(T_1 - T_8 - (c-a_h)\,T_4 + \frac{1}{2}\,T_{11}\right)}{2}\,\delta'(\tau) + \\
& \frac{(T_7 + (c-a_h)\,T_1)}{2}\,\delta''(\tau) + \\
& \pi\,(a_h + 1/2)\left[\left(\frac{1}{\pi}\,T_{10}\,\delta_0 + \frac{1}{2\,\pi}\,T_{11}\,\delta_0'\right)\phi_w(\tau)) + \right. \\
& \left.\int_0^\tau \left(\frac{1}{\pi}\,T_{10}\,\delta' + \frac{1}{2\,\pi}\,T_{11}\,\delta''\right)\phi_w(\tau-\sigma)\,d\sigma\right] \qquad (2.40)
\end{aligned}
$$

The coefficients T_1, T_4, T_7, T_8, T_{10}, and T_{11} are geometric constants that depend on the size of the trailing–edge flap relative to the chord of the wing section. Detailed full expressions can be found in [144].

2.3.3 Atmospheric Gust

The last term on the right hand side of Eq. (2.35) describes the effect that atmospheric gust and turbulence have on the build–up of aerodynamic loads. For an arbitrary gust time history, the load coefficients are computed by the following relations as in [31].

$$C_{L,g}(\tau) = \frac{2\,\pi}{U^*}\left(w_{g0}\,\Psi_k(\tau) + \int_0^\tau \Psi_k(\tau-\sigma)\,\frac{d\,w_g}{d\sigma}\,d\sigma\right) \qquad (2.41)$$

$$C_{m,g}(\tau) = \frac{\pi}{U^*}\,(1/2 + a_h)\left(w_{g0}\,\Psi_k(\tau) + \int_0^\tau \Psi_k(\tau-\sigma)\,\frac{d\,w_g}{d\sigma}\,d\sigma\right) \qquad (2.42)$$

The integration uses the exponential approximation of the Küssner function

$$\Psi_k(\tau) = 1 - \Psi_3\,e^{-\varepsilon_3\,\tau} - \Psi_4\,e^{-\varepsilon_4\,\tau} \qquad (2.43)$$

where the coefficients $\Psi_3 = 0.5792$, $\Psi_4 = 0.4208$, $\varepsilon_3 = 0.1393$, and $\varepsilon_4 = 1.802$ are from [31]. Appropriate forms of w_g to model realistic atmospheric gust and turbulence time histories are presented in some detail in Section 2.4.

2.4 Atmospheric Turbulence Models

In flight, aircraft regularly encounter atmospheric turbulence. The turbulence is regarded for linear analysis as a set of component velocities superimposed on the background steady flow. The aircraft experiences rapid changes in the lift and the moment, which causes rigid and flexible dynamic responses of the entire body. These responses may introduce large loads on the structure which can cause passenger discomfort, compromise the overall aircraft safety, and as a result, need to be accounted for during the early design stage. The numerical models used for the prediction of the aircraft response under these discrete deterministic or random turbulence are well established. A concise summary of the mathematical models used to approximate discrete and continuous turbulent events is given next. A more extensive review can be found in [145, 146].

2.4.1 Discrete Deterministic Gusts Models

Discrete gusts are defined as distinct steep gradients in the speed of air. These typically occur at the edges of thermals and downdrafts, in the wakes of structures or mountains, or inside clouds. However, the description of these events is not allowed for in the typical Gaussian models of continuous stochastic turbulence. In addition, some discrete deterministic functions are used.

The most common discrete gust model, which has evolved over the years from the isolated sharped–edge gust function in the earliest airworthiness requirements, is the "1-minus-cosine" function. Its formulation is

$$w_g\left(x,\, t\right) \,=\, \begin{cases} \frac{1}{2}\, w_{g0}\, \left(1 - \cos\left(\frac{\pi U_\infty}{H_g}\, \left(t - \frac{x}{U_\infty}\right)\right)\right) & x \in [tU_\infty - 2H_g,\, tU_\infty] \\ 0 & \text{otherwise} \end{cases} \tag{2.44}$$

where w_{g0} is the gust intensity, H_g is the gust length, and x is the position of a point on the aircraft relative to an aircraft–attached frame of reference, see Figure 2.2. The design gust velocity, w_{g0}, varies with the gust length, altitude, and flight speed [146]. In the simple case of Equation (5.7), the gust intensity depends on one spatial coordinate, x, in addition to the time coordinate, t. The rate of change of the gust intensity at different points located on the aircraft, e.g. main wing and tailplane, largely depends on two ratios, see Figure 2.2. The first ratio describes the relative size of the gust compared to the aircraft characteristic length. The second ratio relates to the time it takes for the aircraft to fly over the gusty field. As these two ratios decrease, the dependence on the spatial coordinate becomes more and more apparent and should be modelled appropriately in simulating the aircraft response to relatively short gusts.

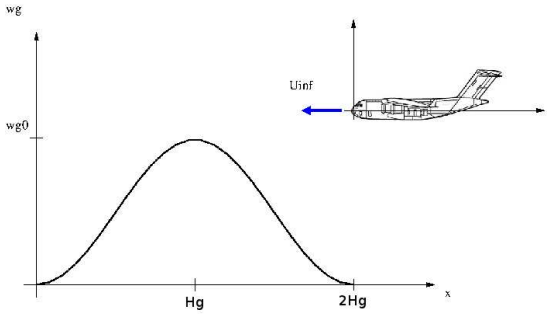

(a) Frames in relative motion

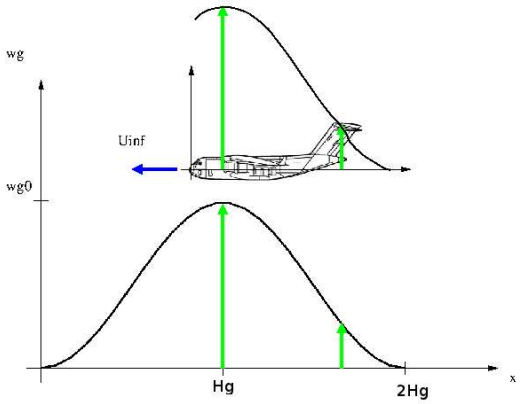

(b) Gust penetration effect

Figure 2.2: Discrete model of a "1-minus-cosine" gust, as in [142]

2.4.2 Random Turbulence

Random turbulence refers to the chaotic motion of the air that is described by its statistical properties. The main statistical features that need to be considered are: stationarity, homogeneity, isotropy, time and distance scales, probability distributions, correlations, and spectra. Atmospheric turbulence is a vector process in which the velocity vector is a random function of time and of the position vector. Because of the complexity introduced by this multi–dimensionality, the description of turbulence and the associated input/response problems are often simplified, whether justified or not, to a one–dimensional representation.

The engineering model of random turbulence at altitude has been established for many years, see for example [147]. It is now widely accepted that it is satisfactory to treat atmospheric turbulence as frozen, homogeneous, and isotropic in relatively large patches. There are two widely accepted mathematical models to describe the random turbulence, the Dryden, and the Von Kármán. Experimental evidence has suggested that these models and especially the Von Kármán, predict well the correlation and the spectra of the stochastic turbulence. Although there is much evidence that turbulence is not in fact a Gaussian process, with small and large values both occurring more frequently than in a normal distribution, the assumption that individual patches are Gaussian is widely used because of the great analytical advantage it offers.

A commonly used spectrum that matches experimental data is the von Kármán model. The power spectral density (PSD, in $[\mathrm{m}^2/(\mathrm{s}^2\ \mathrm{Hz})]$) for the vertical velocity, Φ_z, according to the Military Specification MIL–F–8785C, see [148], is given by

$$\Phi_z(\Omega) = \frac{\sigma_z^2\, 2L_z}{U_\infty} \frac{1 + 8/3\,(a\,L_z\,\Omega)^2}{\left(1 + (a\,L_z\,\Omega)^2\right)^{11/6}} \tag{2.45}$$

where $\Omega = \omega/U_\infty$ is the scaled frequency (in [rad/m]), σ_z is the root mean square turbulence velocity (in [m/s]), L_z is the characteristic scale wavelength of the turbulence (in [m]), and $a = 1.339$ is the von Kármán constant. Figure 2.3 illustrates the PSD spectrum as a function of the frequency. The system response in the frequency domain to a random turbulence can easily be calculated once the frequency response function is known [149]. This approach is linear and does not permit nonlinear effects to be included in the analysis. An alternative approach is to generate a random turbulence time signal with the required spectral characteristics defined in Eq. (2.45).

A method to calculate the time–domain response of a nonlinear aeroelastic model to random turbulence is based on the following steps. First, take the Fourier transform of a unit variance band–limited white noise signal, $X(\Omega)$, and pass it through a filter defined as the square root of the PSD spectrum in Eq. (2.45), $H_z(\Omega)$. Then, calculate

the output signal using the relation

$$W_g(\Omega) = H_z(\Omega)\, X(\Omega) \tag{2.46}$$

Take the inverse Fourier transform of $W_g(\Omega)$ to obtain the random turbulence in the time–domain, w_g. This method, which applies a Fourier transform twice, is preferred over an alternative method that does not make use of the Fourier transform. More details can be found in [150]. The method described above is implemented in an open source MATLAB toolbox and is referred to as the Von Kármán Turbulence Generator (VKTG). The VKTG toolbox implements the mathematical representation of random turbulence in the Military Specification MIL–F–8785C and Military Handbook MIL–HDBK–1797, allowing for the dependence of the root mean square turbulent velocity and turbulence length scale on aircraft mission parameters and weather conditions. As demonstrated in Figure 2.3, the PSD of the VKTG model shows a closer correlation at higher frequencies with the von Kármán spectrum of Eq. (2.45) compared to the off-the-shelf Simulink model.

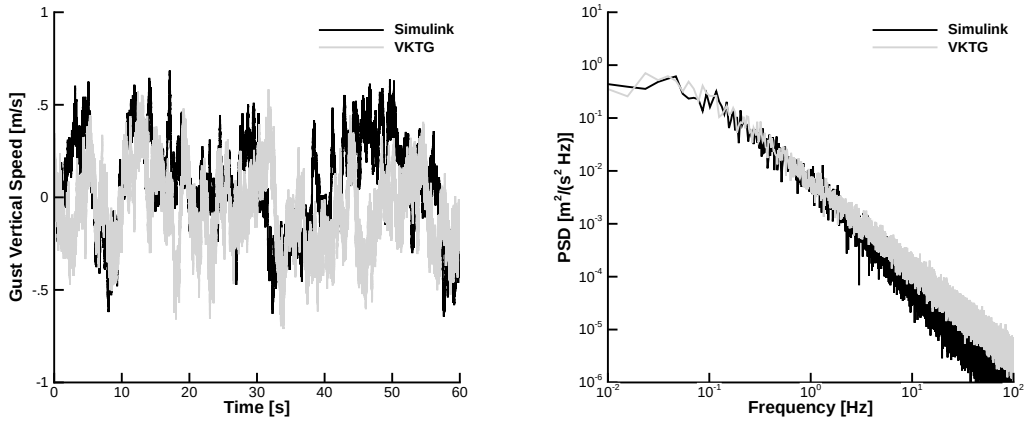

(a) Time history of stochastic vertical gust

(b) Power spectral density (PSD)

Figure 2.3: Random vertical gust intensity using the Von Kármán spectral representation (Military Specification: MIL–F–8785C; flight speed: $V = 280$ m/s; altitude: $h = 10,000$ m; and turbulence intensity: "light 10^{-2}"); the terms "Simulink" and "VKTG" denote, respectively, the Von Kármán Wind Turbulence Model block of MATLAB and the present Von Kármán Turbulence Generator implementation, as in [142]

2.5 Control Design Using Nonlinear Reduced Models

2.5.1 Overview

As already reviewed, there are many different techniques in control theory, linear and nonlinear, static and adaptive. However, all of these techniques have been applied to very small systems and in large complicated models, most times, very simple controllers are implemented (e.g. $\mathcal{PID}$). This is also the case when dealing with flexible aircraft control and the control of large–order nonlinear systems. Herein, the implementation of more unconventional controllers such as $\mathcal{H}_\infty$ and adaptive control is made possible by the model order reduction technique. As a result, two inherently different control methodologies are derived and applied to nonlinear systems of thousands degrees–of–freedom, based on the same reduced–order model.

The first methodology based on the $\mathcal{H}_\infty$ robust control is well established and its mathematical derivation and stability aspects are detailed in [151]. In flexible aircraft dynamics, a small order linear controller is derived based on the reduced–order model that measures physical displacements of the output of the system, either the pitch or the plunging motion of the aircraft, and applies the resulting control input signal on the nonlinear full–order model.

One of the fundamental ideas of adaptive control is to estimate uncertain plant or controller parameters on–line, while using measured signals. These estimated parameters are used to update the dynamic controller at the current timestep. As a result, an adaptive controller can be viewed as a dynamic system with on–line parameter estimation. This adaptive design is inherently nonlinear and the analysis and its design relies on Lyapunov stability theory. Initial interest in adaptive control techniques is found in the early 1950s with an autopilot design for high performance aircraft even though the interest was diminished due to the crash of a test flight. The reason it failed was that the Lyapunov stability for nonlinear systems was not well established and the stability of the systems relied mostly upon the selection of the adaptation parameters. However, Lyapunov stability analysis in the 1960s made possible the first applications in adaptive control.

The most well known method in adaptive control is the model reference adaptive control ($\mathcal{MRAC}$). In this case, the plant has a known structure with some unknown parameters. There is also a reference model which consists the ideal model of which one desires to match the response. The controller is parametrised and provides tracking. The adaptation is used to adjust the parameters in the control law at every time step. Model reference adaptive control can be distinguished between the direct and the indirect approach. The first one does not use any plant parameters estimation but estimates the controller gains instead. In the indirect approach, the plant parameters are estimated and this is used to compute the controller parameters. The latter method depends on the convergence of the estimated parameters to their true unknown value.

The examination of this methodology when dealing with flexible aircraft control design is crucial. The reason is that the dynamics of the coupled nonlinear system is a function of the density, freestream speed and deformations. A controller derived at a specific freestream is maybe able to control the nonlinear system in a robust way at the specific flow conditions, or slight variations from the design speed (e.g. $\mathcal{H}_\infty$). However, if the freestream speed changes, the dynamics of the system change as well and nothing can guarantee the stability of the closed–loop nonlinear system in that case. Furthermore, the dynamics of the flexible aircraft change even more drastically with the flow conditions which makes the concept of one controller for a large flight envelope unrealistic. Thus, the testing of the adaptive control methodology becomes important for a realistic application where there are changes in the density that are simply caused by changes in the altitude, or changes in the freestream speed. Herein, the nonlinear reduced–order model is interconnected with an ideal reference model. A full state–feedback information is assumed available from the reduced–order model and the control signal, flap rotation, is directly applied on the nonlinear full–order model.

2.5.1.1 $\mathcal{H}_\infty$ Synthesis

This section describes the $\mathcal{H}_\infty$ control design process for the reduced–order models. The $\mathcal{H}_\infty$ controller, designed based on the linear reduced–order model, is directly applied on the nonlinear full–order model in Eq. (2.2) and can be expressed as

$$\dot{\boldsymbol{x}}(t) = \boldsymbol{A}\,\boldsymbol{x}(t) + \boldsymbol{B}_c\,\boldsymbol{u}_c(t) + \boldsymbol{B}_{c1}\,\dot{\boldsymbol{u}}_c(t) + \boldsymbol{B}_{c2}\,\ddot{\boldsymbol{u}}_c(t) + \boldsymbol{B}_g\,\boldsymbol{u}_d(t) \tag{2.47}$$

The matrix $\boldsymbol{A}$ contains the eigenvalues of the coupled reduced system and $\boldsymbol{B}_c, \boldsymbol{B}_{c1}, \boldsymbol{B}_{c2}$ are the control derivatives corresponding to rotation, angular velocity and angular acceleration of the control surfaces. The gust terms are given in $\boldsymbol{B}_g$. The system is rewritten introducing the flap rotation and angular velocity into the state vector, with the angular acceleration as a control input.

$$\begin{Bmatrix} \boldsymbol{x} \\ \boldsymbol{u}_c \\ \dot{\boldsymbol{u}}_c \end{Bmatrix}' = \begin{bmatrix} \boldsymbol{A} & \boldsymbol{B}_c & \boldsymbol{B}_{c1} \\ \boldsymbol{0} & 0 & 1 \\ \boldsymbol{0} & 0 & 0 \end{bmatrix} \begin{Bmatrix} \boldsymbol{x} \\ \boldsymbol{u}_c \\ \dot{\boldsymbol{u}}_c \end{Bmatrix} + \begin{Bmatrix} \boldsymbol{B}_{c2} \\ 0 \\ 1 \end{Bmatrix} \ddot{\boldsymbol{u}}_c + \begin{Bmatrix} \boldsymbol{B}_g \\ 0 \\ 0 \end{Bmatrix} \boldsymbol{u}_d \tag{2.48}$$

Rewrite the above equation as

$$\dot{\boldsymbol{x}}_e(t) = \boldsymbol{A}_e\,\boldsymbol{x}_e(t) + \boldsymbol{B}_e\,\ddot{\boldsymbol{u}}_c(t) + \boldsymbol{D}_e\,\boldsymbol{u}_d(t) \tag{2.49}$$

where $\ddot{\boldsymbol{u}}_{\boldsymbol{c}}$ is the flap angular acceleration. The output equation is derived from Eq. (2.11). The $\mathcal{H}_\infty$ control problem with additional input-shaping techniques for control tuning purposes for the classical $\mathcal{H}_\infty$ problem formulation is solved as in Ref. [151].

Thus, the complete set of equations for the control problem design become

$$\left\{ \begin{array}{c} \boldsymbol{x}'_e \\ \boldsymbol{y}_{ctl} \\ \boldsymbol{y}_{meas} \end{array} \right\} = \left[\begin{array}{ccc} \boldsymbol{A}_e & \boldsymbol{D}_e & \boldsymbol{B}_e \\ C_1 & \boldsymbol{D_{11}} & \boldsymbol{D_{12}} \\ C_2 & \boldsymbol{D_{21}} & \boldsymbol{D_{22}} \end{array} \right] \left\{ \begin{array}{c} \boldsymbol{x_e} \\ \boldsymbol{u}_d \\ \ddot{\boldsymbol{u}}_c \end{array} \right\} \tag{2.50}$$

where C_1, C_2 are the representative eigenvectors of the reduced–order model dynamics. where $\boldsymbol{D}_{12} = [0 \qquad \boldsymbol{K}_c]$ and $\boldsymbol{D}_{11} = 0$, $\boldsymbol{D}_{21} = [0 \qquad \boldsymbol{K}_d]$, $\boldsymbol{D}_{22} = 0$. The output is distinguished by what the controller is aiming to control $\boldsymbol{y}_{ctl}$ and what the controller has information about $\boldsymbol{y}_{meas}$ which in that case is the structural wing deformation. The resulting controller has the linear form

$$\boldsymbol{u}(s) = \boldsymbol{K}(s)\, \boldsymbol{y}_{meas}(s) \tag{2.51}$$

where $\boldsymbol{K}(s)$ is the $\mathcal{H}_\infty$ controller transfer function in the Laplace domain. It is one that aims to minimise the transfer of the disturbance signal from $\boldsymbol{u}_d$ to $\boldsymbol{y}_{ctl}$ by creating a controller that uses information from $\boldsymbol{y}_{meas}$ to change the input $\boldsymbol{u}_c$. This can be written as

$$\frac{sup \int_0^\infty ||\boldsymbol{y}_{meas}(t)||^2 dt}{sup \int_0^\infty ||\boldsymbol{u}_d(t)||^2 dt} \leq \gamma \tag{2.52}$$

where γ represents the ratio of the maximum output energy to the maximum input energy. The problem is expanded to include a weight on inputs ($\boldsymbol{K}_c$) which carries over to an additional element on controlled output and a weight on measurement noise ($\boldsymbol{K}_d$) which carries over to an additional element on measured output. The parameter $\boldsymbol{K}_c$ feeds the controlled output via $\ddot{\boldsymbol{u}}(s) = \boldsymbol{K}_c \boldsymbol{K}(s)\, \boldsymbol{y}_{meas}$. The $\mathcal{H}_\infty$ control is derived based on the linearised reduced model and is applied directly to the nonlinear full–order model. Additional information on the control design based on $\mathcal{H}_\infty$ are given in Appendix A.1.

2.5.1.2 Model Reference Adaptive Control

This section describes how linear and nonlinear reduced models are used to design control laws based on model reference adaptive control. The stability proof of this methodology for linear systems is well known [152]. This approach assumes an ideal reference model which will induce some constraints on the response of the actual aeroelastic system. For simplicity, the dynamics of the reduced model without including small control contributions arising from velocity and acceleration are given by

$$\boldsymbol{x}\left(t\right)' \;=\; \boldsymbol{A}\,\boldsymbol{x}\left(t\right) \;+\; \boldsymbol{B}_{c1}\,\boldsymbol{u}_{c}\left(t\right) + \boldsymbol{B}_{g1}\boldsymbol{u}_{d}\left(t\right) \;+\; \boldsymbol{F}_{NR}\left(\boldsymbol{x}\right) \tag{2.53}$$

where $\boldsymbol{F}_{NR}$ is the nonlinearity that results from the nonlinear model order reduction technique. The assumed ideal model reference follows dynamics of the form

$$\boldsymbol{x}_{m}\left(t\right)' \;=\; \boldsymbol{A}_{m}\,\boldsymbol{x}_{m}\left(t\right) \;+\; \boldsymbol{B}_{m}\,\boldsymbol{u}_{c}\left(t\right) \;+\; \boldsymbol{B}_{g1}\boldsymbol{u}_{d}\left(t\right) \;+\; \boldsymbol{F}_{NR}\left(\boldsymbol{x}_{m}\right) \tag{2.54}$$

Matrix $\boldsymbol{A}_{m}$ is a stable Hurwitz matrix that satisfies the desired properties of the reference system. This could mean eigenvalues with increased damping compared to the actual aeroelastic system. Matrix $\boldsymbol{B}_{m}$ is user defined and describes the influence of the control inputs on the states of the reference model. The states of the reference model due to the increased damping in matrix $\boldsymbol{A}_{m}$ will decay to zero faster under the same disturbances or flap actuation while their magnitude will be in general smaller as well. The physical displacements of the system can be retrieved by using the eigenvectors which is linear in the output as described in § 2.1 .

$$\begin{aligned} y\left(t\right) \;&=\; C\boldsymbol{x}\left(t\right) \\ y_{m}\left(t\right) \;&=\; C\boldsymbol{x}_{m}\left(t\right) \end{aligned} \tag{2.55}$$

The goal is to find a dynamic control input $\boldsymbol{u}_{c}\left(t\right)$ such that $\lim_{t\to\infty}\left\|y\left(t\right) - y_{m}\left(t\right)\right\|$. The exact control feedback for the model matching conditions is defined as

$$\boldsymbol{u}_{c}\left(t\right) \;=\; \boldsymbol{K}_{x}^{*}\boldsymbol{x}\left(t\right) \;+\; \boldsymbol{K}_{r}^{*}r\left(t\right) \tag{2.56}$$

where $\boldsymbol{r}\left(t\right)$ is a reference signal applied in both systems as shown in Figure 2.4 (e.g. flap angle for the flexible wing case) and $\boldsymbol{K}_{x}^{*}, \boldsymbol{K}_{r}^{*}$ are the exact gains acting on the states and control input to match the two models. By replacing Eq. (2.56) in Eq. (2.53) and satisfying the model matching conditions yields

$$\begin{aligned} \boldsymbol{A} \;+\; \boldsymbol{B}_{c1}\boldsymbol{K}_{x}^{*} &= \boldsymbol{A}_{m} \\ \boldsymbol{B}_{c1}\boldsymbol{K}_{r}^{*} \qquad &= \boldsymbol{B}_{m} \end{aligned} \tag{2.57}$$

Since $\boldsymbol{A}$ and $\boldsymbol{B}_{c1}$ are considered to be unknown to the controller the values denoted in Eq. (2.56) (e.g $\boldsymbol{K}_x^*, \boldsymbol{K}_r^*$) are also unknown at initial time and the actual control signal applied at the current timestep is defined as

$$\boldsymbol{u}_c\left(t\right) \,=\, \boldsymbol{K}_x\left(t\right)\boldsymbol{x}\left(t\right) \,+\, \boldsymbol{K}_r\left(t\right)\boldsymbol{r}\left(t\right) \tag{2.58}$$

The gains $\boldsymbol{K}_x\left(t\right)$ and $\boldsymbol{K}_r\left(t\right)$ in Eq.(2.58) are dynamic gains that need to be solved and at the end will be required to converge to the values that provide a solution to Eq. (2.57). However, in adaptive control systems there is a big uncertainty about the convergence of the adaptive gains even in deterministic ideal situations. There are many cases where the adaptive gains converge to different values than the actual analytical precalculated ideal gains even without the presence of disturbances. Barkana [153] showed that in cases where the adaptive gains do not reach the unique solution that the preliminary design suggests, it is not because there is something wrong with the control design. This is because, the adaptive controller only needs a specific set of gains that correspond to a particular input command compared to a unique solution of gains for all inputs that an exact design suggests. The closed–loop dynamics of the nonlinear reduced model at this point can be expressed as

$$\boldsymbol{x}\left(t\right)' \,=\, \left(\boldsymbol{A} \,+\, \boldsymbol{B}_{c1}\boldsymbol{K}_x\left(t\right)\right)\boldsymbol{x}\left(t\right) \,+\, \boldsymbol{B}_{c1}\boldsymbol{K}_r\left(t\right)\boldsymbol{r}\left(t\right) \,+\, \boldsymbol{B}_{g1}\boldsymbol{u}_d\left(t\right) \,+\, \boldsymbol{F}_{NR}\left(\boldsymbol{x}\right) \tag{2.59}$$

Let $\theta^* \,=\, \left\{\boldsymbol{K}_x^* \;\; \boldsymbol{K}_r^*\right\}^T$ and $\theta \,=\, \left\{\boldsymbol{K}_x\left(t\right) \;\; \boldsymbol{K}_r\left(t\right)\right\}^T$. The estimation error between the instantaneous and the ideal gains is defined as

$$\bar{\theta} = \theta^* - \theta = \left\{\bar{\theta}_x \;\; \bar{\theta}_r\right\}^T \tag{2.60}$$

with $\bar{\theta}_x = \boldsymbol{K}_x^* - \boldsymbol{K}_x\left(t\right)$, $\bar{\theta}_r = \boldsymbol{K}_r^* - \boldsymbol{K}_r\left(t\right)$. Now define $\phi = \left\{\boldsymbol{x}\left(t\right)^T \;\; \boldsymbol{r}\left(t\right)\right\}^T$. In that case the closed–loop system dynamics in Eq. (2.59) are expressed as

$$\begin{aligned}\boldsymbol{x}\left(t\right)' \,=\, &\left(\,\boldsymbol{A} \,+\, \boldsymbol{B}_{c1}\boldsymbol{K}_x^*\,\right)\boldsymbol{x}\left(t\right) \,+\, \boldsymbol{B}_{c1}\boldsymbol{K}_r^*\boldsymbol{r}\left(t\right) - \boldsymbol{B}_{c1}\bar{\theta}_x\boldsymbol{x}\left(t\right) \,-\, \boldsymbol{B}_{c1}\bar{\theta}_r\boldsymbol{r}\left(t\right) &(2.61)\\ &+\, \boldsymbol{B}_{g1}\boldsymbol{u}_d\left(t\right) \;+\, \boldsymbol{F}_{NR}\left(\boldsymbol{x}\right)\\ &= \boldsymbol{A}_m\,\boldsymbol{x}\left(t\right) \,+\, \boldsymbol{B}_m\boldsymbol{r}\left(t\right) \,-\, \boldsymbol{B}_{c1}\phi^T\bar{\theta} \,+\, \boldsymbol{B}_{g1}\boldsymbol{u}_d\left(t\right) \,+\, \boldsymbol{F}_{NR}\left(\boldsymbol{x}\right) &(2.62)\end{aligned}$$

For the purpose of the stability proof of the closed–loop system one needs to define the error dynamics between the two systems [154].

$$\boldsymbol{e}\left(t\right) \,=\, \boldsymbol{x}\left(t\right) - \,\boldsymbol{x}_m\left(t\right) \tag{2.63}$$

The derivative of which, expresses the rate of change between the two systems and can be written as

$$\begin{aligned}\boldsymbol{e}(t)' &= \boldsymbol{x}(t)' - \boldsymbol{x}_m(t)' \\ &= \boldsymbol{A}_m\left(\boldsymbol{x}(t) - \boldsymbol{x}_m(t)\right) - \boldsymbol{B}_{c1}\phi^T\bar{\theta} + \left(\boldsymbol{F}_{NR}(\boldsymbol{x}) - \boldsymbol{F}_{NR}(\boldsymbol{x}_m)\right) \\ &= \boldsymbol{A}_m\boldsymbol{e}(t) - \boldsymbol{B}_{c1}\phi^T\bar{\theta} + \boldsymbol{F}_{Df}(\boldsymbol{x}, \boldsymbol{x}_m) \end{aligned} \tag{2.64}$$

At this point, the Lyapunov equation needs to be solved for the reference model because its solution will be part of the steady part of the Lyapunov candidate function that we define and that will lead to the stability proof of the nonlinear reduced model [152].

$$\boldsymbol{P}\boldsymbol{A}_m + \boldsymbol{A}_m{}^T\boldsymbol{P} = -\boldsymbol{Q}, \qquad \boldsymbol{Q} = \boldsymbol{Q}^T \geq 0 \tag{2.65}$$

where in Eq.(2.65) $\boldsymbol{Q}$ is a semi–definite positive user defined matrix. A scalar quadratic Lyapunov function $\boldsymbol{V}$ in $\boldsymbol{e}$ and $\bar{\theta}$ may be defined, such that the system becomes asymptotically stable by satisfying $\boldsymbol{V} > 0$ and its time derivative is semi definite negative $\boldsymbol{V}' \leq 0$ [152] . This function will provide insight on the selection of the parameter update law of the time varying gains in Eq. (2.58). The Lyapunov function

$$\boldsymbol{V}(\boldsymbol{e}(t), \theta) = \boldsymbol{e}(t)^T\boldsymbol{P}\boldsymbol{e}(t) + \bar{\theta}^T\boldsymbol{\Gamma}^{-1}\bar{\theta} > 0 \tag{2.66}$$

is considered, where $\boldsymbol{P} = \boldsymbol{P}^T > 0$ is the solution of the algebraic Lyapunov Eq. (2.65) for a particular selection of $\boldsymbol{Q}$ while $\boldsymbol{\Gamma} = \boldsymbol{\Gamma}^T \geq 0$ is a user defined semi–definite positive matrix. Note that the positiveness of the above Lyapunov function is guaranteed only if the system under examination is a minimum-phase system. Differentiating the above equation with respect to time yields

$$\boldsymbol{V}'(\boldsymbol{e}(t), \theta) = \boldsymbol{e}(t)'^T\left(\boldsymbol{P} + \boldsymbol{P}^T\right)\boldsymbol{e}(t) + 2\bar{\theta}^T\boldsymbol{\Gamma}^{-1}\bar{\theta}' + \boldsymbol{e}(t)\boldsymbol{P}\boldsymbol{F}_{Df}(\boldsymbol{x}, \boldsymbol{x}_m) \tag{2.67}$$

By substitution of the error dynamics and by using Eq. (2.65) , Eq. (2.67) is expanded as follows

$$\begin{aligned}\boldsymbol{V}'(\boldsymbol{e}(t), \theta) &= \boldsymbol{e}(t)^T\left(\boldsymbol{A}_m\boldsymbol{P} + \boldsymbol{A}_m{}^TP\right)\boldsymbol{e}(t) + 2\boldsymbol{e}(t)^T\boldsymbol{P}\boldsymbol{B}_{c1}\phi^T\bar{\theta} + 2\bar{\theta}^T\boldsymbol{\Gamma}^{-1}\bar{\theta}' \\ &\quad + \boldsymbol{e}(t)\boldsymbol{P}\boldsymbol{F}_{Df}(\boldsymbol{x}, \boldsymbol{x}_m) \\ &= -\boldsymbol{e}(t)^T\boldsymbol{Q}\boldsymbol{e}(t) + 2\bar{\theta}^T\boldsymbol{\Gamma}^{-1}\left(\boldsymbol{\Gamma}\phi\boldsymbol{e}(t)^T\boldsymbol{P}\boldsymbol{B}_{c1} + \bar{\theta}'\right) + \boldsymbol{e}(t)\boldsymbol{P}\boldsymbol{F}_{Df}(\boldsymbol{x}, \boldsymbol{x}_m)\end{aligned} \tag{2.68}$$

In the above equation one can determine the adaptation parameter to satisfy the semi definite negativeness of the derivative of the Lyapunov function as

$$\bar{\theta}' = -\boldsymbol{\Gamma}\phi\boldsymbol{e}(t)^T\boldsymbol{P}\boldsymbol{B}_{c1} \tag{2.69}$$

which leads to

$$\boldsymbol{V}'\left(\boldsymbol{e}\left(t\right),\theta\right) \;=\; -\boldsymbol{e}\left(t\right)^{T}\boldsymbol{Q}\boldsymbol{e}\left(t\right) \;+\; +\boldsymbol{e}\left(t\right)\boldsymbol{P}\left(\boldsymbol{F}_{NR}\left(\boldsymbol{x}\right) \;-\; \boldsymbol{F}_{NR}\left(\boldsymbol{x}_{m}\right)\right) \tag{2.70}$$

The term $-\boldsymbol{e}\left(t\right)^{T}\boldsymbol{Q}\boldsymbol{e}\left(t\right)$ in Eq. (2.70) is semi negative definite with respect to $\boldsymbol{e}\left(t\right)$ and this is enforced by the semi definitive positive matrix $\boldsymbol{Q}$. The derivative of the Lyapunov function remains semi negative definite in both $\boldsymbol{x}\left(t\right)$ and $\boldsymbol{e}\left(t\right)$ if additionally the second term in Eq. (2.70) is not too large, or alternatively if the following inequality is satisfied [155].

$$||\boldsymbol{F}_{NR}\left(\boldsymbol{x}\right) \;-\; \boldsymbol{F}_{NR}\left(\boldsymbol{x}_{m}\right)|| \leq \frac{||\boldsymbol{Q}||}{||\boldsymbol{P}||}||\boldsymbol{x}\left(t\right) \;-\; \boldsymbol{x}_{m}\left(t\right)|| \tag{2.71}$$

Since $\boldsymbol{F}_{NR}$ is an arbitrary function, it is not possible to show stability of the nonlinear adaptive control scheme for all types of nonlinearities in the model. Instead, the efficiency of the control design is demonstrated on the nonlinear system for realistic amplitudes of external disturbances. The dynamic time varying gains in Eq. (2.58) are updated by the adaptive law so that the time derivative of the Lyapunov function decreases along the error dynamic trajectories as in Eq. (2.70). By using Barbalat's lemma this translates in boundness of the error dynamics with respect to the time evolution and as a result satisfaction of the model matching conditions. In general, this control approach is limited to minimum phase systems. Thus, when applied in unstable nonminimum phase systems, unstable zero-pole cancellation may occur and the error between the two assumed models slowly diverges to infinity. However, a simple feedback based on the Bass-Gura formula [156] can be applied on the ROM to place any unstable zeros on the left half plane. The implementation of the computational algorithm can be summarised in the block diagram shown in Figure 2.4. Additional information on the $\mathcal{MRAC}$ control design is given in Appendix A.1.

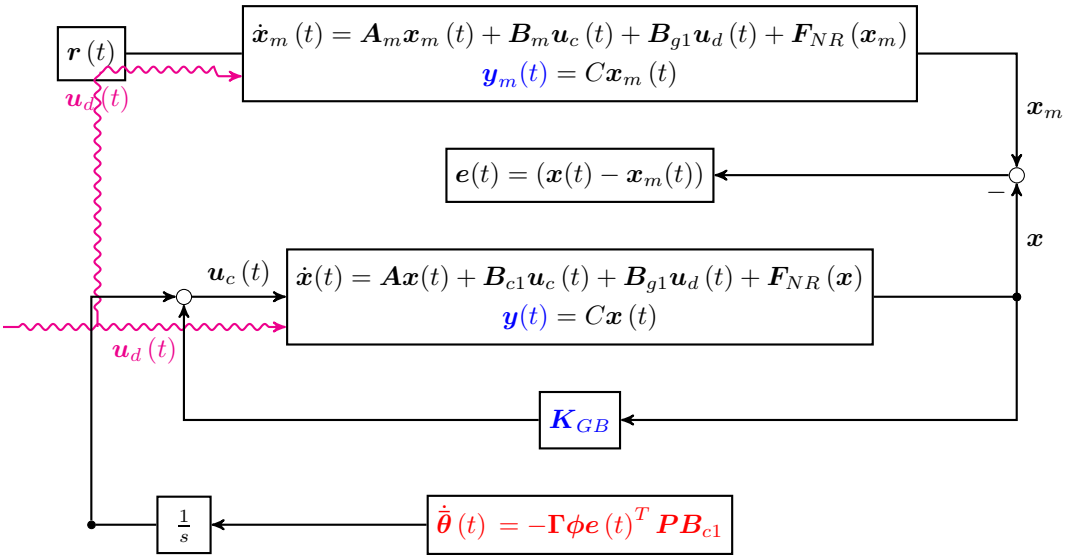

Figure 2.4: Nonlinear Adaptive Control Algorithm

Chapter 3

Validations

In this Chapter, results from four different combinations of aerodynamic models are provided to assess the impact of the aerodynamic modelling of two–dimensional potential theory against higher–fidelity methods, when dealing with very flexible aircraft flight dynamics. In particular, a validation for two–dimensional and three–dimensional test cases with aerodynamics from CFD, UVLM, potential strip theory and DLM is provided. Due to the reason that there has been extensive use of indicial aerodynamic functions [157] for the calculation of steady loads, the focus here is on the calculation of unsteady loads. Firstly, an aerofoil model with cubic and quintic structural nonlinearities in the pitch and the plunge degree–of–freedom is coupled with CFD and strip theory aerodynamics. The model order reduction method described in the previous Chapter is implemented in both codes. Comparisons between the two different frameworks, are given for unsteady aeroelastic responses at low speed, for full and reduced–order models which demonstrates the applicability of the reduction technique in all the aerodynamic formulations.

Following this, a higher–fidelity structural beam model with a geometrically-exact nonlinearity, is coupled with strip aerodynamics and gust responses are compared against commercial software. A further validation is provided with the inclusion of the flight dynamics degrees–of–freedom for a rigid flying–wing. Flight dynamic responses given by CFD, strip theory and UVLM are presented and the significant impact of the aerodynamic modelling is discussed.

3.1 Solvers

3.1.1 Computational Fluid Dynamics

The first CFD code used is the Parallel Meshless solver of the University of Liverpool (PML) which solves the Euler, laminar and Reynolds–Averaged Navier–Stokes equations (with the Spalart–Almaras turbulence model) on a point cloud. This code is used to compute the aerofoil results shown below. The solver is summarised in [158]. Time–

domain calculations are done using the pseudo time stepping method, which solves a modified steady–state problem for the updated solution at each new time step.

The second CFD code used here, which is applied to the three–dimensional case computed, is based on the University of Liverpool parallel multiblock solver. The Euler equations are discretized on curvilinear multiblock body-conforming grids using a cell–centred finite–volume method. The residual is formed using Osher's approximate Riemann solver with the monotone upwind scheme for conservation laws interpolation. Exact Jacobian matrices are formed. The mesh can be deformed using transfinite interpolation. The steady–state and time accurate solvers are identical to those used for the previous CFD solver (PML) described above. More details on the CFD formulation can be found in Badcock et al. [159], and on the application to problems in aeroelasticity in Badcock et al. [160].

3.1.2 Linear Aerodynamic Model

A cheaper computational alternative to the computational fluid dynamics (CFD) codes, valid for an irrotational and incompressible two–dimensional flow is the aerodynamic model given by the classical theory of Theodorsen [22]. This is a reasonable assumption when dealing with low–speed flow characteristics in 2-D at low angle of attack. The total unsteady aerodynamic forces and moments can be separated into three components, circulatory, non-circulatory due to the wing motion and a contribution from the gust disturbance. The aerodynamic loads due to an arbitrary input time–history are obtained through convolution against a kernel function. For the influence of aerofoil motion on the loads, the Wagner function is used [143]. In a similar way, the influence of the gust is performed by introducing the Küssner function [31]. Since the assumption is of linear aerodynamics, the effects of both influences are added together to find the variation of the forces and moments for a given motion and gust. For a practical evaluation of the integral, a two lag exponential approximation is used for the Wagner and Küssner functions. This aerodynamic model is coupled with a two degree–of–freedom aerofoil with structural nonlinearity and with a geometrically–exact nonlinear beam model.

3.1.3 Unsteady Vortex–Lattice Method

The unsteady vortex lattice method (UVLM) is used to obtain a medium–fidelity three–dimensional solution of the unsteady aerodynamics [47, 48]. UVLM is a geometrically nonlinear method in which the shape of a force–free wake is obtained as part of the solution procedure. Herein, the code developed in [47], the Sharp, written in MATLAB, couples UVLM with the geometrically–exact nonlinear beam equations [48]. Flight dynamics degrees–of–freedom are included in the model, allowing options for fully coupled nonlinear calculations.

3.2 Two Degree–of–Freedom Model

The structural model of the two degree–of–freedom aerofoil model presented here, follows the formulation in [161]. The aerofoil shown in Figure 3.1 has two degrees–of–freedom about the reference elastic axis (*e.a.*), in pitch, and in plunge respectively. The plunge deflection is denoted by h, positive downward. The angle of attack about the elastic axis is positive with nose up and it is denoted by α.

A massless trailing–edge flap with the hinge line placed at a distance $c\,b$ from the midchord is assumed. The flap deflection, δ, is defined relative to the undeflected position and not relative to the wind direction.

The motion is restrained by two springs, K_ξ and K_α, and is assumed to have a horizontal equilibrium position at $h = \alpha = \delta = 0$. The system also contains structural damping in both degrees–of–freedom, not shown in the figure.

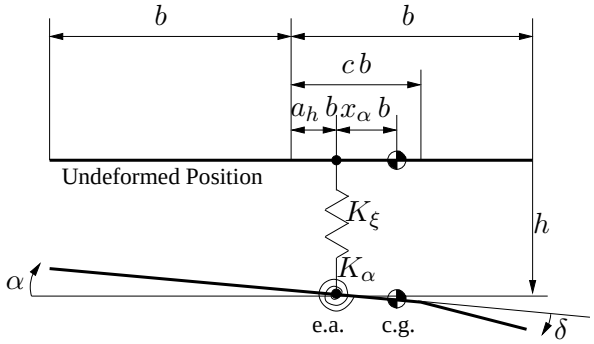

Figure 3.1: Schematic of an aerofoil section with trailing-edge flap; the wind velocity is to the right and horizontal; e.a. and c.g. denote, respectively, the elastic axis and centre of gravity (from [98])

The equations of motion in dimensional form with nonlinear cubic and quintic restoring forces in pitch and plunge can be derived, for example, using the Lagrange equations [162]

$$m\,\ddot{h} + S_\alpha\,\ddot{\alpha} + C_\xi\,\dot{h} + \left(h + \beta_{\xi_3}\,h^3 + \beta_{\xi_5}\,h^5\right) = -\,L \tag{3.1}$$

$$S_\alpha\,\ddot{h} + I_\alpha\,\ddot{\alpha} + C_\alpha\,\dot{\alpha} + \left(\alpha + \beta_{\alpha_3}\,\alpha^3 + \beta_{\alpha_5}\,\alpha^5\right) = M \tag{3.2}$$

with the structural nonlinearity approximated by a polynomial form [163]. The lift, L, is defined positive upward according to the usual sign convention in the aerodynamics. The plunge displacement, h, is positive downward, as it is conventionally done in aeroelasticity. In nondimensional form, the equations of motion can be expressed as

$$\xi'' + x_\alpha\,\alpha'' + 2\,\zeta_\xi\,\frac{\bar{\omega}}{U^*}\,\xi' + \left(\frac{\bar{\omega}}{U^*}\right)^2\left(\xi + \beta_{\xi_3}\,\xi^3 + \beta_{\xi_5}\,\xi^5\right) = -\frac{1}{\pi\,\mu}\,C_L\,(\tau) \tag{3.3}$$

$$\frac{x_\alpha}{r_a^2}\,\xi'' + \alpha'' + 2\,\zeta_\alpha\,\frac{1}{U^*}\,\alpha' + \left(\frac{1}{U^*}\right)^2\left(\alpha + \beta_{\alpha_3}\,\alpha^3 + \beta_{\alpha_5}\,\alpha^5\right) = \frac{2}{\pi\,\mu\,r_a^2}\,C_m\,(\tau) \tag{3.4}$$

where the nondimensional parameters are defined in the list of symbols. Differentiation with respect to t, indicated by $\dot{(\,)}$, is replaced by a differentiation with respect to τ, $\dot{(\,)} = U/b\,(\,)'$. These equations are rewritten to define the residual contribution. The above nonlinear structural model equations can be coupled with a variety of options for the aerodynamic model.

3.2.1 CFD Aerodynamic Model

The test problem considered is for a NACA0012 aerofoil at zero incidence. The parameters for the structural model are given in Table 3.1. The test case corresponds to the "heavy-case" described in Badcock et al. [164]. In this case, the Euler equations are used and the point distribution near the aerofoil shown in Figure 3.2 consists of 7974 points.

Parameter	Value
$\bar{\omega}$	0.343
μ	100.0
a_h	-0.2
x_α	0.2
r_α	0.539
β_{ξ_3}	24.0

Table 3.1: Reference values of the pitch–plunge aerofoil model

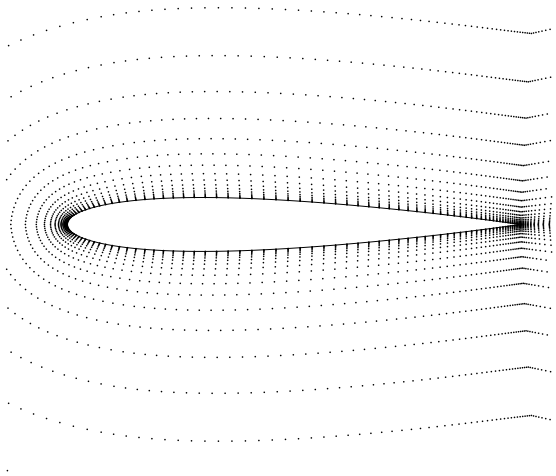

Figure 3.2: Point distribution for the NACA0012 aerofoil

3.2.1.1 Steady–State CFD solution

The investigation starts with an evaluation of the required size of the grid for the set of the calculations. A steady–state CFD computation at a Mach number of 0.85 and

an angle of attack of 1.0 degree is carried out for a coarse point cloud of 7974 points, a medium point cloud of 22380 points and a finer point cloud of 88792 points. Figure 3.3 shows the pressure coefficient over the NACA0012 for three different point distributions. The experimental measurements are taken from [165]. The agreement for the solution on the point cloud used for the aeroelastic predictions below is satisfactory.

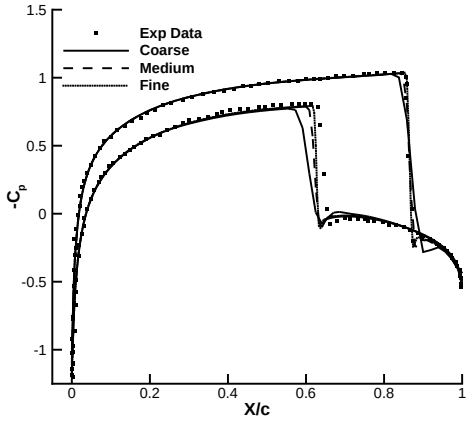

Figure 3.3: Comparison of the pressure distribution for NACA0012 aerofoil at $\mathbf{M}_\infty = \mathbf{0.85}$ and $\alpha = \mathbf{1.0}$ deg for three point cloud densities, and measurements taken from [165].

3.2.1.2 Flutter Analysis

The model reduction as previously described, requires the coupled system (i.e. aeroelastic) eigenvectors as input. These are obtained from the solution of the eigenvalue problem that also provides the flutter speed prediction. This was done for the CFD aerodynamics model using the Schur method summarised in the previous Chapter. More specifically, the expensive term in the calculation, $(A_{ff} - \lambda I)^{-1}$, is expanded in a first order Taylor series about a chosen shift λ_0, which is based on the structural frequencies, and then the eigenvalue problem in Eq. (2.31) is solved easily for increasing values of the reduced velocity for the deviation from this shift.

Figure 3.4 shows the eigenvalues with respect to reduced velocities for a fixed Mach number of 0.8. In this case, it is shown that the damping of mode 1 which refers to the plunging motion, becomes negative at about 3.577 reduced velocity. Herein, the eigenvectors for the generation of the reduced–order model have been calculated at a reduced velocity of $U^* = 2.0$. However, several tests to confirm the model reduction were performed at various speeds as shown in Figure 3.5.

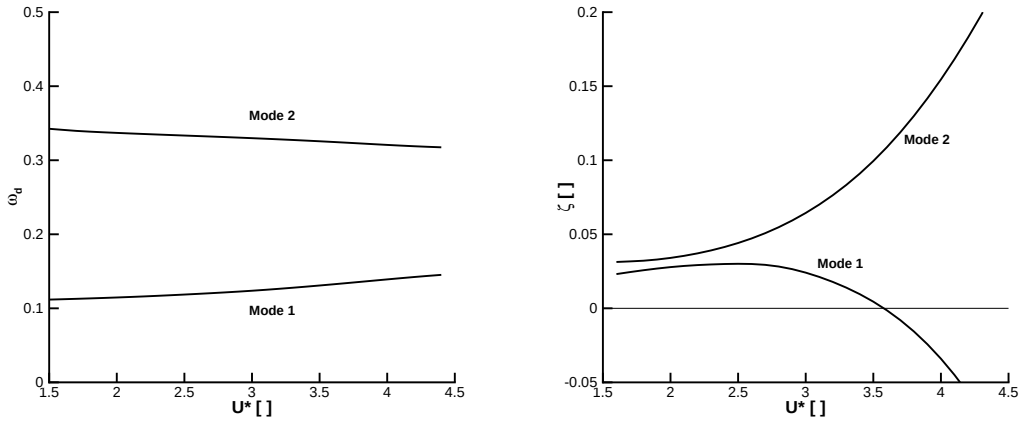

(a) Damped natural frequency, ω_d

(b) Damping ratio, ζ

Figure 3.4: Trace of the aeroelastic eigenvalues using the CFD as a function of the reduced velocity for a Mach number of 0.8 for the test case in Table 3.1

3.2.1.3 Evaluation of the Reduced Model

The reduced–order model was evaluated in two different coupled aerodynamic solvers, one with the strip theory and the other with a CFD model. Two aeroelastic modes associated with the pitching and the plunging motions were retained. An evaluation of introducing additional modeshapes in the reduced model was presented in Da Ronch et al. [98]. There are several options for the number of the nonlinear terms retained in the reduced model. Herein, a linear reduced–order model has been used as it proved adequate to represent the gust response as in this case the nonlinearity did not affect the full–order dynamic response. This was tested by comparison with the nonlinear full–order model, which has a structural nonlinearity in the plunging degree-of-freedom against the linear reduced–order model. If this had not been the case then the option would have been to include quadratic and cubic terms in the nonlinear reduced–order model in a straightforward fashion. The form of the reduced model at a freestream Mach number of 0.8 without the gust term contribution is

$$\frac{\mathrm{d}\boldsymbol{z}}{\mathrm{d}t} = \begin{bmatrix} \lambda_1 & 0 \\ 0 & \lambda_2 \end{bmatrix} \boldsymbol{z} \tag{3.5}$$

where $\lambda_1 = -1.00031 \cdot 10^{-2} + i \cdot 3.60176 \cdot 10^{-1}$ and $\lambda_2 = -3.61915 \cdot 10^{-2} + i \cdot 1.05872$.

The reduced models were first tested for a problem without a gust, involving the free response to an initial plunging perturbation, $\xi' = 0.01$. The time response of the reduced and full–order model is shown in Figure 3.5. It is shown that the CFD and the linear results from potential flow theory are close at the lower Mach number and as expected, differ significantly at the transonic Mach number of 0.8. However, in all cases the corresponding full–order and reduced–order model predictions were identical and it was independent of the aerodynamic modelling.

Next, the gust term was added to the reduced model, and the reduced predictions were compared with a full–order calculation of the same case. The gust used was the discrete "1–minus–cosine" gust with an intensity of 1% of the freestream speed and a length of 25 semichords. The comparison for the case with a freestream Mach number of 0.8 is shown in Figure 3.6 and again shows a good agreement between the reduced and full model results. However, some differences between the two models are observed for small times. While the peak to peak amplitude between two consecutive peaks predicted by the reduced model is in agreement with the full model results, the actual values at the first peak differ somewhat. A reason for this could be that the reduced model is initially driven by a perturbation which does not belong to the eigenvector basis used in the model projection, Eq. (2.11), or that some information on the gust term is missing. More modes could be added to enhance the eigenvector basis, as shown in Da Ronch et al. [98]. However, after the gust perturbation the purely fluid–structure response of the aerofoil can be perfectly described by the modal basis of the ROM which contained only

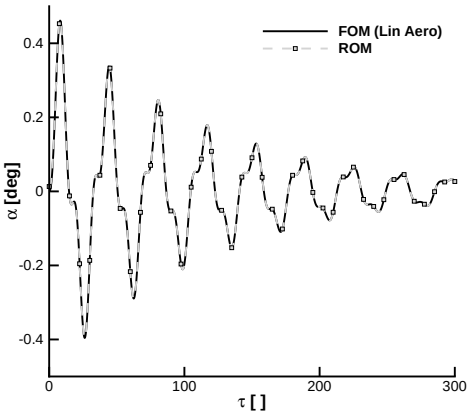

(a) Pitch, incompressible flow, strip theory

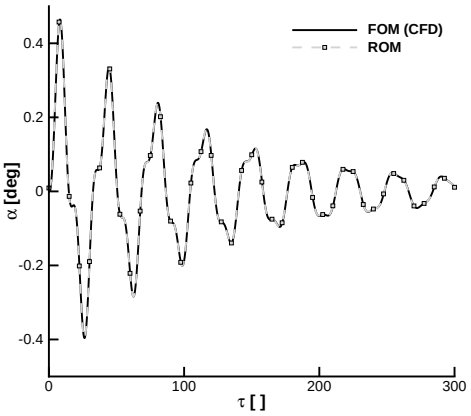

(b) Pitch at $M = 0.3$, CFD

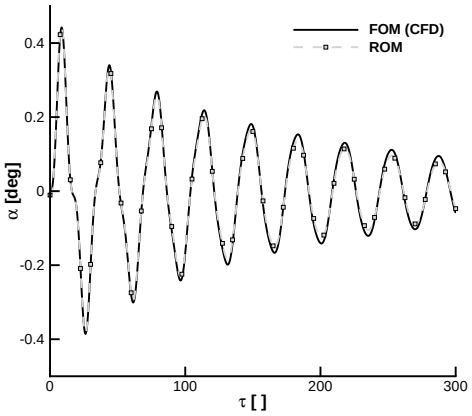

(c) Pitch at $M = 0.8$, CFD

Figure 3.5: Free response comparisons using CFD and strip theory aerodynamics at $\mathbf{U}^* = \mathbf{2.0}$ for two Mach numbers and initial condition $\xi' = \mathbf{0.01}$

two complex eigenvalues associated with the structural degrees–of–freedom, the pitch and the plunge.

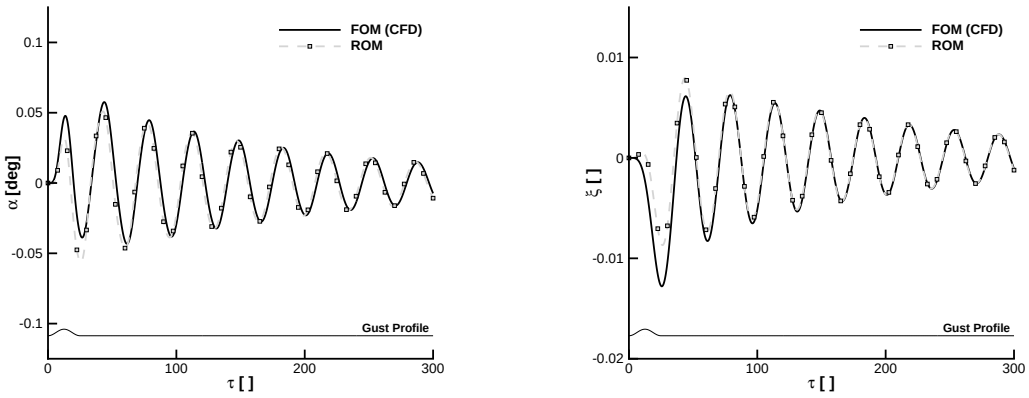

(a) Pitch, α, CFD gust response

(b) Plunge, ξ, CFD gust response

Figure 3.6: CFD Response to a discrete "1–minus–cosine" gust with intensity of 1% of the freestream speed and a duration of 25 in nondimensional time, at Mach 0.8.

The total computational cost for the gust response of the nonlinear and the linear reduced–order model is summarised in Table 3.2.. The time–domain response was computed with a nondimensional time step of 0.05 for 2000 iterations. Note that the cost of the ROM generation is incurred only once, and includes the costs of forming the eigenvector basis and the computation of the gust term. The gust coefficient matrix was computed by finite differences with two residual evaluations for each cloud point in the absence of an analytic evaluation, which would have reduced drastically the time required for this step. The time–domain response of the reduced model for any type of gust disturbance, e.g. discrete and continuous, is about 2 orders of magnitude faster than the full–order calculation.

Item	Cost (sec)
Time–Domain Full–Order Calculation	5105
Reduced Model Generation	444
a) Calculating Eigenvector Basis	148
b) Calculating Gust Influence Matrix	296
Time–Domain Reduced Model Calculation	68

Table 3.2: Computational cost summary

3.2.2 Strip Theory Aerodynamic Model

The coupled system of equations resulting from combining Eq. (3.4) with the two–dimensional aerodynamic model detailed in § 2.3 is integro–differential. It is difficult to

study the dynamic behaviour of the system analytically. In addition, most of the methods for studying nonlinear systems are developed for ordinary differential equations. The mathematical procedure to avoid the convolution integral term has been applied to several systems in the literature. It is essentially based on defining additional variables and equations describing their evolution.

Following the approach of Lee et al. [161], the system of integro–differential equations is recast as a set of ordinary differential equations in first–order by defining eight aerodynamic states and their dynamics [2]

$$
\begin{aligned}
w_1 &= \int_0^\tau e^{-\varepsilon_1(\tau-\sigma)}\,\alpha\,(\sigma)\;d\sigma & w_1' &= \alpha - \varepsilon_1\, w_1 \\
w_2 &= \int_0^\tau e^{-\varepsilon_2(\tau-\sigma)}\,\alpha\,(\sigma)\;d\sigma & w_2' &= \alpha - \varepsilon_2\, w_2 \\
w_3 &= \int_0^\tau e^{-\varepsilon_1(\tau-\sigma)}\,\xi\,(\sigma)\;d\sigma & w_3' &= \xi - \varepsilon_1\, w_3 \\
w_4 &= \int_0^\tau e^{-\varepsilon_2(\tau-\sigma)}\,\xi\,(\sigma)\;d\sigma & w_4' &= \xi - \varepsilon_2\, w_4 \\
w_5 &= \int_0^\tau e^{-\varepsilon_1(\tau-\sigma)}\,\delta\,(\sigma)\;d\sigma & w_5' &= \delta - \varepsilon_1\, w_5 \\
w_6 &= \int_0^\tau e^{-\varepsilon_2(\tau-\sigma)}\,\delta\,(\sigma)\;d\sigma & w_6' &= \delta - \varepsilon_2\, w_6 \\
w_7 &= \int_0^\tau e^{-\varepsilon_3(\tau-\sigma)}\,W_g\,(\sigma)\;d\sigma & w_7' &= W_g - \varepsilon_3\, w_7 \\
w_8 &= \int_0^\tau e^{-\varepsilon_4(\tau-\sigma)}\,W_g\,(\sigma)\;d\sigma & w_8' &= W_g - \varepsilon_3\, w_8
\end{aligned}
$$

The size of the coupled aeroelastic model is 12, and consists of 8 aerodynamic states and 4 structural states. The trailing–edge flap rotation is used as control input. Define the state vector (of dimension 12),

$$
\boldsymbol{x} = \left\{\alpha,\, \alpha',\, \xi,\, \xi',\, w_1,\, w_2,\, w_3,\, w_4,\, w_5,\, w_6,\, w_7,\, w_8\right\}^T \tag{3.7}
$$

then, the coupled system of equations is

[2] A useful tool for the calculation of w_j', for $j = 1, \ldots, 8$, is the Leibniz integral role [166]:

$$
\frac{\partial}{\partial z}\int_{a(z)}^{b(z)} f\,(x,\, z)\;dx = \int_{a(z)}^{b(z)} \frac{\partial\, f}{\partial z}\,dx + f\,(b(z),\, z)\,\frac{\partial\, b}{\partial z} - f\,(a(z),\, z)\,\frac{\partial\, a}{\partial z} \tag{3.6}
$$

$$
\begin{aligned}
x_1' &= x_2 \\
x_2' &= p_1 H(\boldsymbol{x}) + p_2 P(\boldsymbol{x}) \\
x_3' &= x_4 \\
x_4' &= p_3 H(\boldsymbol{x}) + p_4 P(\boldsymbol{x}) \\
x_5' &= x_1 - \varepsilon_1 x_5 \\
x_6' &= x_1 - \varepsilon_2 x_6 \\
x_7' &= x_3 - \varepsilon_1 x_7 \\
x_8' &= x_3 - \varepsilon_2 x_8 \\
x_9' &= \delta - \varepsilon_1 x_5 \\
x_{10}' &= \delta - \varepsilon_2 x_6 \\
x_{11}' &= W_g - \varepsilon_3 x_{11} \\
x_{12}' &= W_g - \varepsilon_4 x_{12}
\end{aligned}
$$

It is convenient for the remaining part of this work to recast the above set of equations in a matrix-vector form

$$
\boldsymbol{x}' = \boldsymbol{f}(\boldsymbol{x}) + \boldsymbol{g}\, u \tag{3.8}
$$

where u represents the flap rotation. The coefficients of the above aeroelastic system are detailed fully in the Appendix A.2 at the end of this thesis.

3.2.2.1 Evaluation of the Reduced Model

The test case considered is for an aerofoil section at zero incidence. The parameters for the structural model are given in Table 3.3 and they are the same as in the CFD model in section 3.2 . The test case corresponds to the "heavy case" described in Badcock et al. [164]. The traces of the pitching and plunging modes for increasing reduced velocity have been calculated to compute the dynamic instability. The instability occurs for a linear reduced flutter velocity of $U_L^* = 4.6137$. The code has been validated in the previous section and against other independent investigations, and more details on this can be found in Da Ronch et al. [98].

To generate the reduced model in Eq. (2.11), the eigenvectors of the coupled system are required. This is done here using standard routines readily available for the solution of the eigenvalue problem. The eigenvalue problem is solved for the aerofoil with linear structure and the eigenvector basis is calculated once at a reduced velocity of 4.6, which corresponds to 99.7% of the computed reduced linear flutter speed. The eigenvalues at that speed are given in Table 3.4.

Parameter	Value
$\bar{\omega}$	0.343
μ	100.0
a_h	-0.2
x_α	0.2
r_α	0.539

Table 3.3: Reference values of the pitch–plunge aerofoil model for the "heavy case" (linear structure)

Mode number	Real part	Imaginary part
1	$-1.343 \cdot 10^{-3}$	$\pm 1.238 \cdot 10^{-1}$
2	$-3.443 \cdot 10^{-2}$	$\pm 1.216 \cdot 10^{-1}$
3	$-3.650 \cdot 10^{-2}$	0.000
4	$-4.550 \cdot 10^{-2}$	0.000
5	$-3.000 \cdot 10^{-1}$	0.000
6	$-4.550 \cdot 10^{-2}$	0.000
7	$-3.000 \cdot 10^{-1}$	0.000
8	$-1.393 \cdot 10^{-1}$	0.000
9	-1.802	0.000
10	$-2.571 \cdot 10^{-1}$	0.000

Table 3.4: Nondimensional eigenvalues of the model from Table 3.3 at $U_L^* = 4.6$

The reduced model is first tested for a problem without a gust encounter. In this case, only two modes need to be retained in the basis of the reduced model, the plunging mode and the pitching mode which correspond to mode 1 and 2 from Table 3.4. The initial condition driving both reduced and full model responses is a perturbation in the plunge velocity, $\xi' = 0.01$. The reduced velocity is 99.7% of the flutter speed. The agreement between the reduced and full models shown in Figure 3.7 is satisfactory. The decay of oscillations is slow because the system is very close to the instability point and as a result very lightly damped. This is an interesting condition that suggests that a gust encounter of sufficient intensity could trigger an instability in the system response.

The gust term is then added to the reduced model, and the comparison for a "1–minus–cosine" gust of intensity 5% of the freestream speed and a length of 25 semichords is made. The reduced–order model basis selection is shown in Figure 3.8 and included mode number 1, 2 and 8 from Table 3.4. It is shown that one additional eigenvalue is directly associated to the gust influence and in this nondimensional model it can be automatically selected and identified for all cases. This eigenvalue is the lowest Küssner constant, $\epsilon_3 = 0.1393$, as in section 2.3.3 that is introduced by the aerodynamics. As a result, a perfect match for a gust response between the reduced model and the full–order

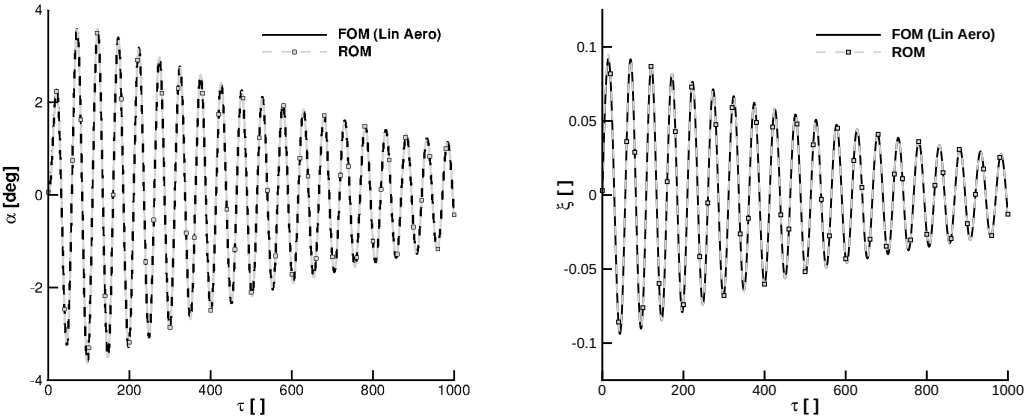

(a) Pitch, α, strip aerodynamics

(b) Plunge, ξ, strip aerodynamics

Figure 3.7: Free response of aerofoil model to $\xi' = 0.01$ at $U^* = 4.6$, for the reference parameters in Table 3.3

model is accomplished by retaining three eigenvalues in total, two associated with the fluid–structure, and a third one associated with the gust. Thus, a reduction from 12 states to 3 is achieved.

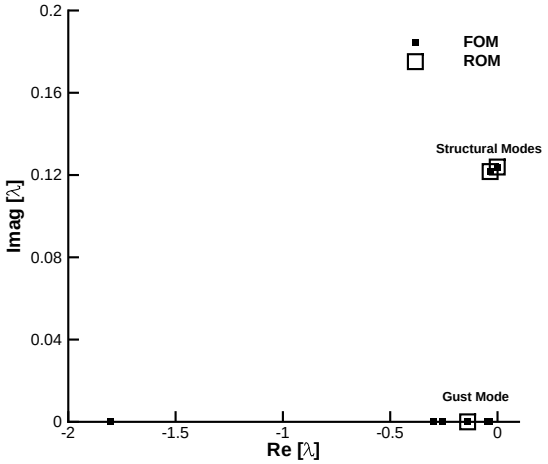

Figure 3.8: Full–order (FOM) and reduced–order model (ROM) eigenvalues in [rad/s^*]

The time response from the reduced and full–order models is shown in Fig. 3.9, and shows that the reduced model is accurate and because it is independent of the gust profile, now it can be used for a worst–case gust search, which is presented in the next section.

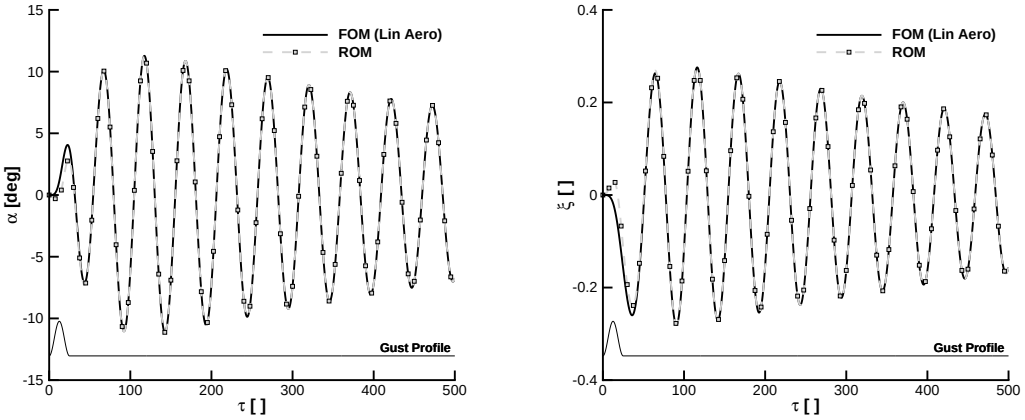

(a) Pitch, α (b) Plunge, ξ

Figure 3.9: Response to a "1-minus-cosine" gust of intensity 5% of the freestream speed and a length of 25 semichords at $U^* = 4.6$, for the model in Table 3.3

3.2.2.2 Worst–Case Gust Search

The reduced model is used to perform a worst–case gust search for the discrete "1–minus–cosine" family. The gust intensity is 5% of the freestream speed at $U^* = 4.6$, and the search is made for gust lengths up to 100 aerofoil semichords. The parameter space is divided into 1000 design sites, and Kriging interpolation is used to drive the search and obtain the maximum and minimum responses in Figure 3.10. The worst–case gust was found to be for a gust length of $H_g = 41$ semichords.

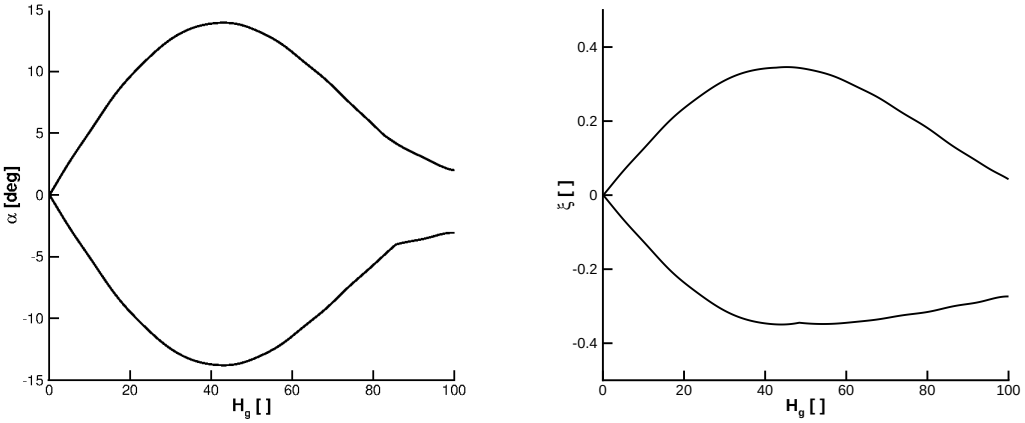

(a) Pitch, α (b) Plunge, ξ

Figure 3.10: Worst–case gust search at $U^* = 4.6$ for a "1–minus–cosine" gust of constant intensity $w_g = 0.05$, for the reduced–order model with parameters as in Table 3.3

3.3 Flexible Wing Test Case

3.3.1 Aeroelastic Solver

For the structural model, the geometrically–exact nonlinear beam equations are used [20]. Results are obtained using two–node displacement–based elements. In a displacement–based formulation, nonlinearities arising from large deformations are cubic terms, as opposed to an intrinsic description where they appear up to second order. The coupled flexible multibody nonlinear equations are expressed in the form

$$\boldsymbol{M}\left[\boldsymbol{w}_s\right]\left\{\begin{array}{c}\ddot{\boldsymbol{w}}_s\\ \ddot{\boldsymbol{w}}_r\end{array}\right\}+\boldsymbol{Q}_{\text{gyr}}\left[\dot{\boldsymbol{w}}_s,\,\boldsymbol{w}_s,\,\boldsymbol{w}_r\right]\left\{\begin{array}{c}\dot{\boldsymbol{w}}_s\\ \dot{\boldsymbol{w}}_r\end{array}\right\}+\boldsymbol{Q}_{\text{stiff}}\left[\boldsymbol{w}_s\right]\left\{\begin{array}{c}\boldsymbol{w}_s\\ \boldsymbol{w}_r\end{array}\right\}=\boldsymbol{R}_F \quad (3.9)$$

The subscripts s and r denote elastic and rigid–body degrees–of–freedom, respectively. The terms $\boldsymbol{Q}_{\text{gyr}}$ and $\boldsymbol{Q}_{\text{stiff}}$ indicate, respectively, gyroscopic and elastic forces, whereas $\boldsymbol{R}_F$ contains all external forces acting on the system, including aerodynamic contributions and we will expand on this more on the following Chapters. More details into the structural modelling of multibody dynamics using finite elements can be found in [167].

3.3.2 Gust Response of a Flexible Wing

In this section a nonlinear beam structural model is coupled with the strip theory aerodynamics already presented, and a gust response comparison is carried out against the commercial software MSC/NASTRAN. The rigid–body degrees–of–freedom are not included in the model and only the flexibility effects are taken into account in this particular analysis. Table 3.5 summarises the geometrical and material properties of the wing.

Young's Modulus E	$7.130{\cdot}10^8$N m^-2
Poisson's Ration ν	0.330
Material Density ρ	$2.703{\cdot}10^4$Nm^-3
Beam Length L	16 m
Beam Square Cross–Section d	0.28 m
Chord	1 m
Elastic–Axis	50% chord

Table 3.5: Flexible wing material properties and basic geometric characteristics

The beam model discretisation is done in the same way in both NASTRAN and the beam code by using 16 elements after having run a convergence study by applying a static force at the wing tip. Herein, we are interested in the aeroelastic response. Fig. 3.11 shows the flexible wing with 16 aerodynamic sections formed around the finite element model. The gust model used here is a discrete "1–minus–cosine" gust. The

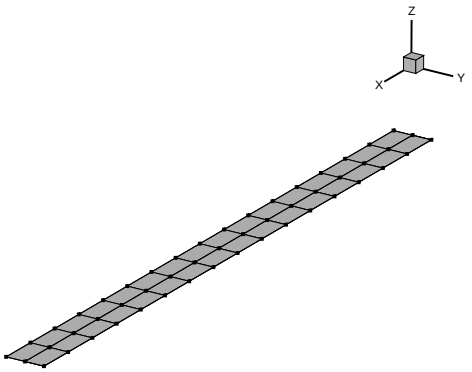

Figure 3.11: Flexible wing model together with the aerodynamic sections

flow conditions and the gust properties are given in Table 3.6. The aerodynamic model in NASTRAN is formed by Doublet–Lattice (DLM) panels distributed over the beam elements.

Gust Profile	1–minus–cosine
w_{go}	0.08
H_g [m]	40
cycles	1
Angle of attack [deg]	0.0
Freestream speed [m/s]	10.0
Density [kg/m^3]	0.0899

Table 3.6: Flow conditions and gust properties

As shown in Figure 3.12 both aerodynamic theories can predict the same wing tip deformation during the gust–fluid–structure interaction when there is a strong gust effect on the aerodynamics. The small differences after the gust, are due to the fact that the aerodynamic models are different.

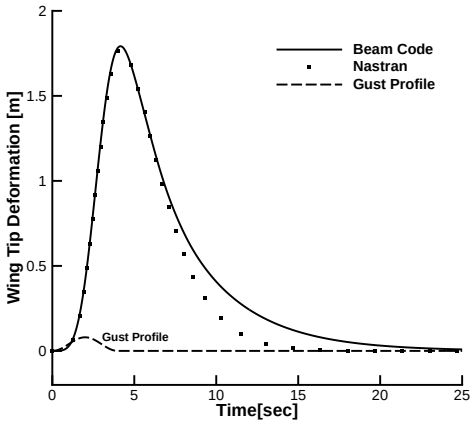

Figure 3.12: Wing tip response of the HALE wing at a "1-minus-cosine" gust of normalised intensity $w_{g0} = 0.08$ against MSC/NASTRAN at ($U_\infty = 10$ [m/s] and $\rho_\infty = 0.0899$ [kg/m^3])

3.4 Rigid Flying–Wing

3.4.1 Two–dimensional Wing Section

A prototype flying–wing is introduced to study the impact of the aerodynamic models on the flight dynamics. The geometry of the flying–wing has a constant chord of 1.0 m and a NACA0012 aerofoil is used to model the wing section.

The strip theory and the UVLM used here, are unable to capture three–dimensional aerodynamic effects around a finite span wing (e.g. wing tip vortices). As a result, the wing is assumed two–dimensional. Moreover, a unit span wing was used for the strip theory and a preliminary study with a varying aspect ratio of 1, 10, and 100 was performed in the UVLM to assess the influence on the response. It was found that the flight response was the same between an aspect ratio of 10 and an aspect ratio of 100 and as a result an aspect ratio of 10 was chosen.

The use of a unit wing span for the CFD results, reduces significantly the computational cost. In this case, a two–dimensional solution of the flow was obtained around a NACA0012 aerofoil. The geometrical and material properties of the wing are given in Table 3.7. The flight response is performed at 50.0 m/s and sea level density. A free response is studied for an initial angle of attack of 1 deg. Herein, only the pitching flight dynamic degree–of–freedom is unconstrained to isolate the impact of the aerodynamic modelling on the response.

Table 3.7: Reference values of the two–dimensional wing section

Parameter	Value
Elastic axis	5% chord
Centre of gravity	5% chord
Inertia properties	
Mass per unit length	10.0 kg/m
Mass moment of inertia (torsional)	10.0 kg·m
Geometry	
Chord	1.0 m
Span	∞

Both the horizontal and vertical displacements are constrained and the flying–wing is only free to rotate about the elastic axis (e.a) which is placed at 5% of the chord from the leading–edge. Thin aerofoil theory suggests that the centre of pressure is at one quarter of the chord from the leading–edge and it is expected that this particular wing configuration would be dynamically stable.

Figure 3.13 shows the comparison of the free–to–pitch case for the three different aerodynamic models. The wing section is rotated for 1 degree positive nose up and is let free in both the UVLM and the strip Theory. The wing section in the CFD is not rotated and the flow direction is set to 1 degree angle of attack instead.

A study was performed to verify that the CFD solution was independent of the time step used. Two time steps were used (in physical time: $4.9 \cdot 10^{-3}$ s and $1.0 \cdot 10^{-3}$ s; in nondimensional time: $2.4 \cdot 10^{-1}$ and $5.0 \cdot 10^{-2}$ based on the wing chord and freestream speed). Because no significant differences were found, the results presented subsequently are for the larger time step.

It is found that all three coupled computations are dynamically stable and in agreement with low speed aerodynamic theories. The differences between the flight responses are attributed to the different aerodynamic models used. Moreover, the oscillatory behaviour of the flight response is caused by the absence of structural damping and stiffness, and the different aerodynamic damping that is introduced by the different aerodynamic theories. However, all three predictions are very close to each other with the three–dimensional UVLM to predict, as expected, slightly better the CFD solution and strip theory, to be closer to the UVLM solution.

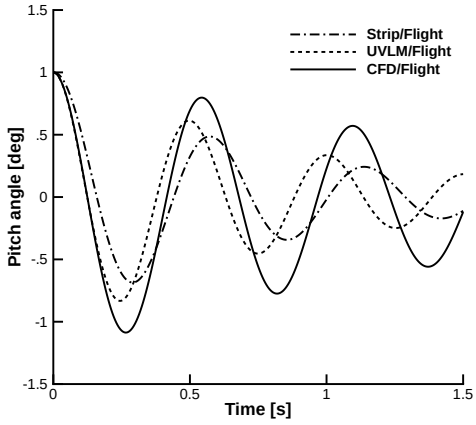

Figure 3.13: Time–domain response of a free–to–pitch two–dimensional wing section; "Strip" denotes two–dimensional thin aerofoil theory ($\alpha_\infty = 1.0$ deg, $U_\infty = 50.0$ m/s, $h = 0.0$ m, and $\mathrm{Re} = 3.5 \cdot 10^6$)

The impact of the aerodynamic models is assessed for the inclusion of additional flight dynamics degrees–of–freedom. The same wing configuration used here has two rigid–body degrees–of–freedom, one in the pitch rotation and one for the plunging motion. The horizontal degree–of–freedom is kept constrained because linear aerodynamic models lack the ability to realistically predict the drag contributions. This allows a direct comparison of the responses computed by linear aerodynamic models with the CFD solution.

The time–domain solution of the angle of attack and the vertical displacement for the same initial condition already discussed above are shown in Figure 3.14. The aeroelastic behaviour predicted by the three coupled models is similar. Moreover, the steady–state response of the potential flow aerodynamics is identical as they both predict a similar steady–state pitching and vertical displacement.

Figure 3.13 and Figure 3.14 show that the wing response reaches the steady–state solution faster in the thin aerofoil aerodynamics which confirms that the aerodynamic damping in this case is larger. The least damped response is for the CFD predictions. Furthermore, the predicted steady–state solution is not always the same as it is shown to depend highly on the aerodynamic model used. For example, potential aerodynamics computed similar steady–state solutions whereas CFD gave different predictions. With no gravity acting on the system, the free–flying wing reaches a steady–state equilibrium when the effective angle of attack is zero. For a two degree–of–freedom system, the effective angle of attack is expressed as

$$\alpha_{eff} = \theta_z - \frac{\dot{y}}{U_\infty} \tag{3.10}$$

where $\dot{y}$ is the velocity component in the vertical direction. From the above equation, it is apparent that the values of rigid–body pitch angle and vertical velocity component need to cancel out each other to yield an effective angle of attack equal to zero, e.g. $\alpha_{eff} = 0$.

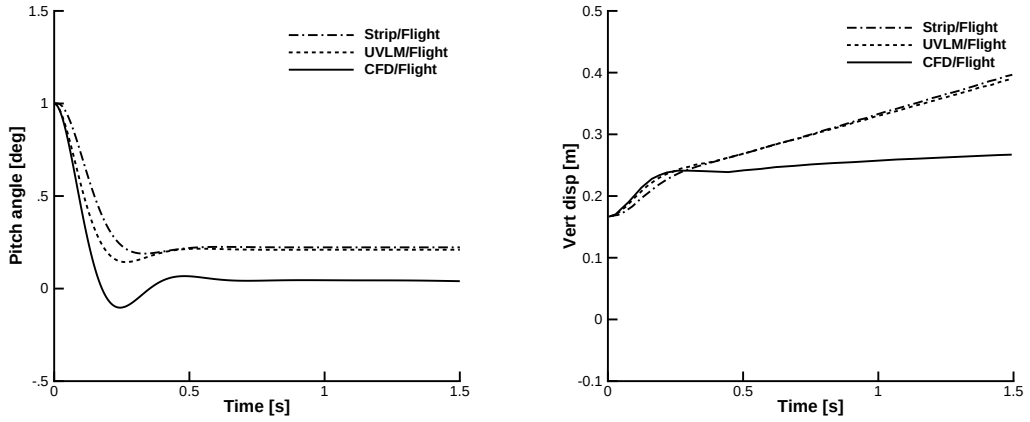

(a) Pitch angle

(b) Vertical displacement

Figure 3.14: Time–domain response of a free–flying two–dimensional wing section; "Strip" denotes two–dimensional thin aerofoil theory ($\alpha_\infty = 1.0$ deg, $U_\infty = 50.0$ m/s, $h = 0.0$ m, and $\mathrm{Re} = 3.5 \cdot 10^6$)

3.5 Summary

The work presented in this Chapter demonstrated the following:

1. A two degree-of-freedom aerofoil model with a structural nonlinearity in the plunge degree–of–freedom was coupled with CFD and strip aerodynamics. The strip aerodynamics gave the exact same solution with the CFD for a free response driven by an initial perturbation in the plunging at low–speed.

2. The ability of the reduced–order model to predict nonlinear aeroelastic responses in any Mach number and its independence from the aerodynamic modelling technique as it was shown in Figure 3.5 at low speed with CFD and the low–order aerodynamics and at 0.8 Mach number for the CFD aerodynamics. Similarly, the same is presented for a gust response since after the reduced–order models were derived, they could be used for parametric worst–case gust searches. This was shown for both CFD and strip theory aerodynamics. In strip aerodynamics in particular, it was shown how to select the eigenvalues for the model order reduction when dealing with a gust response computation.

3. A geometrically-exact nonlinear beam model was coupled with two–dimensional aerodynamics and the same beam structure was assembled in NASTRAN allowing a gust response comparison between the two frameworks. It was shown that the current assumption to model the gust and the aerodynamics agreed well with results provided by commercial solvers for high–aspect–ratio wings exhibiting large deformations.

4. The flight dynamics degrees–of–freedom were included, and completely free–flying wing responses driven by an initial angle of attack were compared between CFD, a UVLM solver and the current strip theory assumption. As expected, at low speed, strip theory gave good predictions. However, being able to capture some three–dimensional aerodynamic effects, UVLM predicted a solution closer to the CFD results.

Chapter 4

Numerical Models and Their Application to Experiments and Control Design

4.1 Control Design for Load Alleviation of a Two Degree–of–Freedom Aerofoil Model

The reduced–order model used for a worst–case gust search in § 3.2.2.2 will now be exploited for gust load alleviation. The method documented is extended in the next chapters in a straightforward manner to systems of larger dimension. The strength of the approach is to allow control design to be done on a state–space system of small size which is independent of the underlying physical model.

The control design for the worst–case gust is done using the standard H_∞ technique. The control effector is the trailing–edge flap and herein, the pitch degree–of–freedom is measured in the feedback loop as detailed in the mathematical formulation § 2.5.1.1 for the H_∞ control design. The open and closed–loop responses are compared in Figure 4.1, and a significant alleviation in both degrees–of–freedom is achieved with a reasonable control input.

In the case that the full–order model exhibits a nonlinear behaviour in the gust response, quadratic and cubic terms are included in the reduced model in a straightforward fashion. Consider, for example, the full model responses in Figure 4.2. The nonlinearity in the full–order model was obtained by adding a cubic spring constant $\beta_{\alpha 3} = 2.0$ in the pitch and $\beta_{\xi 3} = 1.0$ in the plunge degree–of–freedom. The effect of structural nonlinearity is evident because the nonlinear response differs greatly from the linear. Nonlinear terms were then generated and included in the dynamics of the reduced model, and the predictions shown in Figure 4.2 are in good agreement with the nonlinear full model.

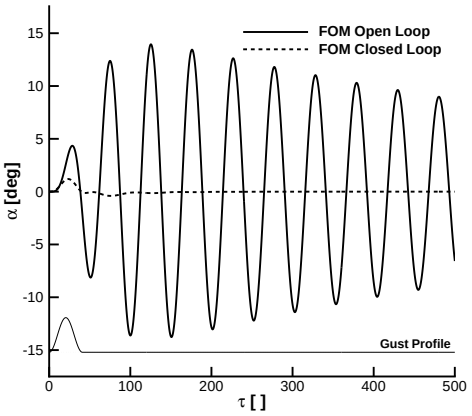

(a) Pitch, α

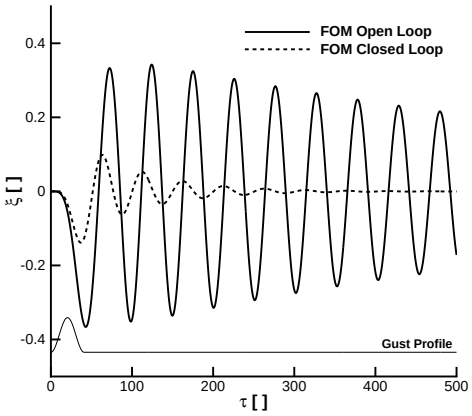

(b) Plunge, ξ

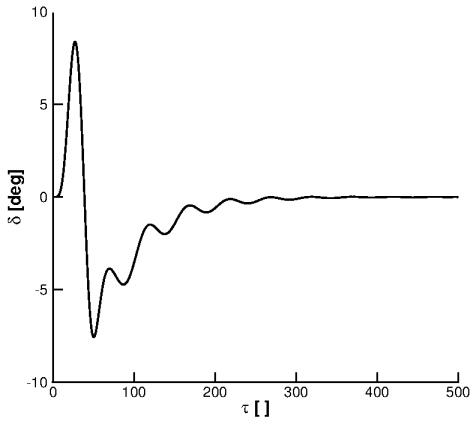

(c) Flap Rotation, δ

Figure 4.1: Open–loop and closed–loop responses for the worst–case gust for the aerofoil model in Table 3.3

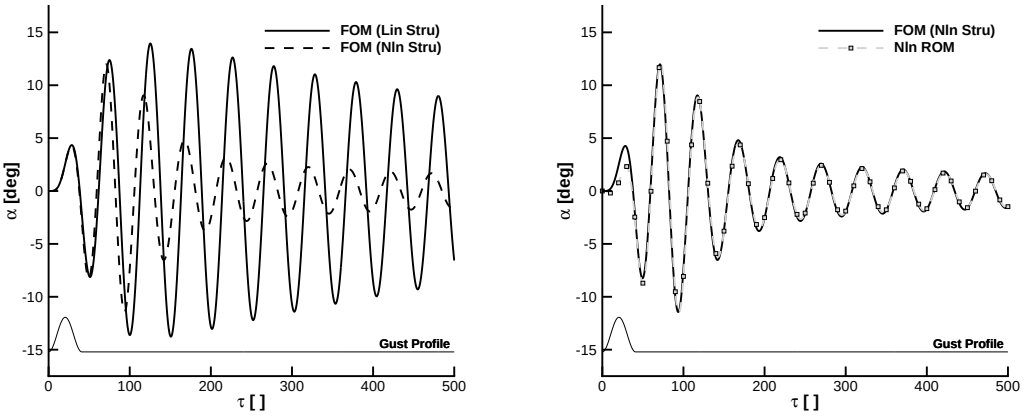

(a) Linear/nonlinear full–order models (b) Nonlinear full and reduced–order models

Figure 4.2: Response to a "1-minus-cosine" gust of intensity 5% of the freestream speed and a length of 25 semichords at $U^* = 4.6$

The ability to retain relevant nonlinearities in the reduced model is exploited for gust loads alleviation. The control design was performed as in the linear case, with the exception that the reduced model now includes the nonlinear vector in Eq. (2.16). Comparing the time responses in Figure 4.3 indicates a good alleviation in the pitch motion. The control deflection required is similar to the linear case, as the nonlinearity used here reduces the system response. Furthermore, the same linear H_∞ controller derived based on the linearised reduced model is efficient when applied on the nonlinear reduced–order model.

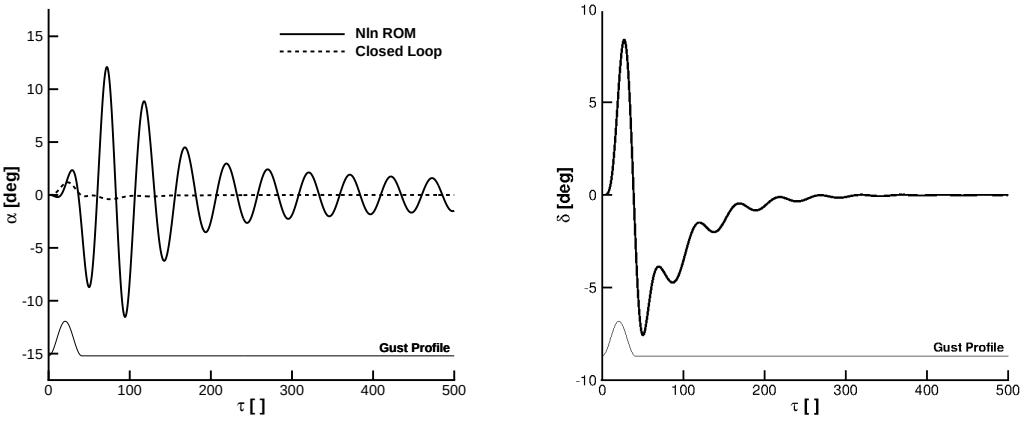

(a) Pitch, α (b) Flap Rotation, δ

Figure 4.3: Open–loop and closed–loop responses for the aerofoil with structural nonlinearities ($\beta_{\alpha 3} = 2.0$, $\beta_{\xi 3} = 1.0$), at $U^* = 4.6$, gust intensity 5% of the freestream speed and a length of 25 semichords

4.2 An Experimental Investigation on the Active Control

4.2.1 Experimental Low–Speed Wind–Tunnel Section

The developed numerical model presented in the previous section was tested in wind–tunnel at the University of Liverpool. The numerical model was used to cross–validate a stability analysis against available experimental measurements and then was used for numerical control design for flutter suppression. Experimental work was carried out and the flutter speed of this test–rig has been measured at around 20 m/s in past studies by Papatheou et al. [101]. Figure 4.4 shows the wing section that is mounted horizontally and is supported by adjustable vertical and torsional leaf springs. The wing section weighs 6.5 kg and consists of a NACA0018 aerofoil, with a chord of 0.35 m and a span of 1.2 m. A V–stack piezoelectric actuator is used to drive the control surfaces with a maximum deflection of ±7 deg. Pitch and plunge degree–of–freedom measurements are readily available by two laser sensors that are attached to the main body of the wing section. Preliminary tests were made to guarantee that the flexible modes of the wing, e.g. spanwise bending modes, are well above the pitch and plunge frequencies, and a separation of one order of magnitude was found. More details on the (linear) baseline aeroelastic wind–tunnel model have been presented in Papatheou et al. [101]

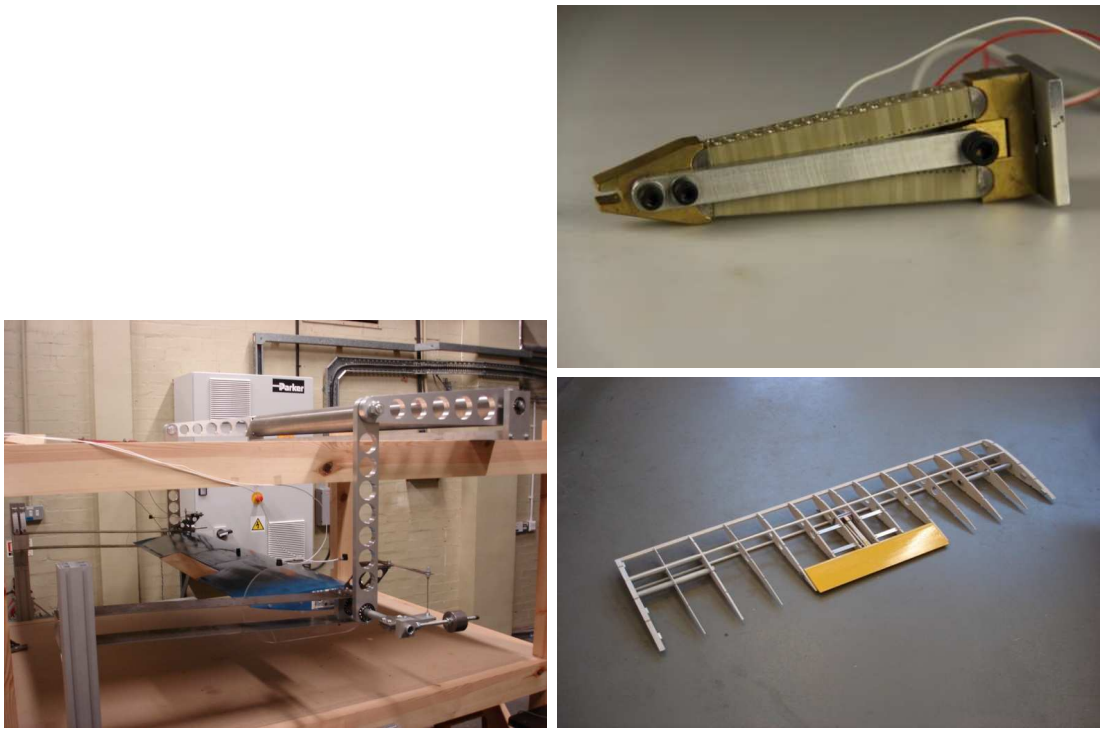

(a) Wind–tunnel test section (b) Trailing–edge control surface and actuator

Figure 4.4: Schematic view of the experimental setup of the aeroelastic model at the University of Liverpool

Modifications were made and a concentrated hardening nonlinearity in the plunge degree–of–freedom was introduced in the model. The design follows Chianetta [168]. The nonlinearity in the restoring force on each end of the aerofoil is realised by a clamped cable under tension, which acts as a hardening spring. Figure 4.5 shows the system of cables used to introduce the nonlinearity in the wind–tunnel rig.

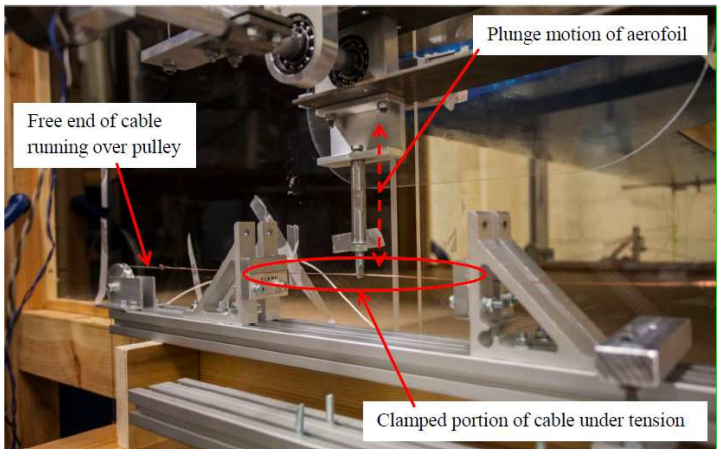

Figure 4.5: Schematic view of the system of cables used to introduce a nonlinearity in the wind–tunnel test–rig (from Ref. [168])

The tension in the cables can be varied by altering the weights hanging at the free ends of the cables passing over the pulleys on both sides of the aerofoil. Thus, the strength of the nonlinearity is adjusted as required. At present, a weight of 2 kg is hung on each side, and the force-deflection profile was found by applying known, equal, downward loads at each end of the aerofoil and measuring the deflection. A non–contact laser displacement sensor was used to measure deflection. Figure 4.6 shows the measured points for the nonlinear case along with a polynomial fit. The nonlinear relation between the force and the vertical displacement is formulated as

$$F_{nl} \;=\; K_{\xi\,1}\,h \;+\; K_{\xi\,3}\,h^3 \;+\; K_{\xi\,5}\,h^5 \tag{4.1}$$

where the stiffness constants $K_{\xi\,1} = 7.886 \times 10^3$ N/m, $K_{\xi\,3} = 1.603 \times 10^8$ N/m^3, and $K_{\xi\,5} = -8.226 \times 10^{10}$ N/m^5 were calculated by a least–squares fit.

4.2.2 Numerical Model

The numerical model was first validated against available wind–tunnel measurements. A comparison in terms of eigenvalues tracing is illustrated in Figure 4.7 for increasing freestream speed. The analytical results were obtained solving for each freestream speed an eigenvalue problem of the coupled full–order model. For the wind–tunnel data, measurements of the frequency response functions (FRF) were obtained by a stepped sine forced motion of the control surface. Since the FRFs relate the input voltage applied

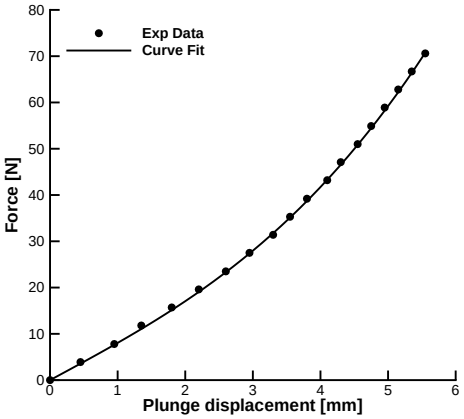

Figure 4.6: Structural nonlinearity in plunge displacement measured experimentally as in Ref. [144]

to a power amplifier of the V–stack piezoelectric actuator to the output displacements of two points attached to the aerofoil shaft, the dynamics of the system as well as the dynamics of actuators/sensors are included in the measurements.

Table 4.1: Aeroelastic experiment parameters of the wing section–linear case

Parameter	Value
μ	69.0
$\bar{\omega}$	0.6491
x_α	0.09
a_h	-0.333
ζ_ξ	0.002
ζ_α	0.015
r_α^2	0.40

Analytical results are in good agreement with wind–tunnel measurements. For increasing freestream speed, the damping of the coupled system increases. At the flutter point, which occurs for a speed of $U_L = 17.63$ m/s, the damping ratio becomes negative and a coalescence of the pitch and plunge frequencies is observed. The predicted flutter speed compares well with the value of about 17.5 m/s extrapolated using the flutter margin method [169] from the available measurements.

4.2.3 Open–Loop Simulations

The parameters of the nondimensional numerical elastic model are set to those of the nonlinear experimental wind–tunnel aerofoil rig, and open–loop responses were run. The corresponding system parameters used are summarised in Table 4.2.

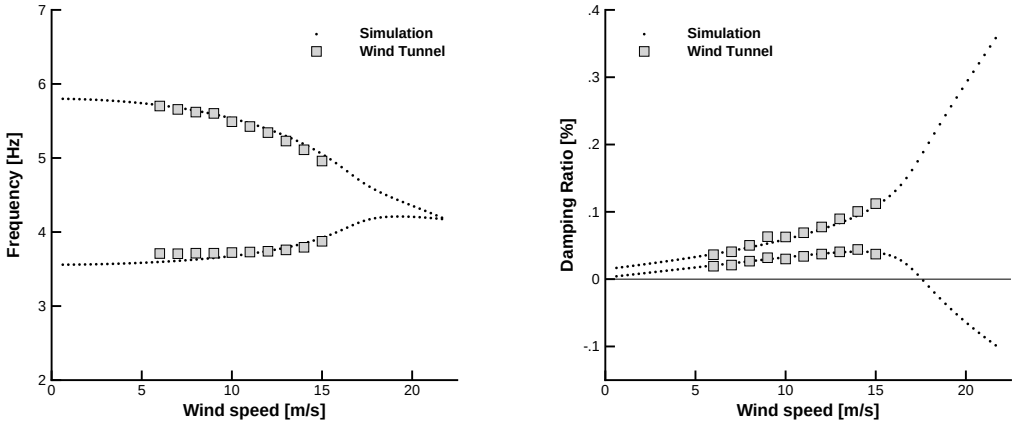

(a) Damped frequency, ω_d

(b) Damping ratio, ζ

Figure 4.7: Eigenvalues tracing for varying freestream speed from simulation performed here and wind–tunnel measurements taken from Ref. [101]

Table 4.2: Aeroelastic numerical parameters representative of the wing section–Non Linear case

Parameter	Value
μ	69.0
$\bar{\omega}$	0.721655
x_α	0.09
a_h	-0.3333
ζ_ξ	0.002
ζ_α	0.015
r_α^2	0.40
$\beta_{\xi 3}$	622.519
$\beta_{\xi 5}$	-9783.27
c_{flap}	0.5428

Note that the coefficients describing the plunge nonlinearity, $\beta_{\xi 3}$,$\beta_{\xi 5}$, have been obtained by converting the coefficients $K_{\xi 1}$, $K_{\xi 3}$, $K_{\xi 5}$ in Eq. (4.1) into the nondimensional form in which the aeroelastic system equations have been expressed.

The linear flutter speed of the system with the parameters given in Table 4.2 was found to be 16.24 m/s (note the reduction from 17.63 m/s due to the change in linear stiffness caused by the addition of the nonlinear spring). The objective here is to see how this implemented nonlinearity affects the system behaviour above the linear flutter speed. Thus, the freestream speed for the simulation is chosen to be slightly above this value, at 17 m/s. An initial condition of $\alpha = 5\,\text{deg}$ is set, and the uncontrolled simulation is run for a period of 5 seconds. The resulting open–loop response is plotted in Figure 4.8

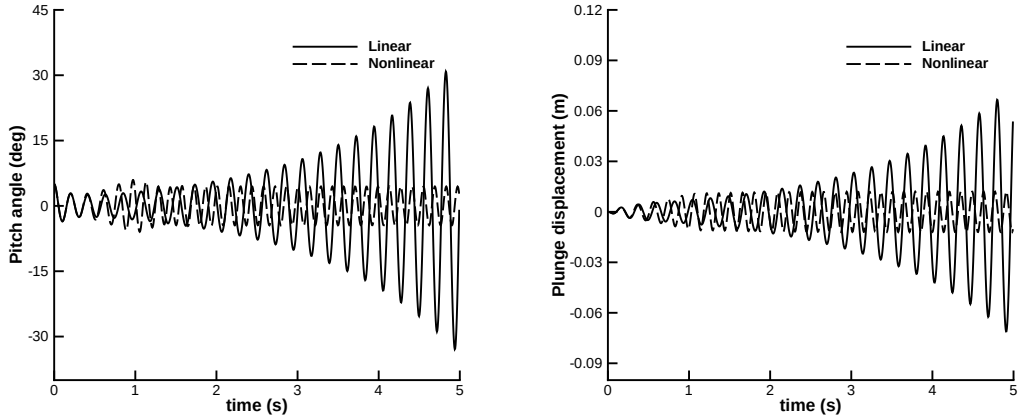

(a) Pitch in degrees

(b) Plunge displacement in metres

Figure 4.8: Open–loop response comparison of the linear against the nonlinear system at $U = 17.0$ m/s with parameters from Table 4.2

It is clear that the linear system will be unstable above the flutter speed due to the coalescence of the pitch and plunge frequencies. The nonlinear system exhibits LCO which can be attributed to the fact that the structural nonlinearity acts as a hardening spring and thus preventing the aeroelastic response from becoming unstable.

This nonlinear response may be eliminated by applying feedback linearisation, setting the poles of the linearised system as desired.

4.2.4 Control Strategies

Two different control strategies are used, one linear and one nonlinear. Herein, it is desirable to show a case where a linear controller with the same design specifications is inferior to the nonlinear control design. The linear controller is based on a pole-placement technique. The nonlinear controller is based on a classical approach to control nonlinear systems, the feedback linearisation. A brief review of the pole–placement method is first presented, while a detailed derivation of the feedback linearisation as designed and applied in [144] is given in the Appendix A.2.

4.2.4.1 Pole Placement

There are a variety of available pole-placement techniques, for example the Ackerman or the Kura–Bass formula as in Ogata [156]. Most of them focus on the derivation of a linear feedback based on the eigenvalue solution of the linearised part of the system dynamics to change the location of the eigenvalues of the closed–loop system. In this case the algorithm presented in Kautsky et al. [170] was used and the derived feedback is applied according to the block diagram in Figure 4.9. The open–loop dynamics of

the system can be written as

$$\boldsymbol{x}' = \boldsymbol{A}x + \boldsymbol{g}u + \boldsymbol{f}_{nln} \tag{4.2}$$

Once the pole–placement feedback K is calculated, the closed–loop system dynamics become

$$\boldsymbol{x}' = (\boldsymbol{A} - \boldsymbol{g}K)\, x + \boldsymbol{f}_{nln} \tag{4.3}$$

where the solution of the eigenvalue problem of $(\boldsymbol{A} - \boldsymbol{g}K)$ gives the desired poles.

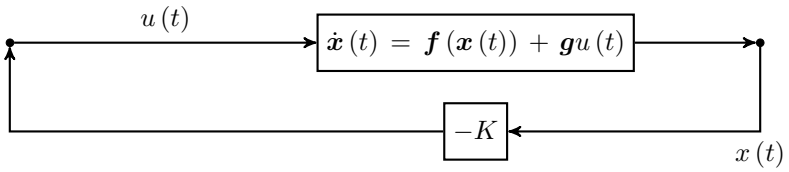

Figure 4.9: Pole Placement Diagram

A simple linear control technique based on a pole–placement algorithm [170] was used to add damping to the eigenvalue associated with the pitching mode and the linear controller was integrated together with the nonlinear system dynamics. The open and closed–loop eigenvalues of the system for these flow conditions are shown in table 4.3. The necessary control feedback K to achieve the specified closed–loop eigenvalues in

Table 4.3: Open and closed–loop eigenvalues in [rad/s^*]

Open–Loop	Closed–Loop
-0.0586 ± 0.3049i	-0.0162 ± 0.0626i
0.0061 ± 0.2927i	0.0061 ± 0.2927i
-0.2755	-0.2755
-0.3000	-0.3000
-0.0432	-0.0432
-0.0455	-0.0455
-0.0455	-0.0455
-0.3000	-0.3000

Table 4.3 is given in nondimensional values in Table 4.4.

The unstable eigenvalue with the small real part related to the plunging motion is not moved and this is done for direct comparison with the nonlinear controller. In this way, the efficiency of the linear controller for flutter suppression is tested by keeping this unstable mode and separating the torsional from the plunging mode by moving the pitching eigenvalue.

Table 4.4: Feedback Gains for Pole Placement

State Related	Gains in nondimensional units
x_1	$1.591{\cdot}10^{-3}$
x_2	$-1.598{\cdot}10^{-1}$
x_3	$4.620{\cdot}10^{-2}$
x_4	$1.478{\cdot}10^{-1}$
x_5	$1.412{\cdot}10^{-4}$
x_6	$-7.028{\cdot}10^{-4}$
x_7	$-6.679{\cdot}10^{-6}$
x_8	$2.811{\cdot}10^{-4}$
x_9	$8.462{\cdot}10^{-5}$
x_{10}	$-4.969{\cdot}10^{-4}$
x_{11}	0
x_{12}	0

The closed–loop response of the nonlinear system in this case is given in Figure 4.10.

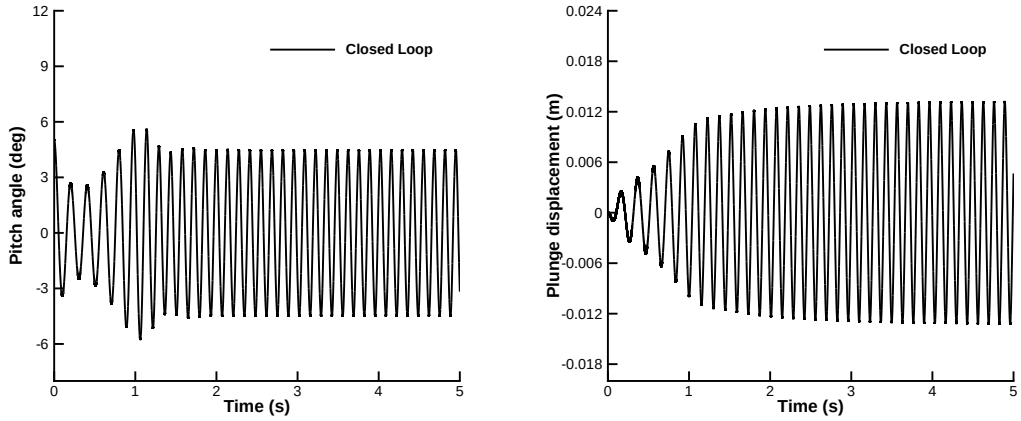

(a) Pitch angle (deg)

(b) Plunge displacement(m)

Figure 4.10: Pitch and plunge time history of the closed–loop system for the linear controller at $U = 17$ m/s

The system exhibits LCO under the linear controller implementation and this can be confirmed also by the flap angle in Figure 4.11. As expected, the nonlinear system cannot be stabilised by keeping this unstable plunging mode and move only the pitching mode as the unstable plunging mode becomes dominant in the system's response.

4.2.4.2 Feedback Linearisation and Pole Placement

Feedback Linearisation, as detailed in Isidori and Khalil, [171, 172] is a widely used method in the control of nonlinear systems. The method is based on providing a non-

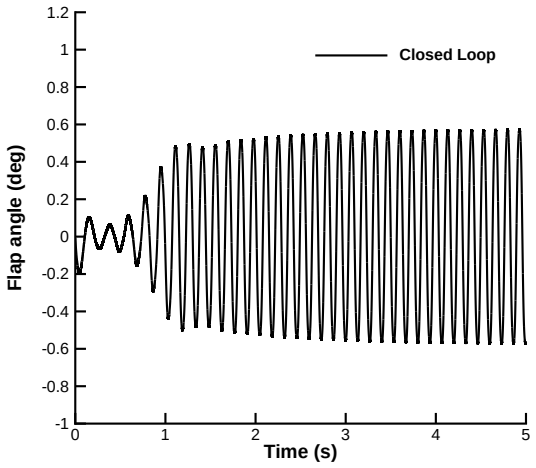

Figure 4.11: Flap response of the linear controller at $U = 17$ m/s

linear feedback to the system which effectively eliminates the nonlinearity and applies a linear control strategy such as pole placement. This method is used to control the nonlinear aeroelastic model detailed above. More details on the derivation of the control law can be found in the Appendix A.2 and in Da Ronch et al. [144].

Prior to the application of feedback linearisation one needs to check the stability of the resulting zero–dynamics of the system according to the output that was chosen for the control. This is important because the stability of the zero–dynamics is a precondition for the stability of the closed–loop system. Herein, if the plunge is chosen as the controlled output, unstable zero–dynamics occur and in that case this methodology is not applicable and the pitch is selected as the controlled output. Therefore, simulating the zero–dynamics when the pitch is selected as the controlled output, at the same freestream speed chosen above, a stable response is found for the particular parameters of the wind–tunnel aeroelastic model. In fact, it is found that the underlying linear system is also stable, as the real parts of the eigenvalues are negative. Thus, one may conclude that partial feedback linearisation of the aeroelastic model based on pitch output is feasible.

The pole–placement design requirement here is set to assign a natural frequency of $1\,Hz$, and a damping ratio of 0.25 to the pitch mode, resulting in a closed–loop pole of $-0.01617 \pm 0.06263i$. In the linear version of the open–loop system, these quantities were $4.8\,Hz$ and 0.1886 respectively, with the open–loop pole of the pitch mode being $-0.05855 \pm 0.3049i$. Assuming knowledge of the system nonlinearity and availability of the other state variables, a nonlinear feedback is derived as described in the Appendix A.2. Subsequently, the required controller gains for the pole–placement of the resulting feedback linearisable system, $g_1 = 0.0041835\,(rad)$ and $g_2 = 0.03234\ (rad \times s^*)$ respectively, and the total artificial control input, flap deflection is computed. The

resulting closed–loop response is shown in Figure 4.12

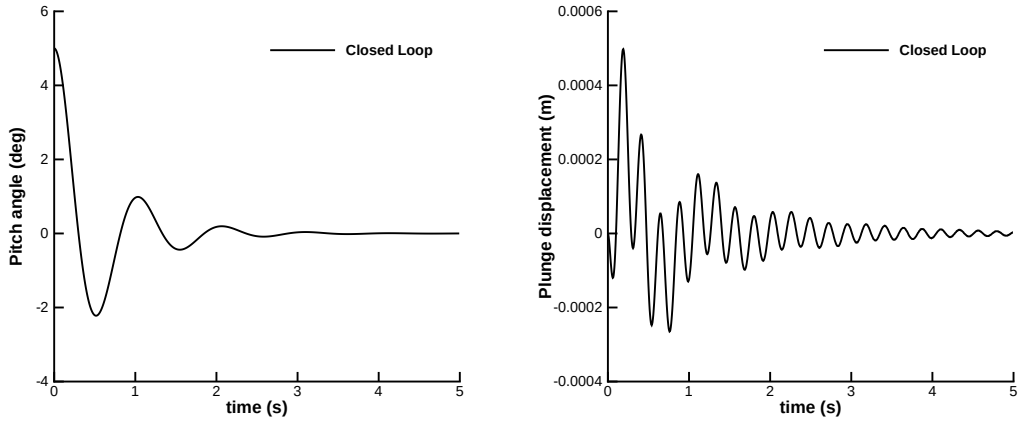

(a) Pitch angle (deg)

(b) Plunge displacement(m)

Figure 4.12: Pitch and plunge time history of the closed–loop system at $U = 17$ m/s with the nonlinear controller

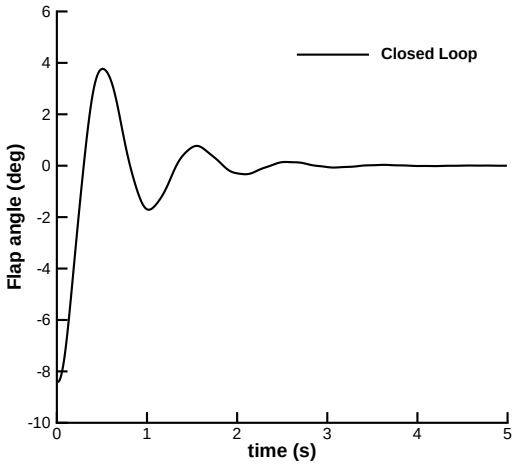

Figure 4.13: Flap response at $U = 17$ m/s of the nonlinear controller

It can be seen from the closed–loop response that the required pole placement of the pitch mode has been achieved. The flap deflection angles required to implement the nonlinear controller shown in Figure 4.13 are expected to be feasible in the experimental wind–tunnel model, as the rotation angle stays between $-7 \leq \delta \leq 7\,\text{deg}$ after the initial times of the calculation. Furthermore, it can be seen that the (uncontrolled) plunge mode also decays to zero, as do the remaining (aerodynamic) uncontrolled states, which is a reflection of the stability of the internal–dynamics for this particular choice of control output.

4.3 Summary

A two degree–of–freedom aerofoil model with the option of structural nonlinearity in either the pitch or the plunge degree–of–freedom was developed and was coupled with a potential flow assumption by strip theory. A cubic nonlinearity was included in both the pitch and the plunge degree–of–freedom and additional nonlinear terms up to third order expansion in the Taylor series were included in the dynamics of the reduced model, making it nonlinear.

An $\mathcal{H}_\infty$ control design was then feasible based on the nonlinear reduced model. The controller was applied to the linear and the nonlinear cases for the worst–case gust length, offering very good alleviation under realistic control surface deflection.

Secondly, this developed numerical model was compared against an experimental wind–tunnel model for stability analysis. It was found that the nonlinearity of the experimental rig can be described by the numerical model and that the numerical model can be used as a benchmark to design complex control methodologies. Due to its size, it can also run in parallel with the experimental setup as has been shown in [173] where this numerical model was compared against the experiment for open–loop time–domain responses. Herein, the simulations were run above the flutter speed where the linear model was unstable and the nonlinear system exhibited LCO because of its nonlinearity. Two different control approaches were compared, one linear based on pole–placement, and one nonlinear based on the feedback linearisation. It was found that the nonlinear controller was able to suppress the LCO and extend the flight envelope, whereas the linear controller was inadequate to suppress the flutter.

Chapter 5

Nonlinear Model Order Reduction for Control Applications

5.1 Three Degree–of–Freedom Aerofoil Model

5.1.1 Residual Formulation

A more complicated aerofoil model was developed. The size of the coupled aeroelastic model is 14 and consists of 8 aerodynamic states and 6 structural states (pitch, plunge and flap degrees–of–freedom and their corresponding velocities) . The schematic of the three degree–of–freedom aerofoil is given in Figure 5.1. The nondimensional torque is

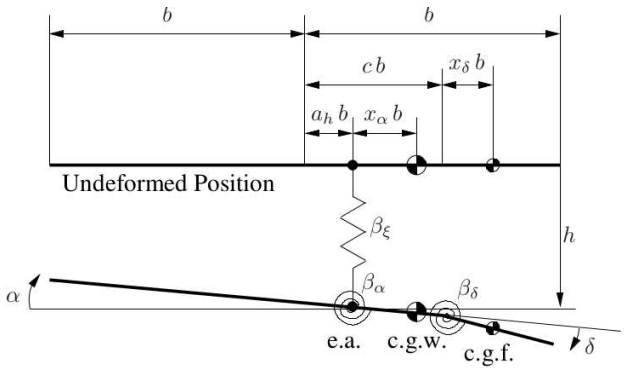

Figure 5.1: Schematic of a three degree–of–freedom aeroelastic system (pitch, α, plunge $\xi = h/b$, and flap deflection, δ), the wind velocity is to the right and horizontal

used as control input related to the flap rotation. Define the state vector $\boldsymbol{x_s}$ of the structural degrees–of–freedom and $\boldsymbol{w_f}$ for the augmented aerodynamic states.

$$\boldsymbol{x_s} = \{\xi, \alpha, \delta\}^T \tag{5.1}$$

$$\boldsymbol{w_f} = \{w_1, w_2, w_3, w_4, w_5, w_6, w_7, w_8\}^T \tag{5.2}$$

Following the general definition of the Residual in § 2.1 the system is recast as a coupled first order ODE of the general form where the unknowns are partitioned into structural and fluid contribution as

$$\boldsymbol{w} = \left\{\boldsymbol{w}_s^T, \boldsymbol{w}_f^T\right\}^T \quad \text{where} \quad \boldsymbol{w}_s = \left\{\boldsymbol{x}_s^T, \dot{\boldsymbol{x}}_s^T\right\}^T \tag{5.3}$$

and the residual $\boldsymbol{R}$ is given by

$$\boldsymbol{R} = \boldsymbol{A}_L\boldsymbol{w} + \boldsymbol{b}_N(\boldsymbol{w}) + \boldsymbol{b}_a + \boldsymbol{b}_e \tag{5.4}$$

The matrix A_L is defined as

$$\boldsymbol{A}_L = \begin{bmatrix} \boldsymbol{0} & \boldsymbol{I} & \boldsymbol{0} \\ -\boldsymbol{M}^{-1}\boldsymbol{K} & -\boldsymbol{M}^{-1}\boldsymbol{C} & \boldsymbol{A}_{sf} \\ \boldsymbol{A}_{fs} & \boldsymbol{0} & \boldsymbol{A}_{ff} \end{bmatrix} \tag{5.5}$$

$$\boldsymbol{b}_N = \begin{Bmatrix} \boldsymbol{0} \\ -\boldsymbol{M}^{-1}\boldsymbol{F}_N \\ \boldsymbol{0} \end{Bmatrix}, \quad \boldsymbol{b}_a = \begin{Bmatrix} \boldsymbol{0} \\ -\boldsymbol{M}^{-1}\boldsymbol{f}_a \\ \boldsymbol{0} \end{Bmatrix}, \quad \boldsymbol{b}_e = \begin{Bmatrix} \boldsymbol{0} \\ -\boldsymbol{M}^{-1}\boldsymbol{f}_e \\ \boldsymbol{A}_{fg}\boldsymbol{u}_d \end{Bmatrix} \tag{5.6}$$

The matrix terms $\boldsymbol{M}$, $\boldsymbol{C}$ and $\boldsymbol{K}$ are the effective mass, damping and stiffness matrices containing structural and aerodynamic contributions. The matrix blocks $\boldsymbol{A}_{sf}$ and $\boldsymbol{A}_{fs}$ couple the structural equations and the fluid equations. The matrix $\boldsymbol{A}_{ff}$ relates the fluid unknowns to their first time derivatives. The term $\boldsymbol{F}_N$ is a nonlinear vector arising from the polynomial stiffness. The vector $\boldsymbol{f}_a$ arises from the influence of initial conditions on the unsteady aerodynamic forces. The term $\boldsymbol{f}_e$ is the nondimensionalised form of any applied external force or moment, for example the flap hinge moment for control input. The vectors $\boldsymbol{b}_N$, $\boldsymbol{b}_a$ and $\boldsymbol{b}_e$ denote contributions from nonlinear terms, aerodynamics due to initial conditions and external inputs, respectively. The explicit formulation of the residual in Eq. (5.4) is given in Appendix A.4.

5.1.2 Validation

Two sets of parameters are considered, given in Table 5.1. These two sets differ in the ratio of the uncoupled plunging to pitching mode $\overline{\omega}_1$ and c_h which is the nondimensional distance from the midchord to the flap hinge.

Case	$\overline{\omega}_1$	$\overline{\omega}_2$	μ	a_h	x_α	x_δ	r_α	r_δ	c_h
1	0.2	300	100.0	-0.5	0.25	0.0125	0.5	0.0791	0.5
2	1.2	3.5	100.0	-0.5	0.25	0.0125	0.5	0.0791	0.6

Table 5.1: Model parameters for aerofoil test cases

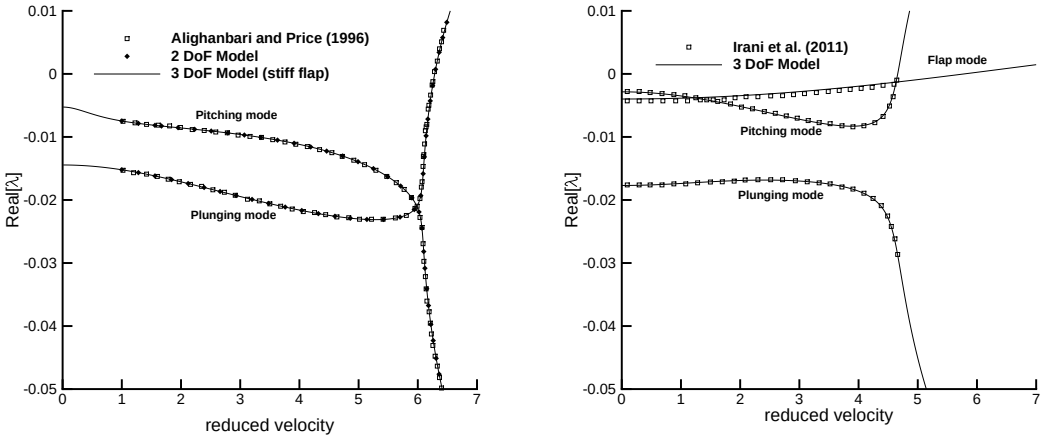

(a) mode trace for case 1

(b) mode trace for case 2

Figure 5.2: Mode traces for validation test cases 1 and 2

Linear stability analysis provides a convenient way to check the linear part of the aerofoil model. In the following results, the Schur complement form of the eigenvalue problem presented by Badcock et al. [139] is used to track the migration of the three structural eigenvalues with the reduced velocity. The first comparison is made with a two degree–of–freedom (DoF) aerofoil model presented by Alighanbari et al. [174] as well as the original two degree–of–freedom model by Da Ronch et al. [98]. Since this specific comparison is made between a three degree–of–freedom and a two degree–of–freedom model, a high value of $\overline{\omega}_2$ is enforced. The system parameters used are given in Table 5.1 for Case 1 with $\overline{\omega}_2 = 300$. The nonlinear stiffness coefficients are all set to zero. The mode tracing shows excellent agreement with the result presented by Alighanbari et al. [174] in Figure 5.2 (a). The linear instability point is found to be $U_L^* = 6.285$.

The flutter speed is also validated against the results presented by Irani et al. [175]. The model presented by Irani et al. [175] is a three degree–of–freedom aerofoil and the

aeroelastic parameters are as for Case 2. The linear flutter speed is calculated to be $U_L^* = 4.663$ which matches the reported value. Figure 5.2(b) shows the corresponding mode trace comparison. In the aerofoil case the nonlinearity is a polynomial cubic nonlinearity in either the pitch or the plunge degree–of–freedom stiffness and is fully deterministic.

5.1.3 Nonlinear Reduced Models for Worst Case Gust Search

Two families of atmospheric gusts are used, discrete and continuous. The discrete model for the "1–minus–cosine" gust is formulated as

$$W_g(\tau) = \begin{cases} \frac{1}{2} w_g \left(1 - \cos\left(\frac{2\pi}{H_g}(\tau - \tau_0)\right)\right) & \tau \in [\tau_0, \tau_0 + H_g] \\ 0 & \text{otherwise} \end{cases} \tag{5.7}$$

where w_g is the gust intensity normalised by the freestream speed and H_g is the gust length. For the generation of continuous models of atmospheric Von Kármán turbulence, the rational approximation documented in Ref. [142] can be used. A cubic hardening nonlinearity is considered for the pitch degree–of–freedom $\beta_{\alpha 3} = 3$ and in the plunge degree–of–freedom $\beta_{\xi 3} = 1.0$, the same way it was done in [144]. The aeroelastic nondimensional model parameters given, are the same as Case 2 in Table 5.1 with the difference that $\overline{\omega}_1 = 0.2$. From the bifurcation method and the eigenvalue solution of the linearised system, the instability for this model selection occurs for $U_L^* = 6.37$.

The concept here is to identify the basis for the model order reduction and generate a small nonlinear reduced–order model which can be used for parametric gust searches to speed up the calculations and at the same time to simplify an adaptive control design implementation. The reduced–order model is generated at an operating flight speed condition below the instability at $U^* = 4.5$ or 70.64% of the linear predicted flutter speed. The eigenvalues of the full–order model and the eigenvalues selected to be included in the basis for the reduction are shown in Figure 5.3. The reduced–order models are generated by including the three complex eigenvalues corresponding to the structural degrees–of–freedom and one additional eigenvalue related to the gust influence which is equal to the Küssner constant $\epsilon_3 = -0.1393$ as in Ref. [144], and this is shown in Table 5.2. This is of great importance and it is emphasised throughout this investigation. As a result of the aerodynamic modelling with strip theory, Wagner and Küssner functions, the eigenvalues related to the gust disturbance can be selected automatically as it is equal to the Küssner constant. The reduced–order model eigenvalue basis, is constructed by choosing the complex conjugate eigenvalues of the aeroelastic system. Furthermore, the gust interaction with the fluid/structure depends on the aerodynamic modelling which in that case comes from the Küssner constant ϵ_3.

The nonlinear reduced model is used to perform a worst–case gust search for the "1–minus–cosine" family. The gust intensity is 14% of the freestream speed at $U^* =$

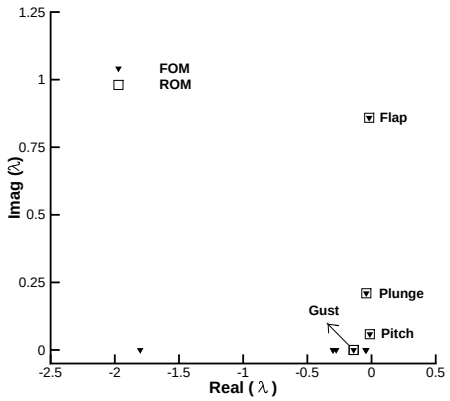

Figure 5.3: Full model and reduced–order model basis selection at $U^* = 4.5$

4.5, as it was done in Ref. [98] and the search is made for gust lengths up to 100 aerofoil semichords. The parameter space of the gust length is divided into 1000 design sites starting from a gust length of 0.1 semichords up to 100 semichords. The worst–case gust was found to be for $H_g = 55$ semichords, corresponding to maximum loads in the pitching angle largest fluctuations that are related to structural fatigue of the aircraft components. Figure 5.4 shows the maximum and minimum amplitude of the corresponding degrees–of–freedom for full nonlinear and reduced model against different gust lengths. Behind each pair of max–min there is a time–domain analysis and only the max–min values of the response are plotted.

As shown, the nonlinear reduced model can efficiently predict aeroelastic responses if the three complex eigenvalues related to the structural degrees–of–freedom together with the one real eigenvalue equal to the Küssner constant and related to the gust are included in the projection basis. The effect of the nonlinearity in the systems dynamics becomes important and is more evident under larger loads for the worst–case gust. The full nonlinear aeroelastic response against the linear and reduced models for that worst–case gust is given in Figure 5.5. The nonlinearity in this case has increased the loads. The overall system is reduced from the 14 original states to 4 and the calculations are now performed three times faster than before. Moreover, it will be shown that the larger the original system, the larger is the reduction of the computational cost achieved by the proposed model order reduction technique.

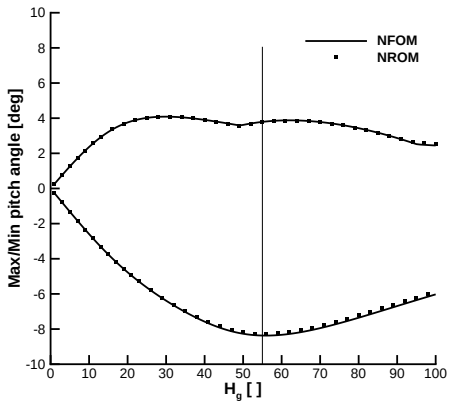

(a) Angle of attack in degrees

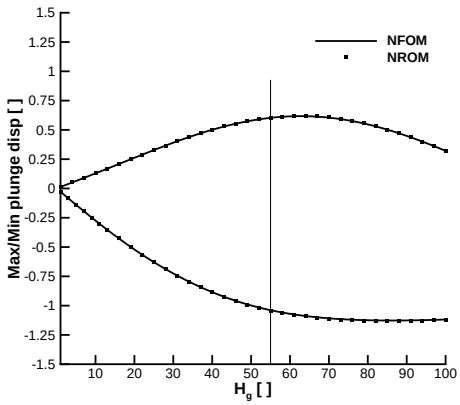

(b) Nondimensional Plunge displacement

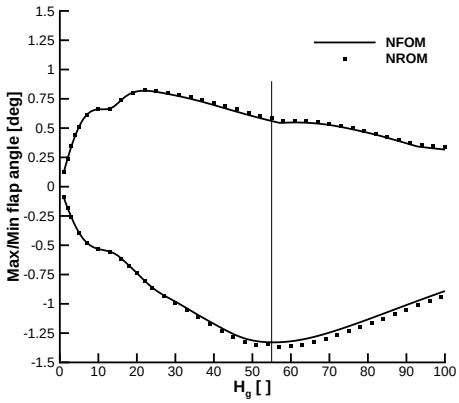

(c) Flap angle in degrees

Figure 5.4: Worst–case gust search at ($U^* = 4.5$) for a "1–minus–cosine" gust of intensity $w_g = 0.14$ for nonlinear full and reduced model for the aerofoil case

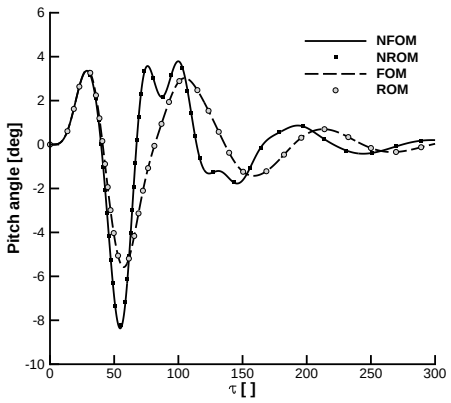

(a) Angle of attack in degrees

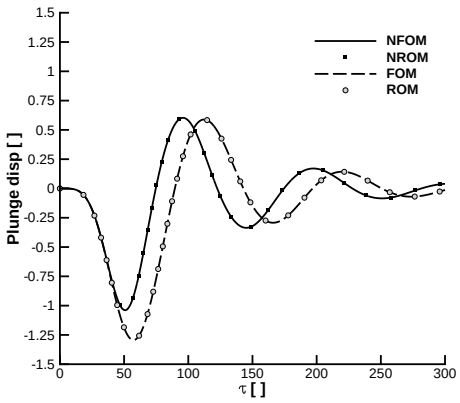

(b) Nondimensional Plunge displacement

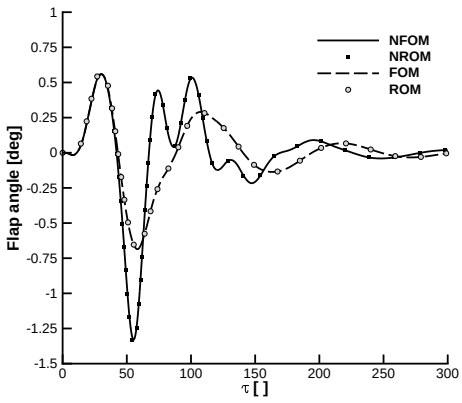

(c) Flap angle in degrees

Figure 5.5: Aeroelastic response at ($U^* = 4.5$) for the worst "1–minus–cosine" gust of intensity $w_g = 0.14$ for nonlinear full against linear and the reduced models for the aerofoil case

5.1.4 Adaptive Gust Load Alleviation

The control design for the worst–case gust is done using the model reference adaptive controller. The eigenvalues of the nonlinear reduced–order model and that of the reference model are given in Table 5.2. The reference model is chosen to be stable and to have the same order as the reduced–order model. It is desired to have more damping to be more robust under disturbances. Apart from an increase in damping, the first bending frequency is placed further from the first torsional mode frequency which also results in an increase of the flutter speed [101].

Table 5.2: Nondimensional Reduced and Reference Model eigenvalues

ROM	Reference
-0.0407 ± 0.2098i	-0.0626 ± 3.8664i
-0.0182 ± 0.8588i	-0.1043 ± 1.0918i
-0.0132 ± 0.0583i	-0.1859 ± 0.0956i
-0.1393	-0.1393
-0.1393	-0.1393

A comparison of the open–loop response between the reference model and the nonlinear reduced–order model under the worst–case gust disturbance is shown in Figure 5.6. The trajectories of the reference system in Figure 5.6 describe the ideal trajectories for our system under this particular gust disturbance.

The model reference control design was based on a particular selection of a semi–definite positive matrix $\boldsymbol{Q}$ and additional tuning of the control matrix $\boldsymbol{\Gamma}$. Matrix $\boldsymbol{Q}$ was defined as a diagonal matrix with positive elements ($Q_{11} = 10, Q_{22} = 10, Q_{33} = 30, Q_{44} = 30, Q_{55} = 30, Q_{66} = 10, Q_{77} = 30, Q_{88} = 30$). The selection of that matrix will provide a solution to the Lyapunov equation in Eq. (2.65) which is a constant in the adaptation of the control law. The design also depends on the selection of the matrix $\boldsymbol{\Gamma}$ as in Eq. (2.69). In this case for simplicity and in order to demonstrate the effect of that selection on the closed–loop performance the above matrix was scaled by matrix $\boldsymbol{Q}$ and three cases were examined for ($\boldsymbol{\Gamma} = 0.1\boldsymbol{Q}, \boldsymbol{\Gamma} = 0.5\boldsymbol{Q}, \boldsymbol{\Gamma} = 1\boldsymbol{Q}$).

The adaptive controller in general is not expected to be optimal under unknown disturbances as the disturbance vector is not used in the calculation of the controller as it is done in other designs such as $\mathcal{H}_\infty$. In Figure 5.7 for the angle of attack of the closed–loop system, there is an initial overshooting at larger adaptation rates but the subsequent oscillations decay to zero faster. For the plunge degree–of–freedom, the controller provided overall better response. As expected, the flap angle is affected by the adaptation rate. For a larger adaptation rate the flap angle became larger during the structure–gust interaction. As a result, a very large adaptation rate may lead to an unrealistic flap actuation either in frequency or rotation which can result in an initial overshooting that can cause structural damage. This should be addressed carefully.

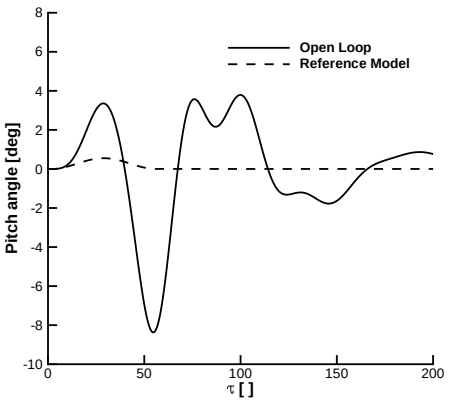

(a) Angle of attack in degrees

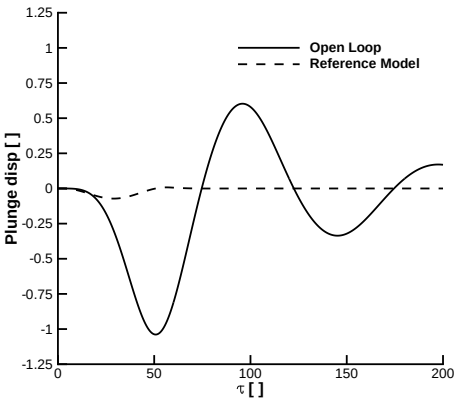

(b) Nondimensional Plunge displacement

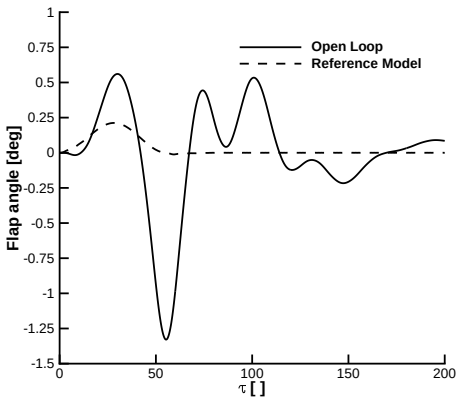

(c) Flap angle in degrees

Figure 5.6: Aeroelastic response at ($U^* = 4.5$) for the worst "1–minus–cosine" gust of intensity $w_g = 0.14$ for nonlinear reduced model against the reference model selection

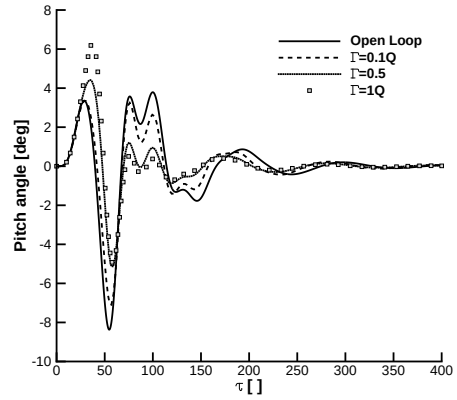

(a) Angle of attack in degrees

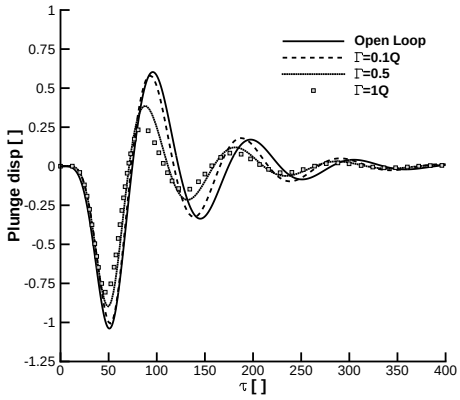

(b) Nondimensional Plunge displacement

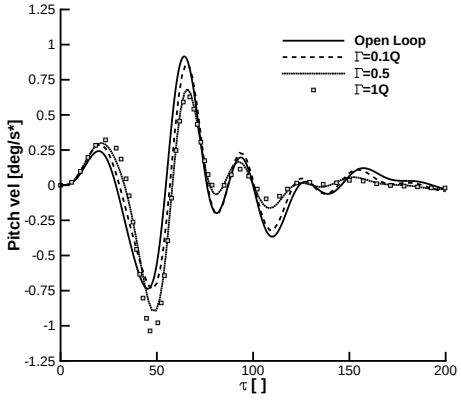

(c) Pitch Velocity in degrees/s*

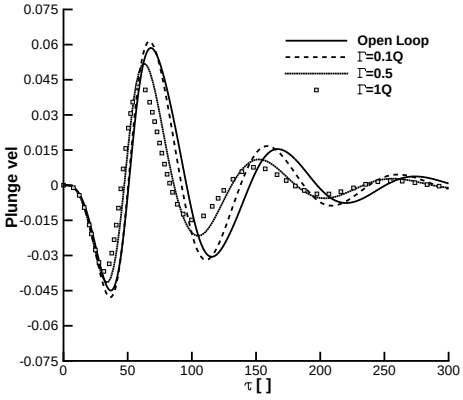

(d) Nondimensional Plunge Velocity

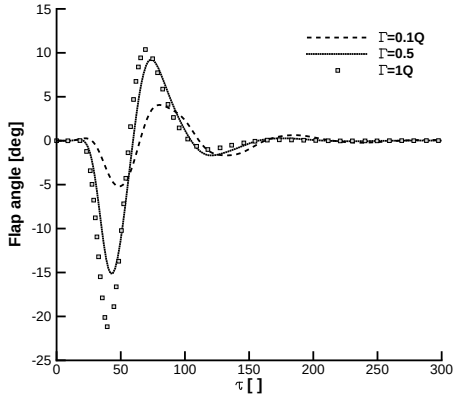

(e) Flap angle in degrees

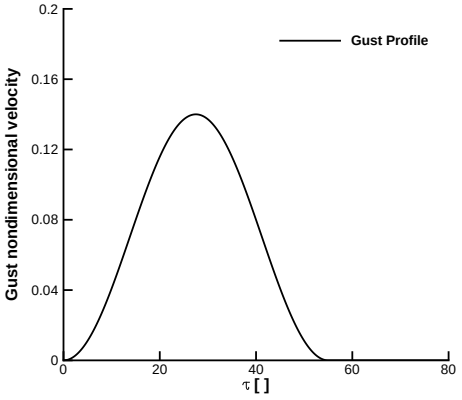

(f) Worst Case Gust Profile

Figure 5.7: Closed–loop response predictions from nonlinear reduced–order model for different adaptation rates at ($U^* = 4.5$)

Furthermore, for the plunging degree–of–freedom it is shown that by increasing the adaptation rate there is a load reduction. For the pitching degree–of–freedom this is the case for $\boldsymbol{\Gamma} = 0.5\boldsymbol{Q}$ and a further increase causes an overshooting in the pitch response of the closed–loop system but efficiently decreases the loads faster. A desired choice would be to minimise the loads in both the pitching and the plunging and at the same time keeping the maximum closed–loop angle of attack smaller than the open–loop maximum and this is well achieved with the current implementation. Also, it should be noted that for smaller values of the semi–definite positive matrix $\boldsymbol{Q}$ the possible range of matrix $\boldsymbol{\Gamma}$ would have been broader. This is attributed to the fact that the overall derivative of the adaptation law is affected by the magnitude of the above selections as shown in Eq. (2.69).

5.2 Flexible Unmanned Aerial Vehicle

5.2.1 Residual Formulation

The structural dynamic description based on the geometrically–exact nonlinear beam equations detailed in Hesse et al. [20] is used for the structural model and a thin–strip theory is used for the unsteady aerodynamics. The coupled full–order model follows the formulation presented in Ref. [98]. Results are obtained using two–nodes displacement–based elements. In a displacement–based formulation, dominant nonlinearities arising from large deformations are cubic terms, as opposed to an intrinsic description where they appear up to second order [176]. The nonlinear beam code was coupled with strip aerodynamics using the description above. The motion of each structural node is described by 6 degrees–of–freedom. The coupling between aerodynamic and structural models is performed considering that each structural node coincides with an aerodynamic section. No aeroelastic interface is required in this case, as the aerodynamic forces and moments are applied directly on each structural node. For cases where an aeroelastic interface is required to couple non–coincident and non–overlapping aerodynamic/structural models, the method described in McCracken et al. [177] provides an excellent solution to the problem. Similarly, the system is recast as a coupled first order ODE of the general form as in Eq. (2.2)

$$\boldsymbol{R} = \boldsymbol{A}\boldsymbol{w} + \boldsymbol{B}_c\boldsymbol{u}_c + \boldsymbol{B}_g\boldsymbol{u}_d + \boldsymbol{F}_N(\boldsymbol{w}) \tag{5.8}$$

where the unknowns are partitioned into structural and fluid contribution as Eq. (5.3)

$$\boldsymbol{w} = \left\{\boldsymbol{w}_s^T, \boldsymbol{w}_f^T\right\}^T \quad \text{where} \quad \boldsymbol{w}_s = \left\{\boldsymbol{x}_s^T, \dot{\boldsymbol{x}}_s^T\right\}^T \tag{5.9}$$

The matrix $\boldsymbol{A}$ is defined as,

$$\boldsymbol{A} = \begin{bmatrix} \boldsymbol{0} & \boldsymbol{I} & \boldsymbol{0} \\ -\boldsymbol{M}_T^{-1}\boldsymbol{K}_T & -\boldsymbol{M}_T^{-1}\boldsymbol{C}_T & \boldsymbol{A}_{sf} \\ \boldsymbol{A}_{fs} & \boldsymbol{0} & \boldsymbol{A}_{ff} \end{bmatrix} \tag{5.10}$$

while the contributions from gust and control rotation are given such as

$$\boldsymbol{B}_c = \begin{Bmatrix} \boldsymbol{0} \\ \boldsymbol{M}_T^{-1}\boldsymbol{A}_{sc} \\ \boldsymbol{A}_{fc} \end{Bmatrix}, \qquad \boldsymbol{B}_g = \begin{Bmatrix} \boldsymbol{0} \\ \boldsymbol{0} \\ \boldsymbol{A}_{fg} \end{Bmatrix} \tag{5.11}$$

Lastly the structural nonlinearities are assembled in the vector $\boldsymbol{F}_N$ forming the nonlinear residual. Note that Eq. (5.8) has the same structure that Eq. (5.4) has, even though they were derived from different modelling techniques. A detailed derivation of the global equations of motion of the flexible wing is given in Appendix A.5. The above system

can be solved as a second order ODE by a nonlinear Newmark integration method as described in Geradin et al. [167] or as a first order ODE by Runge–Kutta.

5.2.2 Unmanned Aerial Vehicle Test Case

The test case is a flexible unmanned aerial vehicle (UAV) that generally resembles the RQ4 Global Hawk aircraft. Figure 5.8 presents a three–dimensional view of the aircraft test case, which features high–aspect–ratio wings, a fairly rigid streamlined fuselage, and a V–tail. A set of trailing–edge control surfaces is located on each semi wing between 37 and 77% of the wing span measured from the wing root, and at 32% of the local chord from the wing trailing–edge. Basic geometric characteristics are shown in Figure 5.9.

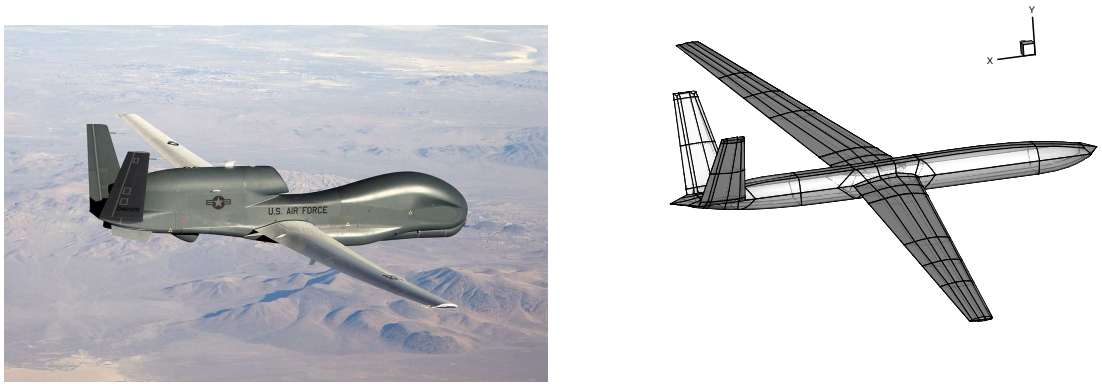

(a) RQ4 Global Hawk in flight

(b) Test case of this Chapter

Figure 5.8: Examples of high–altitude unmanned aerial vehicle (UAV); (a) RQ4 Global Hawk in flight (courtesy U.S. Air Force), and (b) the test case of this Chapter–DSTL wing

A detailed finite element structural model of the airframe created by DSTL in MSC/NASTRAN was available for accurate stress calculations, and this was later used to create an equivalent beam model. The structure was built of composite material, and the structural model included a combination of various finite element types. With fuel tanks on the wings between the front and rear spars accounting for over 4,700 kg, the centre of gravity resulted to be at 6.38 m from the nose of the aircraft.

The starting finite element model of the structure was then reduced to an equivalent beam model. A beam stick representation of the aircraft follows easily as lifting surfaces are of high–aspect–ratio. For the wings and tail, the beam model was located at the centre of the corresponding structural box, between front and rear spars. The mass and stiffness properties of the beam model were iteratively refined to ensure a good agreement of the lowest modeshapes and frequencies with the original detailed structural model.

A comparison of the first five lowest modeshapes and frequencies is shown in Table 5.4 between the original detailed model and the beam stick model. Tuning the mass and stiffness properties of the beam model reveals a reasonably good agreement for all

Table 5.3: Unmmaned aerial vehicle geometrical characteristics

Parameter	Wing [m]	Tail [m]
Span	17.75	3.23
Root chord	1.66	1.39
Tip chord	0.73	0.68

the modeshapes shown, with increasing inaccuracies at higher frequencies. Following a study aimed at investigating the dependency of the frequencies on the number of beam elements used, it was found that 20 elements were adequate to discretise the aircraft wing, and 4 were used for the tail. The fuselage, on the other hand, is modelled as a rigid–body with 3 elements.

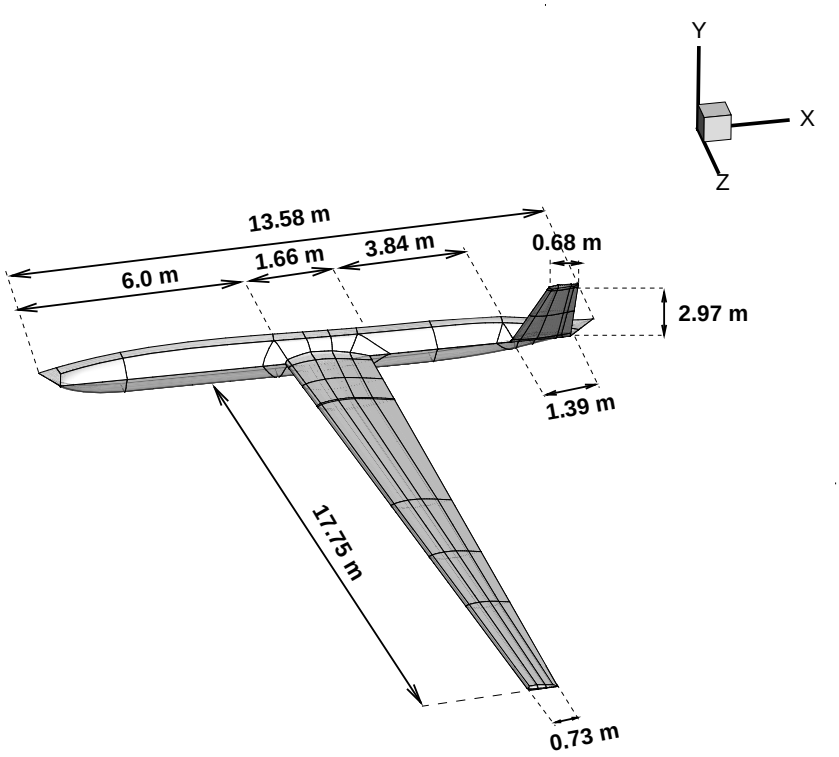

Figure 5.9: Geometric characteristics of the aircraft test case

The tail and the fuselage were designed as very stiff and their dynamics were represented by a small number of elements 4 and 3, respectively. The structural model has varying stiffness and mass matrices along the wing span and those values were used to match the first and second bending frequencies and modeshapes. The frequencies pre-

dictions become worse for higher bending modes but this results from the reduction of a three–dimensional unknown structural model to a two–dimensional beam stick model.

Table 5.4: First five modeshapes and frequencies of the UAV test case main wing in [Hz]

Mode	Modeshape	Original Model [Hz]	Beam Model [Hz]
1	Wing First Bending	3.56	3.58
2	Wing Second Bending	7.75	6.84
4	Wing First Torsion	14.93	17.18
5	Wing Third Bending	15.72	11.98
6	Wing Fourth Bending	24.64	19.82

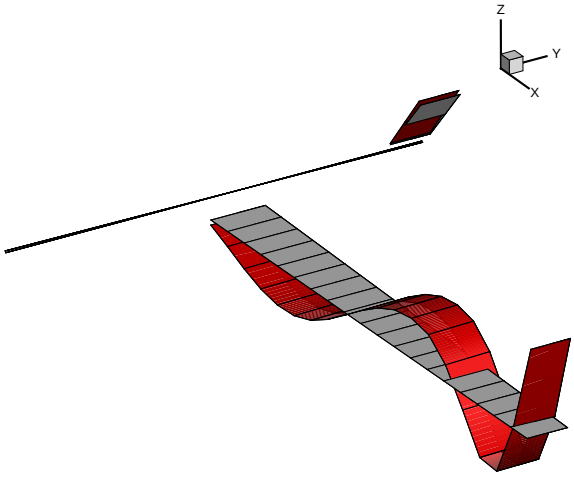

Figure 5.10: Fourth bending mode of the UAV test case mapped to the aerodynamic surface

Moreover, convergence studies were conducted in order to decide the number of elements needed for the description of the physics. A nonlinear static solution was carried out at sea level for 2 degrees angle of attack and a Mach number of 0.1. The wing deformation for different number of elements in that case is shown in Figure 6.9.

As a result, 20 elements are found adequate for the wing and a fairly large aeroelastic model is built for the full–order model consisting of 540 degrees–of–freedom that follows the formulation described in section 5.2.1. Only half model configuration is considered due to the symmetry of the problem. Control surfaces are mounted on both main wing and canted tail to provide longitudinal control and trim characteristics.

5.2.3 Evaluation of the Reduced–Order Model

Having presented a set of mathematical models for the description of the flexible aircraft dynamics and a model reduction strategy to reduce costs, a demonstration of these tools

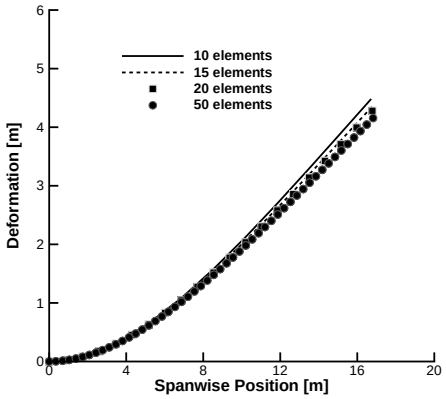

Figure 5.11: Nonlinear static deformation for different number of elements at sea level, 0.1 Mach number and 2 degrees angle of attack

is now performed for the flexible unmanned aircraft test case. Two reduced models were generated at 59 m/s and density $\rho = 0.0789$ kg/m^3 at an initial angle of attack of 4 degrees. The aeroelastic solver has been previously validated against commercial software in Chapter 3. In flight, the aircraft exhibits large wing deformations equal to 26 % of the wingspan. The deformed shape is computed from a static aeroelastic solution and is taken as the equilibrium point for the reduced model generation.

First, the right and left eigenvalue problems are solved around the static aeroelastic deformed shape. As the identification of an adequate basis for the model projection is critical for the analysis, a preliminary study was done to ensure convergence by increasing the size of the modal basis. A reasonable approach is to initially include a number of coupled modes that are dominated by the structural response. These modes are associated with the normal modes of the structure when the surrounding fluid is removed. In addition to this clear choice, the inclusion of the so called "gust modes" is needed to enrich the modal basis for gust loads prediction. In linear aerodynamics, these modes are easily identified being related to the smallest Küssner constant, $\epsilon_3 = 0.1393$. The eigenvalues of the "gust modes" in [Hz] are $\lambda_i = -\epsilon_3 U_\infty / b_i$. Tests to ensure convergence of the modal basis were done using up to eight eigenvalues, as summarised in Table 5.5. The first five coupled modes are mainly dominated by the structural response and are traced at this flight conditions from their corresponding normal modes of the structure. The remaining modes are "gust modes" and provide the mechanisms to describe the influence of the atmospheric gust on the structural response. The variation of the structural modes frequencies with respect to the freestream speed is shown in Figure 5.12.

One model represents the linearised aeroelastic system, and the other one includes the nonlinear terms up to second order. Both models were build using 8 modes for the projection.

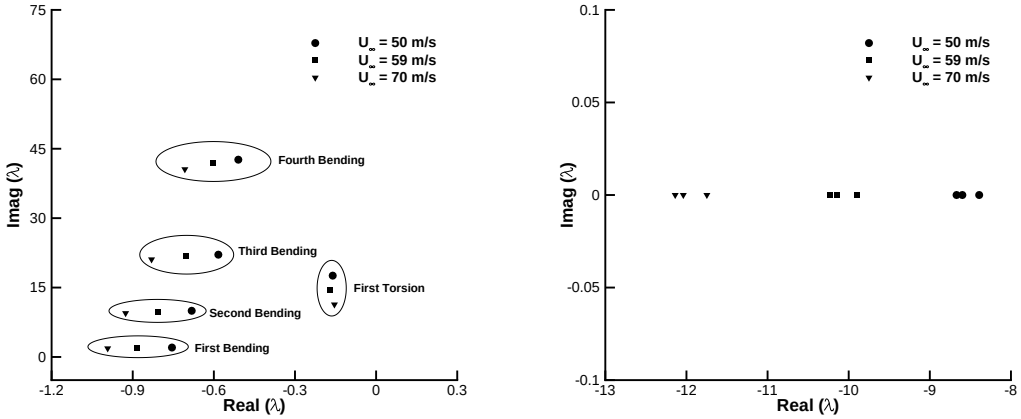

(a) Structural modes eigenvalues

(b) Gust modes eigenvalues

Figure 5.12: Variation of the structural modes (a), and gust modes eigenvalues (b), with respect to the freestream speed

Table 5.5: Basis of coupled eigenvalues used for the model projection. Real and imaginary parts in [Hz]

Mode number	Modeshape	Real part	Imaginary part
1	First bending	$-8.82 \cdot 10^{-1}$	1.97
2	Second bending	$-8.04 \cdot 10^{-1}$	$9.81 \cdot 10^{1}$
3	First Torsion	$-1.71 \cdot 10^{-1}$	$1.45 \cdot 10^{1}$
4	Third Bending	$-7.03 \cdot 10^{-1}$	$2.17 \cdot 10^{1}$
5	Fourth Bending	$-6.04 \cdot 10^{-1}$	$4.19 \cdot 10^{1}$
6	Gust mode	-9.90	0.00
7	Gust mode	-1.01	0.00
8	Gust mode	-1.02	0.00

The convergence of the reduced model predictions to a strong intensity Von Kármán turbulence gust for increasing size of the modal basis is shown in Figure 5.13. The open–loop response is computed in response to a random turbulence with its statistical properties defined by the Von Kármán spectrum. The reduced–order model predictions are compared to those of the original large–order model, of dimension 540 degrees–of–freedom. A good agreement is observed with as low as eight coupled modes for the reduced–order model.

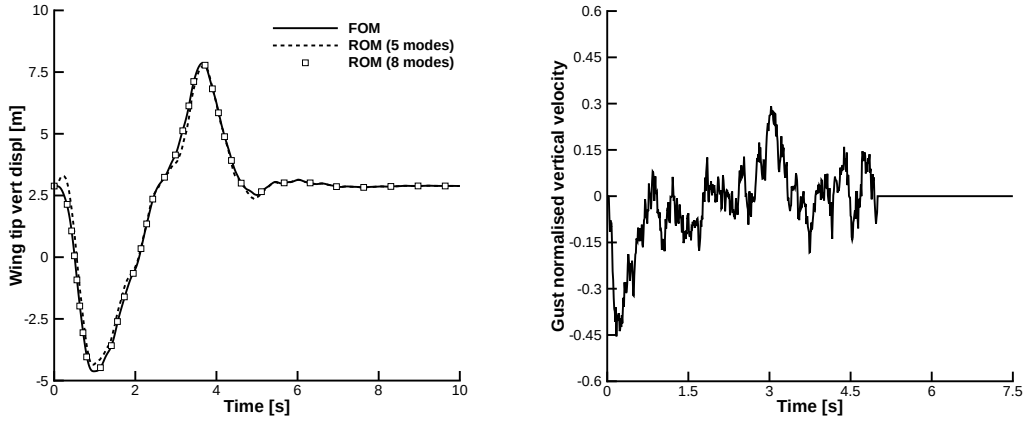

(a) Wing tip vertical deformation in body–attached frame of reference

(b) Random turbulence according to Von kármán spectrum

Figure 5.13: Gust response of the aircraft test case ($U_\infty = 59$ m/s, $\alpha_\infty = 4$ deg, and $\rho_\infty = 0.0789$ kg/m^3); (a) convergence for increasing number of coupled modes, and (b) vertical gust intensity normalised by U_∞ (Military specification MIL-F-8785C and turbulence intensity "severe")

5.2.4 Worst–Case Gust Search

Next, the reduced order model is demonstrated for the efficient search of the worst–case gust. The search is conducted for the "1–minus–cosine" gust family considering gust wavelengths between 0 and 776 aircraft mean chords (with a step size of 9.7 chords). A strong gust intensity, 14% of the freestream speed U_∞, causes large wing structural deformations. In addition to the linear reduced model above, a nonlinear reduced–order model was generated with the same modes including terms up to second order. The inclusion of higher–order terms did not modify the convergence properties of the model. The search was performed using both the full and reduced–order models and 80 calculations were performed in total. Figure 5.14 illustrates the largest upward and downward structural deflections at the wing tip for various gust wavelengths that are reported along the horizontal axis.

The worst–case gust causing the largest structural deformations is seen to have a 4 s duration, that corresponds to a length of 197 mean aerodynamic chords at the flying speed of 59 m/s. A comparison of the dynamic response to the worst–case gust is made between the linearised and nonlinear models, and between the full and reduced–order models. Deformations of 9 m are considered large as the wing span is 17.75 m, and it is not unexpected in this case that the linearised (full and reduced) models over–predict the deformations. The computational cost to obtain the gust profiles in Figure 5.14 with the reduced models was a fraction of that needed for the original full model: for the linear case, the reduced model demonstrated a speedup of about 10 times; for the nonlinear case, an increased performance of about 30 times was recorded. These indicative values are expected to increase considerably as the size of the original model increases [99], demonstrating the practical use and advantage of the developed approach to model reduction. The nonlinear reduced–order model overpredicts the response but gives the right indication, hence a smaller safety factor could be used, underpinning a more efficient design.

To conclude, it is demonstrated through application to a realistic HALE test case that the reduced–order models significantly reduce the computational cost for parametric worst–case gust searches up to 30 times for the nonlinear computations. Sections 5.2.5 and 5.2.6 will also show that the reduced–order models are adequate for a variety of control designs for gust load alleviation

5.2.5 $\mathcal{H}_\infty$ Control Design

The design of a controller for load alleviation is carried out on the linear reduced model for the worst–case gust. No information was assumed on the measurement of the aerodynamic states and the controller takes information only from the plunging motion of the wing that was assumed to be taken by laser sensors placed on the wingtip. The good performance of the controller to suppress the vibrations of the linear model that were

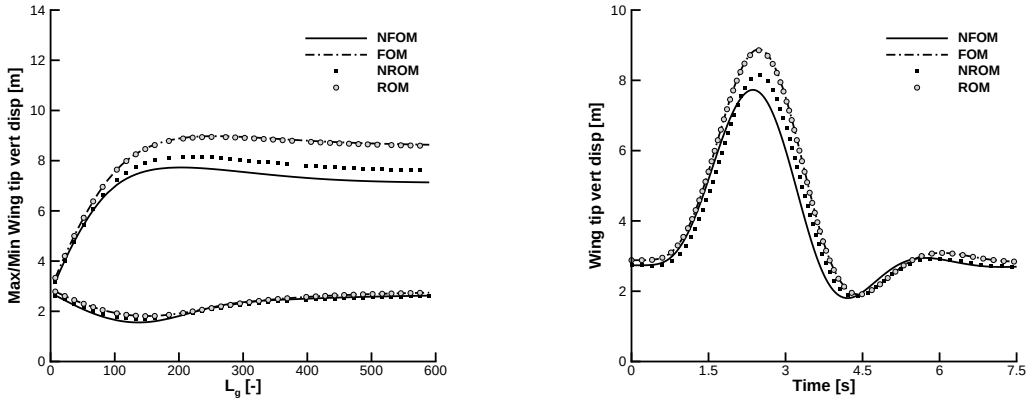

(a) Profile of max/min deflections

(b) Tuned worst–case gust

Figure 5.14: (a) Aeroelastic response for the worst "1–minus–cosine" gust of intensity 14% of the freestream speed for nonlinear full against linear and the reduced models, and (b) dynamic response for the tuned worst–case gust at ($U_\infty = 59$ m/s, $\alpha_\infty = 4$ deg, and $\rho_\infty = 0.0789$ kg/m^3)

induced by the worst–case gust is not unexpected, as the controller was designed specifically for that. However, its performance will be shown on the nonlinear full model. The question addressed in this section is whether a good alleviation can be achieved when considering a different gust type, but using the same controller. The responses shown in Figure 5.15 are for the discrete worst–case gust and Figure 5.16 for a continuous gust model based on the Von Kármán spectrum. The vibrations of the closed–loop system are significantly reduced when compared to the open–loop response.

However, the performance of the optimal robust controller is reduced when applied on the nonlinear system for very strong stochastic disturbances as the reduction of the wing tip deformation is smaller even if a larger control effort is present as illustrated in Figure 5.16.

The efficiency of the optimal control approach using the reduced models for gust load alleviation can be demonstrated in a case with noticeable differences between the linear and nonlinear full order models as shown in Figure 5.14.

5.2.6 Model Reference Adaptive Controller ($\mathcal{MRAC}$)

A key goal with the nonlinear reduced model was to simplify and speed up the calculation of an adaptive model reference control framework. The resulting control surface deflection is then applied on the nonlinear full–order model which is under external disturbances. The selection of the reference model is of critical importance as a bad choice could potentially lead the flap to experience unrealistic rotations. Control input saturation can be added to avoid unrealistic rotation. However, this can induce instabilities on the resulting closed–loop system and thus it is desired to be careful in the selection of the reference model. In this case a reference model was selected with addi-

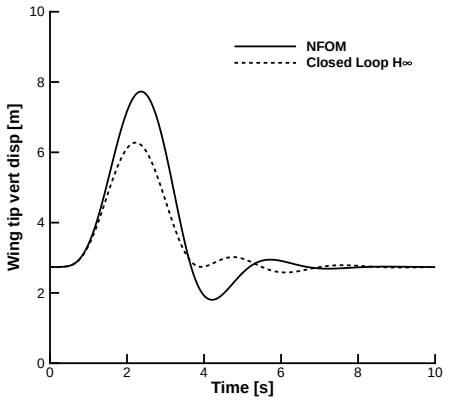

(a) Wing tip deformation in metres

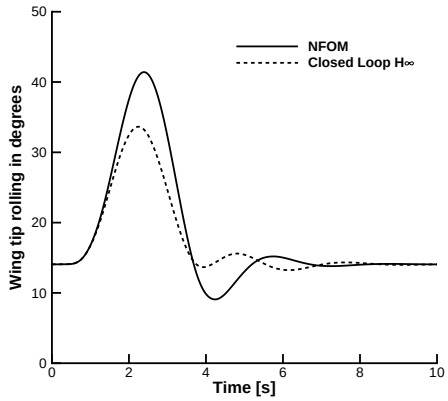

(b) Wing tip rolling in degrees

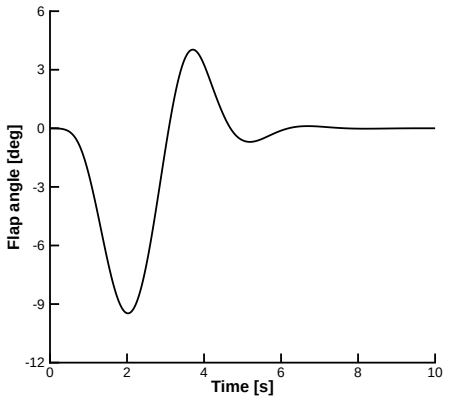

(c) Flap Angle in degrees

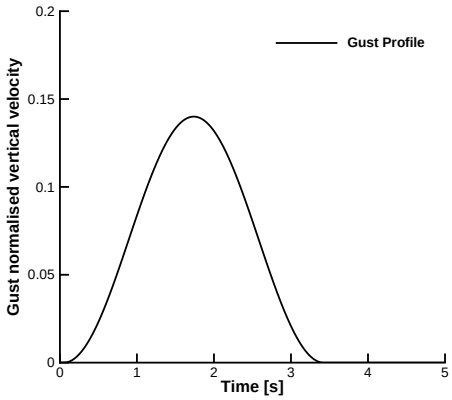

(d) Nondimensional gust vertical velocity

Figure 5.15: Closed–loop response of the $\mathcal{H}_\infty$ controller for the worst–case "1–minus–cosine" gust for nonlinear full against open–loop responses at ($U_\infty = 59$ m/s, $\alpha_\infty = 4$ deg, and $\rho_\infty = 0.0789$ kg/m^3)

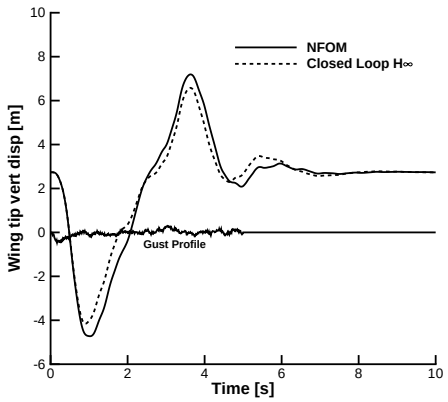

(a) Wing tip deformation in metres

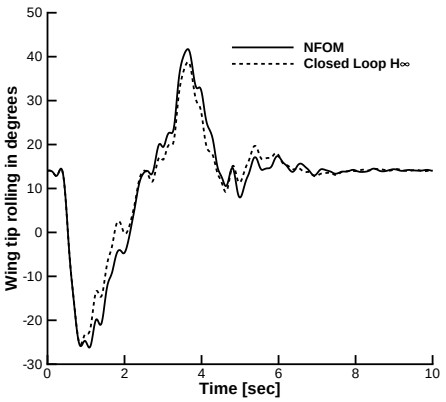

(b) Wing tip rolling in degrees

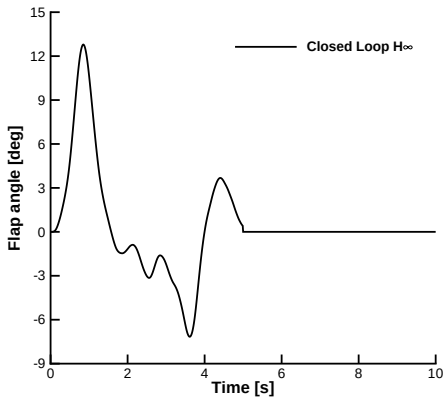

(c) Flap Angle in degrees

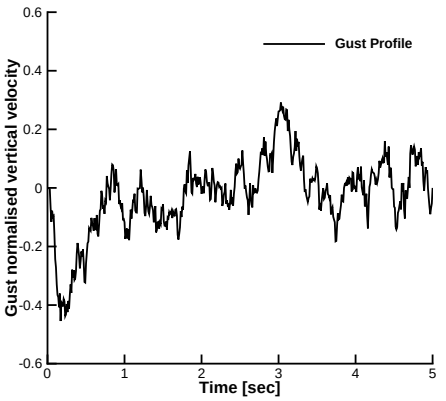

(d) Nondimensional gust vertical velocity

Figure 5.16: Closed–loop response of the $\mathcal{H}_\infty$ controller for a continuous gust for nonlinear full against open–loop responses at ($U_\infty = 59$ m/s, $\alpha_\infty = 4$ deg, and $\rho_\infty = 0.0789$ kg/m^3)

tional damping added to first bending and torsional modes. As a result, the reference system exhibits significantly smaller vibrations than the plant system. The eigenvalues of the linearised reference system are given in Table 5.6, while its eigenvectors are equal to the eigenvectors of the reduced–order model.

Damping is added in the first five complex conjugate eigenvalues while no damping is added to the three gust modes of the form $\lambda_i = -\epsilon_3 \times \frac{U_\infty}{b_i}$. The eigenvalues and a

Mode	Real Part	Imaginary Part
1	-9.53·10^{-1}	±2.01
2	-8.53·10^{-1}	±1.02·10^{1}
3	-1.71·10^{1}	±2.79·10^{1}
4	-5.73·10^{-1}	±4.74·10^{1}
5	-1.21·10^{1}	±6.55·10^{1}
6	-9.90	0.00
7	-1.01·10^{1}	0.00
8	-1.01·10^{1}	0.00

Table 5.6: Reference Model Eigenvalues. Real and imaginary parts in [Hz]

comparison between the plant model and the selected reference model for the worst–case gust are shown in Figure 5.17.

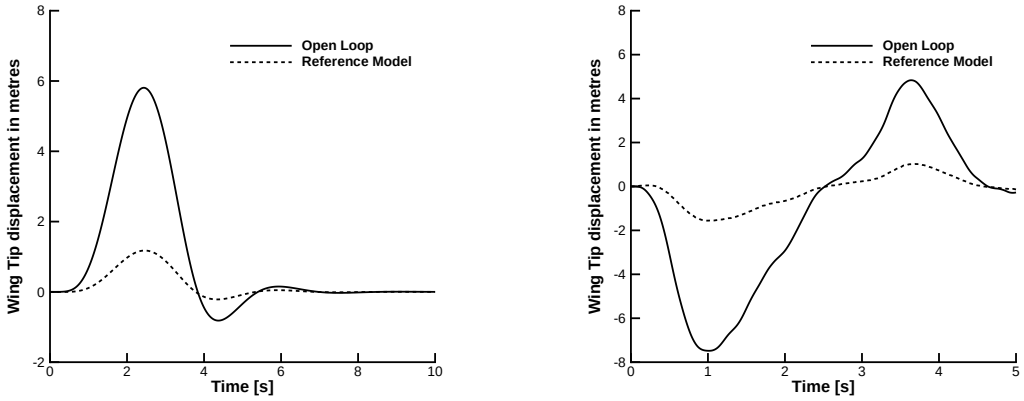

(a) Worst–case "1–minus–cosine" gust

(b) Von Kármán turbulence

Figure 5.17: Ideal reference model for the $\mathcal{MRAC}$ controller design compared to the open–loop response for: (a) worst–case "1–minus–cosine" gust from Figure 5.14, and (b) Von Kármán turbulence model at ($U_\infty = 59$ m/s, $\alpha_\infty = 0$ deg, and $\rho_\infty = 0.0789$ kg/m^3)

The selection of the semi–definite positive matrix $\boldsymbol{Q}$ which provides a solution to the Lyapunov equation given a stable Hurwitz matrix of a reference model $\boldsymbol{A_m}$ is also critical. In this case, $\boldsymbol{Q}$ was chosen to be a diagonal matrix with elements $Q_{ii} = 10^{-4}$. As shown in Eq. (2.69) the selection of the reference model will affect how $\boldsymbol{e}(t)$ will evolve during the time integration which is part of the adaptation parameter. The reference

model in that case needs to be stable so that the error decreases asymptotically. Also, the adaptation parameter is furthermore affected by $\boldsymbol{P}$ and as a result by matrix $\boldsymbol{Q}$ and $\boldsymbol{\Gamma}$.

The effect of the adaptation matrix $\boldsymbol{\Gamma}$ is therefore investigated for the performance of the closed-loop system. The discrete selection of the semi definite positive matrix $\boldsymbol{\Gamma}$ is shown in Table 5.7 for both discrete and continuous gust loads alleviation.

	Discrete Gust case	Continuous Gust case
$\boldsymbol{\Gamma}$	$0.01\,\boldsymbol{Q}$	$0.01\,\boldsymbol{Q}$
$\boldsymbol{\Gamma}$	$0.10\,\boldsymbol{Q}$	$0.10\,\boldsymbol{Q}$
$\boldsymbol{\Gamma}$	$1.00\,\boldsymbol{Q}$	$1.00\,\boldsymbol{Q}$

Table 5.7: Adaptation Parameter selection

The derived controller based on the reduced model is directly applied on the full–order nonlinear aeroelastic system. The wing tip vertical displacement for different adaptation rates for the worst–case "1–minus–cosine" gust and for a continuous gust are shown in Figure 5.18 and Figure 5.19 respectively.

Results show significant reduction of the wing tip deformation for the closed–loop system in both linear and nonlinear case and could be achieved under realistic flap deflections. It can be seen that for the particular selection of the semi–definite positive matrix $\boldsymbol{Q}$ a larger adaptation gain $\boldsymbol{\Gamma}$ is required during the fluid–structure and gust interaction to alleviate the disturbances. A further increase though of the adaptation gain may lead in a non–realistic flap rotation with a flap angle of over 15 degrees which is the most common constraint of the flap's maximum rotation. As a result, it is dangerous to choose very large adaptation rates because the flap might overshoot during the aeroelastic/gust interaction.

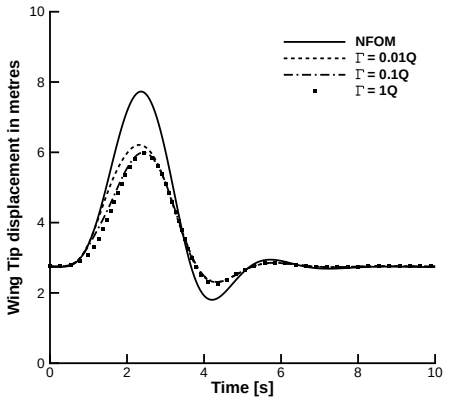

(a) Wing tip displacement in metres

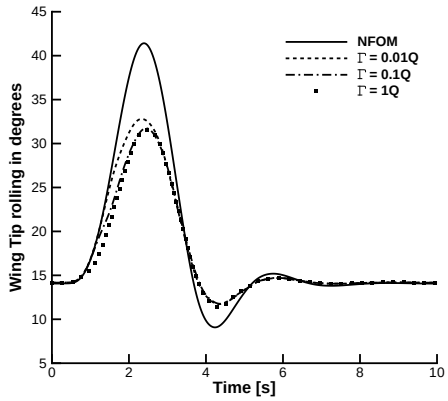

(b) Wing tip rolling in degrees

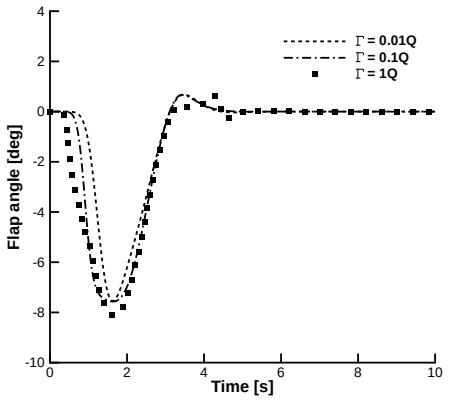

(c) Flap Angle in degrees

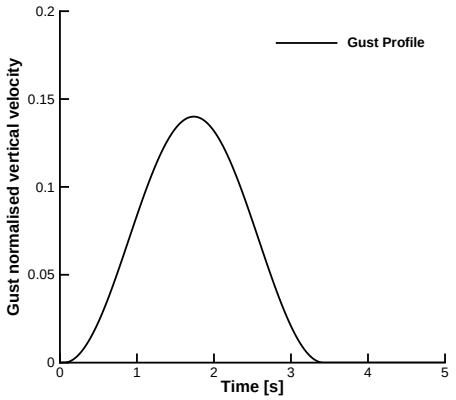

(d) Nondimensional vertical gust velocity

Figure 5.18: Closed–loop response using the $\mathcal{MRAC}$ controller for various adaptation gains compared to the open–loop response for the worst–case "1-minus-cosine" gust at ($U_\infty = 59$ m/s, $\alpha_\infty = 4$ deg, and $\rho_\infty = 0.0789$ kg/m^3)

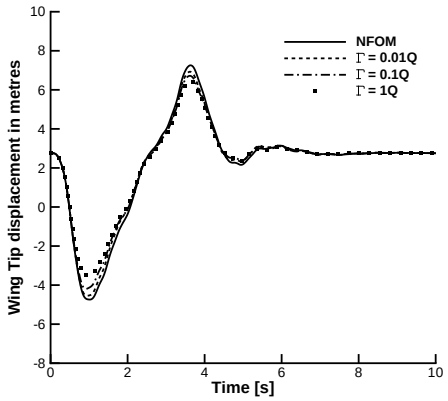

(a) Wing tip displacement in metres

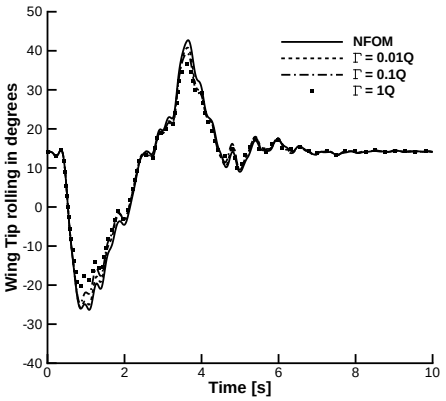

(b) Wing tip rolling in degrees

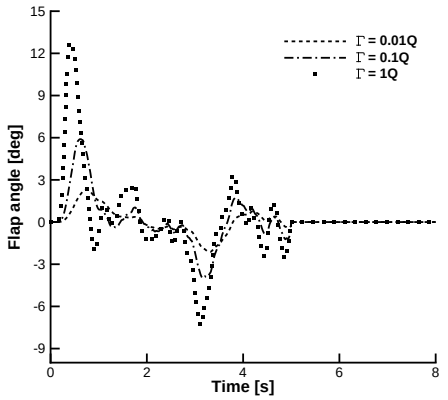

(c) Flap Angle in degrees

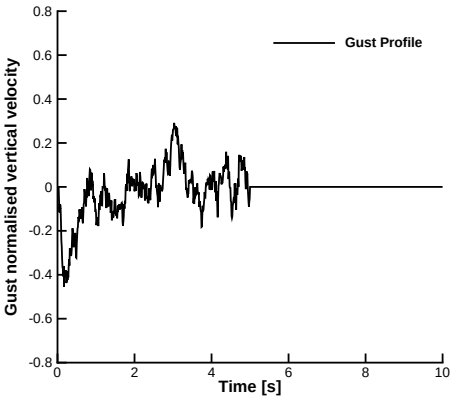

(d) Nondimensional vertical gust velocity

Figure 5.19: Closed–loop response using the $\mathcal{MRAC}$ controller for various adaptation gains compared to the open–loop response for a continuous gust at ($U_\infty = 59$ m/s, $\alpha_\infty = 4$ deg, and $\rho_\infty = 0.0789$ kg/m^3)

5.2.7 Control Design Comparison

Both control designs were found adequate for gust loads alleviation of a very flexible aircraft. However, a "good" controller does not only guarantee that closed–loop structural deformations are smaller than those of the open–loop counterpart, but also that this is achieved by a realistic, optimal, and minimum control effort. The performance of the $\mathcal{H}_\infty$ and $\mathcal{MRAC}$ controllers for the discrete "1–minus–cosine" gust is reported in Table 5.8. It is found that the adaptive control methodology achieves a better performance in reducing the wing tip deflection than the $\mathcal{H}_\infty$ control strategy, and the performance in gust loads alleviation increases for increasing adaptation rates. The reduction in the wing tip deflection is also achieved with a smaller control effort. Finally, the performance of the two controllers is summarised in Table 5.9 for the random turbulence based on the Von Kármán spectrum. The gust loads alleviation proves more challenging in this case because of the larger frequency content than that for the "1–minus–cosine" gust. The choice of the adaptation rate is critical, as it affects the capability of the control system to follow the rapid changes in the gust loads. It is not unexpected, therefore, that the performance of the $\mathcal{MRAC}$ controller degrades for smaller adaptation rates. For larger adaptation rates, the adaptive control design achieves about the same level of gust loads alleviation, but with a smaller control effort, than the H_∞ controller.

Controller design	Reduction in maximum wing tip deflection [%]	Maximum flap rotation [deg]
$\mathcal{H}_\infty$	23.15	-9.47
$\mathcal{MRAC}$, $\mathbf{\Gamma} = 10^{-2}\boldsymbol{Q}$	24.45	-7.54
$\mathcal{MRAC}$, $\mathbf{\Gamma} = 10^{-1}\boldsymbol{Q}$	28.89	-7.56
$\mathcal{MRAC}$, $\mathbf{\Gamma} = 1\boldsymbol{Q}$	29.45	-8.11

Table 5.8: Comparison of control performance for a discrete "1–minus–cosine" gust

Controller design	Reduction in maximum wing tip deflection [%]	Maximum flap rotation [deg]
$\mathcal{H}_\infty$	10.26	12.79
$\mathcal{MRAC}$, $\mathbf{\Gamma} = 10^{-2}\boldsymbol{Q}$	4.73	2.31
$\mathcal{MRAC}$, $\mathbf{\Gamma} = 10^{-1}\boldsymbol{Q}$	8.00	5.89
$\mathcal{MRAC}$, $\mathbf{\Gamma} = 1\boldsymbol{Q}$	12.68	12.83

Table 5.9: Comparison of control performance for a stochastic gust

The comparison of the performance of the two control strategies indicates that, in general, the gust loads alleviation with a random turbulence is more challenging and may result in degraded performances, at least to some degree, compared to a discrete

gust case. Note that the ability to investigate two control strategies is enabled by the proposed model reduction technique, demonstrating the readiness level for practical use.

5.3 Summary

This investigation presented a detailed aeroelastic model of a three degree–of–freedom aerofoil and coupled a nonlinear structural beam model with linear potential aerodynamics to describe low speed aeroelastic responses. It focused on the identification of the eigenvalue basis for an automatic generation of nonlinear reduced models able to be used for a cheaper computation of an $\mathcal{H}_\infty$ and an adaptive controller based on the model reference adaptive control scheme and also for a cheaper solution of open–loop parametric worst–case gust predictions for nonlinear aeroelastic systems. More importantly, it demonstrated a significant reduction of the computational time up to 30 times for the nonlinear full model calculations of a flexible UAV. This emphasises the fact that the nonlinear reduced models can and should be used for worst–case gust searches. Furthermore, it presented the synthesis, design, and testing of two inherently different control strategies developed around the nonlinear reduced–order model for gust loads alleviation and this was shown to be systematic because it was independent of the original equations. The $\mathcal{H}_\infty$ design was found robust when applied on the nonlinear full model for the worst–case gust search. The model reference adaptive controller was also found suitable for deterministic and stochastic disturbance rejection. However, in both test cases, the selection of the adaptation law is critical when dealing with flexible aircraft flight systems in adaptive control design. A sufficient enough adaptation rate is needed during the disturbance interaction to regulate the system under deterministic and stochastic disturbances and in these cases it was found superior compared to the $\mathcal{H}_\infty$ control design.

Chapter 6

Nonlinear Model Order Reduction and Control Design of Flexible Free-Flying Aircraft

The first test case used for the verification of the flight dynamics against previous published results is a high–altitude long–endurance vehicle. Following this, a flexible high–aspect–ratio flying–wing is assembled to check flight dynamic responses under strong discrete and stochastic gusts. Linear reduced–order models are generated to run hundred times faster a parametric worst–case gust search with respect to the gust length. For the cases where the deformations are large and thus nonlinear, a nonlinear reduced–order model is used to predict the aeroelastic response. Furthermore, an $\mathcal{H}_\infty$ controller is designed based on the linear reduced–order model and is applied to the worst–case gust length and its performance when applied to the nonlinear full model is assessed.

6.1 Residual Evaluation

For the structural model, the geometrically-exact nonlinear beam equations are used [20]. Results are obtained using two–node displacement–based elements. The nonlinear beam code was coupled with strip aerodynamics. Also here, the motion of each structural node is described by 6 degrees-of-freedom. The coupling between aerodynamic and structural models is performed considering that each structural node coincides with an aerodynamic section. The system states follows first the structural degrees–of–freedoms, then 6 rigid body degrees–of–freedom. Moreover, it is coupled with the quaternions equation for the propagation of the beam with respect to the inertial frame and the aerodynamic states for each deformable aerofoil section.

The dynamic equations of the coupled structural/flight model are written

$$\boldsymbol{M}\left[\boldsymbol{w}_s\right]\begin{Bmatrix}\ddot{\boldsymbol{w}}_s\\ \ddot{\boldsymbol{w}}_r\end{Bmatrix}+\boldsymbol{Q}_{gyr}\left[\dot{\boldsymbol{w}}_s,\boldsymbol{w}_s,\boldsymbol{w}_r\right]\begin{Bmatrix}\dot{\boldsymbol{w}}_s\\ \dot{\boldsymbol{w}}_r\end{Bmatrix}+\boldsymbol{Q}_{stiff}\left[\boldsymbol{w}_s\right]\begin{Bmatrix}\boldsymbol{w}_s\\ \boldsymbol{w}_r\end{Bmatrix}=\boldsymbol{R}_F\left\{\dot{\boldsymbol{w}},\boldsymbol{w},\boldsymbol{u}_c\right\} \tag{6.1}$$

$$\dot{\boldsymbol{\zeta}}_i+\boldsymbol{C}_{QR}\left[\boldsymbol{w}_r\right]\dot{\boldsymbol{w}}_r+\boldsymbol{C}_{QQ}\left[\boldsymbol{\zeta}_i\right]\boldsymbol{\zeta}_i=0$$

$$\dot{\boldsymbol{w}}_f=\boldsymbol{A}_{fs}\boldsymbol{q}+\boldsymbol{A}_{ff}\boldsymbol{w}_f+\boldsymbol{A}_{fc}\boldsymbol{u}_c+\boldsymbol{A}_{fg}\boldsymbol{u}_d$$

The subscripts S and R and F denote elastic, rigid–body, and fluid properties respectively. The basic body reference frame and the frozen deformed geometry of a free–flying aircraft are given in Figure 6.1

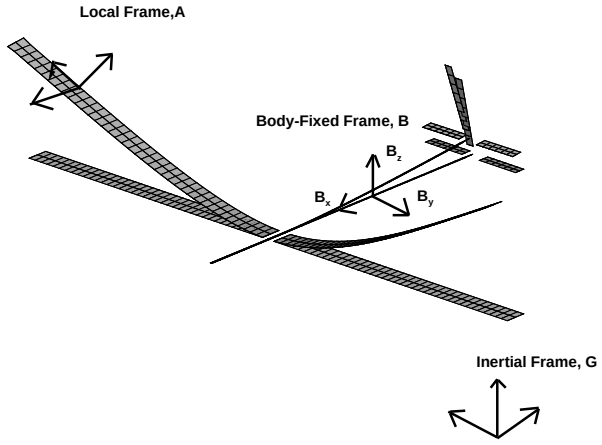

Figure 6.1: Body reference frame and vehicle deformed coordinates

The above global equations can be written as a linear and a nonlinear contribution from the structure and the fluid from both sides and together with the quaternions and the augmented aerodynamic states are explicitly expressed as follows

$$\begin{cases}\boldsymbol{M}_T\ddot{\boldsymbol{q}}+\boldsymbol{C}_T\dot{\boldsymbol{q}}+\boldsymbol{K}_T\boldsymbol{q}=\boldsymbol{A}_{sf}\boldsymbol{w}_f+\boldsymbol{A}_{sc}\boldsymbol{u}_c+\boldsymbol{A}_{rf}\boldsymbol{w}_f+\boldsymbol{A}_{rc}\boldsymbol{u}_c+\boldsymbol{F}_N\left(\boldsymbol{q}\right)\\ \dot{\boldsymbol{\zeta}}_i+\boldsymbol{C}_{QR}\left[\boldsymbol{w}_r\right]\dot{\boldsymbol{w}}_r+\boldsymbol{C}_{QQ}\left[\boldsymbol{\zeta}_i\right]\boldsymbol{\zeta}_i=\boldsymbol{0}\\ \dot{\boldsymbol{w}}_f=\boldsymbol{A}_{fs}\boldsymbol{q}+\boldsymbol{A}_{ff}\boldsymbol{w}_f+\boldsymbol{A}_{fc}\boldsymbol{u}_c\;\boldsymbol{A}_{fg}\boldsymbol{u}_d\end{cases} \tag{6.2}$$

where $\boldsymbol{q}=\left\{\boldsymbol{w}_s^T,\boldsymbol{w}_r^T\right\}^T$. A new state vector is defined such as $\boldsymbol{w}=\left\{\boldsymbol{q}^T,\dot{\boldsymbol{q}}^T,\boldsymbol{\zeta}_i^T,\boldsymbol{w}_f^T\right\}^T$. By taking the derivative of the new state vector and manipulating the above equations

which are coupled the system is recast as a first order ODE as follows.

$$\boldsymbol{R} = \boldsymbol{A}\boldsymbol{w} + \boldsymbol{B}_c\boldsymbol{u}_c + \boldsymbol{B}_g\boldsymbol{u}_d + \boldsymbol{F}_{Nnl}(\boldsymbol{w}) \tag{6.3}$$

The matrix $\boldsymbol{A}$ is defined as

$$\boldsymbol{A} = \begin{bmatrix} \mathbf{0} & \boldsymbol{I} & \mathbf{0} & \mathbf{0} \\ -\boldsymbol{M}_T^{-1}\boldsymbol{K}_T & -\boldsymbol{M}_T^{-1}\boldsymbol{C}_T & \mathbf{0} & \boldsymbol{M}_T^{-1}\boldsymbol{A}_{sf} + \boldsymbol{M}_T^{-1}\boldsymbol{A}_{rf} \\ \mathbf{0} & -\boldsymbol{C}_{QR} & -\boldsymbol{C}_{QQ} & \mathbf{0} \\ \boldsymbol{A}_{fs} & \mathbf{0} & \mathbf{0} & \boldsymbol{A}_{ff} \end{bmatrix},$$

$$\boldsymbol{B}_c = \begin{Bmatrix} \mathbf{0} \\ \boldsymbol{M}_T^{-1}\boldsymbol{A}_{sc} + \boldsymbol{M}_T^{-1}\boldsymbol{A}_{rc} \\ \mathbf{0} \\ \boldsymbol{A}_{fc} \end{Bmatrix}, \boldsymbol{B}_g = \begin{Bmatrix} \mathbf{0} \\ \mathbf{0} \\ \mathbf{0} \\ \boldsymbol{A}_{fg} \end{Bmatrix}, \boldsymbol{F}_{Nnl} = \begin{Bmatrix} \mathbf{0} \\ \boldsymbol{F}_N \\ \mathbf{0} \\ \mathbf{0} \end{Bmatrix} \tag{6.4}$$

The solution of the eigenvalue problem of Eq. (6.4) provides insight on the stability of the nonlinear system at the equilibrium point the linearisation was performed and can be used to construct the basis for the free-flying nonlinear model order reduction as described in Section 2.2. A more detailed derivation of the nonlinear residual can be found in Appendix A.6.

6.2 Validation

6.2.1 High–Altitude–Long–Endurance Vehicle

The test case is a very flexible configuration characteristic of a HALE aircraft unmanned aerial vehicle. The 32-m span high–aspect–ratio wing has also been the focus of previous researchers [30, 48, 52]. The wing is straight and consists of a rigid fuselage and a horizontal (HTP) and a vertical tail (VTP). Elevators with a length of 25% of the chord are mounted on the horizontal tail plane (HTP) to provide aircraft trimming and closed–loop control for gust load alleviation. The fuselage and the vertical tail plane are modelled as simple beams without aerodynamic surfaces. Furthermore, a payload of 50 kg is placed on the fuselage and can be modelled as a point load, located at a distance d_{pl} from the elastic axis of the main wing. To provide thrust, two propellers modelled as point forces are attached to the wing. The configuration of the whole aircraft is shown in Figure 6.2. The aeroelastic model is shown in Figure 6.3.

The structural properties of the aircraft are summarised in Table 6.1. A convergence study was carried out and several calculations for normal modes analysis were conducted to decide the size of the finite element model. Excellent agreement against published data was found for a finite element of 100 nodes. The normal modes of the implemented clamped structural model are given in Table 6.2. The structural frequencies of the first

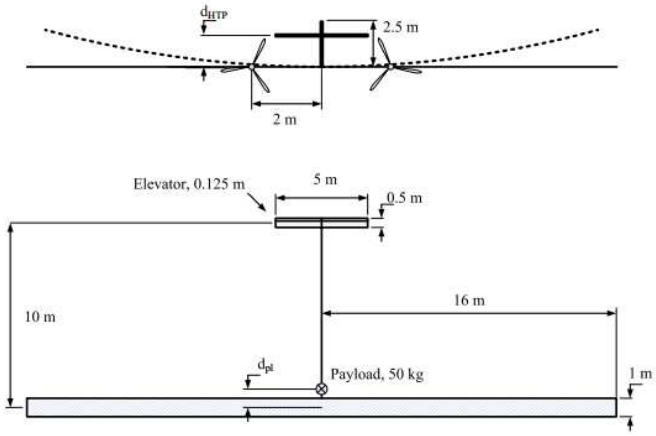

Figure 6.2: Flying Hale Aircraft Geometry from Ref. [52]

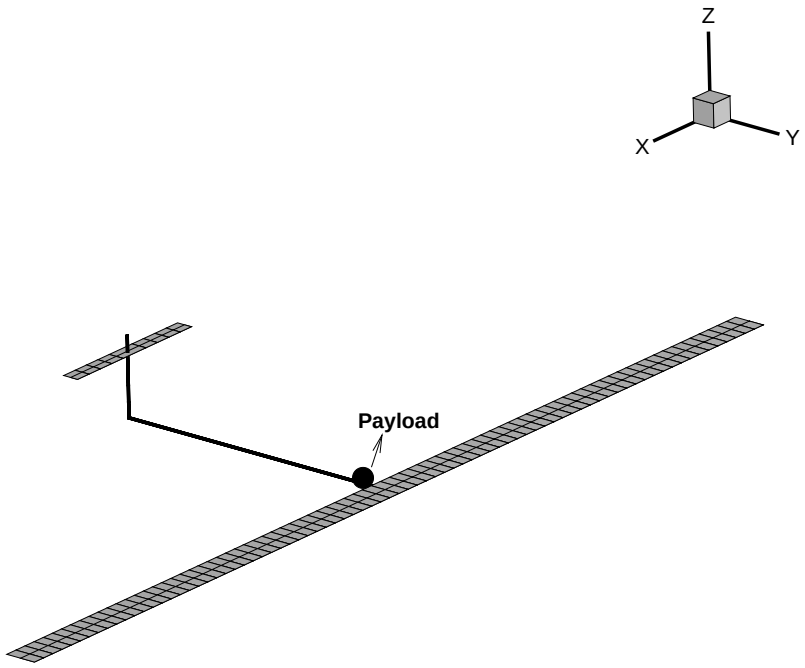

Figure 6.3: Test case 1– Present HALE aircraft model with the aerodynamic surfaces

Table 6.1: HALE aircraft structural properties

	Main wing	HTP	VTP
Chord [m]	1	0.5	0.5
Semi-span [m]	16	2.5	2.5
Elastic-axis	50% chord	50% chord	50% chord
Centre of gravity	50% chord	50% chord	50% chord
Mass per unit length [kg/m]	0.75	0.08	0.08
Moment of inertia [kg/m]	0.1	0.01	0.01
Torsional stiffness [Nm^2]	$\sigma_1 \times 10^4$	∞	∞
Bending stiffness [Nm^2]	$2\sigma_1 \times 10^4$	∞	∞
Chordwise bending stiffness [Nm^2]	$\sigma_2 \times 10^6$	∞	∞

Table 6.2: Comparison of vibration structural frequencies of the entire configuration in [rad/s], for ($\sigma_1 = 1$, $\sigma_2 = 5$)

Mode	Present Analysis	Patil et al. [30]	Exact, Beam–Theory
First Bending Mode	2.243	2.247	2.243
Second Bending Mode	14.075	14.606	14.056
First Torsion	31.047	31.146	31.046
First Inplane Mode	31.719	31.739	31.718
Third Bending Mode	39.521	44.012	39.356

bending and torsional modes match well previous published data and this agreement is better compared to the published data as shown for the third bending mode. This is attributed to the fact that significantly more beam elements were used for the structural model compared to past studies.

The resulting nonlinear structural dynamics model with rigid–body degrees–of–freedom is coupled with two–dimensional aerodynamics. The number of structural degrees–of–freedom is 1200. The number of rigid–body degrees–of–freedom is 12, followed by 4 quaternions and 8 augmented states for each deformable section making the number of augmented states 800 and increasing the total dimension of the system to 2016 states. The flexibility of the wing increases as σ_1 and σ_2 in Table 6.1 decrease. The mass per unit length of the fuselage is the same with the mass per unit length of the tail parts. The total mass of the aircraft, including the payload, is 75.4 kg.

6.2.2 Clamped Static Aeroelastic Calculations

The flow conditions for the following calculations are summarised in Table 6.3. The

Table 6.3: Flow conditions

Altitude [m]	20.000
Freestream speed U_∞ [m/s]	25.0
Density ρ_∞ [kg/m^3]	0.0889

rigid–body degrees-of-freedom are neglected and a typical cantilever beam with nonlinear structure is examined for initial angle of attack and nonlinear aeroelastic static computations. Results are compared against higher–fidelity models using a three–dimensional Euler solver [178], and Unsteady–Vortex–Lattice–Method (UVLM) three–dimensional aerodynamics [48]. In this case, gravitational forces were neglected, while the stiffness parameters were set as $\sigma_1 = 1$ and $\sigma_2 = 5$. For the CFD results a NACA0012 was considered to model the three–dimensional problem from wing to tip. Differences between this implementation arise due to the fact the two–dimensional aerodynamics ignore the thickness and do not account for wing tip corrections on the aerodynamic forces. However, they compare well with higher–fidelity aerodynamics, as shown in Figure 6.4. This agreement though with the Euler equations at higher angle of at-

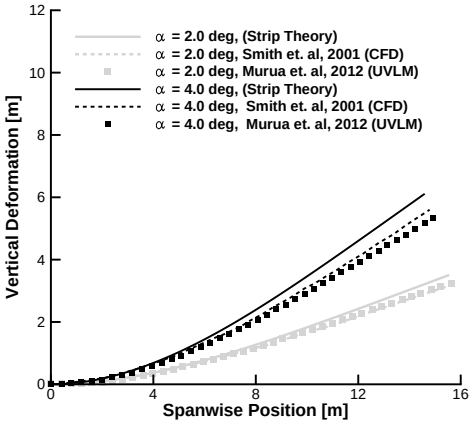

Figure 6.4: Static deflections of the clamped wing for different angle of attack for flow conditions as in Table 6.3

tack, starts becoming unsatisfactory for the strip theory assumption, while UVLM, still manages to capture part of the three-dimensional aerodynamic effect.

The same model was used to perform a flutter speed calculation and a comparison against other aerodynamic modelling techniques. Results are summarised in Table 6.4. It is found that the strip theory assumption is closer to the results presented in Patil et al. [30] where Peters' two–dimensional aerodynamic modelling is used [179]. The

Table 6.4: Flutter Speed Comparison for the cantilever beam

	U_L [m/s]	ω [rad/s]
Present Analysis	31.2	22.1
Murua et al. [51]	33.0	22.0
Patil et al. [30]	32.2	22.6

above results demonstrate that the structural model was coupled correctly with the fluid solver.

6.2.3 Vertical Equilibrium Trimming

The rigid–body degrees–of–freedom introduce additional aerodynamic forces and as a result the first step towards the validation of a free–flying aircraft flight dynamics is to investigate these effects by trimming the aircraft.

The inclusion of the rigid–body degrees–of–freedom is examined. In the following case the aircraft was trimmed only for the vertical force equilibrium. Thus, the angle of attack that is needed to counterbalance gravitational forces at different freestream speed was computed. The payload was placed at a distance $d_{pl} = 2$ m. Figure 6.5 shows that the flexible wing gives different predictions from the rigid wing even without control surface rotation. Furthermore, it is shown that the current strip theory assumption gives the same predictions as with other two–dimensional potential aerodynamics. On the other hand, UVLM slightly overpredicts the angle of attack compared to two–dimensional lower–fidelity methods. The static results of the trim angle of attack for the

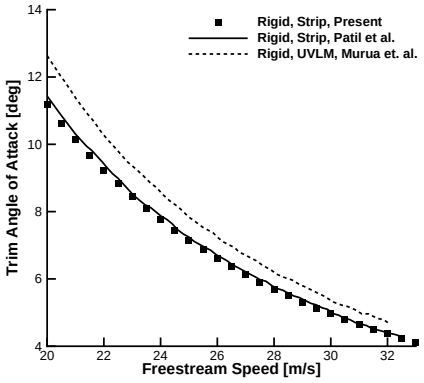

(a) Rigid Trim Angle of Attack in degrees

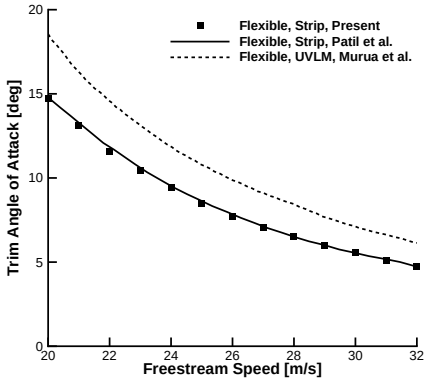

(b) Flexible Trim Angle of Attack in degrees

Figure 6.5: Variation of angle of attack with flight speed for vertical force equilibrium. ($\sigma_1 = 1$, $\sigma_2 = 2$, $d_{pl} = 2$, $d_{HTP} = 0$). Current results compared to Murua et al. [48] and Patil et al. [30]

flexible wing show that when the deformations and bending are very large, a larger angle of attack is needed for the vertical force equilibrium. This is because the lift force does

not act in the vertical direction when the wing exhibits large nonlinear deformations. The deformed configuration of the trimmed aircraft including rigid–body degrees–of–freedom at 25 m/s is shown in comparison with published results in Figure 6.6. The results presented here demonstrate that the two–dimensional aerodynamics used provide the same description of the physics of flexible aircraft undergoing large deformations and rigid–body motion compared to previously published data.

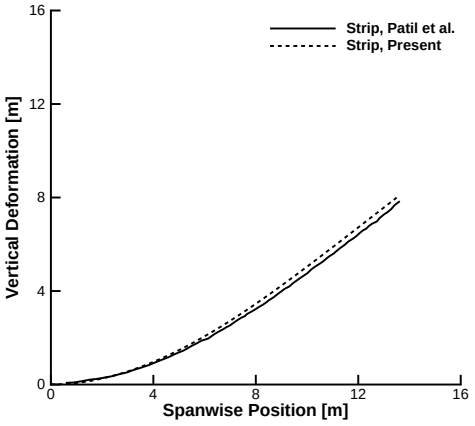

Figure 6.6: Wing displacement of the trimmed aircraft at 25 m/s against published data from Patil et al. [30]

6.2.4 Full Trimming of the Flying Aircraft

There is an impact in the aerodynamic modelling between UVLM and the Strip theory even when the aircraft is rigid and only for the lift force calculation of the vertical equilibrium, which suggests that the impact will only grow larger as the flexibility increases. This becomes evident when the elevator rotation is used for the cancellation of the moments as the flexibility effects increase. The aircraft is trimmed in both vertical and moment equilibrium by using the elevator located at the horizontal tail of the HALE configuration. The varying parameter in this case is the wing flexibility σ which divides the stiffness matrix. Thus, the nominal flexible aircraft is for $\sigma = 1.0$ and for very small values the aircraft becomes rigid. The flow conditions are at a freestream speed of 25 m/s with full payload at $\rho_\infty = 0.0899$ kg/m^3. In Figure 6.7, the trim angle of attack and the elevator rotation to balance out gravitational forces and moments is given for varying flexibility. As expected, when the flexibility increases the deformations of the wing increase as illustrated in Figure 6.8. This causes a change in the desired angle of attack and the moments needed. As a result, both the desired elevator rotation and the angle of attack change as the flexibility increases and deformations become larger.

In conclusion, the trimming results for rigid and flexible aircraft between different aerodynamics in steady level flight confirm previously published results in Ref. [180]

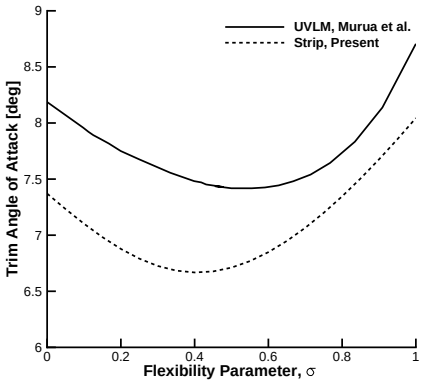

(a) Flexible Trim Angle of Attack in degrees

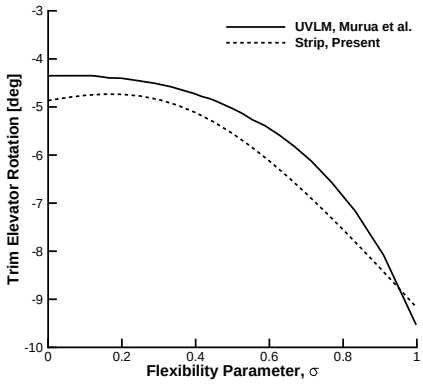

(b) Flexible Trim Elevator Rotation in degrees

Figure 6.7: Full trimming at 25 m/s for varying flexibility σ ($d_{pl} = 2$, $d_{HTP} = 0$) from Murua et al. [48]

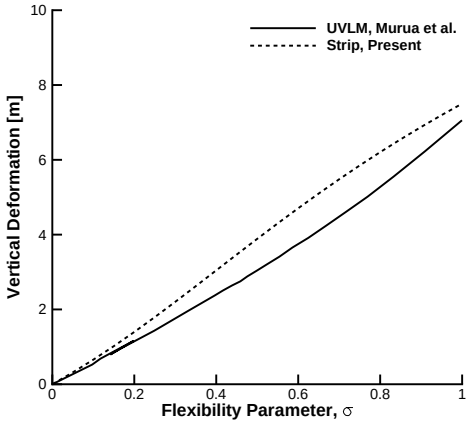

Figure 6.8: Wing displacement of the trimmed aircraft at 25 m/s for varying flexibility σ

where the impact of aerodynamic modelling was assessed for a free–flying rigid wing and comparisons were given in unsteady dynamic calculations between the current implementation, a UVLM implementation and CFD.

6.3 Very Flexible Flying–Wing

6.3.1 Structural Model

Having verified key details of implementation, the test case under investigation is a very flexible high–aspect–ratio flying–wing. The interest here is to investigate the behaviour of the flying–wing when the tail is missing and the flight dynamics are less stable. In addition, it is desired to also investigate the flexibility effects on the flight dynamic response under strong gust disturbances. Linear and nonlinear reduced–order models are derived to predict faster parametric gust searches and design a controller that is applied for loads alleviation. The total wing span is 32 m with a chord of 1 m. No payload is placed in that case on the aircraft. The structural properties are summarised in Table 6.5. Convergence studies were conducted to decide the number of elements

Table 6.5: Test case 2– Very flexible high–aspect–ratio flying–wing structural properties

Chord [m]	1
Semi-span [m]	16
Elastic-axis	25% chord
Centre of gravity	25% chord
Mass per unit length [kg/m]	10
Moment of inertia [kg/m]	10
Torsional stiffness [Nm^2]	1.25 $\times 10^4$
Bending stiffness [Nm^2]	2.5$\times 10^4$
Chordwise bending stiffness [Nm^2]	6.25 $\times 10^6$

needed for the description of the nonlinear physics. Convergence is influenced by both the structure and the aerodynamic discretisation. Herein, the convergence is checked by examining the coupled nonlinear aeroelastic static solution. A nonlinear static solution was carried out at density $\rho_\infty = 0.25$ kg/m^3 corresponding to an altitude $h = 13500$ m, and freestream speed $U_\infty = 25$ m/s for an initial 3 degrees angle of attack without including the rigid–body degrees–of–freedom. The nonlinear wing deformation for different number of elements in that case is shown in Figure 6.9. As a result, 80 elements were found adequate and a large aeroelastic model is built for the full–order model that consists of 960 structural degrees–of–freedom, 640 aerodynamic degrees–of–freedom, 12 rigid–body degrees–of–freedom and 4 quaternions, resulting in 1616 degrees–of–freedom in the fully coupled case. Single control surfaces with single input are mounted across the wing span to provide longitudinal control and trim characteristics having a 10% of

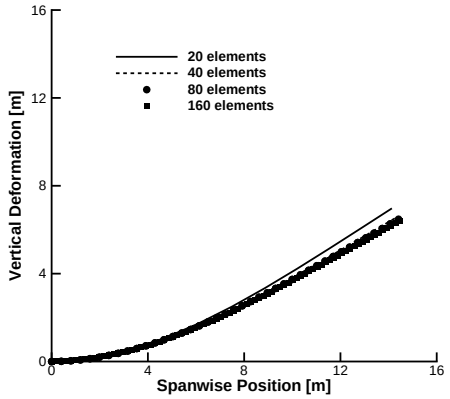

Figure 6.9: Nonlinear static deformation for different number of elements at $\rho_\infty = 0.25$ kg/m^3, $U_\infty = 25$ m/s and an initial 3 degrees angle of attack

the chord length. This modelling neglects the bending of the hinges of the flaps. The nonlinear effect in the static deformation is evident at larger deformations with respect to the wing span. In Figure 6.10 a comparison of the nonlinear against linear static deformation is shown for 3 degrees initial angle of attack. As expected, the linear is well above the nonlinear prediction which assumes a nonlinear structural model. The

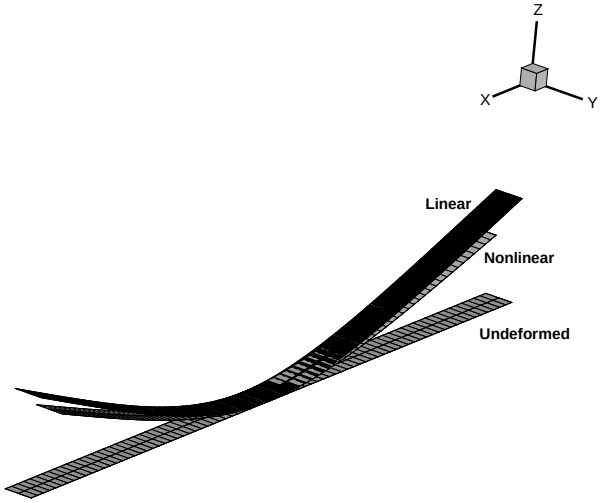

Figure 6.10: Static aeroelastic deformations of linear against nonlinear structure

normal modes about the undeformed configuration for the above clamped structural model are given in Table 6.6

Table 6.6: Test case 2– Vibration structural frequencies in [rad/s]

Mode	Present Analysis
First Bending Mode	4.28
Second Bending Mode	11.92
First Inplane Mode	10.84
Third Bending Mode	17.38
First Torsional Mode	10.41

6.3.2 Flexibility Effect on the Flight Dynamics

In this section the flexibility effect on the coupled flight dynamic response is examined. The coupled system, initially at the equilibrium condition, encounters a strong discrete "1–minus–cosine" gust of 125 m length with a maximum velocity of 0.8 of the freestream speed which can cause large wing deformation and thus affect the flight dynamic response of the vehicle when compared to a rigid–flying wing.

In this case, the varying parameter is the flexibility parameter σ which scales the whole stiffness matrix of the beam elements while the flow condition are given in Table 6.3. Starting from a very stiff wing $\sigma = 0.001$ and a nominal flexibility $\sigma = 1$, the flexibility parameter is increased up to 4 times and thus the aircraft becomes very flexible and is expected to have a different flight dynamic behaviour when compared to a rigid configuration. Gravitational forces have been excluded. However, the flight dynamic response is stable for all cases of the flexibility parameter as shown in Figure 6.11.

The vertical displacement, angle of attack and wing tip deformation are shown for four different stiffness parameters. As expected, for increasing the flexibility, the wing tip deformation increases, affecting the aerodynamic forces and as a result, affecting marginally the flight dynamic response. After the gust disturbance the pitch angle will slowly return to a zero equilibrium which will make the rate of change in the altitude to go to zero. It can be seen that the flight response of the flexible wing is slightly different from the flight response of the rigid wing and this confirms earlier findings also shown by Patil et al. [30], that the flexibility effects always need to be included in the analysis of very flexible and light vehicles and that a gust response analysis based on rigid aircraft and assumptions based on linear aeroelasticity, is not appropriate for these aerial vehicles.

6.3.3 Nonlinear Model Order Reduction

Traditionally in structural dynamics without rigid–body degrees–of–freedom, for example for a flexible cantilever beam in vacuum, only the lowest bending and torsional modes need to be included in the reduced–order model basis for the description of the response

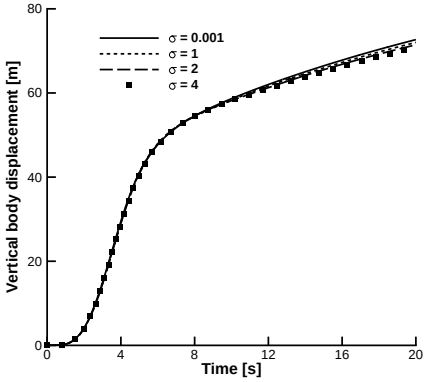

(a) Vertical body displacement in metres

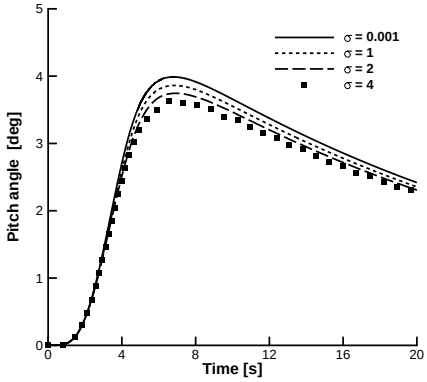

(b) Pitch angle in degrees

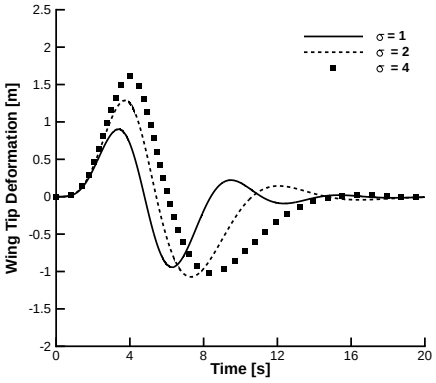

(c) Wing tip deformation in metres

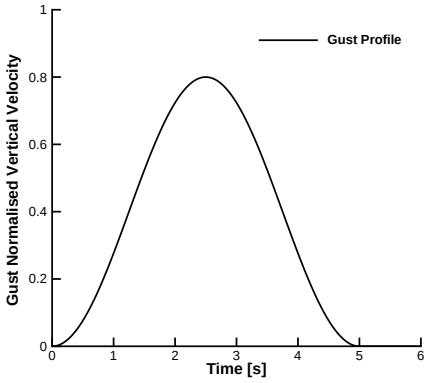

(d) Gust nondimensional vertical velocity

Figure 6.11: Flight dynamics gust response for increasing stiffness parameter σ at ($\rho_\infty = 0.25$ kg/m^3, $U = 25$) m/s

when for example a harmonic follower force is applied. When there is coupling between fluid/structural dynamics and gust interaction some additional eigenvalues need to be taken into account. In this extension from structural dynamics to a coupled problem, damping is now caused by the aerodynamics. The interest here is in gust response predictions, and therefore a mechanism to characterise the aeroelastic response during the gust interaction is needed. This mechanism is called a "gust mode". One way to identify these modes is to calculate the controllability and observability Grammians of the full coupled system and compute the Hankel singular values to check which modes contribute to the overall energy of the system. Nevertheless, this Grammians computation can be extremely expensive to solve for a large–order system coupled with higher–fidelity aerodynamics.

However, for this particular aerodynamic modelling used here, these additional aerodynamic eigenvalues associated to the gust can be automatically identified, because they are associated with the Küssner function. In specific, in previous two–dimensional cases for the aerofoil models in section 3.2 and section 5.1, this gust–associated eigenvalue was found to be $\lambda_i = -0.1393 = -\epsilon_3$ for the nondimensional model as detailed also in [142]. As a result, in the nonlinear beam dimensional model the aerodynamic eigenvalue associated with the gust influence for the unmanned aerial vehicle presented in 5.2 was found to be, $\lambda_i = -\epsilon_3 \frac{U_\infty}{b}$.

In addition, in the fully coupled case with rigid–body dynamics the basis selection includes also the eigenvalues corresponding to the rigid–body degrees–of–freedom. In particular, the gust disturbance affects significantly the evolution of the augmented aerodynamic states which in return affects the rigid–body motion and the overall structural response of the wings. Moreover, this influence is captured in the eigenvalues associated with the coupled rigid/fluid body dynamics.

If the fluid has no internal dynamics, the coupled rigid/fluid eigenvalues are 12. Six related to displacement and rotation, and 6 related to their velocities, and all of them have negative real part due to the aerodynamic damping in the coupled system. Out of those 12 eigenvalues, 3-4 of them are significant and starting with the one with the smallest damping close to the origin, they are included in the basis for convergence as the damping is increased. These eigenvalues introduce the gust effect in the coupled system.

As discussed above, the total number of eigenvalues corresponding to the coupled fluid/structure equations is 960 ($80 \times 6 \times 2$) and in this case, the normal modes modified by the flow are included. In specific, the first complex normal modes modified by the flow are directly associated with the structural dynamics response. The first coupled bending mode is a lightly damped complex eigenvalue and its damping is affected by the freestream speed with respect to the flutter boundary or even the nonlinear deformations. Furthermore, other complex eigenvalues of higher frequency with some damping need to be included to capture the fast dynamics of the structural response.

A strong stochastic Von Kármán gust of 750 m length–scale corresponding to a total simulation of 30 s was chosen to demonstrate the ability of the reduced model to capture the fast dynamics of the full model. The same reduced–order model can thus be used for a variety of gust profiles as it is independent of the gust formulation for this particular flight condition. In Figure 6.12 the eigenvalues of the linearised system are shown together with the eigenvalues that are selected for the basis. The eigenvalues of the reduced–order model included in the basis are given in Table. 6.7.

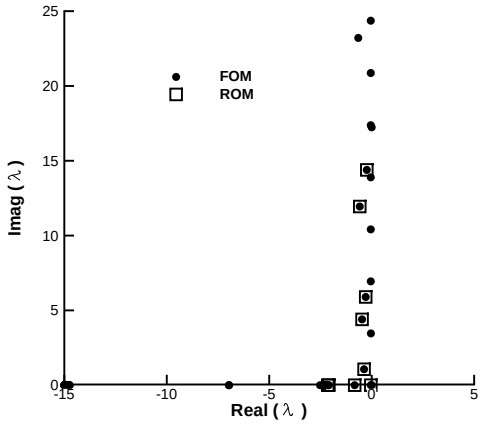

Figure 6.12: Eigenvalues of full model (circles) and reduced–order model (squares) real and imaginary part

Table 6.7: Reduced–Order Model Eigenvalues in [rad/s]

Number	Mode	Real part	Imaginary part
1	gust/fluid/rigid	$-4.147 \cdot 10^{-2}$	0.000
2	gust/fluid/rigid	$-8.285 \cdot 10^{-1}$	0.000
3	gust/fluid/rigid	-2.087	0.000
4	gust/fluid/rigid	-2.143	0.000
5	fluid/structure	$-3.715 \cdot 10^{-1}$	1.065
6	fluid/structure	$-4.695 \cdot 10^{-1}$	4.398
7	fluid/structure	$-2.918 \cdot 10^{-1}$	5.896
8	fluid/structure	$-5.817 \cdot 10^{-1}$	$1.194 \cdot 10^{1}$
9	fluid/structure	$-2.383 \cdot 10^{-1}$	$1.438 \cdot 10^{1}$

In order to analyse how the selected modes contribute to the dynamics of the reduced–order model, 5 ROMs were constructed. The first one contained only mode No.1 from Table 6.7. This is an eigenvalue associated to the rigid–body dynamics that contains the coupling of the augmented aerodynamic states and rigid–body motion and has significant contribution to the angle of attack of the aircraft during the gust response but not to the structural aeroelastic response as shown in Figure 6.13(b).

The second ROM was constructed by also including the other rigid–body modes No.2, No.3 and No.4 which provide additional convergence of the rigid–body motion and introduce the aerodynamic gust effect on the structural wing response as shown in Figure 6.13(a),(b). Following this, the first coupled bending mode No.5 which contains the coupling between fluid/structural dynamics and therefore has a significant impact in the dynamic response of the structure was included in the basis. The second bending and first torsional modes No.6 and mode No.7, respectively, were included to provide additional convergence in the wing response during the gust perturbation.

The final ROM was constructed by including some higher frequency complex eigenvalues related to the third and the fourth bending modes No.8. and mode No.9, respectively, with significant real damping which provide convergence in the description of the wing response and the coupled aeroelastic structural dynamic problem under the fast stochastic gust as shown in Figure 6.13(b).

Note that mode 8 and mode 9 could have not been included in the basis if a long gust length was of interest, for example a long "1-minus-cosine" gust where fast changes in the system dynamics and the structural vibrations are not present and thus very low frequency modes are sufficient. However, it provides good convergence in the case of the stochastic gust by the Von Kármán turbulence. In Fig. 6.13 the convergence of the reduced–order model for the different set of modes is given. In addition, the error $\boldsymbol{e} = ||Y_{FOM}| - |Y_{ROM}||$ between the full model response and the corresponding solution of each mode is shown in Fig 6.14.

Indeed, the flight dynamic modes No.1–No.4 provide good convergence in the coupled rigid–body dynamics problem. After the inclusion of the first bending mode 5 modified by the flow, there is convergence in the structural/fluid dynamics response. Finally, with the inclusion of the second bending mode and some higher frequency bendings, the solution of the reduced–order model matches perfectly the solution of the nonlinear full–order model for small deformations with respect to the wing span less than 10% in the linear regime.

Similar results on how to select the basis and which eigenvalues contribute in the fully coupled case with rigid–body degrees–of–freedom included, were presented in Wang et al. [96] for a flexible wing with a dihedral coupled with two–dimensional aerodynamics. It was found that with the balance truncation, the modes retained were some real eigenvalues starting with the one with the smallest damping and adding for convergence, together with the first two complex eigenvalues. However, an analysis of the convergence of the modes and the impact on the ROM was not investigated.

Herein, the smallest damping real eigenvalues are related to the coupling between gust/fluid/rigid dynamics. They are included in the basis until convergence in the rigid–body motion is achieved. Thereafter, the coupled fluid/structure complex eigenvalues are included for the fluid/structure interaction and the description of the vibrations on the wing.

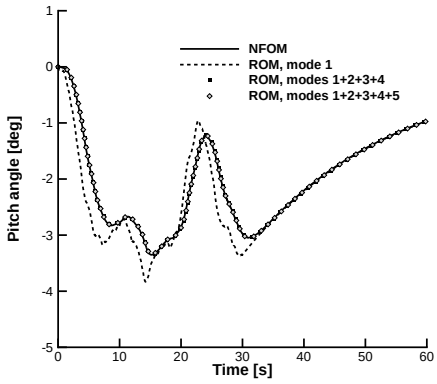

(a) Pitch in degrees

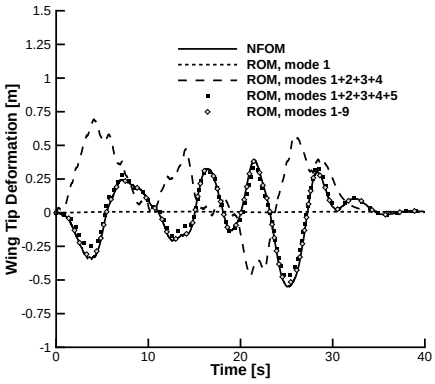

(b) Wing tip deformation in metres

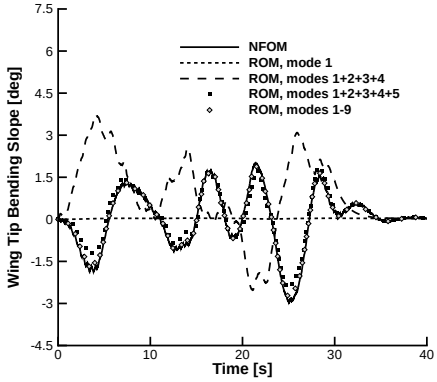

(c) Wing tip bending slope in degrees

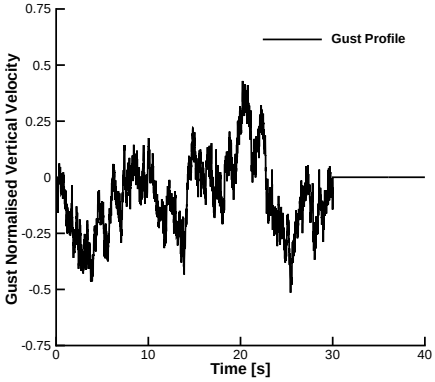

(d) Stochastic gust nondimensional vertical velocity

Figure 6.13: Full nonlinear against linear reduced–order model for a stochastic gust for the different set of modes as in Table 6.7 at ($U_\infty = 25$ m/s, $\rho_\infty = 0.0889$ kg/m^3)

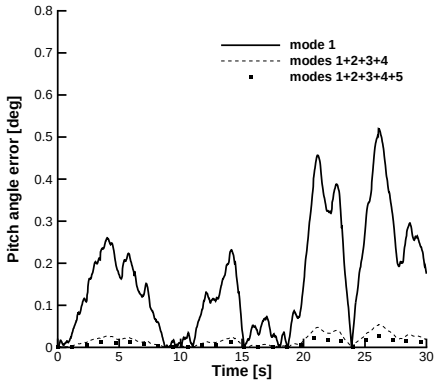

(a) Error pitch angle in degrees

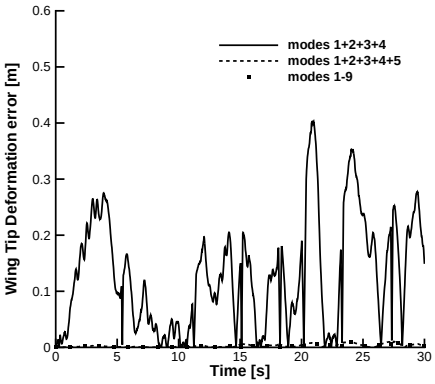

(b) Error wing tip deformation in metres

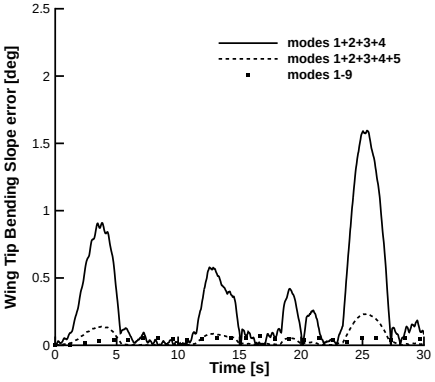

(c) Error wing tip bending slope in degrees

Figure 6.14: Error of nonlinear full against linear reduced–order model for a stochastic Von Kármán gust for the different set of modes as in Table 6.7 at ($U_\infty = 25$ m/s, $\rho_\infty = 0.0889$ kg/m^3)

6.3.4 Rapid Worst–Case Gust Search

Fully nonlinear coupled calculations were run in order to identify a worst–case gust for the flow conditions in Table 6.3. In that case, the flying–wing originally at the undeformed position is assumed at nominal flexibility and a very strong "1-minus-cosine" gust with vertical velocity equal to 1.25 is applied to cause large deformations and introduce the nonlinearities in the fluid/structure. In addition, it is shown that the nonlinearities induced by the strong gust will be captured by the nonlinear reduced–order model The gust duration is varied from $t_g = 0.5$ s up to $t_g = 20.0$ s which corresponds to a gust length of 12.5 m and 500 m respectively, and 37 calculations were run in total for the nonlinear full–order model. Each nonlinear full model calculation to capture 20 s of real time simulation with a timestep of $dt = 0.01$ and convergence in the residual 10^{-5} takes on average, 6 hours on a single processor in a 4-core Intel Xeon 3.3 GHz computer which is taken here as the reference to demonstrate speed–up. This cost is expected to be significantly reduced when the calculations are run using the reduced–order model. The maximum and minimum magnitude of the degrees–of–freedom with respect to the gust length are extracted from the unsteady time–domain calculations and are shown in Figure 6.15.

The worst–case gust duration is found for $t_g = 5.0$ s corresponding to a gust length of 125 m and in this case the wing experiences the maximum loads. In particular, the maximum wing tip deformation is around 10% of the wing span in absolute values and the maximum wing tip bending slope angle around 7.7 degrees. Furthermore, both the vertical displacement of the aircraft and the aircraft pitch angle grow for increasing the gust length. However, in this case it makes sense that as long as the gust is applied, the pitch angle of the aircraft and the rigid–body displacement will keep growing. The linear reduced–order model developed in the previous section by including 9 modes is now used to run the parametric worst–case gust search. Regarding the nonlinearity in the full model, it comes from the large structural deformations and large rigid body rotations that change the total mass, damping and stiffness matrices but also change the effective freestream speed in the streamwise component. However, when the structural deformations and rigid body motion are small, the effective freestream in the streamwise component remains unchanged and the linear–reduced order model is able to predict the full–order model response. This is shown for short gust lengths when the structural deformations and rigid–body pitch angle are small. The computational cost in hours of these 37 calculations for the parametric study using the nonlinear full–order model and the linear reduced model together with the cost of model reduction is given in Table 6.8.

The linear reduced–order model is used for worst–case gust search and then a nonlinear reduced–order model with expansion up to second order terms in the Taylor series was computed to predict more accurately the nonlinear case for the maximum

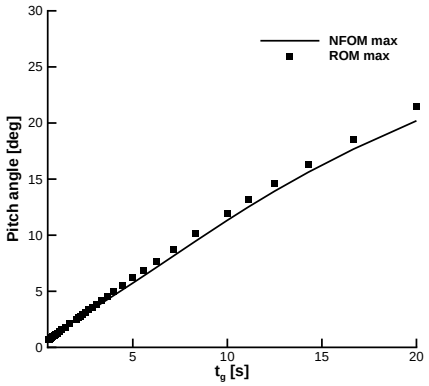

(a) Pitch angle in degrees

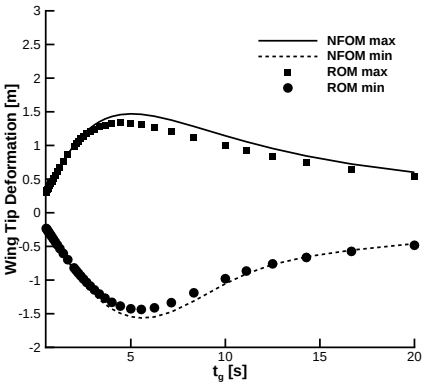

(b) Wing tip deformation in metres

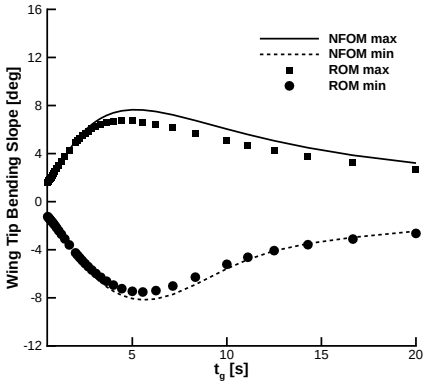

(c) Wing tip bending slope in degrees

Figure 6.15: Maximum and minimum magnitude of the nonlinear flight dynamic response against the linear reduced–order model for a "1–minus–cosine" gust of 1.25 intensity with varying gust length at ($U_\infty = 25$ m/s, $\rho_\infty = 0.0889$ kg/m^3)

Table 6.8: Computational cost in hours

Full Model	Reduced Model	Reduced Model creation	Speed–Up
222	0.37	0.15	600

loads. Figure 6.16 shows the comparison between the nonlinear full–order against the linear and nonlinear reduced–order model. It is shown that with 2nd order expansion the structural nonlinearity under large deformations that causes increased loads is efficiently described. This confirms also previous studies presented in [98] where it was shown that the second order expansion in the Taylor series provided satisfactory prediction of the cubic nonlinearities in the nonlinear beam model without having to resort to more complex computations of a third order expansion in the Taylor series.

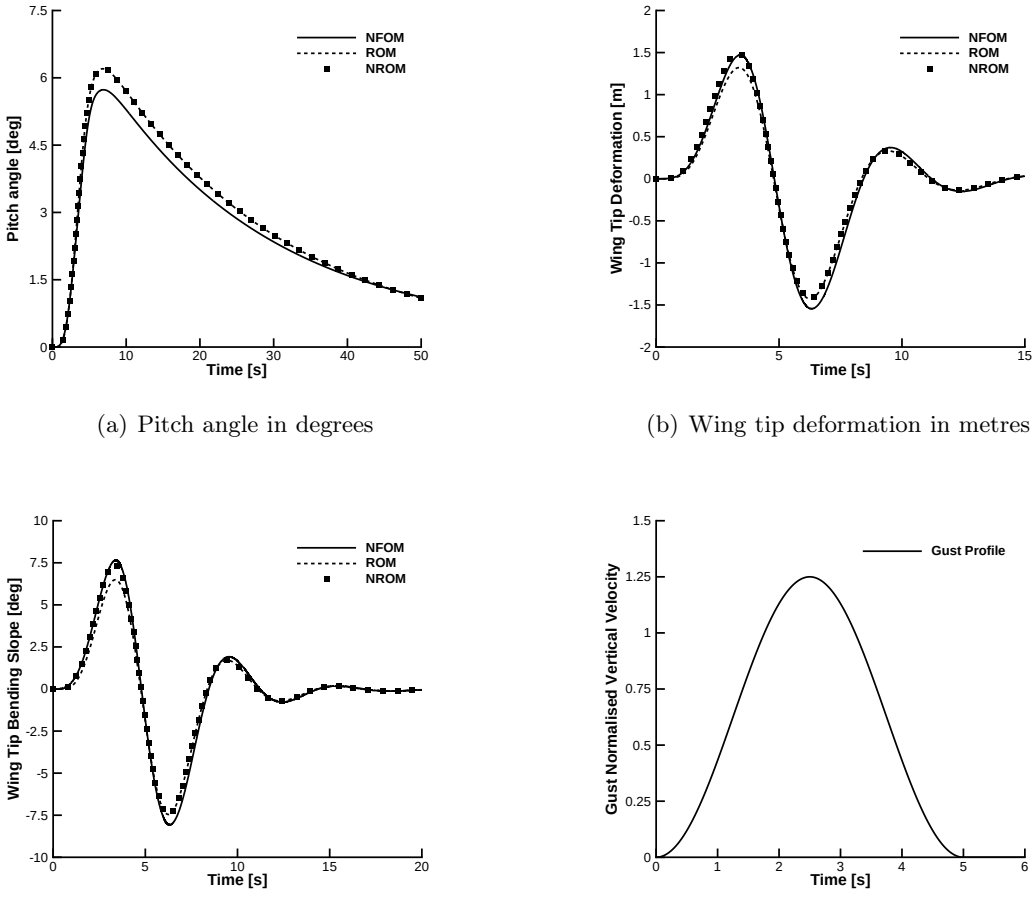

(a) Pitch angle in degrees

(b) Wing tip deformation in metres

(c) Wing tip bending slope in degrees

(d) Worst–case gust length

Figure 6.16: Nonlinear flight dynamic response against the linear and the nonlinear reduced–order model for the worst–case "1–minus–cosine" gust of 1.25 intensity and $t_g = 5.0$ s at ($U_\infty = 25$ m/s, $\rho_\infty = 0.0889$ kg/m^3)

The generality of the reduced models to be used for parametric studies of different

gusts is demonstrated. Furthermore, a reduction of the computational cost by 600 times is achieved. This demonstrates in practice the usefulness of the reduced–order models presented here. The computed reduced models are now used to design a gust load alleviation system which will be applied on the nonlinear full system of equations, for a variety of gust lengths including the worst–case.

6.3.4.1 H_∞ Control Design for Gust Load Alleviation

Previous work on the control of flexible free–flying HALE type vehicles based on the H_∞ control found that the controller was able to alleviate by 9% the root bending moments for the worst–case gust length [32]. Moreover, when the controller was applied on the nonlinear full–order model, it provided good performance in response to short gusts with even better reductions than the linear case. However, the performance gap was decreased as the gust length increased. Herein, the $\mathcal{H}_\infty$ controller based on the reduced–order model is eventually applied on the nonlinear full–order model. The control surfaces used here are times larger in size and it is expected to achieve better alleviation compared to past studies because of the increased control authority. As described in section 2.5.1.1 the objective is to minimise the structural deformations in the closed–loop system and at the same time to maintain a reasonable trajectory for the rigid–body motion as the latter is very sensitive to the trailing–edge flap rotation and responds more slowly. For this purpose, the controller is tuned with respect to $\boldsymbol{K}_c$ such as $\ddot{\boldsymbol{u}}(s) = \boldsymbol{K}_c \boldsymbol{K}(s)\, \boldsymbol{y}_{meas}$ which is a weighting function that feeds the controlled output and penalises the magnitude of the control input $\boldsymbol{u}_c$. The closed–loop system is stable and additional damping is added in the eigenvalues but most importantly to the rigid–body mode, and the first complex conjugate dynamic modes. The eigenvalues of the closed–loop against the open–loop system eigenvalues of the reduced model are shown in Figure 6.17.

Previous studies on the input shape investigation of the $\mathcal{H}_\infty$ methodology suggested that an increase of the weighting function of the control input $\boldsymbol{K}_c$, resulted in larger load alleviation [98]. However, in the case of free–flying aircraft this weighting function will have an impact on the rigid–body trajectory at the expense of minimising the structural deformations. Herein, this impact is assessed.

One of the other challenges of the control design is that its design is based on a linearised reduced–order model of the order of 9 and it is applied on a nonlinear system of approximately 1616 degrees–of–freedom. However, as long as the controller is designed based on a reduced–order model that is representative of the dynamics of the linear full–order model, it is expected in general to provide satisfactory performance when applied on the nonlinear full–order model around the linearisation point for realistic amplitudes of external disturbances.

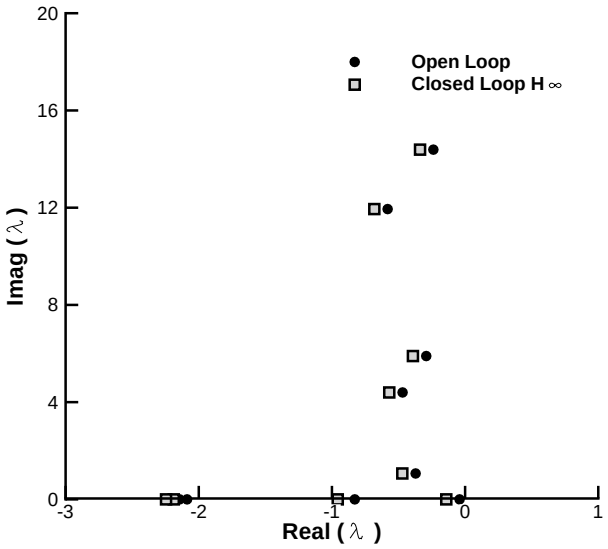

Figure 6.17: Closed loop (square) against open loop (circle) linearised system eigenvalues in [rad/s]

6.3.4.2 Load Alleviation in the Worst–Case Gust Length

The controller is applied on the nonlinear full–order model for the identified worst–case gust length of 125 m in section 6.3.4. Here, the performance is shown when the nonlinear system initially is not at the equilibrium where the control design was made and an initial pitching angle is prescribed. The aircraft encounters the worst–case gust with an initial rigid–body angle of attack of 5 degrees as shown in Figure 6.18. The trailing–edge flap in all cases is initially rotated upwards, making the nose of the aircraft to pitch down, alleviating the loads on the wing. The angle of attack is reduced significantly and in some cases it reaches negative magnitudes. Moreover, the amplitude of the flap's rotation is analogous to the weighting function that penalises the controller. For increasing the weighting function, a better alleviation is achieved. However, this is done at the expense of a significant rigid–body pitching rotation and the equivalent change in the total altitude of the aircraft. Figure 6.18 illustrates that for a very large weighting function the angle of attack of the aircraft becomes very small and in steady state reaches negative magnitudes. As a result, this generates a negative change in the rate of rigid–body vertical velocity and the aircraft loses altitude. Furthermore, it alleviates more the vibrations on the wing and the altitude loss may force the wing to dive into the gusty–field and cancel additional forces induced by the gust.

The best alleviation of the structural loading is shown for $\boldsymbol{K}_c = 4$ where the wing deflection of the closed–loop system is significantly reduced compared to the open–loop system and at the same time the rigid–body motion is reasonable. In that case, the

angle of attack reaches zero equilibrium at steady state, making the rigid–body vertical velocity zero.

6.3.4.3 Load Alleviation for a Longer Gust Length

Herein, the same $\mathcal{H}_\infty$ controller is applied to a longer gust length of $t_g = 25$ s of the same intensity as we are interested to check the control performance when slow changes in the system dynamics are present. The open–loop deformations in that case are smaller, as shown also in Figure 6.15 in the parametric worst–case gust search. The system is initially at the equilibrium and encounters the discrete "1–minus–cosine" gust. The controller is parametrised with respect to the weighting function which has an effect on the body motion and the maximum control surface rotation. Also here, the controller based on the same reduced–order model is directly applied on the nonlinear full–order model for a different gust length.

Moreover, it is expected that a larger weighting function will yield a larger load alleviation and as a result smaller structural deformations. The impact of the control surface rotation on the body motion is assessed. Figure 6.19 shows the open and closed–loop responses of the nonlinear full–order model for varying weighting control penalties. As the gust reaches the leading–edge of the wing, the wing begins to vibrate for as long as it remains inside the gusty field during the fluid/structure and gust interaction for 25 s. The open loop angle of attack of the aircraft becomes very large which causes a significant change in the altitude of the aircraft. Furthermore, as soon as the body exits the gusty field the angle of attack reaches a constant positive value, making the rate of change of the body altitude constant. However, in cases where the angle of attack reaches very large values, there is the danger of stalling and the controller is desired to be able to reduce it. In general, this reduction will positively affect the rate of change of the body altitude.

Indeed, the control surface is rotated positively upwards at initial times which makes the nose of the aircraft to pitch down. The larger the weighting function the better the alleviation in both the structural deformations and the maximum pitching and altitude of the aircraft. However, for a large control penalty the aircraft reaches a negative steady state angle of attack and as a result the aircraft begins to loose altitude. It is concluded that for a longer gust length the controller was able to adapt better in the slow dynamic changes of the system and that for longer gust lengths better gust load alleviation can be achieved with significantly less control effort. This is shown in Figure 6.18 and Figure 6.19 where it is presented that for the worst–case gust of $t_g = 5$ s a larger control surface rotation was needed to achieve the same alleviation on the structure of the wing compared to the longer gust length case.

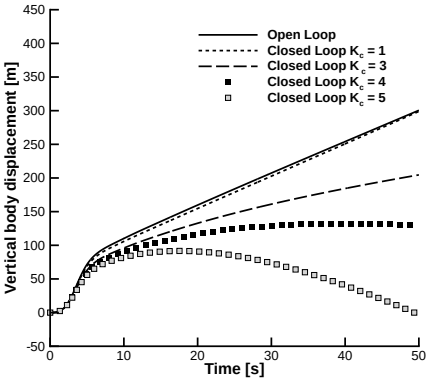

(a) Vertical body displacement in metres

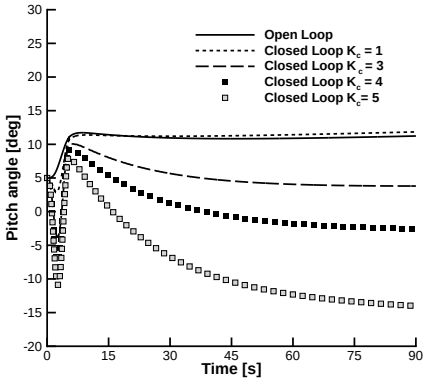

(b) Pitch angle in degrees

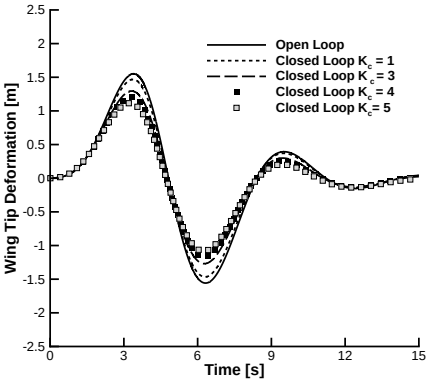

(c) Wing tip deformation in metres

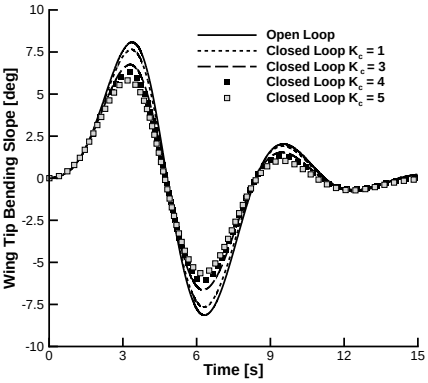

(d) Wing tip bending slope in degrees

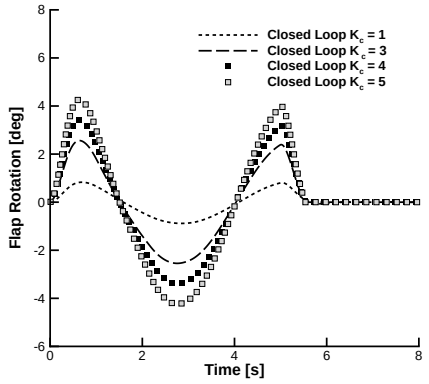

(e) Flap rotation in degrees

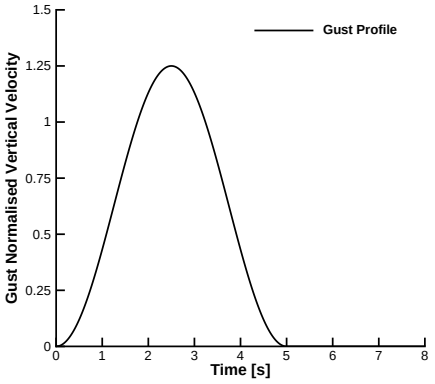

(f) Gust nondimensional vertical velocity

Figure 6.18: Open–loop against closed–loop responses of the nonlinear full order model for different weighting functions $\boldsymbol{K}_c$ for the worst–case gust at an initial rigid–body pitch angle of 5 degrees at ($U_\infty = 25$ m/s, $\rho_\infty = 0.0889$ kg/m^3)

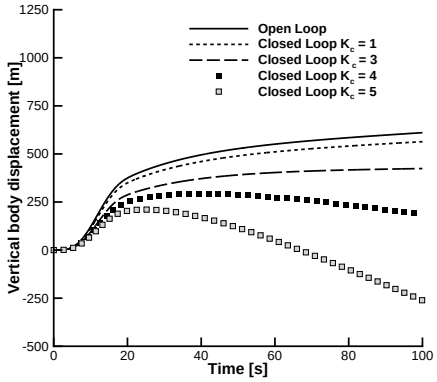

(a) Vertical body displacement in metres

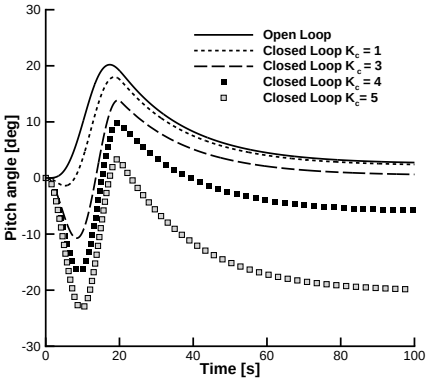

(b) Pitch angle in degrees

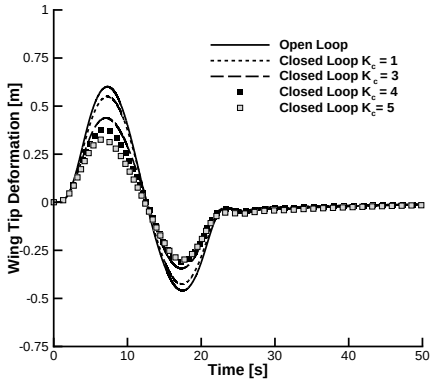

(c) Wing tip deformation in metres

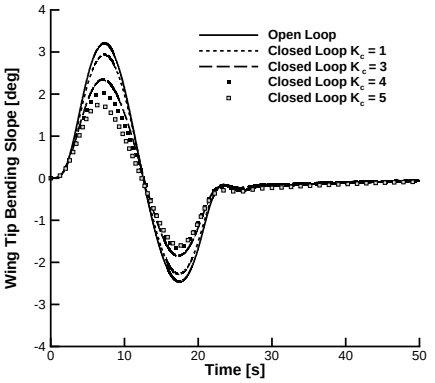

(d) Wing tip bending slope in degrees

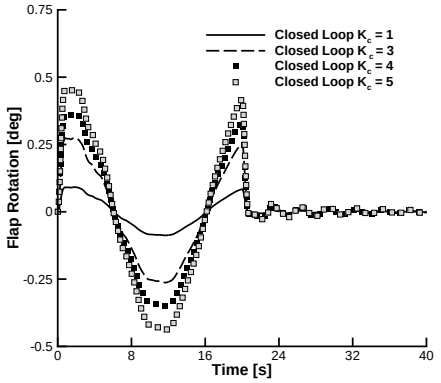

(e) Flap rotation in degrees

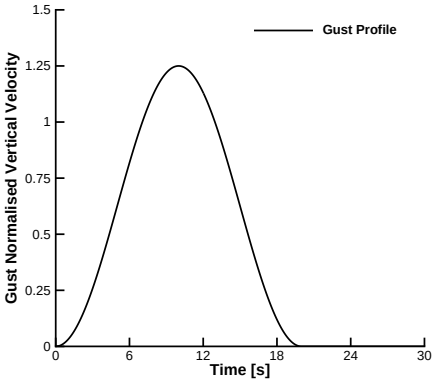

(f) Gust nondimensional vertical velocity

Figure 6.19: Open–loop against closed–loop responses of the nonlinear full–order model for different weighting functions $\boldsymbol{K}_c$ for a long gust length of $t_g = 25$s and vertical normalised intensity of 1.25

6.4 Summary

In this chapter the evaluation of the residual and the aerodynamic modelling and coupling of the flight dynamic degrees–of–freedom for free–flying flexible vehicles was presented. Moreover, an approach to the nonlinear model reduction, which was shown capable through a variety of test cases to generate small order systems while retaining the important nonlinear features of the large computational coupled models was extended to include the flight dynamics degrees–of–freedom. The approach is applied to coupled fluid/structure/flight dynamic models that exhibit nonlinear effects due to large structural deformations.

The advantages of the above model are the reduction of the model size that speeds up the calculation times considerably, up to 600 times, and the retention of nonlinear effects that can be used to synthesise an appropriate control law strategy. Herein, the aeroelastic framework was validated for a rigid and a flexible aircraft against published data. A set of results were presented, starting from static calculations and flutter speed prediction towards the comparison of the current implementation of the two–dimensional aerodynamic model against other aerodynamic theories with the inclusion of the flight dynamics degrees–of–freedom. Moreover, it was found that the flexibility effects were important and one needs to take into account these effect for a careful analysis of flexible vehicles. In addition, it was found that partial and full trimming of the aircraft differed greatly between the aerodynamics and these differences only grew larger as the flexibility increased. This comparison was performed between Strip aerodynamics, UVLM and CFD.

Furthermore, a very flexible wing configuration was assembled. Firstly, convergence studies together with a normal mode analysis were carried out to decided the needed number of beam elements for the structural/fluid modelling. Secondly, the impact of the flexibility effects on the flight dynamic response was examined for a gust response and comparisons were made between fully rigid and fully flexible wing configurations. Thirdly, it was used for a worst–case gust search. A reduced–order model was derived and a method to construct its eigenvector basis was presented. The reduced–order model, was used to perform the worst–case gust search hundred times faster for a variety of gusts.

It was seen that when the wing exhibits larger deformations or deformations more than 10% of the wingspan, the linear reduced–order model is not in the position to predict the nonlinear behaviour. However, a nonlinear reduced–order model was developed, retaining only terms up to 2nd order expansion in the Taylor series, and this was shown to predict the nonlinear physics during larger deformations.

Furthermore, due to its simplicity it was ideal for control design and herein an optimal robust $\mathcal{H}_\infty$ controller was designed for the worst–case gust. Its efficiency was demonstrated when applied on the full–order nonlinear coupled equations and an in-

vestigation of the controllers parameters was assessed. The optimal robust controller was suitable for loads alleviation and some of the challenges on the control of flexible free–flying aircraft [32] were confirmed and overcome. In particular, it was found that the weighting function of the controller was important for the gust load alleviation on the structure and the body altitude trajectory. The control design was applied to the worst–case gust length and to a longer gust length. It is shown that the controller is more efficient on longer gust lengths and in these cases the control effort to perform gust load alleviation was less when compared to the worst–case gust length.

Chapter 7

Conclusions

This work focused on the development of aeroelastic models for the description of the physics of flexible aircraft. In particular, a two degree–of–freedom aerofoil, a three degree–of–freedom aerofoil and several models of flexible wings, with and without flight dynamics degrees–of–freedom were presented.

A two–dimensional aerodynamic model was coupled with the corresponding structural equations, leading to the development of several individual aeroelastic solvers. A key contribution was the development and implementation of a nonlinear model order reduction technique, general and capable of retaining the structural nonlinearity in all the cases, whether this was a geometric nonlinearity, or just a nonlinear spring stiffness. The derived nonlinear ROMs were parametrised with respect to several variables such as controls, gusts or even the flow conditions. Firstly, this made feasible the use of the nonlinear ROMs for faster parametric worst–case gust searches while retaining significant nonlinear effects. Secondly, it made possible a design of inherently different complex control methodologies based on a small nonlinear system, but at the same time, suitable to be applied on the original large nonlinear system of equations.

A validation was provided at low–speed for the two–dimensional aerodynamic model against CFD. This was shown for a two degree–of–freedom aerofoil model with a structural nonlinearity in the plunge degree–of–freedom, coupled with CFD and with a two–dimensional aerodynamic model. It was seen that the strip aerodynamics predict the same solution with CFD for a free response at low–speed. In the transonic regime the two theories gave different predictions. Furthermore, reduced–order models were derived using the same nonlinear model order reduction technique in both solvers and it was shown that the technique developed is independent of the aerodynamics used and can be applied in all types of systems, while its applicability can be extended to other fields related to structural, electrical, robotics and mechanical engineering. A further validation was carried out for a flexible wing model coupled with the two–dimensional aerodynamics against available commercial software. Gust responses were simulated and the aeroelastic prediction between the two solvers was satisfactory. Similar effort

was made to assess the impact of the flight dynamics degrees–of–freedom on the aerodynamic modelling. As a result, free–flying wing responses driven by an initial angle of attack were compared between CFD, a UVLM solver and the model used. At low–speed the current assumption agreed well with medium–fidelity aerodynamics given by the UVLM when compared to the CFD solution.

The implementation of the developed numerical models and their application to experiments was also examined. A set of numerical studies was carried out first for a two degree–of–freedom aerofoil. The linear flutter speed was computed and a reduced–order model was derived very close to the predicted stability boundary. It was then used to perform a worst–case gust search faster and to calculate an $\mathcal{H}_\infty$ controller for gust load alleviation. The identification of the eigenvalue related to the gust disturbance in the reduced–order model basis was also studied. This eigenvalue was independent of the flight conditions as it was equal to the lowest Küssner constant. In this manner, the automatic generation of nonlinear reduced–order models capable of describing fully nonlinear gust responses became feasible. Moreover, the computed reduced–order controller based on the reduced–order model was found suitable to alleviate the gust loads under realistic flap rotations.

The numerical model above was tested on an experimental low–speed wind–tunnel model at the University of Liverpool. Firstly, it was shown that the numerical model predicted well the flutter speed against experimental data taken from the wind–tunnel. In addition, the numerical model was used to design a linear and a nonlinear controller for flutter suppression and extension of the flight envelope. When tested at the computed flutter speed, the linear controller was unable to suppress the LCOs whereas the nonlinear controller drove the system back to equilibrium. This result shows a case where a nonlinear control design outperforms conventional linear techniques.

More complicated aeroelastic models were also developed to emphasise the generality of the approach. In particular, a three degree–of–freedom aerofoil and a nonlinear structural beam model were coupled with linear aerodynamics. Herein, the interest focused on the identification of the eigenvalue basis for the automatic generation of nonlinear reduced models able to be used for a cheaper gust computation. In this case, the "gust mode" was the same in these two different structural models and again it was related to the lowest Küssner constant. More importantly, as the size of the aeroelastic system grew, a significant reduction of the computational time up to 30 times was achieved when using the nonlinear reduced–order model for the nonlinear computations. This emphasised the fact that the nonlinear reduced models should be used for worst–case gust searches. Furthermore, it presented the synthesis, design, and testing of two inherently different control strategies developed around the nonlinear reduced–order model for gust loads alleviation and this was shown to be systematic as it was independent of the original equations. An $\mathcal{H}_\infty$ and an adaptive control design based on the model reference adaptive control ($\mathcal{MRAC}$) scheme were developed. A further

investigation was carried out to study the effect that the adaptation parameters in the control law had on the closed–loop stability and the control effort. It was found that a sufficient large enough adaptation rate is needed during the disturbance interaction to regulate the system under deterministic and stochastic disturbances and in these cases the adaptive controller was found superior when compared to the $\mathcal{H}_\infty$ controller.

Lastly, the developed methods here were investigated for cases with flight dynamics degrees–of–freedom included. The structural models were coupled with rigid–body degrees–of–freedom and a potential flow assumption, and a whole aircraft HALE configuration was assembled. A set of static results, flutter speed predictions, partial and full aircraft trimming were presented. It was found that the current strip theory compared well against previously published data that used similar two–dimensional aerodynamics. However, the impact of the aerodynamic modelling remained, and this was shown for the current assumption against CFD and UVLM. Moreover, it was found that a rigid wing had different trimming conditions with respect to the angle of attack, compared to a flexible wing configuration. The aerodynamic theories, provided different partial trimming for the vertical force equilibrium for both rigid and flexible wings with UVLM overpredicting the results by some margin. Furthermore, it was seen that this impact in the prediction, only grew larger for the full trimming of the aircraft where the elevator was used to cancel out the moments. The methods developed in this work were also tested on a flexible free–flying wing configuration. Firstly, a normal mode analysis was carried out for the high–aspect–ratio flying–wing followed by convergence studies and static aeroelastic calculations to decide the number of structural beam elements. Secondly, it was desired to study the flexibility effects on a dynamic gust response. Two configurations were assumed, one rigid, and one flexible. The flexibility was varied and it was found that by increasing the flexibility the vehicle experienced slightly different dynamic response. This emphasises the fact that the flexibility and the structural deformations introduce contributions in the aerodynamic forces and as a result changes in the total lift and moment.

Moreover, a convergence of the eigenvalue basis for the reduced–order model was carried out to identify the most important eigenvalues and how each one of them contributed to the dynamics of the system during a gust response. As a result, a linear reduced–order model suitable for predicting stochastic gusts and at the same time, to be used for a parametric worst–case gust search for a particular flight condition, was developed. In this case, a discrete "1–minus–cosine" gust with varying gust length was used for both nonlinear full model and linear reduced–order model. As expected, under small rigid–body rotations and structural deformations, the linear ROM gave the same prediction as the nonlinear full–order model. A worst–case gust length was identified and for that particular case the large wing deformation introduced differences between the linear and the nonlinear solution. The nonlinear terms up to second order expansion in the Taylor series were computed and were added to the dynamics of the ROM.

The resulting nonlinear ROM gave good predictions when compared to the nonlinear full–order model, suggesting that a second order expansion is sufficient to describe the structural nonlinearity of the nonlinear beam in a computationally cheap manner. The ROM had a dimension of 9 while the full model consisted of 1616 degrees–of–freedom, and a reduction of 600 times of the computational cost was achieved when the ROM was used for the parametric gust studies.

In addition, the nonlinear ROM was used for the design of a gust load alleviation system with the $\mathcal{H}_\infty$ control design. The controller was applied both to the worst–case gust length, and to longer gust lengths. A relationship between the gust length and the control effectiveness was found, with longer gusts to require smaller control deflection for the same load alleviation. However, an input–shape investigation of the controller showed the impact it has on the rigid–body trajectories. A larger control penalty achieved better load alleviation, but at the same time caused unreasonable aircraft trajectories even though the whole closed–loop system remained stable. A parametrisation for the penalties of the controller was carried out to decide the optimal gains of the design for the different gust lengths.

7.1 Future Work

Although a large body of work was carried out, additional implementations can be done. These can either be in the aerodynamic model or the structural model. Firstly, a stall and a wing tip correction model can be implemented in the current aerodynamic assumption, allowing more realistic aeroelastic predictions at higher angle of attack and strong gust disturbances. Moreover, it would be interesting to see how the nonlinear model order reduction technique would treat these additional aerodynamic implementations. Secondly, a discrete polynomial structural nonlinearity can be defined in the nonlinear beam to investigate gust load alleviation and model reduction techniques. This is currently developed at the University of Liverpool [181]. Additional implementations can include the freestream speed parametrisation in the reduced–order model that was also part of the work in Ref. [101], but this time applied to nonlinear beam models.

The reduced–order model may yield significant advantages also in experimental problems. In real time experimental control, a low–order numerical model can be implemented. For example, the reduced–order model due to its small size, can be implemented in parallel with an experimental wind–tunnel model and used to obtain measurements of the unmeasurable aerodynamic states without the need to design a nonlinear observer for the nonlinear aeroelastic wing–section. In this case, the physical measurements can be obtained by the laser sensors (pitch and plunge and their velocities), and the augmented aerodynamic states can be predicted by the reduced–order model. If the reduced–order model is further parametrised with respect to the

freestream speed, then it could also provide the aerodynamic states and offer real time control for a larger speed regime.

Apart from the application of the ROM in real time control, many advances need to be made on the simulation of flexible aircraft with higher–fidelity aerodynamics from CFD. Currently, the identification of the "gust mode" for very large aeroelastic models is under investigation [99]. However, if a systematic way is developed to identify the "gust mode" in large coupled CSD/CFD models, very cheap computations would be feasible. Under these circumstances, a worst–case gust search with a large CFD model would become possible even by home computers in a matter of minutes, yielding a positive impact in the industry.

Strip theory aerodynamics represent a very cheap alternative to compute the stability boundaries of high–aspect–ratio wings at low–speed and this was shown for two–dimensional and three–dimensional cases. The model order reduction can be applied to all types of aeroelastic models and it was seen to be independent of the aerodynamics used. These reduced–order models can be used to synthesise a variety of inherently different control methodologies, linear and nonlinear. A key target here is to demonstrate in future work that a reduced–order controller based on two–dimensional flow assumption which at low–speed has been shown to compare well with higher–fidelity CFD models, has the potential to be applied to a large CFD system.

From a control design point of view, there is a need to interface novel methods of nonlinear control such as the Sum–of–Squares (SOS) with the nonlinear reduced–order models. This is urgent as there are countless cases in the literature and also presented here where linear control designs were inferior to nonlinear designs. In aeroelasticity the size of the system makes the direct application of novel nonlinear control designs challenging. However, the nonlinear reduced–order models can potentially be used to overcome theses problems and make the design of complex nonlinear controllers feasible even for large CSD/CFD models.

Bibliography

[1] Noll, T. E., Brown, J. M., Perez-Davids, M. E., Ishmael, D., Tiffany, G. C., and Gaier, M., "Investigation of the Helios Prototype Aircraft Mishap Volume I: Mishap Report," *NASA Tech. Rep.*, January, 2004.

[2] Langford, J., "The Daedalus Project: A summary of Lessons Learned," *AIAA 89-2048*, 1989.

[3] Drela, M., "Aerodynamics of Human-Powered Flight," *Annual Review in Fluid Mechanics.*, Vol. 22, 1990, pp. 93–110, doi: 10.1146/annurev.fl.22.010190.000521.

[4] Allen, B., "Winged Victory of Gossamer Albatros," *National Geographic*, 1979.

[5] Van Schoor, M. C. and Von Flotow, A. H., "Aeroelastic Characteristics of a Highly Flexible Aircraft," *Journal of Aircraft*, Vol. 27, No. 10, doi: 10.2514/3.45955.

[6] Patil, M. J. and Hodges, D. H., "Flight Dynamics of Highly Flexible Flying Wings," *Journal of Aircraft*, Vol. 43, No. 6, 2006, pp. 1790–1799, doi: 10.2514/1.17640.

[7] Drela, M., "Integrated Simulation Model For Preliminary Aerodynamic, Structural, and Control-Law Design of Aircraft," *Proceedings of the 1999 AIAA/ASME/ASCE/AHS/ASC Structures, Structural Dynamics, and Materials Conference and Exhibit, St. Louis, MO, USA*, Vol. 3, pp. 1644–1656.

[8] Cesnik, C. S. and Brown, E. L., "Modelling of High Aspect Ratio Active Flexible Wings for Roll Control," *Proceeding of the 43rd AIAA/ASME/ASCE/AHS Structures, Structural Dynamics, and Materials Conferences, Denver CO, AIAA Paper 2002–1719*, 2002, doi: 10.2514/6.2002-1719.

[9] Cesnik, C. S. and Brown, E. L., "Active Wing Warping Control of a Joined Wing/Tail Airplane Configuration," *Proceedings of the 44th AIAA/ASME/ASCE/AHS Structures,Structural Dynamics, and Materials Conferences, Norfolk, Virginia , AIAA Paper 2003–1715*, Vol. 4, 2003, pp. 2847–2861, doi: 10.2514/6.2003-1715.

[10] Palacios, R. and Cesnik, C. S., "Static Nonlinear Aeroelasticity of Flexible Slender Wings in Compressible Flow," *46th AIAA/ASME/ASCE/AHS/ASC Structures, Structural Dynamics and Materials Conference, Austin, TX*, AIAA Paper 2005-1945, 2005.

[11] Su, W. and Cesnik, C. S., "Nonlinear Aeroelasticity of a Very Flexible Blended-Wing-Body Aircraft," *Journal of Aircraft*, Vol. 47, No. 5, Oct. 2010, pp. 1539–1553, doi: 10.2514/1.47317.

[12] Jones, R. I., "Design Challenge of High Altitude Long Endurance (Hale) Unmanned Aircraft," *The Aeronautical Journal*, Vol. 103, June 1999.

[13] Jones, R. I., "Selection and Comparison of Unmanned Aircraft Configurations," *In RPVs International Conference, 12th, Bristol, United Kingdom*, Sept. 9-11, 1996.

[14] Raghavan, B., "Flight Dynamics and Control of Highly Flexible Flying–Wings," *PhD Dissertation, Virginia Polytechnic Institute and State University*.

[15] Su, W. and Cesnik, C. S., "Dynamic Response of Highly Flexible Flying Wings," *AIAA Paper 2006–1636*, Vol. 47th AIAA/ASME/ASCE/AHS/ASC Structures, Structural Dynamics, and Materials Conference, 1-4 May 2006, Newport, Rhode Island.

[16] Shearer, C. M. and Cesnik, C. S., "Nonlinear Flight Dynamics of Very Flexible Aircraft," *Journal of Aircraft*, Vol. 44, No. 5, 2007, doi: 10.1.1.457.4058.

[17] Cesnik, C. S. and Su, W., "Nonlinear Aeroelastic Simulation of X-HALE:a very Flexible UAV," *49th AIAA Aerospace Sciences Meeting Including the New Horizons Forum and Aerospace Exposition, AIAA Paper 2011-1226*, 4–7 January 2011, Orlando, Florida, doi: 10.2514/6.2011-1226.

[18] Cesnik, C. S., Senatore, P. J., Su, W., Atkins, E. M., Shearer, C. M., and Pitcher, N. A., "X-HALE: A Very Flexible UAV for Nonlinear Aeroelastic Tests," *AIAA Journal*, Vol. 50, No. 12, 2012, pp. 2820–2833, doi: 10.2514/1.J051392.

[19] Palacios, R., Murua, J., and Cook, R., "Structural and Aerodynamic Models in Nonlinear Flight Dynamics of Very Flexible Aircraft," *AIAA Journal*, Vol. 48, No. 11, 2010, pp. 2648–2659, doi: 10.2514/1.J050513.

[20] Hesse, H. and Palacios, R., "Consistent Structural Linearisation in Flexible–Body Dynamics with Large Rigid–Body Motion," *Computers & Structures*, Vol. 110–111, 2012, pp. 1–14, doi: 10.1016/j.compstruc.2012.05.011.

[21] Bisplinghoff, R. L., Ashley, H., and Halfman, R. L., *Aeroelasticity*, Dover Publications, 1955.

[22] Theodorsen, T., "General Theory of Aerodynamic Instability and the Mechanism of Flutter," Tech. Rep. NACA–496, National Advisory Committee for Aeronautics, 1935.

[23] Tang, D. and Dowell, E. H., "Experimental and Theoritical Study on Aeroelastic Response of High-Aspect-Ratio Wings," *AIAA Journal*, Vol. 39, No. 8, August 2001, pp. 1430–1431, doi: 10.2514/2.1484.

[24] Wagner, H., "Uber die Enstehung des dynamischen Auftriebs von Tragflugeln," *ZAMM, Bd.5, Heft1*, Feb. 1925, pp. 17–35.

[25] Jones, R. T., "Operational Treatment of the Nonuniform Lift Theory to Airplane Dynamics," *NACA TN 667*, March 1938, pp. 347–350.

[26] Vepa, R., "On the Use of Pade Approximants to Represent Unsteady Aerodynamic Loads for Arbitrarily Small Motions of Wings," *AIAA Paper 1976-17*, 1976, doi: 10.2514/6.1976-17.

[27] Dowel, E. H., "A Simple Method for Converting Frequency Domain Aerodynamics to the Time Domain," *NASA TM-81844*, Oct.1980.

[28] Peters, D. A. and Cao, W., "Finite State Induced Flow Models, Part 1:Two Dimensional Thin Airfoil," *Journal of Aircraft*, Vol. 32, No. 2, Mar.-Apr. 1995, pp. 313–322, doi: 10.2514/3.46718.

[29] Dillsaver, M. J., Cesnik, C. E., and Kolmanovsky, I. V., "Gust Load Alleviation Control for Very Flexible Aircraft," *AIAA Atmospheric Flight Mechanics Conference, AIAA Paper 2011-6368*, 2011, Oregon, doi: 10.2514/6.2011-6368.

[30] Patil, M. J., Hodges, D. H., and Cesnik, C. E. S., "Nonlinear Aeroelasticity and Flight Dynamics of High-Altitude Long-Endurance aircraft," *Journal of Aircraft*, Vol. 38, No. 1, 2001, pp. 88–94, doi: 10.2514/2.2738.

[31] Leishman, J. G., "Unsteady Lift of a Flapped Airfoil by Indicial Concepts," *Journal of Aircraft*, Vol. 31, No. 2, 1994, pp. 288–297.

[32] Cook, R. G., Palacios, R., and Goulart, P., "Robust Gust Alleviation and Stabilization of Very Flexible Aircraft," *AIAA Journal*, Vol. 51, No. 2, Feb. 2013, pp. 330–340, doi: 10.2514/1.J051697.

[33] "A Compilation of the Mathematics Leading to the Doublet-Lattice Method," *USAF WL-TR-95-3022*, 1992.

[34] Albano, E. and Rodden, W. P., "A Doublet-Lattice Method for Calculating Lift Distributions on Oscillating Surfaces in Subsonic Flows," *AIAA Journal*, Vol. 7, No. 2, 1969, pp. 279–285, doi: 10.2514/3.5086.

[35] Kier, T. M., "Comparison of Unsteady Aerodynamic Modelling Methodologies with Respect to Flight Loads Analysis," *AIAA Atmospheric Flight Mechanics Conference*, Vol. 1, 2005, pp. 616–629, doi: 10.2514/6.2005-6027.

[36] Baldelli, D. H. and Chen, P. C., "Unified Aeroelastic and Flight Dynamic Formulation via Rational Function Approximations," *Journal of Aircraft*, Vol. 43, No. 3, May-June 2006, pp. 763–772, doi: 10.2514/1.16620.

[37] Baldelli, D. H., Lee, D. H., Sanchez Pena, R. S., and Cannon, B., "Modelling and Control of an Aeroelastic Morphing Vehicle," *Journal of Guidance, Control and Dynamics*, Vol. 31, No. 6, November-December 2008, pp. 1687–1699, doi: 10.2514/1.35445.

[38] Patil, M. J. and Hodges, D. H., "On the Importance of Aerodynamic and Structural Geometrical Nonlinearities in Aeroelastic Behaviour of High-Aspect-Ratio Wing," *Journal of Fluids and Structures*, Vol. 31, No. 7, August 2004, pp. 905–915, doi: 10.1016/j.jfluidstructs.2004.04.012.

[39] Rodden, W. P., Taylor, P., and McIntosh Jr., S. C., "Further Refinement of the Subsonic Doublet-Lattice Method," *Journal of Aircraft*, Vol. 35, No. 5, September-October 1998, pp. 720–727, doi: 10.2514/2.2382.

[40] Baker, M. L. and Rodden, W. P., "Improving the Convergence of the Doublet-Lattice Method Through Tip Corrections," *Journal of Aircraft*, Vol. 38, No. 4, 2001, pp. 772–776, doi: 10.2514/2.2831.

[41] Hedman, S. G., "Vortex Lattice Method for Calculation of Quasi Steady State Loadings on Thin Elastic Wings in Subsonic Flow," *Aeronautical Research Institute of Sweden*, 1966.

[42] Lan, C. E., "A Quasi-Vortex-Lattice Method in Thin Wing Theory," *Journal of Aircraft*, Vol. 11, No. 9, 1974, pp. 518–527, doi: 10.2514/3.60381.

[43] Mook, D. and Nayfeh, A., "Application of the Vortex-Lattice Method to High-Angle-of-Attack Subsonic Aerodynamics," *SAE Technical Paper, No. 851817*, October 1985, doi: 10.4271/851817.

[44] Konstadinopoulos, P., Thrasher, D. F., Mook, D. T., Nayfeh, A. H., and Watson, L., "A Vortex-Lattice Method for General, Unsteady Aerodynamics," *Journal of Aircraft*, Vol. 22, No. 1, January 1985, pp. 43–49, doi: 10.2514/3.45078.

[45] Katz, J., "Lateral Aerodynamics of Delta Wings with Leading-Edge Separation," *AIAA Journal*, Vol. 22, No. 3, 1984, pp. 323–328, doi: 102514/3.8395.

[46] Katz, J. and Plotkin, A., *Low-Speed Aerodynamics*, Cambridge Aerospace Series, Cambridge University Press, New York, NY, USA, 2nd ed., 2001.

[47] Murua, J., Palacios, R., and Graham, J. M. R., "Assessment of Wake–Tail Interference Effects on the Dynamics of Flexible Aircraft," *AIAA Journal*, Vol. 50, No. 7, 2012, pp. 1575–1585, doi: 10.2514/1.J051543.

[48] Murua, J., Palacios, R., and Graham, J. M. R., "Applications of the Unsteady Vortex–Lattice Method in Aircraft Aeroelasticity and Flight Dynamics," *Progress in Aerospace Sciences*, Vol. 55, 2012, pp. 46–72, doi: 10.1016/j.paerosci.2012.06.001.

[49] Fritz, T. E. and Long, L. N., "Object-Oriented Unsteady Vortex Lattice Method for Flapping Flight," *Journal of Aircraft*, Vol. 41, No. 6, November-December 2004, pp. 1275–1290, doi: 10.2514/1.7357.

[50] Murua, J., Hesse, H., Palacios, R., and Graham, J. M. R., "Stability and Open-Loop Dynamics of Very Flexible Aircraft including Free-Wake Effects," *52nd AIAA/ASME/ASCE/AHS/ASC Structures, Structural Dynamics and Materials Conference, AIAA Paper 2011–1915*, Denver, Colorado, 2011, doi: 10.2514/6.2011-1915.

[51] Murua, J., "Flexible Aircraft Dynamics with a Geometrically-Nonlinear Description of the Unsteady Aerodynamics," *PhD Thesis, Imperial College London*, 2012.

[52] Hesse, H., Palacios, R., and Murua, J., "Consistent Structural Linearisation in Flexible Aircraft Dynamics with Large Rigid-Body Motion," *AIAA Journal*, Vol. 52, No. 3, January 2014, pp. 528–538, doi: 10.2514/1.J052316.

[53] Ide, H. and Ominsky, D., "Simulation of Static and Dynamic Aeroelastic Behavior of a Flexible Wing with Multiple Control Surfaces," *Collection of Technical Papers-AIAA/ASME/ASCE/AHS/ASC Structures, Structural Dynamics and Materials Conference, AIAA Paper 1990–1075, Long Beach, CA, USA*, 1990, pp. 1582–1588, doi: 10.2514/6.1990-1075.

[54] Farhat, C., Pierson, K., and Degand, C., "Multidisciplinary Simulation of The Maneuvering of an Aircraft," *Engineering with Computers*, Vol. 17, 2001, pp. 16–27, doi: 10.1007/PL00007193.

[55] Heinrich, R., Kroll, N., Neumann, J., and Nagel, B., "Fluid-Structure Coupling for Aerodynamic Analysis and Design-A DLR Perspective," *AIAA Paper 2008-0561, 46th AIAA Aerospace Sciences Meeting and Exhibit, Reno, Nevada, USA*, January 2008, doi: 10.2514/6.2008-561.

[56] Wiart, L. and Carrier, G., "Accounting for Wing Flexibility in the Aerodynamic Calculation of Transport Aircraft Using Equivalent Beam Model," *13th AIAA/ISSMO Multidisciplinary Analysis Optimization Conference, AIAA Paper 2010–9135, Fort Worth, Texas*, 13-15 September 2010, doi: 10.2514/6.2010-9135.

[57] Song, P. S., Qiu, J. H., Ji, H. L., and Chen, N., "The Aerodynamic Characteristics Analysis of an Adaptive Wing with Flexible Trailing Edge Using CFD," *21st International Conference on Adaptive Structures and Technologies 2010*, October 2010, pp. 162–175.

[58] Raveh, D., "CFD-Based Gust Response Analysis of Free Elastic Aircraft," *Journal of Aeroelasticity and Structural Dynamics*, Vol. 2, No. 1, 2010, pp. 23–34, doi: 10.3293/asdj.2010.3.

[59] Raveh, D. E., "Gust-Response Analysis of Free Elastic Aircraft in the Transonic Flight Regime," *Journal of Aircraft*, Vol. 48, No. 4, 2011, pp. 1204–1211, doi: 10.2514/1.C031224.

[60] Guo, D., Xu, M., and Chen, S., "Numerical Simulation of Discrete Gust Response for a Free Flexible Aircraft," *Communications in Computer and Information Science*, Vol. 324, 2012, pp. 319–327, doi: $10.1007/978 - 3 - 642 - 34390 - 2_36$.

[61] Kenway, G. W., Kennedy, G. J., and Martins, J., "A Scalable Parallel Approach for High-Fidelity Aerostructural Analysis and Optimization," *53rd AIAA/ASME/ASCE/AHS/ASC Structures, Structural Dynamics and Materials Conference 2012, AIAA Paper 2012–1922, Honolulu, HI, USA*, April 2012, doi: 10.2514/6.2012-1922.

[62] Romanelli, G., Castellani, M., Mantegazza, P., and Ricci, S., "Coupled CSD/CFD Non-Linear Aeroelastic Trim of Free-Flying Flexible Aircraft," *53rd AIAA/ASME/ASCE/AHS/ASC Structures, Structural Dynamics and Materials Conference 2012, AIAA Paper 2012–1562, Honolulu, HI, USA*, April 2012, doi: 10.2514/6.2012-1562.

[63] Sotoudeh, Z., Canfield, R. A., Patil, M. J., Liu, S., and Ricciardi, A. P., "A Hybrid Quasi-Steady CFD-inflow Approach for Gust Response Analysis of Highly Flexible Aircraft," *53rd AIAA/ASME/ASCE/AHS/ASC Structures, Structural Dynamics and Materials Conference 2012, AIAA Paper 2012–1717, Honolulu, HI, USA*, April 2012, doi: 10.2514/6.2012-1717.

[64] Hasselbring, J. and Jenaro, G., "Use of Linearised CFD for Unsteady Aerodynamics for Gust Loads," *International Forum on Aeroelasticity and Structural Dynamics, IFASD 2013*, Bristol, United Kingdom, June 2013.

[65] Ritter, M., "Nonlinear Numerical Flight Dynamics of Flexible Aircraft in the Time Domain by Coupling of CFD, Flight Mechanincs, and Structural Mechanics," *Notes on Numerical Fluid Mechanics and Multidisciplinary Design*, Vol. 121, 2013, pp. 339–347, doi: 10.1007/978-3-642-35680-3-41.

[66] Guo, D., Xu, M., and Chen, S. L., "CFD Based Simulation of Elastic Aircraft in Maneuvering Flight," *51st AIAA Aerospace Sciences Meeting including the New Horizons Forum and Aerospace Exposition 2013, AIAA Paper 2013-948, Grapevine, Texas, USA*, January 2013, doi: 10.2514/6.2013-948.

[67] Liu, W. G., Mei, R., Zhang, W. W., and Ye, Z. Y., "Efficient Numerical Simulation Based on Computational Fluid Dynamics for the Dynamic Stability Analysis of Flexible Aircraft," *Advanced Engineering and Technology-Proceedings of the 2014 Anuual Congress on Advanced Engineering and Technology, CAET 2014*, April 2014, pp. 373–378, doi: 10.1201/b16699-61.

[68] El-Zobaidi, H. M. and Jaimoukhai, I., "Robust control and Model Reduction on Linear Parameter Varying Systems," *In 37th IEEE Conference on Decision and Control, Tampa, Florida, USA*, 1998.

[69] Zhou, K., Salomon, G., and Wu, E., "Balanced Realization and Model Reduction for Unstable Systems," *International Journal of Robust and Nonlinear Control*, Vol. 9, 1999, pp. 183–198.

[70] Lall, S., Marsden, J., and Glavaski, S., "Empirical Model Reduction of Controlled Nonlinear Systems," *Proceedings of the IFAC World Congress,International Federation of Automatic Control*, Vol. F, 1999, pp. 473–478.

[71] Guyan, R., "Reduction of Stiffness and Mass Matrices," *AIAA Journal*, Vol. 3, No. 2, 1965, pp. 380–380, doi: 10.2514/3.2874.

[72] Han, S. and Feeny, B., "Enhanced Proper Orthogonal Decomposition for the Modal Analysis of Homogeneous Structures," *Journal of Vibration and Control*, Vol. 8, No. 1, 2002, pp. 19–40, doi: 10.1177/1077546302008001518.

[73] Kerschen, G., Golinval, J. C., Vakakis, A., and Bergman, L., "The Method of Proper Orthogonal Decomposition for Dynamic Characterisation and Order Reduction of Mechanical Systems," *Nonlinear Dynamics*, Vol. 41, 2005, pp. 147–169, doi: 10.1007/s11071-005-2803-2.

[74] Lucia, D. J., Beran, P. S., and Silva, W. A., "Reduced-Order Modelling: New Approaches for Computational Physics," *Progress in Aerospace Sciences*, Vol. 40, No. 1–2, 2004, pp. 51–117, doi: 10.1016/j.paerosci.2003.12.001.

[75] Roy, C. J. and Zhenhau, N., "Component Mode Synthesis for Model Order Reduction of Nonclassically Damped Systems," *Journal of Guidance, Control, and Dynamics*, Vol. 12, No. 4, 1989, pp. 577–584.

[76] Galerkin, "Proper Orthogonal Decomposition Methods for a General Equation in Fluid Dynamics," *SIAM Journal of Numerical Analysis*, Vol. 40, 2002, pp. 492–515.

[77] Willcox, K. and Peraire, J., "Balanced Model Reduction via Proper Orthogonal Decomposition," *AIAA Journal*, Vol. 40, No. 11, Nov. 2002, pp. 2323–2330, doi: 10.1.1.144.7137.

[78] Aouf, N., Boulet, B., and Botez, R., "Model and Controller Reduction for Flexible Aircraft Preserving Robust Performance," *IEEE Transactions on Control Systems Technology*, Vol. 10, No. 2, 2 March 2002, pp. 229–237, doi: 10.1109/87.987068.

[79] Penzl, T., "Algorithms for Model Reduction of Large Dynamical Systems," *Linear Algebra and its Applications*, Vol. 415, No. 2-–3, 2006, pp. 322–343, doi: 10.1016/j.laa.2006.01.007.

[80] Feng, Z. and Soulaimani, A., "Reduced Order Modelling Based on POD Method for 3D Nonlinear Aeroelasticity," *Proceeding of the 18th IASTED International Conference Modelling and Simulation*, May 30-June 1, 2007, Montreal, Quebec, Canada.

[81] Beran, P., Pettit, C., and Millman, D., "Uncertainty Quantification of Limit Cycle Oscillations." *Journal of Computational Physics*, Vol. 217, 2006, pp. 217–247, doi: 10.1016/j.jcp.2006.03.038.

[82] Kim, T., Hong, M., Bhatia, K. G., and Sengupta, G., "Aeroelastic Model Reduction for Affordable Computational Fluid Dynamics-Based Flutter Analysis," *AIAA Journal*, Vol. 43, No. 12, December 2005, pp. 2487–2495, doi: 10.2514/1.11246.

[83] Woodgate, M. A. and Badcock, K. J., "Fast Prediction of Transonic Aeroelastic Stability and Limit Cycles," *AIAA Journal*, Vol. 45, No. 6, 2007, pp. 1370–1381, doi: 10.2514/1.25604.

[84] Badcock, K. J., Woodgate, M. A., Allan, M. R., and Beran, P. S., "Wing-Rock Limit Cycle Oscillation Prediction based on Computational Fluid Dynamics," *Journal of Aircraft*, Vol. 45, No. 3, 2008, pp. 954–961, doi: 10.2514/1.32812.

[85] Badcock, K. J. an Timme, S., Khodaparast, H., and Mottershead, J. E., "The Influence of Structural Parameter Variability on Aeroelastic LCO Amplitude," *In:Proceedings of the royal aeronautical society aerodynamics conference.*

[86] Badcock, K. J., Timme, S., Marques, S., Khodaparast, H., Prandina, M., Mottershead, J. E., Swift, A., Da Ronch, A., and Woodgate, M. A., "Transonic Aeroelastic Simulation for Instability Searches and Uncertainty Analy-

sis," *Progress in Aerospace Sciences*, Vol. 47, No. 5, 2011, pp. 392–423, doi: 10.1016/j.paerosci.2011.05.002.

[87] Amsallem, D. Farhat, C., "Interpolation Method for Adapting Reduced-Order Models and Application to Aeroelasticity," *AIAA Journal*, Vol. 46(7), 2008, pp. 1803–1813, doi: 10.2514/1.35374.

[88] Amsallem, D. and Farhat, C., "Stabilization of Projection-Based Reduced-Order Models," *International Journal for Numerical Methods in Engineering*, Vol. 91, No. 4, 2012, pp. 358–377, doi: 10.1002/nme.4274.

[89] Amsallem, D. and Hetmaniuk, U., "Error Estimates for Galerkin Reduced-Order Models of the Semi-Discrete Wave Equation," *ESAIM: Mathematical Modelling and Numerical Analysis*, Vol. 48, No. 1, January 2014, pp. 135–163, doi: http://dx.doi.org/10.1051/m2an/2013099.

[90] Amsallem, D., Cortial, J., Carlberg, K., and Farhat, C., "Toward Real-Time Computational-Fluid-Dynamics-Based Aeroelastic Computations Using a Database of Reduced-Order Information," *AIAA Journal*, Vol. 48, No. 9, 2010, pp. 2029–2037, doi: 10.2514/1.J050233.

[91] Huang, Y., Hu, D., and Liu, X., "Center Manifold Reduction For The Flutter of Airfoils with Gust Loading," *Journal of Fluids and Structures*, Vol. 30, 2012, pp. 133–140, doi: 10.1016/j.jfluidstructs.2012.02.009.

[92] Poussot-Vassal, C. and Roos, C., "Generation of a Reduced-Order MLPV/LFT Model from a set of Large-Scale MIMO LTI Flexible Aircraft Models," *Control Engineering Practice*, Vol. 20, September 2012, pp. 919–930.

[93] Sofrony, J., Moreno, C., Seiler, P., and Balas, G., "Close-Loop Stabilization of a Flexible Wing Aircraft," *IEEE 9th Latin American Robotics Symposium and IEEE Colombian Conference on Automatic Control, Pogota, Colombia*, 2011, pp. 1–6, doi: 10.1016/j.paerosci.2011.05.002.

[94] Wang, K., Wu, F., and Jiang, C. S., "Balanced Proper Orthogonal Decomposition and its Application on Order Reduction to Aeroelastic Models on Aircraft Wing," *Zhendong yu Chongji/Journal of Vibration and Shock*, Vol. 31, No. 9, 2012, pp. 69–72.

[95] Holm-Hansen, B., Atkinson, C., Beranek, J., Burnett, E. L., Nicolai, L., and Youssef, H., "Envelope Expansion of a Flexible Flying Wing by Active Flutter Suppression," *AUVSI's Unmanned Systems Conference*, Denver, Colorado.

[96] Wang, Y., Wynn, A., and Palacios, R., "Nonlinear Model Reduction for Aeroelastic Control of Flexible Aircraft Described by Large Finite-Element Models," *55th*

AIAA/ASME/AHS/ASC Structures, Structural Dynamics, and Materias Conference, AIAA Paper 2014–0842, National Harbor, MD, USA, 13-17 January 2014, doi: 10.2514/6.2014-0842.

[97] Simpson, R. S., Palacios, R., Hesse, H., and Goulart, P., "Predictive Control for Alleviation of Gust Loads on Very Flexible Aircraft," *55th AIAA/ASME/ASCE/AHS/ACS Structures, Structural Dynamics, and Materials Conference-Scitech Forum and Exposition 2014, AIAA Paper 2014–0843, National Harbor, MD, USA*, January 2014, doi: 10.2514/6.2014-0843.

[98] Da Ronch, A., Badcock, K. J., Wang, Y., Wynn, A., and Palacios, R. N., "Nonlinear Model Reduction for Flexible Aircraft Control Design," *AIAA Atmospheric Flight Mechanics Conference*, AIAA Paper 2012–4404, Minneapolis, MN, 13–16 August 2012, doi: 10.2514/6.2012-4404.

[99] Da Ronch, A., Tantaroudas, N. D., Timme, S., and Badcock, K. J., "Model Reduction for Linear and Nonlinear Gust Loads Analysis," *54th AIAA/ASME/ASCE/AHS/ASC Structures, Structural Dynamics, and Materials Conference*, AIAA Paper 2013–1492, Boston, MA, 08–11 April 2013, doi: 10.2514/6.2013-1492.

[100] Tantaroudas, N. D., Da Ronch, A., Gai, G., Badcock, K. J., and Palacios, R., "An Adaptive Control Approach using Nonlinear Reduced Order Models," *14th AIAA Aviation Technology, Integration, and Operations Conference*, AIAA Paper 2014–2590, Atlanta, Georgia, June 2014, doi: 10.2514/6.2014-2590.

[101] Papatheou, E., Tantaroudas, N. D., Da Ronch, A., Cooper, J. E., and Mottershead, J. E., "Active Control for Flutter Suppression: an Experimental Investigation," *International Forum on Aeroelasticity and Structural Dynamics*, IFASD Paper 2013–8D, Bristol, U.K., 24–27 June 2013.

[102] Da Ronch, A., Tantaroudas, N. D., and Badcock, K. J., "Reduction of Nonlinear Models for Control Applications," *Proceedings of the AIAA 54th Structures, Structural Dynamics and Materials Conference, AIAA Paper 2013–1491, Boston, MA, USA*, 08-11 April 2013, doi: 10.2514/6.2013-1491.

[103] Tantaroudas, N. D., Da Ronch, A., Badcock, K., and Palacios, R., "Model Order Reduction for Control Design of Flexible Free-Flying Aircraft," *AIAA Atmospheric Flight Mechanics Conference, AIAA Paper 2015–0240, Kissimme, Florida, USA*, January 2015, doi: 10.2514/6.2015-0240.

[104] Gregory, I. M., "Dynamic Inversion to Control Large Flexible Transport Aircraft," *AIAA Paper 98-4323*, 1998, doi: 10.2514/6.1998-4323.

[105] Gregory, I. M., "Modified Dynamic Inversion to Control Large Flexible Aircraft-Whats Going On?" *AIAA 99-3998*, 1999, doi: 10.2514/6.1999-3998.

[106] Gregory, I. M., "Stability Result for Dynamic Inversion Devised to Control Large Flexible Aircraft," *AIAA Paper 2001-4284*, AIAA Guidance, Navigation, and Control Conference and Exhibit, Montreal, Canada, 2001, doi: 10.2514/6.2001-4284.

[107] Strganac, T. W., Ko, J., Thompson, D. E., and Kurdila, A. J., "Identification and Control of Limit Cycle Oscillations in Aeroelastic Systems," *Journal of Guidance, Control, and Dynamics*, Vol. 23, No. 6, 2000, pp. 1127–1133, doi: 10.2514/2.4664.

[108] Huang, R., Hu, H., and Zhao, Y., "Designing Active Flutter Suppression for High-Dimensional Aeroelastic Systems Involving a Control Delay," *Journal of Fluids and Structures*, Vol. 34, No. 6, 2012, pp. 33–50, doi: 10.1016/j.jfluidstructs.2012.05.012.

[109] Yu, M. and Hu, H., "Flutter Control Based on Ultrasonic Motor for a Two-Dimensional Airfoil Section," *Journal of Fluids and Structures*, Vol. 28, 2012, pp. 89–102, doi: 10.1016/j.jfluidstructs.2011.08.015.

[110] Shearer, C. M. and Cesnik, C. S., "Trajectory Control for Very Flexible Aircraft," *Journal of Guidance, Control, and Dynamics*, Vol. 31, No. 2, March-April 2008, pp. 340–357.

[111] Van der Schaft, A. J., "L-gain Analysis of Nonlinear Systems and Nonlinear State Feedback H Infinity Control," *IEEE Transactions on Automatic Control*, Vol. 37, 1992, pp. 770–784, doi: 10.1109/9.256331.

[112] Goman, M., Sidoryuk, M., and Ustinov, A., "Control Law Design for Flexible Aircraft: Comparison of the H Infinity Based and Classical Methods," *AIAA Guidance, Navigation, and Control Conference 2005, San Francisco; CA; United States*, Vol. 6, 2005, pp. 4089–4109.

[113] Fradkov, A. and Andrievsky, B., "Passification-Based Robust Control Design," *Automatica*, Vol. 47, 12, December 2011, pp. 2743–2748, doi: 10.1016/j.automatica.2011.09.004.

[114] Schirrer, A., Westermayer, C., Hemedi, M., and Kozek, M., "Robust Convex Lateral Feedback Control Synthesis for a BWB Aircraft," *18th IFAC World Congress; Milano; Italy, August, 2011*, doi: 10.3182/20110828-6-IT-1002.01543.

[115] Schirrer, A., Westermayer, C., Hemedi, M., and M., K., "Robust H_∞ Control Design Parameter Optimization via Genetic Algorithm for Lateral Control of

BWB type Aircraft," *IFAC Workshop on Intelligent Control Systems, WICS2010; Sinaia; Romania*, pp. 57–63, doi: 10.3182/20100929-3-RO-4017.00011.

[116] Smain, D. and Brahim, B., "μ -Synthesis Controller Design GLA for the Longitudinal Flexible Aircraft," *ICCAIE 2010-2010 International Conference on Computer Applications and Industrial Electronics, Kuala Lumpur, Malaysia*, 5 December 2010, pp. 558–563, doi: 10.1109/ICCAIE.2010.5735143.

[117] Meng, W. J., Li, A. J., Tan, J., and Wang, C., "Design and Simulation of $\mathcal{H}_\infty$ Controller for Flexible Aircraft," *11th International Conference on Control, Automation, Robotics and Vision, ICARCV 2010, Singapore, Dec. 2010*, pp. 1900–1904, doi: 10.1109/ICARCV.2010.5707237.

[118] Cao, C. and Hovakimyan, N., "L_1 Adaptive Controller for nonlinear Systems in the Presence of Unmodelled Dynamics: Part II," *Proceedings of the American Control Conference, Seattle, WA*, pp. 4099–4104, doi: 10.1109/ACC.2008.4587135.

[119] Cao, C. and Hovakimyan, N., "Application of L_1 Adaptive Controller to Wing Rock," *In: Proceedings of AIAAA Guidance, Navigation and Control Conference, AIAA Paper 2006–6426*, Keystone, Colorado, USA, 2006, doi: 102514/6.2006-6426.

[120] Cao, C. and Hovakimyan, N., "L_1 Adaptive Output–Feedback Controller for Non–Strictly–Positive–Real Reference Systems: Missile Longitudinal Autopilot Design," *Journal of Guidance, Control, and Dynamics*, Vol. 32, No. 3, 2009, pp. 717–726, doi: 10.2514/4.140877.

[121] Keum, W. L. and Sahjendra, N. S., "L_1 Adaptive Control of a Nonlinear Aeroelastic System Despite Gust Load," *Journal of Vibration and Control*, Vol. 19, No. 12, 2013, pp. 1807–1821, doi: 10.1177/1077546312452315.

[122] Ponnusamy, S. and Guibe, J. B., "Adaptive Output Feedback Control of Aircraft Flexible Modes," *2nd International Conference on Communications Computing and Control Applications,CCCA 2012*, Marseille, France, 6 December, doi: 10.1109/CCCA.2012.6417915.

[123] Chowdhary, G., Johnson, E. R., Kimbrell, M. S., Chandramohan, R., and Calise, A., "Flight Test Results of Adaptive Controllers in Presence of Severe Structural Damage," *AIAA Guidance, Navigation and Control Conference, Toronto, Ontario, Canada*, August 2010, doi: 10.2514/6.2010-8010.

[124] Yucelen, T. and Calise, A. J., "Derivative–Free Model Reference Adaptive Control of a Generic Transport Model," *AIAA Guidance Navigation and Control Conference, AIAA Paper 2010–8402, Toronto, Ontario, Canada*, 2 August 2010 through 5 August 2010, doi: 10.2514/6.2010-8402.

[125] Yucelen, T. and Haddad, W. M., "A Robust Adaptive Control Architecture for Disturbance Rejection and Uncertainty Suppression with L_∞ Transient and Steady-State Performance Guarantees," *International Journal of Adaptive Control and Signal Processing*, Vol. 26, No. 11, 2012, pp. 1024–1055, doi: 10.1002/acs.2281.

[126] Gibson, T. E. and Annaswamy, A. M., "Modelling for Control of Very Flexible Aircraft," *AIAA Guidance, Navigation, and Control Conference*, 08-11 August 2011, Portland, Oregon, AIAA Paper 2011–6202.

[127] Kwon, W. and Han, S., "Receding Horizon Control:Model Predictive Control for State Models," *Springer, New York*, 2005.

[128] Giesseler, H. G., Kopf, M., Faulwasser, T., Varutti, P., and Findeisen, R., "Gust Load Alleviation Based on Model Predictive Control," *International Forum on Aeroelasticity and Structural Dynamics, IFASD*, June 2013, Bristol, UK.

[129] Haghighat, S., Liu, H. T., and Martins, J. R., "Model-Predictive Gust Load Alleviation Controller for a Highly Flexible Aircraft," *Journal of Guidance, Control, and Dynamics*, Vol. 35, No. 6, November-December 2012, pp. 1751–1766, doi: 10.2514/1.57013.

[130] Daochun Li, Shijun Guo, J. X., "Aeroelastic Dynamic Response and Control of an Airfoil Section with Control Surface Nonlinearities," *Journal of Sound and Vibration*, Vol. 329, No. 22, 2010, pp. 4756–4771, doi: 10.1016/j.jsv.2010.06.006.

[131] Hauser, J. Sastry, S. and Kokotovic, P., "Nonlinear Control via Approximate Input-Output Linearization:The Ball Beam Example," *IEEE Transactions on Automatic Control*, Vol. 37, No. 3, 1992, pp. 392–398, doi: 10.1109/9.119645.

[132] Commuri, S. and Lewis, F. L., "Stabilization of a Class of Nonlinear Systems with Ill-Defined Relative Degree," *Proceedings of the American Control Conference, Seattle, Washington*, Vol. 4, June 1995, pp. 2712–2716, doi: 10.1109/ACC.1995.532341.

[133] Chen, W. H. and Balance, D. J., "On a Switching Control Scheme for Nonlinear Systems with Ill-Defined Relative Degree," *Systems & Control Letter*, Vol. 47, No. 2, Apr. 2002, pp. 159–166.

[134] Parrilo, P., "Structured Semidefinite Programs and Semialgebraic Geometry Methods in Robustness and Optimization," *Ph.D thesis, California Institute of Technology*, 2000.

[135] Papachristodoulou, A. and Prajna, S., "A Tutorial on Sum of Squares Techniques for Systems Analysis," *American Control Conference*, Vol. 4, Jun. 8-10, 2005, pp. 2686–2700, doi: 10.1109/ACC.2005.1470374.

[136] Prajna, S., Papachristodoulou, A., and Wu, F., "Nonlinear Control Synthesis by Sum of Squares Optimization: A Lyapunov based Approach," *Asian Control Conference*, Vol. 1, Jul.2004, pp. 157–165.

[137] Zarvis-Wloszek, Z., Feeley, R., Tan, W., Sun, K., and Packard, A., "Some Controls Applications of Sum of Squares Programming," *IEEE Conference on Decision and Control*, Vol. 5, Dec. 2003, pp. 4676–4681, doi: 10.1.1.68.6396.

[138] De Oliveira, M., "Decomposition of a Polynomial as a Sum-of-Squares of Polynomials and the S-Procedure," *IEEE Conference on Decision and Control*, Dec. 12-15, 2005, pp. 1654–1659, doi: 10.1109/CDC.2005.1582396.

[139] Badcock, K. J. and Woodgate, M. A., "Bifurcation Prediction of Large-Order Aeroelastic Models," *AIAA Journal*, Vol. 48, No. 6, 2010, pp. 1037–1046, doi: 10.2514/1.40961.

[140] Hoblit, F. M., *Gust Loads on Aircraft: Concepts and Applications*, American Institute of Aeronautics and Astronautics, Reston, VA, USA, 1988, doi: 10.2514/4.861888.

[141] Parameswaran, V. and Baeder, J. D., "Indicial Aerodynamics in Compressible Flow - Direct Computational Fluid Dynamic Calculations," *Journal of Aircraft*, Vol. 34, No. 1, 1997, pp. 131–133.

[142] Tantaroudas, N. and Da Ronch, A., *Nonlinear Reduced Order Aeroservoelastic Analysis of Very Flexible Aircraft*, Book chapter in Unmanned Vehicles, John Wiley & Sons, 2015.

[143] Jones, R. T., "The Unsteady Lift of a Wing of Finite Aspect Ratio," Tech. Rep. NACA–681, National Advisory Committee for Aeronautics, 1940.

[144] Da Ronch, A., Tantaroudas, N. D., Jiffri, S., and Mottershead, J. E., "A Nonlinear Controller for Flutter Suppression: from Simulation to Wind Tunnel Testing," *AIAA SciTech 2014, 55th AIAA/ASME/ASCE/AHS/SC Structures, Structural Dynamics, and Materials Conference*, AIAA Paper 2014–0345, National Harbor, MD, 11–15 January 2014, doi:10.2514/6.2014–0345.

[145] Etkin, B., "Turbulent Wind and Its Effect on Flight," *Journal of Aircraft*, Vol. 18, No. 5, 1981, pp. 327–345, doi: 10.2514/3.57498.

[146] Hoblit, F. M., *Gust Loads on Aircraft: Concepts and Applications*, American Institute of Aeronautics & Astronautics, 1988, doi. 10.2514/4.861888.

[147] Houbolt, J. C., "Atmospheric Turbulence," *AIAA Journal*, Vol. 11, No. 4, 1973, pp. 421–437, doi: 10.2514/3.50485.

[148] Moorhouse, D. J. and Woodcock, R. J., "Background Information and User Guide for MIL–F–8785C, Military Specification – Flying Qualities of Piloted Airplanes," Tech. rep., DTIC Document, 1982.

[149] Meirovitch, L., *Introduction to dynamics and control*, Wiley, 1985.

[150] Gianfrancesco, M., *Functional Modelling and Design of Energy Harvesters for Slender wing Structures*, Master's thesis, Politecnico di Torino, Italy & University of Southampton, U.K., 2014.

[151] Zhou, K. and Doyle, J. C., *Essentials of Robust Control*, New York:Prentice Hall, 1998.

[152] Ioannou, P. A. and Sun, J., *Robust Adaptive Control*, Prentice- Hall, 1996.

[153] Barkana, I., "Gain Conditions and Convergence of Simple Adaptive Controls," *International Journal of Adaptive Control and Signal Processing*, Vol. 19, 2005, pp. 13–40, doi: 10.2514/6.2013-1485.

[154] Barkana, I., "Simple Adaptive Control - A Stable Direct Model Reference Adaptive Control Methodology - Brief Survey," *International Journal of Adaptive Control and Signal Processing*, Vol. 28, No. 7-8, July-August 2013, pp. 567–603, doi: 10.1002/acs.2411.

[155] Torres, S. and Mehiel, E., "Nonlinear Direct Adaptive Control and Disturbance Rejection for Spacecraft," *Proceedings of the AIAA Guidance, Navigation and Control Conference*, AIAA Paper 2006-6038, Keystone, Colorado, USA, 2006, doi: 10.2514/6.2006-6038.

[156] Ogata, K., *Modern Control Engineering*, 2010.

[157] Tobak, M., "On the Use of the Indicial Function Concept in the Analysis of the Unsteady Motions of Wing-Tail Combinations," *NACA Report 1188*, 1954.

[158] Kennett, D. J., Timme, S., Angulo, J., and Badcock, K. J., "An Implicit Meshless Method for Application in Computational Fluid Dynamics," *International Journal for Numerical Methods in Fluids*, Vol. 71, No. 8, 2012, pp. 1007–1028, doi: 10.1002/fld.3698.

[159] Badcock, K. J., Richards, B. E., and Woodgate, M. A., "Elements of Computational Fluids Dynamics on Block Structrured Grids using Implicit Solvers," *Progress in Aerospace Sciences*, Vol. 36, No. 5–6, 2000, pp. 351–392, doi:10.1016/S0376-0421(00)00005-1.

[160] Badcock, K. J., Timme, S., Marques, S., Khodaparast, H., Prandina, M., Mottershead, J. E., Swift, A., Da Ronch, A., and Woodgate, M. A., "Transonic Aeroelastic Simulation for Instability Searches and Uncertainty Analysis," *Progress in Aerospace Sciences*, Vol. 47, No. 5, 2011, pp. 392–423, doi: 10.1016/j.paerosci.2011.05.002.

[161] Lee, B. K., Gong, L., and Wong, Y. S., "Analysis and Computation of Nonlinear Dynamic Response of a Two-Degree-of-Freedom System and Its Application in Aeroelasticity," *Journal of Fluids and Structures*, Vol. 11, No. 3, 1997, pp. 225–246, doi: 10.1006/jfls.1996.0075.

[162] Meirovitch, L., *Dynamics and Control of Structures*, Wiley, New York, 1989, pp. 93–98.

[163] Pettit, C. L. and Beran, P. S., "Effects of Parametric Uncertainty on Airfoil Limit Cycle Oscillation," *Journal of Aircraft*, Vol. 40, No. 5, 2003, pp. 1004–1006, doi: 10.2514/2.6889.

[164] Badcock, K. J., Woodgate, M. A., and Richards, B. E., "Hopf Bifurcation Calculations for a Symmetric Airfoil in Transonic Flow," *AIAA Journal*, Vol. 42, No. 5, 2004, pp. 883–892, doi: 10.2514/1.9584.

[165] "Inviscid Flowfield Methods," Tech. Rep. Fluid Dynamics Panel Working Group, AGARD AR 211, 1985.

[166] Abramowitz, M. and Stegun, I. A., *Handbook of Mathematical Functions with Formulas, Graphs, and Mathematical Tables, 9th Printing*, Dover, New York, 1972, pag. 11.

[167] Géradin, M. and Cardona, A., *Flexible Multibody Dynamics: A Finite Element Approach*, John Wiley & Sons Ltd, Chichester, UK, 2001.

[168] Chianetta, S., "Limit Cycle Oscillations on an Aerofoil Test Rig," Tech. Rep. School of Engineering, University of Liverpool, U.K., 2013.

[169] Weissenburger, J. T. and Zimmerman, N. H., "Prediction of Flutter Onset Speed Based on Flight Testing at Subcritical Speeds," *Journal of Aircraft*, Vol. 1, No. 4, 1964, pp. 190–202, doi: 10.2514/3.43581.

[170] Kautsky, J. Nichols, N. K. and Van Dooren, P., "Robust Pole Assignment in Linear State Feedback," *International Journal of Control*, Vol. 41, 1985, pp. 1129–1155.

[171] Isidori, A., "Nonlinear Control Systems," *Berlin Heidelberg New York:*, Springer, 1995.

[172] Khalil, H. K., "Nonlinear Systems," *3rd ed.*, Prentice Hall, 2002.

[173] Fichera, S., Jiffri, S., Wei, X., Da Ronch, A., Tantaroudas, N. D., and Mottershead, J. E., "Experimental and Numerical Study of Nonlinear Dynamic Behaviour of an Aerofoil," ISMA 2014 conference on Noise and Vibration Engineering, Leuven, Belgium, Sept. 2014.

[174] Alighanbari, H. and Price, S. J., "The Post-Hopf-Bifurcation Response of an Airfoil in Incompressible Two-Dimensional Flow," *Nonlinear Dynamics*, Vol. 10, No. 4, 1996, pp. 381–400, doi: 10.1007/BF00045483.

[175] Irani, S., Sarrafzadeh, H., and Amoozgar, M. R., "Bifurcation of a 3-DOF Airfoil with Cubic Structural Nonlinearity," *Chinese Journal of Aeronautics*, Vol. 24, No. 3, 2011, pp. 265–278, doi: 10.1016/S1000-9361(11)60032-0.

[176] Wang, Y., Wynn, A., and Palacios, R., "Robust Aeroelastic Control of Very Flexible Wings using Intrisic Models," *54th AIAA/ASME/ASCE/AHS/ASC Structures, Structural Dynamics, and Materials Conference, AIAA Paper 2013–1485, Boston, Massachusetts, USA*, 08-11 Apr. 2013, doi: 10.2514/6.2013-1485.

[177] McCracken, A. J., Kennett, D. J., Badcock, K. J., and Da Ronch, A., "Assessment of Tabular Models using CFD," *AIAA Atmospheric Flight Mechanics Conference*, AIAA Paper 2013–4978, Boston, MA, 19–22 August 2013, doi: 10.2514/6.2013-4978.

[178] Smith, M., Patil, M., and Hodges, D., "CFD Based Analysis of Nonlinear Aeroelastic Behavior of High–Aspect Ratio Wings," *In 42nd AIAA/ASME/ASCE/AHS/ASC Structures, Structural Dynamics, and Materials Conference,*, April 2011, Anaheim, CA, USA, doi: 10.2514/6.2001-1582.

[179] Peters, D. A. and Johnson, M. J., "Finite-State Airloads for Deformable Airfoils on Fixed and Rotating Wings," *Aeroelasticity and Fluid/Structure Interaction, American Society of Mechanical Engineers, New York*, Vol. 44, Nov. 1994, pp. 1–28.

[180] Da Ronch, A., McCracken, A. J., Tantaroudas, N. D., Badcock, K. J., Hesse, H., and Palacios, R., "Assessing the Impact of Aerodynamic Modelling on Manoeuvring Aircraft," *AIAA SciTech 2014, AIAA Atmospheric Flight Mechanics Conference*, AIAA Paper 2014–0732, National Harbor, MD, 11–15 January 2014, doi:10.2514/6.2014–0732.

[181] Gai, G., "Gust Load Alleviation Exploiting Structural Nonlinearity," *First Year Progress Report University of Liverpool*, 2013.

Appendix A

Appendix

A.1 Control Application with the ROM

The typical equations of the ROM have been given in section 2.2 and here are re–written as

$$\dot{\boldsymbol{z}} = \mathrm{Diag}\left(\lambda_i\right) \boldsymbol{z} + \boldsymbol{B}_{ru1}\, \boldsymbol{u}_c + \boldsymbol{B}_{ru2}\, \dot{\boldsymbol{u}}_{c1} + \boldsymbol{B}_{ru3}\, \ddot{\boldsymbol{u}}_{c2} + \boldsymbol{B}_{rd}\, \boldsymbol{u}_d + \boldsymbol{f}_{nl}\left(\boldsymbol{w}\right) \tag{A.1}$$

where $\boldsymbol{f}_{nl}\left(\boldsymbol{w}\right)$ contains the nonlinear terms of the reduced model. The matrix $\mathrm{Diag}\left(\lambda_i\right) = \boldsymbol{\Lambda}$ is diagonal and contains the eigenvalues of the coupled reduced system , and $\boldsymbol{B}_{ru1}$, $\boldsymbol{B}_{ru2}$, $\boldsymbol{B}_{ru3}$ are the control derivatives corresponding to the flap rotation , angular velocity and angular acceleration of the control surfaces. As this point, the control design requires splitting of the complex states into their real and imaginary parts for the derivation of a linear controller as follows

$$\boldsymbol{x} = \begin{Bmatrix} \mathrm{Re}\left(\boldsymbol{z}\right) \\ \mathrm{Im}\left(\boldsymbol{z}\right) \end{Bmatrix}, \qquad \boldsymbol{B}_c = \begin{Bmatrix} \mathrm{Re}\left(\boldsymbol{B}_{ru1}\right) \\ \mathrm{Im}\left(\boldsymbol{B}_{ru1}\right) \end{Bmatrix}, \qquad \boldsymbol{B}_{c1} = \begin{Bmatrix} \mathrm{Re}\left(\boldsymbol{B}_{ru2}\right) \\ \mathrm{Im}\left(\boldsymbol{B}_{ru2}\right) \end{Bmatrix}, \tag{A.2}$$

$$\boldsymbol{B}_{c2} = \begin{Bmatrix} \mathrm{Re}\left(\boldsymbol{B}_{ru3}\right) \\ \mathrm{Im}\left(\boldsymbol{B}_{ru3}\right) \end{Bmatrix}, \qquad \boldsymbol{B}_g = \begin{Bmatrix} \mathrm{Re}\left(\boldsymbol{B}_{rd}\right) \\ \mathrm{Im}\left(\boldsymbol{B}_{rd}\right) \end{Bmatrix}, \qquad \boldsymbol{F}_{NR} = \begin{Bmatrix} \mathrm{Re}\left(\boldsymbol{f}_{nl}\right) \\ \mathrm{Im}\left(\boldsymbol{f}_{nl}\right) \end{Bmatrix} \tag{A.3}$$

Thus, the complete set of equations suitable for the control problem design become

$$\dot{\boldsymbol{x}}\left(t\right) = \boldsymbol{A}\, \boldsymbol{x}\left(t\right) + \boldsymbol{B}_c\, \boldsymbol{u}_c\left(t\right) + \boldsymbol{B}_{c1}\, \dot{\boldsymbol{u}}_c\left(t\right) + \boldsymbol{B}_{c2}\, \ddot{\boldsymbol{u}}_c\left(t\right) + \boldsymbol{B}_g\, \boldsymbol{u}_d\left(t\right) + \boldsymbol{F}_{NR}\left(\boldsymbol{x}\right) \tag{A.4}$$

where the matrices are expanded in the same way

$$\boldsymbol{A} = \begin{bmatrix} \mathrm{Re}\left(\boldsymbol{\Lambda}\right) & -\mathrm{Im}\left(\boldsymbol{\Lambda}\right) \\ \mathrm{Im}\left(\boldsymbol{\Lambda}\right) & \mathrm{Re}\left(\boldsymbol{\Lambda}\right) \end{bmatrix} \tag{A.5}$$

The last equation is used to formulate the control problems in a state–space representation. The system is linear in the output and can be expressed as a linear combination

of the eigenvectors as follows

$$\Delta \boldsymbol{w} \;=\; \boldsymbol{\Phi}\, \boldsymbol{z} \;+\; \bar{\boldsymbol{\Phi}}\, \bar{\boldsymbol{z}} \tag{A.6}$$

It is easy to show that if the vector z is split to real and imaginary parts then the output equation is written

$$\Delta \boldsymbol{w} \;=\; \boldsymbol{y} \;=\; \begin{bmatrix} 2\mathrm{Re}\,(\boldsymbol{\Phi}) & -2\mathrm{Im}\,(\boldsymbol{\Phi}) \end{bmatrix} \begin{Bmatrix} \mathrm{Re}\,(\boldsymbol{z}) \\ \mathrm{Im}\,(\boldsymbol{z}) \end{Bmatrix} \tag{A.7}$$

which is the common form of $\boldsymbol{y} = \boldsymbol{C}\boldsymbol{x}$

For the application of the nonlinear adaptive controller a transformation of the control gains based on the partioned state vector to derive gains that multiply physical degrees–of–freedom needs to be performed. For that purpose, the eigenvectors can be used.

Without loss of generality, a model reduction performed by retaining n modes, and taking into account the partitioned state of Eq. (A.2), yields a controller of the form

$$\boldsymbol{u} = -\boldsymbol{k}_{1r}\boldsymbol{x}_{1r} - \boldsymbol{K}_{2r}\boldsymbol{x}_{2r} -, \ldots, -\boldsymbol{K}_{n}\boldsymbol{x}_{nr} - \boldsymbol{K}_{1i}\boldsymbol{x}_{1i} - \boldsymbol{K}_{2i}\boldsymbol{x}_{2i} -, \ldots, -\boldsymbol{K}_{ni}\boldsymbol{x}_{ni}$$

where $\boldsymbol{x}_{ij}$ represents the partitioned reduced state of Eq. (A.2) and r, i denote the real and the imaginary part, respectively. The objective is to find an equivalent control law of the form

$$\boldsymbol{u}' = \boldsymbol{K}'\boldsymbol{y} \tag{A.8}$$

where $\boldsymbol{u}' = \boldsymbol{u}$. By using the output Equation (A.7) this is re–written

$$\boldsymbol{u}' = \boldsymbol{K}'\boldsymbol{C}\boldsymbol{x} \tag{A.9}$$

By simply satisfying the equality of $\boldsymbol{u} = \boldsymbol{u}'$, one needs to solve a linear system to get the corresponding physical control gains such as

$$\boldsymbol{K}' = -\boldsymbol{K}\boldsymbol{C}^{-1} \tag{A.10}$$

This can be solved in real time as a small number of eigenvectors is used related to the order of the reduced–order model.

A.2 Pitch–Plunge Aerofoil with Massless Trailing–Edge Flap

The coefficients of the coupled aeroelastic model that is used in this work are detailed below. The four coefficients determining the dynamics of the pitch and plunge degrees–of–freedom are formulated as

$$p_1 = \frac{c_0}{(d_0\,c_1 - c_0\,d_1)}, \qquad p_2 = \frac{-d_0}{(d_0\,c_1 - c_0\,d_1)}$$
$$p_3 = \frac{-c_1}{(d_0\,c_1 - c_0\,d_1)}, \qquad p_4 = \frac{d_1}{(d_0\,c_1 - c_0\,d_1)}$$

The nonlinear dependency of the coefficients $H(\boldsymbol{x})$ and $P(\boldsymbol{x})$ on the state vector is attributed to the structural model. For a polynomial form, as assumed in this work, the term $H(\boldsymbol{x})$ is

$$\begin{aligned} H(\boldsymbol{x}) = {} & d_2\,x_2 + d_3\,x_1 + d_4\,x_1^3 + d_{41}\,x_1^5 + d_5\,x_4 + d_6\,x_3 + d_7 x_5 + \\ & d_8\,x_6 + d_9\,x_7 + d_{10}\,x_8 + d_{11}\,x_9 + d_{12}\,x_{10} + d_{13}\,x_{11} + d_{14}\,x_{14} - g^f \end{aligned}$$

and $P(\boldsymbol{x})$ is

$$\begin{aligned} P(\boldsymbol{x}) = {} & c_2\,x_4 + c_3\,x_2 + c_4\,x_3 + c_5\,x_3^3 + c_{51}\,x_3^5 + c_6\,x_1 + c_7\,x_5 + \\ & c_8\,x_6 + c_9\,x_7 + c_{10}\,x_8 + c_{11}\,x_9 + c_{12}\,x_{10} + c_{13}\,x_{13} + c_{14}\,x_{14} - f^f \end{aligned}$$

The calculation of the coefficients appearing in the above relations is done using the few aeroelastic parameters of the aerofoil problem, listed in Table 4.2. The additional coefficients are

$$c_0 = 1 + \frac{1}{\mu}, \qquad c_1 = x_\alpha - \frac{a_h}{\mu}, \qquad c_2 = \left(2\,\zeta_\xi\,\frac{\bar{\omega}}{U^*} + \frac{2}{\mu}\,(1 - \Psi_1 - \Psi_2)\right)$$
$$c_3 = \left(\frac{1}{\mu} + \frac{2}{\mu}\,(1/2 - a_h)\,(1 - \Psi_1 - \Psi_2)\right), \qquad c_4 = \left(\frac{\bar{\omega}}{U^*}\right)^2 + \frac{2}{\mu}\,(\varepsilon_1\,\Psi_1 + \varepsilon_2\,\Psi_2)$$
$$c_5 = \left(\frac{\bar{\omega}}{U^*}\right)^2 \beta_\xi, \qquad c_{51} = \left(\frac{\bar{\omega}}{U^*}\right)^2 \beta_{\xi_5}$$
$$c_6 = \frac{2}{\mu}\Big((1 - \Psi_1 - \Psi_2) + (1/2 - a_h)\,(\varepsilon_1\,\Psi_1 + \varepsilon_2\,\Psi_2)\Big), \; c_7 = \frac{2}{\mu}\,\varepsilon_1\,\Psi_1\,(1 - \varepsilon_1\,(1/2 - a_h))$$
$$c_8 = \frac{2}{\mu}\,\varepsilon_2\,\Psi_2\,(1 - \varepsilon_2\,(1/2 - a_h)), \qquad c_9 = \left(-\frac{2}{\mu}\,\varepsilon_1^2\,\Psi_1\right), \qquad c_{10} = \left(-\frac{2}{\mu}\,\varepsilon_2^2\,\Psi_2\right)$$
$$c_{11} = \frac{1}{\pi\,\mu}\,\left(\varepsilon_1\,\Psi_1\,2\,T_{10} - \varepsilon_1^2\,\Psi_1\,T_{11}\right), \qquad c_{12} = \frac{1}{\pi\,\mu}\,\left(\varepsilon_2\,\Psi_2\,2\,T_{10} - \varepsilon_2^2\,\Psi_2\,T_{11}\right)$$
$$c_{13} = \frac{2}{\mu\,U}\,\varepsilon_3\,\Psi_3, \qquad c_{14} = \frac{2}{\mu\,U}\,\varepsilon_4\,\Psi_4$$

and

$$
\begin{aligned}
d_0 &= \left(\frac{x_a}{r_a^2} - \frac{a_h}{\mu\, r_a^2}\right), \qquad d_1 = \left(1 + \frac{a_h^2}{\mu\, r_a^2} + \frac{1}{8\,\mu\, r_a^2}\right) \\
d_2 &= \left(2\,\frac{\zeta_\alpha}{U^*} - \frac{1}{2\,\mu\, r_a^2}\left(\left(1 + 2\,a_h\right)\left(1 - 2\,a_h\right)\left(1 - \Psi_1 - \Psi_2\right) - \left(1 - 2\,a_h\right)\right)\right) \\
d_3 &= \left(\frac{1}{U^*} - \frac{1 + 2\,a_h}{\mu\, r_a^2}\left(\left(1 - \Psi_1 - \Psi_2\right) + \left(1/2 - a_h\right)\left(\varepsilon_1\,\Psi_1 + \varepsilon_2\,\Psi_2\right)\right)\right) \\
d_4 &= \frac{\beta_\alpha}{U^{*2}}, \qquad d_{41} = \frac{\beta_{\alpha_5}}{U^{*2}} \\
d_5 &= \left(-\frac{2}{\mu\, r_a^2}\left(1/2 + a_h\right)\left(1 - \Psi_1 - \Psi_2\right)\right) \\
d_6 &= \left(-\frac{1}{\mu\, r_a^2}\left(1 + 2\,a_h\right)\left(\varepsilon_1\,\Psi_1 + \varepsilon_2\,\Psi_2\right)\right), \qquad d_7 = \left(-\frac{1 + 2\,a_h}{\mu\, r_a^2}\,\varepsilon_1\,\Psi_1\left(1 - \varepsilon_1\left(1/2 - a_h\right)\right)\right) \\
d_8 &= \left(-\frac{1 + 2\,a_h}{\mu\, r_a^2}\,\varepsilon_2\,\Psi_2\left(1 - \varepsilon_2\left(1/2 - a_h\right)\right)\right), \\
d_9 &= \left(\frac{1 + 2\,a_h}{\mu\, r_a^2}\,\varepsilon_1^2\,\Psi_1\right), \qquad d_{10} = \left(\frac{1 + 2\,a_h}{\mu\, r_a^2}\,\varepsilon_2^2\,\Psi_2\right) \\
d_{11} &= -\frac{2}{\pi\,\mu\, r_a^2}\left(\left(a_h + \frac{1}{2}\right)\left(T_{10}\,\varepsilon_1\,\Psi_1 - \frac{T_{11}}{2}\,\varepsilon_1^2\,\Psi_1\right)\right), \\
d_{12} &= -\frac{2}{\pi\,\mu\, r_a^2}\left(\left(a_h + \frac{1}{2}\right)\left(T_{10}\,\varepsilon_2\,\Psi_2 - \frac{T_{11}}{2}\,\varepsilon_2^2\,\Psi_2\right)\right) \\
d_{13} &= -\frac{\left(1 + 2\,a_h\right)}{\mu\, r_a^2\, U}\,\varepsilon_3\,\Psi_3, \qquad d_{14} = -\frac{\left(1 + 2\,a_h\right)}{\mu\, r_a^2\, U}\,\varepsilon_4\,\Psi_4
\end{aligned}
$$

The terms f^f and g^f depend on the control input through the trailing–edge flap rotation, angular velocity, and acceleration

$$
\begin{aligned}
f^f\left(\tau\right) &= -\frac{1}{\pi\mu}\left(\delta\, c_\delta + \delta'\, c_{\delta'} + \delta''\, c_{\delta''}\right) \\
g^f\left(\tau\right) &= \frac{2}{\pi\,\mu\, r_\alpha^2}\left(\delta\, d_\delta + \delta'\, d_{\delta'} + \delta''\, d_{\delta''}\right)
\end{aligned}
$$

Note that the time derivatives are with respect to the nondimensional time. The constants are

$$
\begin{aligned}
c_\delta &= \left(2\,T_{10}\left(1 - \Psi_1 - \Psi_2\right) + T_{11}\left(\varepsilon_1\,\Psi_1 + \varepsilon_2\,\Psi_2\right)\right) \\
c_{\delta'} &= \left(-\,T_4 + T_{11}\left(1 - \Psi_1 - \Psi_2\right)\right) \\
c_{\delta''} &= \left(-\,T_1\right) \\
d_\delta &= \left(-\left(T_4 + T_{10}\right) + \left(a_h + \frac{1}{2}\right)\left(T_{10}\left(1 - \Psi_1 - \Psi_2\right) + \frac{T_{11}}{2}\left(\varepsilon_1\,\Psi_1 + \varepsilon_2\,\Psi_2\right)\right)\right) \\
d_{\delta'} &= \left(-\left(T_1 - T_8 - \left(c - a_h\right)T_4 + \frac{1}{2}\,T_{11}\right) + \left(a_h + \frac{1}{2}\right)\frac{T_{11}}{2}\left(1 - \Psi_1 - \Psi_2\right)\right) \\
d_{\delta''} &= \left(T_7 + \left(c - a_h\right)T_1\right)
\end{aligned}
$$

Finally, the constants T_1, T_4, T_7, T_8, T_{10}, and T_{11} are all geometric terms, which depend only on the size of the flap relative to the aerofoil chord, and for a coordinate system located at the midchord are expressed as in Theodorsen [22].

$$
\begin{aligned}
T_1 &= -\frac{1}{3}\sqrt{1-c^2}\left(2+c^2\right) + c\arccos(c) \\
T_4 &= -\arccos(c) + c\sqrt{1-c^2} \\
T_7 &= -\left(\frac{1}{8}+c^2\right)\arccos(c) + \frac{1}{8}c\sqrt{1-c^2}\left(7+2c^2\right) \\
T_8 &= -\frac{1}{3}\sqrt{1-c^2}\left(2c^2+1\right) + c\arccos(c) \\
T_{10} &= \sqrt{1-c^2} + \arccos(c) \\
T_{11} &= \arccos(c)\,(1-2c) + \sqrt{1-c^2}\,(2-c)
\end{aligned}
$$

A.3 Feedback Linearisation for the Wind–Tunnel Model

In the work presented for the wind–tunnel model, the gust disturbance is considered null. This is done for simplification of the nonlinear coupled equations of motion and it is a valid assumption, as no gust disturbance affects the dynamics of the wind–tunnel. The trailing–edge flap rotation, δ, is the control input to the system. The nonlinear state–space form of Eq. (3.8) is restated as

$$\boldsymbol{x}' = \boldsymbol{f}(\boldsymbol{x}) + \boldsymbol{g}u, \qquad \boldsymbol{x}^T = \{x_1 \quad x_2 \quad \dots \quad x_{11} \quad x_{12}\} \tag{A.11}$$

where

$$\boldsymbol{f}(\boldsymbol{x}) = \left\{ \begin{array}{c} x_2 \\ \left(\begin{array}{c} \lambda_1 x_1 + \lambda_2 x_2 + \lambda_3 x_3 + \lambda_4 x_4 + \lambda_5 x_5 + \lambda_6 x_6 \\ + \lambda_7 x_7 + \lambda_8 x_8 + \lambda_9 x_9 + \lambda_{10} x_{10} + \lambda_{11} x_{11} + \lambda_{12} x_{12} + \lambda_{1,3} x_1^3 \\ + \lambda_{3,3} x_3^3 + \lambda_{1,5} x_1^5 + \lambda_{3,5} x_3^5 + \lambda_{\delta'} \delta' + \lambda_{\delta''} \delta'' \end{array} \right) \\ x_4 \\ \left(\begin{array}{c} \gamma_1 x_1 + \gamma_2 x_2 + \gamma_3 x_3 + \gamma_4 x_4 + \gamma_5 x_5 + \gamma_6 x_6 \\ + \gamma_7 x_7 + \gamma_8 x_8 + \gamma_9 x_9 + \gamma_{10} x_{10} + \lambda_{11} x_{11} + \lambda_{12} x_{12} + \gamma_{1,3} x_1^3 \\ + \gamma_{3,3} x_3^3 + \gamma_{1,5} x_1^5 + \gamma_{3,5} x_3^5 + \gamma_{\delta'} \delta' + \gamma_{\delta''} \delta'' \end{array} \right) \\ x_1 - \epsilon_1 x_5 \\ x_1 - \epsilon_2 x_6 \\ x_3 - \epsilon_1 x_7 \\ x_3 - \epsilon_2 x_8 \\ -\epsilon_1 x_9 \\ -\epsilon_2 x_{10} \\ -\epsilon_3 x_{11} \\ -\epsilon_4 x_{12} \end{array} \right\}$$

$$\boldsymbol{g} = \left\{ \begin{array}{c} 0 \\ \lambda_\delta \\ 0 \\ \gamma_\delta \\ 0 \\ 0 \\ 0 \\ 0 \\ 1 \\ 1 \\ 0 \\ 0 \end{array} \right\} \qquad u = \delta \tag{A.12}$$

Note that these equations treat δ, the flap angle, as the only input to the system, whereas its time–derivatives δ', δ'' are treated as time–varying quantities which are part of the system; they are neither inputs nor state variables. δ', δ'' may be computed at each time step using a backward Euler finite difference method, using the values of δ for the present and previous time instants. The various λ, γ terms arise from the linear combinations shown in rows 2 and 4 in Eq. (A.12)

A.3.1 Pitch Output Linearisation

Let us consider input–output linearisation of the above model. The present model consists of a single input, and therefore a single output is also chosen. Choosing the pitch degree–of–freedom as an output,

$$z_1 \;=\; y_\alpha \;=\; x_1 \tag{A.13}$$

Note that this output also forms the first co–ordinate z_1 in the linear domain. Following the standard input–output linearisation procedure, the above expression is repeatedly differentiated until the input term appears, whilst substituting from Eq. (A.12) at each stage.

$$z_2 \;=\; \dot{z}_1 \;=\; \dot{y}_\alpha \;=\; \dot{x}_1 \;=\; x_2 \tag{A.14}$$

Differentiation one more time yields,

$$\dot{z}_2 = \ddot{y}_\alpha = \dot{x_2} = \begin{pmatrix} \lambda_1 x_1 + \lambda_2 x_2 + \lambda_3 x_3 + \lambda_4 x_4 + \lambda_5 x_5 + \lambda_6 x_6 \\ +\lambda_7 x_7 + \lambda_8 x_8 + \lambda_9 x_9 + \lambda_{10} x_{10} + \lambda_{11} x_{11} + \lambda_{12} x_{12} + \lambda_{1,3} x_1^3 \\ +\lambda_{3,3} x_3^3 + \lambda_{1,5} x_1^5 + \lambda_{3,5} x_3^5 + \lambda_{\delta'} \delta' + \lambda_{\delta''} \delta'' \end{pmatrix} + \lambda_\delta u \tag{A.15}$$

Denoting the above equation concisely as

$$\dot{z}_2 \;=\; \ddot{y}_\alpha \;=\; \dot{x}_2 \;=\; f_2(\boldsymbol{x}) \;+\; \lambda_\delta u \tag{A.16}$$

One may express the system in linear co–ordinates as

$$\left\{ \begin{array}{c} \dot{z}_1 \\ \dot{z}_2 \end{array} \right\} = \left[\begin{array}{cc} 0 & 1 \\ 0 & 0 \end{array} \right] \left\{ \begin{array}{c} z_1 \\ z_2 \end{array} \right\} + \left\{ \begin{array}{c} 0 \\ 1 \end{array} \right\} \nu_\alpha \tag{A.17}$$

One may now compute the actual, nonlinear input as

$$u \;=\; \frac{(\nu_\alpha - f_2(\boldsymbol{x}))}{\lambda_\delta} \tag{A.18}$$

The artificial input ν_α can be used to design a controller to achieve pole–placement, which is the objective in the present work. In this case, ν_α will take the form

$$\nu_\alpha \;=\; -g_1 z_1 \;-\; g_2 z_2 \tag{A.19}$$

where g_1, g_2 are appropriately chosen controller gains. The actual input u will then implement this pole placement, while simultaneously eliminating the nonlinearity.

It is evident from Eq. (A.17) that we have a linearised sub–system of dimension 2. Since the dimension of the full system is 12 , there remains an un–linearised portion known as the internal–dynamics, having dimension of 10. Stability of the internal–dynamics is a precondition for the overall stability of the closed–loop system. This in turn can be ensured by verifying the stability of the zero–dynamics found by setting to zero the co–ordinates corresponding to the linearised sub–system (in this case z_1, z_2), in the internal–dynamics expressions. The latter may be chosen arbitrarily, such that the derivatives of each co–ordinate with respect to x is orthogonal to g, such that the normal form of the equations is acquired (in the normal form, the system inputs will not appear in the internal–dynamics equations, making it-and the zero–dynamics uncontrollable). The transformation between the nonlinear and linear domains, $\boldsymbol{T_{zx}}$ is given by

$$\boldsymbol{z} = \boldsymbol{T_{zx}}\boldsymbol{x} \tag{A.20}$$

where,

$$\boldsymbol{T_{zx}} = \begin{bmatrix} 1 & 0 & 0 & 0 & 0 & 0 & 0 & 0 & 0 & 0 & 0 & 0 \\ 0 & 1 & 0 & 0 & 0 & 0 & 0 & 0 & 0 & 0 & 0 & 0 \\ 0 & 0 & 1 & 0 & 0 & 0 & 0 & 0 & 0 & 0 & 0 & 0 \\ 0 & -\frac{\gamma_\delta}{\lambda_\delta} & 0 & 1 & 0 & 0 & 0 & 0 & 0 & 0 & 0 & 0 \\ 0 & 0 & 0 & 0 & 1 & 0 & 0 & 0 & 0 & 0 & 0 & 0 \\ 0 & 0 & 0 & 0 & 0 & 1 & 0 & 0 & 0 & 0 & 0 & 0 \\ 0 & 0 & 0 & 0 & 0 & 0 & 1 & 0 & 0 & 0 & 0 & 0 \\ 0 & 0 & 0 & 0 & 0 & 0 & 0 & 1 & 0 & 0 & 0 & 0 \\ 0 & -\frac{1}{\lambda_\delta} & 0 & 0 & 0 & 0 & 0 & 0 & 1 & 0 & 0 & 0 \\ 0 & -\frac{1}{\lambda_\delta} & 0 & 0 & 0 & 0 & 0 & 0 & 0 & 1 & 0 & 0 \\ 0 & 0 & 0 & 0 & 0 & 0 & 0 & 0 & 0 & 0 & 1 & 0 \\ 0 & 0 & 0 & 0 & 0 & 0 & 0 & 0 & 0 & 0 & 0 & 1 \end{bmatrix} \tag{A.21}$$

Using this transformation, the zero–dynamics is derived as

$$\begin{Bmatrix} \dot{z}_3 \\ \dot{z}_4 \\ \dot{z}_5 \\ \dot{z}_6 \\ \dot{z}_7 \\ \dot{z}_8 \\ \dot{z}_9 \\ \dot{z}_{10} \\ \dot{z}_{11} \\ \dot{z}_{12} \end{Bmatrix}_{zd} = \begin{Bmatrix} z_4 \\ -\frac{\gamma_\delta}{\lambda_\delta} f_2(\boldsymbol{z}) + f_4(\boldsymbol{z}) \\ -\epsilon_1 z_5 \\ -\epsilon_2 z_6 \\ z_3 - \epsilon_1 z_7 \\ z_3 - \epsilon_2 z_8 \\ -\frac{1}{\lambda_\delta} f_2(\boldsymbol{z}) - \epsilon_1 z_9 \\ -\frac{1}{\lambda_\delta} f_2(\boldsymbol{z}) - \epsilon_2 z_{10} \\ -\epsilon_3 z_{11} \\ -\epsilon_4 z_{12} \end{Bmatrix}_{zd} \tag{A.22}$$

where $f_2(\boldsymbol{z})$, $f_4(\boldsymbol{z})$ in the above equation are the second and fourth rows of $\boldsymbol{f}(\boldsymbol{x})$ in Eq. (A.12), specified in terms of $\boldsymbol{z}$, with $z_1 = z_2 = 0$. It is evident that the zero–dynamics are nonlinear, and one must ensure their stability in order to verify the feasibility of the controller in Eq. (A.18).

The implementation of the nonlinear controller is shown in the following block diagram.

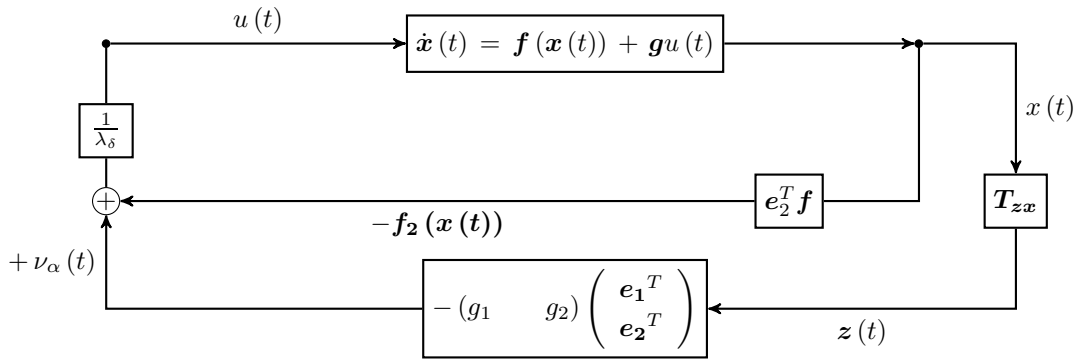

Figure A.1: Nonlinear control block diagram

Here, in Figure A.1 $\boldsymbol{e_1}$,$\boldsymbol{e_2}$ are the 1^{st} and 2^{nd} columns respectively of a 12×12 identity matrix.

A.3.2 A Note on Plunge Output Linearisation

In principle, one may designate any one of the 12 states of the system as an output, but it would be desirable to choose a physical displacement state as it is more straightforward to deal with than an aerodynamic state. Thus, either pitch or plunge may be chosen. For the present model, it transpires that the zero dynamics for plunge control are unstable, ruling out the possibility of plunge control.

A.4 Pitch–Plunge Aerofoil with Trailing–Edge Flap

Equations (5.5) and (5.6) in section 5.1 are re-written here as

$$\boldsymbol{A}_L = \begin{bmatrix} \boldsymbol{0} & \boldsymbol{I} & \boldsymbol{0} \\ -\boldsymbol{M}^{-1}\boldsymbol{K} & -\boldsymbol{M}^{-1}\boldsymbol{C} & \boldsymbol{A}_{sf} \\ \boldsymbol{A}_{fs} & \boldsymbol{0} & \boldsymbol{A}_{ff} \end{bmatrix} \tag{A.23}$$

$$\boldsymbol{b}_N = \begin{Bmatrix} \boldsymbol{0} \\ -\boldsymbol{M}^{-1}\boldsymbol{F}_N \\ \boldsymbol{0} \end{Bmatrix}, \quad \boldsymbol{b}_a = \begin{Bmatrix} \boldsymbol{0} \\ -\boldsymbol{M}^{-1}\boldsymbol{f}_a \\ \boldsymbol{0} \end{Bmatrix}, \quad \boldsymbol{b}_e = \begin{Bmatrix} \boldsymbol{0} \\ -\boldsymbol{M}^{-1}\boldsymbol{f}_e \\ \boldsymbol{A}_{fg}\boldsymbol{u}_d \end{Bmatrix} \tag{A.24}$$

The analytical evaluations of each term in this equation are given as follows

$$\boldsymbol{M} = \begin{bmatrix} c_0 & c_1 & f_{d3} \\ d_0 & d_1 & g_{d3} \\ p_0 & p_1 & p_{16} \end{bmatrix} \tag{A.25}$$

$$\boldsymbol{C} = \begin{bmatrix} c_2 & c_3 & f_{d2} \\ d_5 & d_2 & g_{d2} \\ p_2 & p_3 & p_{15} \end{bmatrix} \tag{A.26}$$

$$\boldsymbol{K} = \begin{bmatrix} c_4 & c_6 & f_{d1} \\ d_6 & d_3 & g_{d1} \\ p_4 & p_5 & p_{12} \end{bmatrix} \tag{A.27}$$

$$\boldsymbol{F}_N = \begin{bmatrix} c_5\xi^3 + c_{51}\xi^5 \\ d_4\alpha^3 + d_{41}\alpha^5 \\ p_{13}\delta^3 + p_{14}\delta^5 \end{bmatrix} \tag{A.28}$$

$$\boldsymbol{A}_{sf} = \begin{bmatrix} c_7 & c_8 & c_9 & c_{10} & c_{11} & c_{12} & c_{13} & c_{14} \\ d_7 & d_8 & d_9 & d_{10} & d_{11} & d_{12} & d_{13} & d_{14} \\ p_6 & p_7 & p_8 & p_9 & p_{10} & p_{11} & 0 & 0 \end{bmatrix} \tag{A.29}$$

$$\boldsymbol{A}_{fs} = \begin{bmatrix} 0 & 1 & 0 \\ 0 & 1 & 0 \\ 1 & 0 & 0 \\ 1 & 0 & 0 \\ 0 & 0 & 1 \\ 0 & 0 & 1 \\ 0 & 0 & 0 \\ 0 & 0 & 0 \end{bmatrix} \tag{A.30}$$

$$\boldsymbol{A}_{ff} = -\text{diag}\left[\varepsilon_1, \varepsilon_2, \varepsilon_1, \varepsilon_2, \varepsilon_1, \varepsilon_2, \varepsilon_3, \varepsilon_4\right] \tag{A.31}$$

$$\boldsymbol{A}_{fg}\boldsymbol{u}_d = \left\{0, 0, 0, 0, 0, 0, w_g, w_g\right\}^T \tag{A.32}$$

$$\begin{aligned} \boldsymbol{f}_a &= \left[f\left(\tau\right), g\left(\tau\right), h\left(\tau\right)\right]^T \\ \boldsymbol{f}_e &= \left[0, 0, \overline{H}_\delta\left(\tau\right)\right]^T \end{aligned} \tag{A.33}$$

The parameters for the plunge equation are

$$
\begin{aligned}
c_0 &= 1 + \frac{1}{\mu} \\
c_1 &= x_\alpha - \frac{a}{\mu} \\
c_2 &= 2\zeta_\xi \frac{\bar{\omega}_1}{\bar{u}} + \frac{2}{\mu}\left(1 - \Psi_1 - \Psi_2\right) \\
c_3 &= \frac{1}{\mu} + \frac{2}{\mu}\left(\tfrac{1}{2} - a\right)\left(1 - \Psi_1 - \Psi_2\right) \\
c_4 &= \left(\frac{\bar{\omega}_1}{\bar{u}}\right)^2 + \frac{2}{\mu}\left(\varepsilon_1\Psi_1 + \varepsilon_2\Psi_2\right) \\
c_5 &= \left(\frac{\bar{\omega}_1}{\bar{u}}\right)^2 \beta_\xi \\
c_{51} &= \left(\frac{\bar{\omega}_1}{\bar{u}}\right)^2 \beta_{\xi 5} \\
c_6 &= \frac{2}{\mu}\left(\left(1 - \Psi_1 - \Psi_2\right) + \left(\tfrac{1}{2} - a\right)\left(\varepsilon_1\Psi_1 + \varepsilon_2\Psi_2\right)\right) \\
c_7 &= \frac{2}{\mu}\varepsilon_1\Psi_1\left(1 - \varepsilon_1\left(\tfrac{1}{2} - a\right)\right) \\
c_8 &= \frac{2}{\mu}\varepsilon_2\Psi_2\left(1 - \varepsilon_2\left(\tfrac{1}{2} - a\right)\right) \\
c_9 &= -\frac{2}{\mu}\varepsilon_1^2\Psi_1 \\
c_{10} &= -\frac{2}{\mu}\varepsilon_2^2\Psi_2 \\
c_{11} &= \varepsilon_1\Psi_1\frac{\left(2T_{10} - \varepsilon_1 T_{11}\right)}{\pi\mu} \\
c_{12} &= \varepsilon_2\Psi_2\frac{\left(2T_{10} - \varepsilon_2 T_{11}\right)}{\pi\mu} \\
c_{13} &= \frac{2}{\mu}\varepsilon_3\Psi_3 \\
c_{14} &= \frac{2}{\mu}\varepsilon_4\Psi_4 \\
fd_1 &= \frac{1}{\pi\mu}\left(2T_{10}\left(1 - \Psi_1 - \Psi_2\right) + T_{11}\left(\varepsilon_1\Psi_1 + \varepsilon_2\Psi_2\right)\right) \\
fd_2 &= \frac{1}{\pi\mu}\left(-T_4 + T_{11}\left(1 - \Psi_1 - \Psi_2\right)\right) \\
fd_3 &= x_\delta - \frac{1}{\pi\mu}T_1
\end{aligned}
\tag{A.34}
$$

The parameters for the pitch equation are

$$
\begin{aligned}
d_0 &= \frac{x_\alpha}{r_\alpha^2} - \frac{a}{\mu r_\alpha^2} \\
d_1 &= 1 + \frac{a^2}{\mu r_\alpha^2} + \frac{1}{8\mu r_\alpha^2} \\
d_2 &= 2\frac{\zeta_\alpha}{\bar{u}} - \frac{1}{\mu r_\alpha^2}\left(\left(2a_h+1\right)\left(\tfrac{1}{2}-a_h\right)\left(1-\Psi_1-\Psi_2\right) - \left(\tfrac{1}{2}-a_h\right)\right) \\
d_3 &= \frac{1}{\bar{u}^2} - \frac{1}{\mu r_\alpha^2}\left(\left(2a_h+1\right)\left(1-\Psi_1-\Psi_2\right) + \left(2a_h+1\right)\left(\tfrac{1}{2}-a\right)\left(\varepsilon_1\Psi_1+\varepsilon_2\Psi_2\right)\right) \\
d_4 &= \left(\frac{1}{\bar{u}}\right)^2 \beta_\alpha \\
d_{41} &= \left(\frac{1}{\bar{u}}\right)^2 \beta_{\alpha 5} \\
d_5 &= -\frac{2}{\mu r_\alpha^2}\left(\tfrac{1}{2}+a\right)\left(1-\Psi_1-\Psi_2\right) \\
d_6 &= -\frac{1}{\mu r_\alpha^2}\left(1+2a\right)\left(\varepsilon_1\Psi_1+\varepsilon_2\Psi_2\right) \\
d_7 &= -\frac{1+2a}{\mu r_\alpha^2}\varepsilon_1\Psi_1\left(1-\varepsilon_1\left(\tfrac{1}{2}-a\right)\right) \\
d_8 &= -\frac{1+2a}{\mu r_\alpha^2}\varepsilon_2\Psi_2\left(1-\varepsilon_2\left(\tfrac{1}{2}-a\right)\right) \\
d_9 &= \frac{1+2a}{\mu r_\alpha^2}\varepsilon_1^2\Psi_1 \\
d_{10} &= \frac{1+2a}{\mu r_\alpha^2}\varepsilon_2^2\Psi_2 \\
d_{11} &= -\frac{2}{\pi\mu r_\alpha^2}\left(\left(a+\tfrac{1}{2}\right)\left(T_{10}\varepsilon_1\Psi_1 - \frac{T_{11}}{2}\varepsilon_1^2\Psi_1\right)\right) \\
d_{12} &= -\frac{2}{\pi\mu r_\alpha^2}\left(\left(a+\tfrac{1}{2}\right)\left(T_{10}\varepsilon_2\Psi_2 - \frac{T_{11}}{2}\varepsilon_2^2\Psi_2\right)\right) \\
d_{13} &= -\frac{1+2a}{\mu r_\alpha^2}\varepsilon_3\Psi_3 \\
d_{14} &= -\frac{1+2a}{\mu r_\alpha^2}\varepsilon_4\Psi_4 \\
gd_1 &= -\frac{2}{\pi\mu r_\alpha^2}\left(-\frac{1}{2}\left(T_4+T_{10}\right) + \left(a+\tfrac{1}{2}\right)\left(T_{10}\left(1-\Psi_1-\Psi_2\right) + \frac{T_{11}}{2}\left(\varepsilon_1\Psi_1+\varepsilon_2\Psi_2\right)\right)\right) \\
gd_2 &= -\frac{2}{\pi\mu r_\alpha^2}\left(-\frac{1}{2}\left(T_1-T_8-\left(c-a\right)T_4\right) + \frac{1}{2}T_{11}\right) + \left(a+\tfrac{1}{2}\right)\frac{T_{11}}{2}\left(1-\Psi_1-\Psi_2\right) \\
gd_3 &= -\frac{2}{\pi\mu r_\alpha^2}\frac{1}{2}\left(T_7+\left(c-a\right)T_1\right) + \left(\frac{r_\delta^2}{r_\alpha^2} + \frac{\left(c-a\right)x_\delta}{r_\alpha^2}\right)
\end{aligned}
\tag{A.35}
$$

The parameters for the flap equation are

$$
\begin{aligned}
p_0 &= \frac{x_\delta}{r_\delta^2} - \frac{Q}{2}T_{11} \\
p_1 &= \left(1 + \frac{(c-a)\,x_\delta}{r_\delta^2}\right) + QT_{13} \\
p_2 &= \frac{1}{2}QT_{12}\left(1 - \Psi_1 - \Psi_2\right) \\
p_3 &= \frac{1}{2}QT_{12}\left(\tfrac{1}{2} - a\right)\left(1 - \Psi_1 - \Psi_2\right) + \tfrac{1}{2}Q\left(T_4\left(a - \frac{1}{2}\right) - T_1 - 2T_9\right) \\
p_4 &= \frac{1}{2}QT_{12}\left(\varepsilon_1\Psi_1 + \varepsilon_2\Psi_2\right) \\
p_5 &= \frac{1}{2}QT_{12}\left(\left(\tfrac{1}{2} - a\right)\left(\varepsilon_1\Psi_1 + \varepsilon_2\Psi_2\right) + \left(1 - \Psi_1 - \Psi_2\right)\right) \\
p_6 &= \frac{1}{2}QT_{12}\left(\left(\tfrac{1}{2} - a\right)\left(-\varepsilon_1^2\Psi_1\right) + \varepsilon_1\Psi_1\right) \\
p_7 &= \frac{1}{2}QT_{12}\left(\left(\tfrac{1}{2} - a\right)\left(-\varepsilon_2^2\Psi_2\right) + \varepsilon_2\Psi_2\right) \\
p_8 &= \frac{1}{2}QT_{12}\left(-\varepsilon_1^2\Psi_1\right) \\
p_9 &= \frac{1}{2}QT_{12}\left(-\varepsilon_2^2\Psi_2\right) \\
p_{10} &= \frac{1}{2}QT_{12}\left(\frac{T_{11}}{2\pi}\left(-\varepsilon_1^2\Psi_1\right) + \frac{T_{10}}{\pi}\left(\varepsilon_1\Psi_1\right)\right) \\
p_{11} &= \frac{1}{2}QT_{12}\left(\frac{T_{11}}{2\pi}\left(-\varepsilon_2^2\Psi_2\right) + \frac{T_{10}}{\pi}\left(\varepsilon_2\Psi_2\right)\right) \\
p_{12} &= \frac{1}{2}QT_{12}\left(\frac{T_{11}}{2\pi}\left(\varepsilon_1\Psi_1 + \varepsilon_2\Psi_2\right) + \frac{T_{10}}{\pi}\left(1 - \Psi_1 - \Psi_2\right)\right) + \frac{1}{2}Q\left(\frac{T_5 - T_4T_{10}}{\pi}\right) + \left(\frac{\bar{\omega}_2}{U^*}\right)^2 \\
p_{13} &= \left(\frac{\bar{\omega}_2}{U^*}\right)^2\beta_\delta \\
p_{14} &= \left(\frac{\bar{\omega}_2}{U^*}\right)^2\beta_{\delta 5} \\
p_{15} &= \frac{1}{2}QT_{12}\left(\frac{T_{11}}{2\pi}\left(1 - \Psi_1 - \Psi_2\right)\right) + \frac{1}{2}Q\left(\frac{-T_4T_{11}}{2\pi}\right) + 2\zeta_\delta\frac{\bar{\omega}_2}{U^*} \\
p_{16} &= 1 - \frac{1}{2}Q\frac{T_3}{\pi} \\
Q &= \frac{2}{\pi\mu r_\delta^2}
\end{aligned}
\tag{A.36}
$$

$$
\begin{aligned}
f\left(\tau\right) &= \frac{2}{\mu}\left(\xi\left(0\right) + \left(\tfrac{1}{2} - a\right)\alpha\left(0\right) + \frac{T_{11}}{2\pi}\delta\left(0\right)\right)\left(\varepsilon_1\Psi_1 e^{-\varepsilon_1\tau} + \varepsilon_2\Psi_2 e^{-\varepsilon_2\tau}\right) \\
g\left(\tau\right) &= -\frac{2a_h + 1}{2r_\alpha^2}f\left(\tau\right) \\
h\left(\tau\right) &= \frac{T_{12}}{2}\frac{\mu}{2}f\left(\tau\right)
\end{aligned}
\tag{A.37}
$$

$$f^g(\tau) = -\frac{2}{\mu U^*}(1 - \Psi_3 - \Psi_4) W_g(\tau) = 0$$
$$g^g(\tau) = \frac{1}{\mu r_\alpha^2 U^*}(2a_h + 1)(1 - \Psi_3 - \Psi_4) W_g(\tau) = 0 \quad \text{(A.38)}$$

Note that 1-Ψ_3-Ψ_4 is zero.

A.5 Flexible Wing Coupled with Strip Aerodynamics

A reasonable approach for slender wing structures is to assume a two–dimensional flow at each spanwise section along the span. The aerodynamic lift and moment coefficients per unit span are given by two–dimensional potential theory, meaning that the aerodynamic forces at each spanwise location depend only on the local elastic deformation. In the following it is assumed that the wing has constant chord, $c = 2b$ and that each aerofoil section is defined in the $y - z$ plane, with the $z-$ axis pointing upward and the $x-$ axis along the beam, starting from the clamped root to the tip. The objective is to rotate the aerodynamic forces from their respective frame to the beam reference frame when the global governing equations are formulated.

In the beam reference frame,the six degrees of freedom for a generic $j-th$ node can be defined as

$$\boldsymbol{x}_s{}^j = \{d_{d1}, d_{d2}, d_{d3}, ad_{d1}, ad_{d2}, ad_{d3}\}^T \tag{A.39}$$

where d_{d3} is the vertical displacement and ad_{d1} is the pitching torsion. The global finite element equations for the nonlinear structural model in dimensional form are

$$\boldsymbol{M_{SS}}\left[\boldsymbol{x}_s\right]\ddot{\boldsymbol{x}}_s + \boldsymbol{C_{SS}}\left[\boldsymbol{x}_s, \dot{\boldsymbol{x}}_s\right]\dot{x}_s + \boldsymbol{K_{SS}}\left[\boldsymbol{x}_s\right]\boldsymbol{x}_s = \boldsymbol{F} \tag{A.40}$$

where subscript SS indicates structure and these are expressed as total nonlinear mass, damping, and stiffness matrices.

Based on the assumption of two–dimensional flow, aerodynamic forces in the vector $\boldsymbol{F}$ depend on the degrees–of–freedom d_{d3} and ad_{d1} of each node. The aerodynamic force vector acting at a generic $j-$th node is defined in the aerodynamic reference frame as follows

$$\boldsymbol{F}^{jA} = \left\{0, -\boldsymbol{L}^j, 0, 0, 0, \boldsymbol{M}^j\right\}^T \tag{A.41}$$

where the subscript A indicates the frame in which the vector is expressed. The expression in Eq. (A.41) when written in matrix–vector form yields

$$\boldsymbol{F}^{jA} = \boldsymbol{M_f}^{jA}\ddot{\boldsymbol{x}}_s^{jA} + \boldsymbol{C_f}^{jA}\dot{\boldsymbol{x}}_s^{jA} + \boldsymbol{K_f}^{jA}\boldsymbol{x}_s^{jA} + \boldsymbol{A}_{sf}^{jA}\boldsymbol{w}_f{}^{jA} + \boldsymbol{A}_{sc}^{jA}\boldsymbol{u}_c^{jA} \tag{A.42}$$

In the above equations matrices $\boldsymbol{M_f}^{jA}$,$\boldsymbol{C_f}^{jA}$ and $\boldsymbol{K_f}^{jA}$ are (6×6) while the matrix $\boldsymbol{A}_{sf}{}^{jA}$ is (6), and the matrix $\boldsymbol{A}_{sc}^{jA}$ is (6×3). Therefore, each finite element node contains

flap for control. The non–zero components of these matrices are

$$
\begin{array}{llll}
\boldsymbol{M}^{jA}_{\boldsymbol{f22}} = -q_0 c_1, & \boldsymbol{M}^{jA}_{\boldsymbol{f26}} = -q_0 c_2, & \boldsymbol{M}^{jA}_{\boldsymbol{f62}} = q_0 cd_1, & \boldsymbol{M}^{jA}_{\boldsymbol{f66}} = q_0 cd_2 \\
\boldsymbol{C}^{jA}_{\boldsymbol{f22}} = -q_1 c_3, & \boldsymbol{C}^{jA}_{\boldsymbol{f26}} = -q_1 c_4, & \boldsymbol{C}^{jA}_{\boldsymbol{f62}} = q_1 cd_3, & \boldsymbol{C}^{jA}_{\boldsymbol{f66}} = q_1 cd_4 \\
\boldsymbol{K}^{jA}_{\boldsymbol{f22}} = -q_2 c_5, & \boldsymbol{K}^{jA}_{\boldsymbol{f26}} = -q_2 c_6, & \boldsymbol{K}^{jA}_{\boldsymbol{f62}} = q_2 cd_5, & \boldsymbol{K}^{jA}_{\boldsymbol{f66}} = q_2 cd_6 \\
\boldsymbol{A}^{jA}_{\boldsymbol{sf_{2k}}} = -q_2 c_{6+k} & & \text{for} & k = 1, 2, ..., 8 \\
\boldsymbol{A}^{jA}_{\boldsymbol{sf_{6k}}} = -q_2 cd_{6+k} & & \text{for} & k = 1, 2, ..., 8 \\
\boldsymbol{A}^{jA}_{\boldsymbol{sc_{21}}} = -q_2 c_{15} & \boldsymbol{A}^{jA}_{\boldsymbol{sc_{22}}} = -q_1 c_{16} & \boldsymbol{A}^{jA}_{\boldsymbol{sc_{23}}} = -q_0 c_{17} & \\
\boldsymbol{A}^{jA}_{\boldsymbol{sc_{61}}} = -q_2 cd_{15} & \boldsymbol{A}^{jA}_{\boldsymbol{sc_{62}}} = -q_1 cd_{16} & \boldsymbol{A}^{jA}_{\boldsymbol{sc_{63}}} = -q_0 cd_{17} &
\end{array}
\tag{A.43}
$$

where $q_0 = 0.5\rho S$, $q_1 = q_0 U_\infty$, $q_2 = q_1 U_\infty$. Note that q_2 is the dynamic pressure and S is the beam finite element reference area. It is assumed that the mode approximation between two consecutive aerofoil sections, delimited between node $j-1$ and j into the $j-th$ node is irrelevant for increasing number of elements. The remaing terms of the aerodynamic model are constant and for a given geometry are computed only once. Now, some geometric terms are introduced. The constants $T_1, T_4, T_7, T_8, T_{10}$ and T_{11} are all geometric terms which depend on the size of the flap relative to the aerofoil chord and for a coordinate system located at the midchord are expressed as in [22].

$$
\begin{aligned}
T_1 &= -\frac{1}{3}\sqrt{1-c^2}(2+c^2) + carccos(c) \\
T_4 &= -arccos(c) + c\sqrt{1-c^2} \\
T_7 &= -(\frac{1}{8}+c^2)arccos(c) + \frac{1}{8}c\sqrt{1-c^2}(7+2c^2) \\
T_8 &= -\frac{1}{3}\sqrt{1-c^2}(2c^2+1) + carccos(c) \\
T_{10} &= \sqrt{1-c^2} + arccos(c) \\
T_{11} &= arccos(c)(1-2c) + \sqrt{1-c^2}(2-c) \\
c_\delta &= (2T_{10}(1-\Psi_1-\Psi_2) + T_{11}(\epsilon_1\Psi_1 + \epsilon_2\Psi_2)) \\
c_{\delta'} &= (-T_4 + T_{11}(1-\Psi_1-\Psi_2)) \\
c_{\delta''} &= -T_1 \\
d_\delta &= (-(T_4+T_{10}) + (a_h+\frac{1}{2})(T_{10}(1-\Psi_1-\Psi_2) + \frac{T_{11}}{2}(\epsilon_1\Psi_1+\epsilon_2\Psi_2))) \\
d_{\delta'} &= (-(T_1 - T_8 - (c-a_h)T_4 + \frac{1}{2}T_{11}) + (a_h+\frac{1}{2})\frac{T_{11}}{2}(1-\Psi_1-\Psi_2)) \\
d_{\delta''} &= (T_7 + (c-a_h)T_1)
\end{aligned}
\tag{A.44}
$$

The coefficients denoted in Eq. (A.43) are written in explicit form as

$$
\begin{aligned}
c_1 &= \pi b \\
c_2 &= -\pi a_h b^2 \\
c_3 &= 2\pi(1-\Psi_1-\Psi_2) \\
c_4 &= \pi b(1+(1-2a_h)(1-\Psi_1-\Psi_2)) \\
c_5 &= \frac{2\pi}{b}(\epsilon_1\Psi_1+\epsilon_2\Psi_2) \\
c_6 &= 2\pi((1-\Psi_1-\Psi_2)+(\frac{1}{2}-a_h)(\epsilon_1\Psi_1+\epsilon_2\Psi_2)) \\
c_7 &= 2\pi\epsilon_1\Psi_1(1-\epsilon_1(1-\frac{1}{2}-a_h)) \\
c_8 &= 2\pi\epsilon_2\Psi_2(1-\epsilon_2(\frac{1}{2}-a_h)) \\
c_9 &= -2\pi\epsilon_1^2\Psi_1 \\
c_{10} &= -2\pi\epsilon_2^2\Psi_2 \\
c_{11} &= \epsilon_1\Psi_1 2T_{10}-\epsilon_1^2\Psi_1 T_{11} \\
c_{12} &= \epsilon_2\Psi_2 2T_{10}-\epsilon_2^2\Psi_2 T_{11} \\
c_{13} &= 2\pi\epsilon_3\Psi_3 \\
c_{14} &= 2\pi\epsilon_4\Psi_4 \\
c_{15} &= c_\delta \qquad c_{16} = bc_{\delta'} \qquad c_{17} = b^2 c_{\delta''}
\end{aligned}
\tag{A.45}
$$

$$
\begin{aligned}
d_1 &= \frac{\pi}{2} a_h b \\
d_2 &= -\frac{1}{2}(a_h^2 + \frac{1}{8}) b^2 \\
d_3 &= \pi(\frac{1}{2} + a_h)(1 - \Psi_1 - \Psi_2) \\
d_4 &= \frac{\pi}{6}(\frac{1}{2} - a_h)((\frac{1}{2} + a_h)(1 - \Psi_1 - \Psi_2) - \frac{1}{2}) \\
d_5 &= \frac{\pi}{6}(\frac{1}{2} + a_h)(\epsilon_1 \Psi_1 + \epsilon_2 \Psi_2) \\
d_6 &= \pi(\frac{1}{2} + a_h)((1 - \Psi_1 - \Psi_2) + (\frac{1}{2} - a_h)((\epsilon_1 \Psi_1 + \epsilon_2 \Psi_2))) \\
d_7 &= \pi(\frac{1}{2} + a_h)(\epsilon_1 \Psi_1 (1 - \epsilon_1 (\frac{1}{2} - a_h))) \\
d_8 &= \pi(\frac{1}{2} + a_h)(\epsilon_2 \Psi_2 (1 - \epsilon_2 (\frac{1}{2} - a_h))) \\
d_9 &= -\pi(\frac{1}{2} + a_h)\epsilon_1^2 \Psi_1 \\
d_{10} &= -\pi(\frac{1}{2} + a_h)\epsilon_2^2 \Psi_2 \\
d_{11} &= (\frac{1}{2} + a_h)(T_{10}\epsilon_1 \Psi_1 - \frac{T_{11}}{2}\epsilon_1^2 \Psi_1) \\
d_{12} &= (\frac{1}{2} + a_h)(T_{10}\epsilon_2 \Psi_2 - \frac{T_{11}}{2}\epsilon_2^2 \Psi_2) \\
d_{13} &= \pi(\frac{1}{2} + a_h)\epsilon_3 \Psi_3 \qquad d_{14} = \pi(\frac{1}{2} + a_h)\epsilon_4 \Psi_4 \\
d_{15} &= d_\delta \qquad d_{16} = b d_{\delta'} \qquad d_{17} = b^2 d_{\delta''}
\end{aligned}
\tag{A.46}
$$

It is important to state the governing equations of the aerodynamic states of a generic $j-$th node. These can be writte in a matrix–vector form as

$$
\dot{\boldsymbol{w}}_{\boldsymbol{f}}^{j} \;=\; \boldsymbol{A}_{fs}^{jA} \boldsymbol{x}_{s}^{jA} \;+\; \boldsymbol{A}_{ff}^{j} \boldsymbol{w}_{f}{}^{j} \;+\; \boldsymbol{A}_{fc}^{j} \boldsymbol{u}_{c}^{j} \;+\; \boldsymbol{A}_{ff}^{j} \boldsymbol{u}_{d} \tag{A.47}
$$

where the vector of the structural degrees–of–freedom is explicitly given in the aerodynamic reference frame. The matrix $\boldsymbol{A}_{fs}^{j}$ has dimension (8×6), the matrix $\boldsymbol{A}_{ff}^{j}$ has dimension (8×8), the matrix $\boldsymbol{A}_{fc}^{j}$ has dimensions (8×3) and the matrix $\boldsymbol{A}_{fg}^{j}$ dimensions (8×3) for the three possible gust components in x, y, z. The non–zero components of those matrices are.

$$
\begin{array}{cccc}
\boldsymbol{A}_{fs16}^{jA} = \frac{U_\infty}{b}, & \boldsymbol{A}_{fs26}^{jA} = \frac{U_\infty}{b}, & \boldsymbol{A}_{fs32}^{jA} = \frac{U_\infty}{b^2}, & \boldsymbol{A}_{fs41}^{jA} = \frac{U_\infty}{b^2} \\
\boldsymbol{A}_{ff11}^{j} = -\frac{\epsilon_1 U_\infty}{b}, & \boldsymbol{A}_{ff22}^{j} = -\frac{\epsilon_2 U_\infty}{b}, & \boldsymbol{A}_{ff33}^{j} = -\frac{\epsilon_1 U_\infty}{b^2}, & \boldsymbol{A}_{ff44}^{j} = -\frac{\epsilon_2 U_\infty}{b^2} \\
\boldsymbol{A}_{ff55}^{j} = -\frac{\epsilon_1 U_\infty}{b}, & \boldsymbol{A}_{ff66}^{j} = -\frac{\epsilon_2 U_\infty}{b}, & \boldsymbol{A}_{ff77}^{j} = -\frac{\epsilon_3 U_\infty}{b^2}, & \boldsymbol{A}_{ff88}^{j} = -\frac{\epsilon_4 U_\infty}{b^2} \\
\boldsymbol{A}_{fc51}^{j} = \frac{U_\infty}{b}, & \boldsymbol{A}_{fc61}^{j} = \frac{U_\infty}{b}, & \boldsymbol{A}_{fg71}^{j} = \frac{U_\infty}{b}, & \boldsymbol{A}_{fg81}^{j} = \frac{U_\infty}{b}
\end{array}
$$

The expressions given in Eq. (A.42) and (A.47) are formulated based on a vector of structural degrees–of–freedom defined in the aerodynamic reference frame $\boldsymbol{x}_{s}^{jA}$. In order to form the global system equations of motion, a coordinate transformation has to be performed to transfer the structural degrees of freedom in the beam reference frame.

This is accomplished by the transformation

$$\boldsymbol{x}_s^{jA} = \boldsymbol{R}\boldsymbol{x}_s^{jB} = \boldsymbol{R}\boldsymbol{x}_s^{j} \tag{A.48}$$

where subscript B indicates the beam reference frame. The transformation matrix for a cantilever beam is given by $\boldsymbol{R}$

$$\boldsymbol{R} = \begin{bmatrix} 0 & 0 & 1 & 0 & 0 & 0 \\ -cos\,(ad_{1d}) & -sin\,(ad_{1d}) & 0 & 0 & 0 & 0 \\ sin\,(ad_{1d}) & -cos\,(ad_{1d}) & 0 & 0 & 0 & 0 \\ 0 & 0 & 0 & 0 & 0 & 1 \\ 0 & 0 & 0 & -cos\,(ad_{1d}) & -sin\,(ad_{1d}) & 0 \\ 0 & 0 & 0 & sin\,(ad_{1d}) & -cos\,(ad_{1d}) & 0 \end{bmatrix} \tag{A.49}$$

If Eq. (A.49) is substituted in Eq. (A.42), yields the aerodynamic forces in the beam reference frame

$$\boldsymbol{F}^{jB} = \boldsymbol{M}_{\boldsymbol{f}}^{jB}\ddot{\boldsymbol{x}}_s^{jB} + \boldsymbol{C}_{\boldsymbol{f}}^{jB}\dot{\boldsymbol{x}}_s^{jB} + \boldsymbol{K}_{\boldsymbol{f}}^{jB}\boldsymbol{x}_s^{jB} + \boldsymbol{A}_{sf}^{jB}\boldsymbol{w}_f{}^{j} + \boldsymbol{B}_{\boldsymbol{c}}^{j}\boldsymbol{u}_c^{j} \tag{A.50}$$

The transformed matrices are defined in an equivalent way as

$$\begin{aligned} \boldsymbol{M}_{\boldsymbol{f}}^{jB} &= \boldsymbol{R}^T\boldsymbol{M}_{\boldsymbol{f}}^{jA}\boldsymbol{R} \\ \boldsymbol{C}_{\boldsymbol{f}}^{jB} &= \boldsymbol{R}^T\boldsymbol{C}_{\boldsymbol{f}}^{jA}\boldsymbol{R} \\ \boldsymbol{K}_{\boldsymbol{f}}^{jB} &= \boldsymbol{R}^T\boldsymbol{K}_{\boldsymbol{f}}^{jA}\boldsymbol{R} \\ \boldsymbol{A}_{sf}^{jB} &= \boldsymbol{R}^T\boldsymbol{A}_{fs}^{jA}\boldsymbol{R} \\ \boldsymbol{A}_{sc}^{j} &= \boldsymbol{R}^T\boldsymbol{A}_{sc}^{j} \end{aligned} \tag{A.51}$$

(A.52)

Similarly Eq. (A.47) becomes

$$\dot{\boldsymbol{w}}_{\boldsymbol{f}}^{j} = \boldsymbol{A}_{fs}^{jB}\boldsymbol{x}_s^{jB} + \boldsymbol{A}_{ff}^{j}\boldsymbol{w}_f{}^{j} + \boldsymbol{A}_{fc}^{j}\boldsymbol{u}_c^{j} + \boldsymbol{A}_{ff}^{j}\boldsymbol{u}_d \tag{A.53}$$

where $\boldsymbol{A}_{fs}^{jB} = \boldsymbol{A}_{fs}^{jA}\boldsymbol{R}$

The vector of aerodynamic forces for each structural node given in Eq. (A.47) can be assembled together to form the global vector of aerodynamic forces which substitution into the original Eq. (A.40) yields the global equation of motion

$$\boldsymbol{M}_T\ddot{\boldsymbol{x}}_s + \boldsymbol{C}_T\dot{\boldsymbol{x}}_s + \boldsymbol{K}_T\boldsymbol{x}_s = \boldsymbol{A}_{sf}\boldsymbol{w}_f + \boldsymbol{A}_{sc}\boldsymbol{u}_c \tag{A.54}$$

where the finite element structural matrices are updated with equivalent aerodynamic mass, damping and stiffness matrices as

$$\boldsymbol{M}_T = \boldsymbol{M_{SS}} - \boldsymbol{M_f} \tag{A.55}$$

$$\boldsymbol{C}_T = \boldsymbol{C_{SS}} - \boldsymbol{C_f}$$

$$\boldsymbol{K}_T = \boldsymbol{K_{SS}} - \boldsymbol{K_f}$$

$$\tag{A.56}$$

The subscript B is ommited for clarity as long as everything now is expressed in the aerodynamic reference frame, thus $\boldsymbol{x}_s = \boldsymbol{x}_s^B$. Eq. (A.47) and Eq. (A.54) can be recast in ODE form by introducing the state vector

$$\boldsymbol{w} = \left\{\boldsymbol{w}_s^T, \boldsymbol{w}_f^T\right\}^T \quad \text{where} \quad \boldsymbol{w}_s = \left\{\boldsymbol{x}_s^T, \dot{\boldsymbol{x}}_s^T\right\}^T \tag{A.57}$$

and the system now can be written in the nonlinear residual form

$$\boldsymbol{R} = \boldsymbol{A}\boldsymbol{w} + \boldsymbol{B}_c\boldsymbol{u}_c + \boldsymbol{B}_g\boldsymbol{u}_d + \boldsymbol{F}_N(\boldsymbol{w}) \tag{A.58}$$

The matrix $\boldsymbol{A}$ is defined as,

$$\boldsymbol{A} = \begin{bmatrix} \boldsymbol{0} & \boldsymbol{I} & \boldsymbol{0} \\ -\boldsymbol{M}_T^{-1}\boldsymbol{K}_T & -\boldsymbol{M}_T^{-1}\boldsymbol{C}_T & \boldsymbol{M}_T^{-1}\boldsymbol{A}_{sf} \\ \boldsymbol{A}_{fs} & \boldsymbol{0} & \boldsymbol{A}_{ff} \end{bmatrix} \tag{A.59}$$

while the contributions from gust and control rotation are given in Eq. (A.60) respectively.

$$\boldsymbol{B}_c = \begin{Bmatrix} \boldsymbol{0} \\ \boldsymbol{M}_T^{-1}\boldsymbol{A}_{sc} \\ \boldsymbol{A}_{fc} \end{Bmatrix}, \qquad \boldsymbol{B}_g = \begin{Bmatrix} \boldsymbol{0} \\ \boldsymbol{0} \\ \boldsymbol{A}_{fg} \end{Bmatrix} \tag{A.60}$$

Lastly the structural nonlinearities are assembled in the vector $\boldsymbol{F}_N$ forming the nonlinear residual. where the Jacobian matrix of the manipulable controls and of the external pertubations are given explicitly. The above system consists of 20× nodes ordinary differential equations where nodes indicates the number of structural nodes (in the case of a clampled wing, it is equal to the number of finite elements used after the removal of the constrained node at the clamped side).

A.6 Free-Flying Wing Coupled with Strip Aerodynamics

The dynamic equations of the coupled structural/flight model are written

$$\boldsymbol{M}\left[\boldsymbol{w}_s\right]\begin{Bmatrix}\ddot{\boldsymbol{w}}_s\\ \ddot{\boldsymbol{w}}_r\end{Bmatrix}+\boldsymbol{Q}_{gyr}\left[\ddot{\boldsymbol{w}}_s,\boldsymbol{w}_s,\boldsymbol{w}_r\right]\begin{Bmatrix}\dot{\boldsymbol{w}}_s\\ \dot{\boldsymbol{w}}_r\end{Bmatrix}+\boldsymbol{Q}_{stiff}\left[\boldsymbol{w}_s\right]\begin{bmatrix}\boldsymbol{w}_s\\ \boldsymbol{w}_r\end{bmatrix}= \tag{A.61}$$
$$\boldsymbol{R}_F\left\{\ddot{\boldsymbol{w}}_s,\dot{\boldsymbol{w}}_s,\boldsymbol{w}_s,\ddot{\boldsymbol{w}}_r,\dot{\boldsymbol{w}}_r,\boldsymbol{w}_r,\boldsymbol{w}_f,\zeta_i,\boldsymbol{u}_c\right\}$$

The subscripts S, R and F denote elastic, rigid-body and fluid properties respectively. The gyroscopic, elastic and external or aerodynamic forces are also discretised into elastic and rigid–body contributions respectively

$$\boldsymbol{Q}_{gyr}=\begin{bmatrix}\boldsymbol{Q}^s_{gyr}\\ \boldsymbol{Q}^r_{gyr}\end{bmatrix},\qquad \boldsymbol{Q}_{stiff}=\begin{bmatrix}\boldsymbol{Q}^s_{stiff}\\ 0\end{bmatrix},\qquad \boldsymbol{R}_F=\begin{Bmatrix}\boldsymbol{R}_S\\ \boldsymbol{R}_R\end{Bmatrix} \tag{A.62}$$

This second order equation is extended by the first–order quaternion dynamics of the attitude propagation describing the orientation of the beam with respect to the inertial frame.

$$\dot{\boldsymbol{\zeta}}_{\boldsymbol{i}}=\begin{Bmatrix}\dot{\zeta}_0\\ \dot{\zeta}_1\\ \dot{\zeta}_2\\ \dot{\zeta}_3\end{Bmatrix}=-\frac{1}{2}\begin{bmatrix}0 & \omega_{a,x} & \omega_{a,y} & \omega_{a,z}\\ -\omega_{a,x} & 0 & -\omega_{a,z} & \omega_{a,y}\\ -\omega_{a,y} & \omega_{a,z} & 0 & -\omega_{a,x}\\ -\omega_{a,z} & -\omega_{a,y} & \omega_{a,x} & 0\end{bmatrix}\begin{Bmatrix}\zeta_0\\ \zeta_1\\ \zeta_2\\ \zeta_3\end{Bmatrix} \tag{A.63}$$

where $\omega_{\alpha i}$ represents the rotation around the i axis. Equation (A.62) is linearised in order to facilitate a Newton–Raphson iterative solution within a Newmark-β integration scheme as detailed in [167]. Linearisation around the equilibrium gives the incremental form of the finite element equation of motion as.

$$\boldsymbol{M}\begin{Bmatrix}\Delta\ddot{\boldsymbol{w}}_s\\ \Delta\ddot{\boldsymbol{w}}_r\end{Bmatrix}+\boldsymbol{C}\begin{Bmatrix}\Delta\dot{\boldsymbol{w}}_s\\ \Delta\dot{\boldsymbol{w}}_r\end{Bmatrix}+\boldsymbol{K}\begin{Bmatrix}\Delta\boldsymbol{w}_s\\ \Delta\boldsymbol{w}_r\end{Bmatrix}=\Delta\boldsymbol{R}_F\left\{\delta\ddot{\boldsymbol{w}}_s,\delta\dot{\boldsymbol{w}}_s,\delta\boldsymbol{w}_s,\delta\ddot{\boldsymbol{w}}_r,\delta\dot{\boldsymbol{w}}_r,\delta\boldsymbol{w}_r,\delta\boldsymbol{w}_f,\delta\zeta_i,\delta\boldsymbol{u}_c\right\} \tag{A.64}$$

This leads to the nonlinear system mass, damping and stiffness matrices

$$\boldsymbol{M}\left[\boldsymbol{w}_s\right]=\begin{bmatrix}\boldsymbol{M}_{SS} & \boldsymbol{M}_{SR}\\ \boldsymbol{M}_{RS} & \boldsymbol{M}_{RR}\end{bmatrix},\ \boldsymbol{C}\left[\boldsymbol{w}_s,\dot{\boldsymbol{w}}_s,\boldsymbol{w}_r\right]=\begin{bmatrix}\boldsymbol{C}_{SS} & \boldsymbol{C}_{SR}\\ \boldsymbol{C}_{RS} & \boldsymbol{C}_{RR}\end{bmatrix},\ \boldsymbol{K}\left[\boldsymbol{w}_s\right]=\begin{bmatrix}\boldsymbol{K}_{SS} & 0\\ \boldsymbol{K}_{RS} & 0\end{bmatrix} \tag{A.65}$$

In the coupled case where we have rigid–body coupled with structural dynamics the solution vector has the following form.

$$\boldsymbol{w}\ =\ \left\{\boldsymbol{w}_s^T\ ,\ \boldsymbol{w}_r^T\ ,\ \boldsymbol{\zeta}_i^T\ ,\ \boldsymbol{w}_f^T,\right\}^T \tag{A.66}$$

where $\boldsymbol{w}$ contains structural, rigid–body degrees–of–freedom, quaternions and additional aerodynamic states. Furthermore, $\boldsymbol{w}_s$ can be written for each deformable aerofoil section as

$$\boldsymbol{w}_s^j = \{d_{d1}\,,\, d_{d2}\,,\, d_{d3}\,,\, \alpha d_{d1}\,,\, \alpha d_{d2}\,,\, \alpha d_{d3}\}^T \tag{A.67}$$

Additionally, $\boldsymbol{w}_r$ represents the rigid–body states which are defined as

$$\boldsymbol{w}_r = \{r_{d1}\,,\, r_{d2}\,,\, r_{d3}\,,\, \alpha r_{d1}\,,\, \alpha r_{d2}\,,\, \alpha r_{d3}\}^T \tag{A.68}$$

Moreover, each aerofoil section introduces 8 additional aerodynamic states

$$\boldsymbol{w}_f = \{w_1\,,\, w_2\,,\, w_3\,,\, w_4\,,\, w_5\,,\, w_6\,,\, w_7\,,\, w_8\}^T \tag{A.69}$$

Finally $\boldsymbol{\zeta}_i$ contains the quaternions $\zeta_0, \zeta_1, \zeta_2, \zeta_3, \zeta_4$. Vector $\boldsymbol{R}_F$ in this case depends on acceleration, velocities and deformations of both the structure and the rigid–body degrees-of-freedom. Some additional vectors are defined such as

$$\begin{aligned}
&P_{aGB} = \{r_{a1}, r_{a2}, r_{a3}\}^T, P_{aBA} = \{d_{a1}, d_{a2}, d_{a3}\}^T \\
&P_{vGB} = \{r_{v1}, r_{v2}, r_{v3}\}^T, P_{vBA} = \{d_{v1}, d_{v2}, d_{v3}\}^T \\
&P_{dGB} = \{r_{d1}, r_{d2}, r_{d3}\}^T, P_{dBA} = \{d_{d1}, d_{d2}, d_{d3}\}^T \\
&c = \{c_x, c_y, c_z\}^T \text{, aerofoil section location with respect to the span}
\end{aligned} \tag{A.70}$$

The total aerodynamic forces are written as

$$\boldsymbol{R_F} = \begin{bmatrix} \boldsymbol{R}_S \\ \boldsymbol{R}_R \end{bmatrix} = \begin{bmatrix} \boldsymbol{F}_S \\ \boldsymbol{F_R} \end{bmatrix} = \begin{bmatrix} \boldsymbol{F}_{EL}\boldsymbol{F}_i \\ \boldsymbol{F}_{rig}\boldsymbol{F}_i \end{bmatrix} \tag{A.71}$$

In Eq. (A.71) the total aerodynamic force vector is a combination of elastic, rigid–body, gravitational and other externally applied forces. $\boldsymbol{F}_i$ denotes an elastic follower force applied at a generic node i. $\boldsymbol{F}_S$ is the sum of all the elastic loads from frame A projected to the beam reference frame. This is done by $\boldsymbol{F}_{EL}$, a transformation matrix which is a function of the orientation of each beam cross–section. The rigid–body forces are the sum of the aerodynamic forces applied at each node times $\boldsymbol{F}_{rig}$ that multiplies forces and moments at nodes and projects them in the beam reference frame B.

For the analytical calculation of $\boldsymbol{F}_{EL}$ the following matrices are defined as

$$\Psi = \begin{bmatrix} 0 & -\alpha d_{d3} & \alpha d_{d2} \\ \alpha d_{d3} & 0 & -\alpha d_{d1} \\ -\alpha d_{d2} & \alpha d_{d1} & 0 \end{bmatrix}, \boldsymbol{I}_3 = \begin{bmatrix} 1 & 0 & 0 \\ 0 & 1 & 0 \\ 0 & 0 & 1 \end{bmatrix}, \boldsymbol{I}_6 = \begin{bmatrix} 1 & 0 & 0 & 0 & 0 & 0 \\ 0 & 1 & 0 & 0 & 0 & 0 \\ 0 & 0 & 1 & 0 & 0 & 0 \\ 0 & 0 & 0 & 1 & 0 & 0 \\ 0 & 0 & 0 & 0 & 1 & 0 \\ 0 & 0 & 0 & 0 & 0 & 1 \end{bmatrix} \tag{A.72}$$

Additional Matrices are calculated as

$$\begin{aligned} \boldsymbol{R}_M &= \boldsymbol{I}_3 + \Psi + \frac{1}{2}\Psi\Psi \\ \boldsymbol{R}_{MT} &= \boldsymbol{R}_M^T \\ \boldsymbol{D} &= \begin{bmatrix} \boldsymbol{R}_{MT} & 0 \\ 0 & \boldsymbol{I}_3 \end{bmatrix} \\ \boldsymbol{R}_\psi &= \boldsymbol{I}_3 - \frac{1}{2}\Psi + \frac{1}{6}\Psi\Psi \\ \boldsymbol{Y}_p &= \begin{bmatrix} \boldsymbol{I}_3 & 0 \\ 0 & \boldsymbol{R}_\psi \end{bmatrix} \end{aligned} \tag{A.73}$$

Finally, for a generic deformable aerofoil section across the wing, $\boldsymbol{F}_{EL}$ is calculated as

$$\boldsymbol{F}_{EL} = [\boldsymbol{Y}_p \boldsymbol{I}_6 \boldsymbol{D}]^T \tag{A.74}$$

In a similar manner the evaluation of the $\boldsymbol{F}_{rig}$ is performed.

$$\Psi_d = \begin{bmatrix} 0 & -d_{d3} & d_{d2} \\ d_{d3} & 0 & d_{d1} \\ -d_{d2} & d_{d1} & 0 \end{bmatrix}, \boldsymbol{C}_{AB} = \boldsymbol{R}_{MT}^T, \boldsymbol{A}_R = \begin{bmatrix} \boldsymbol{C}_{AB} & 0 \\ \Psi_d \boldsymbol{C}_{AB} & \boldsymbol{C}_{AB} \end{bmatrix} \tag{A.75}$$

Finally a section motion yields the following contribution to the $\boldsymbol{F}_{rig}$.

$$\boldsymbol{F}_{rig} = \boldsymbol{A}_R \tag{A.76}$$

The evaluation of the aerodynamic forces applied at each node in the finite element model starts with the evaluation of the displacement and the velocity of an arbitary flexible node and follows the formulation presented in Shearer et al. [16] The rotation matrix S_k and its derivative S_{kd} are defined as

$$\boldsymbol{S}_k = \begin{bmatrix} 0 & -\alpha r_{3v} & \alpha r_{2v} \\ \alpha r_{3v} & 0 & -\alpha r_{1v} \\ -\alpha r_{2v} & \alpha r_{1v} & 0 \end{bmatrix} \tag{A.77}$$

and

$$\boldsymbol{S}_{kd} = \begin{bmatrix} 0 & -\alpha r_{3a} & \alpha r_{2a} \\ \alpha r_{3a} & 0 & -\alpha r_{1a} \\ -\alpha r_{2a} & \alpha r_{1a} & 0 \end{bmatrix} \tag{A.78}$$

The location of the aerofoil reference point with respect to the body fixed frame B is given by

$$\boldsymbol{P}_d \;=\; (P_{dGB} \;+\; P_{dBA} \;+\; c) \tag{A.79}$$

where c represents the location of the aerofoil section with respect to the span. The corresponding velocity is written by taking the derivative of the previous Eq. (A.79).

$$\boldsymbol{P}_v \;=\; \left(P_{vGB} \;+\; P_{vBA} \;+\; \left(\boldsymbol{S}_k^T\right)\right)(P_{dBA} + c) \tag{A.80}$$

In a similar manner the acceleration is given

$$\begin{aligned} \boldsymbol{P}_a \;=\; \left(P_{aGB} \;+\; P_{aBA} \;+\; \left(\boldsymbol{S}_{kd}^T\right)\right)(P_{dBA} + c) \;+\; 2\left(\boldsymbol{S}_k^T\right) P_{vBA} + \\ \boldsymbol{S}_k^T P_{vGB} + \boldsymbol{S}_k^T \boldsymbol{S}_k^T \left(P_{dBA} + c\right) \end{aligned} \tag{A.81}$$

The effective freestream speed is defined as the velocity in which the body is moving with respect to the instantaneous body attitude and for this expression it is necessary to evaluate the transformation matrix from the body frame B to the inertial frame G based on the rigid body rotation angles and as a result, evaluation of the quaternion transformation matrix.

$$\begin{aligned} \zeta_0 &= cos\left(\frac{ar_{1d}}{2}\right) cos\left(\frac{ar_{2d}}{2}\right) cos\left(\frac{ar_{3d}}{2}\right) + sin\left(\frac{ar_{1d}}{2}\right) sin\left(\frac{ar_{2d}}{2}\right) sin\left(\frac{ar_{3d}}{2}\right) \\ \zeta_1 &= cos\left(\frac{ar_{1d}}{2}\right) cos\left(\frac{ar_{2d}}{2}\right) sin\left(\frac{ar_{3d}}{2}\right) + sin\left(\frac{ar_{1d}}{2}\right) sin\left(\frac{ar_{2d}}{2}\right) cos\left(\frac{ar_{3d}}{2}\right) \\ \zeta_2 &= cos\left(\frac{ar_{1d}}{2}\right) sin\left(\frac{ar_{2d}}{2}\right) cos\left(\frac{ar_{3d}}{2}\right) + sin\left(\frac{ar_{1d}}{2}\right) cos\left(\frac{ar_{2d}}{2}\right) sin\left(\frac{ar_{3d}}{2}\right) \\ \zeta_3 &= -cos\left(\frac{ar_{1d}}{2}\right) sin\left(\frac{ar_{2d}}{2}\right) sin\left(\frac{ar_{3d}}{2}\right) + sin\left(\frac{ar_{1d}}{2}\right) cos\left(\frac{ar_{2d}}{2}\right) sin\left(\frac{ar_{3d}}{2}\right) \end{aligned} \tag{A.82}$$

The rotation matrix for the quaternions expression is given by $\boldsymbol{R}_\zeta$

$$\boldsymbol{R}_\zeta = \begin{bmatrix} \zeta_0^2 + \zeta_1^2 - \zeta_2^2 - \zeta_3^2 & 2\left(\zeta_1\zeta_2 + \zeta_0\zeta_3\right) & 2\left(\zeta_1\zeta_3 + \zeta_0\zeta_2\right) \\ 2\left(\zeta_1\zeta_2 + \zeta_0\zeta_3\right) & \zeta_0^2 - \zeta_1^2 + \zeta_2^2 - \zeta_3^2 & 2\left(\zeta_2\zeta_3 - \zeta_0\zeta_1\right) \\ 2\left(\zeta_1\zeta_3 - \zeta_0\zeta_2\right) & 2\left(\zeta_2\zeta_3 + \zeta_0\zeta_1\right) & \zeta_0^2 - \zeta_1^2 - \zeta_2^2 + \zeta_3^2 \end{bmatrix} \tag{A.83}$$

The freestream speed in the inertial frame can be expressed by the rotation matrix and the freestream velocity as

$$U_{eff} = \boldsymbol{R}_{\zeta} \left\{0, U_{\infty}, 0\right\}^{T} \tag{A.84}$$

The aerodynamic mass, damping and stiffness matrices are defined for each aerofoil section as before with the exception that q_1 contains the contribution from the effective freestream component as $q_0 = 0.5\rho S$, $q_1 = q_0 U_{eff}$ and $q_2 = q_1 U_{eff}$. The rigid–body pitching angle is combined with the local aerofoil sectional torsion to give the total angle of attack of each deformable section. The aerodynamic force vector in the local aerofoil frame is given by

$$\boldsymbol{F}_i^A = \boldsymbol{M}_{\boldsymbol{f}}^A \ddot{\boldsymbol{x}}_s^A + \boldsymbol{C}_{\boldsymbol{f}}^A \dot{\boldsymbol{x}}_s^A + \boldsymbol{K}_{\boldsymbol{f}}^A \boldsymbol{x}_s^A + \boldsymbol{A}_{sf}^A \boldsymbol{w}_f + \boldsymbol{A}_{sc}^A \boldsymbol{u_c} \tag{A.85}$$

In the above equations matrices $\boldsymbol{M}_{\boldsymbol{f}}^A$,$\boldsymbol{C}_{\boldsymbol{f}}^A$ and $\boldsymbol{K}_{\boldsymbol{f}}^A$ are (6×6) while matrix $\boldsymbol{A}_{sf}^A$ is (6×8) and matrix $\boldsymbol{A}_{sc}$ is (6×3). The non-zero components of these matrices are

$$\begin{aligned}
&\boldsymbol{M}_{\boldsymbol{f_{22}}}^{jA} = -q_0 c_1, && \boldsymbol{M}_{\boldsymbol{f_{26}}}^{jA} = -q_0 c_2, && \boldsymbol{M}_{\boldsymbol{f_{62}}}^{jA} = q_0 cd_1, && \boldsymbol{M}_{\boldsymbol{f_{66}}}^{jA} = q_0 cd_2 \\
&\boldsymbol{C}_{\boldsymbol{f_{22}}}^{jA} = -q_1 c_3, && \boldsymbol{C}_{\boldsymbol{f_{26}}}^{jA} = -q_1 c_4, && \boldsymbol{C}_{\boldsymbol{f_{62}}}^{jA} = q_1 cd_3, && \boldsymbol{C}_{\boldsymbol{f_{66}}}^{jA} = q_1 cd_4 \\
&\boldsymbol{K}_{\boldsymbol{f_{22}}}^{jA} = -q_2 c_5, && \boldsymbol{K}_{\boldsymbol{f_{26}}}^{jA} = -q_2 c_6, && \boldsymbol{K}_{\boldsymbol{f_{62}}}^{jA} = q_2 cd_5, && \boldsymbol{K}_{\boldsymbol{f_{66}}}^{jA} = q_2 cd_6 \\
&\boldsymbol{A}_{\boldsymbol{sf_{2k}}}^{jA} = -q_2 c_{6+k} && \text{for} && k = 1, 2, ..., 8 \\
&\boldsymbol{A}_{\boldsymbol{sf_{6k}}}^{jA} = -q_2 cd_{6+k} && \text{for} && k = 1, 2, ..., 8 \\
&\boldsymbol{A}_{\boldsymbol{sc_{21}}}^{jA} = -q_2 c_{15} && \boldsymbol{A}_{\boldsymbol{sc_{22}}}^{jA} = -q_1 c_{16} && \boldsymbol{A}_{\boldsymbol{sc_{23}}}^{jA} = -q_0 c_{17} \\
&\boldsymbol{A}_{\boldsymbol{sc_{61}}}^{jA} = -q_2 cd_{15} && \boldsymbol{A}_{\boldsymbol{sc_{62}}}^{jA} = -q_1 cd_{16} && \boldsymbol{A}_{\boldsymbol{sc_{63}}}^{jA} = -q_0 cd_{17}
\end{aligned} \tag{A.86}$$

The remaing terms of the aerodynamic model are constant and for a given geometry are computed only once. Now, like before, some geometric terms are introduced. The constants $T_1, T_4, T_7, T_8, T_{10}$ and T_{11} are all geometric terms which depend on the size of the flap relative to the aerofoil chord and for a coordinate system located at the midchord are expressed as in Theodorsen [22].

$$
\begin{aligned}
T_1 &= -\frac{1}{3}\sqrt{1-c^2}(2+c^2) + carccos(c) \\
T_4 &= -arccos(c) + c\sqrt{1-c^2} \\
T_7 &= -(\frac{1}{8}+c^2)arccos(c) + \frac{1}{8}c\sqrt{1-c^2}(7+2c^2) \\
T_8 &= -\frac{1}{3}\sqrt{1-c^2}(2c^2+1) + carccos(c) \\
T_{10} &= \sqrt{1-c^2} + arccos(c) \\
T_{11} &= arccos(c)(1-2c) + \sqrt{1-c^2}(2-c) \\
c_\delta &= (2T_{10}(1-\Psi_1-\Psi_2) + T_{11}(\epsilon_1\Psi_1 + \epsilon_2\Psi_2)) \\
c_{\delta'} &= (-T_4 + T_{11}(1-\Psi_1-\Psi_2)) \\
c_{\delta''} &= -T_1 \\
d_\delta &= (-(T_4+T_{10}) + (a_h+\frac{1}{2})(T_{10}(1-\Psi_1-\Psi_2) + \frac{T_{11}}{2}(\epsilon_1\Psi_1+\epsilon_2\Psi_2))) \\
d_{\delta'} &= (-(T_1 - T_8 - (c-a_h)T_4 + \frac{1}{2}T_{11}) + (a_h+\frac{1}{2})\frac{T_{11}}{2}(1-\Psi_1-\Psi_2)) \\
d_{\delta''} &= (T_7 + (c-a_h)T_1)
\end{aligned}
\tag{A.87}
$$

The coefficients denoted in Eq. (A.86) are written in explicit form as

$$
\begin{aligned}
c_1 &= \pi b \\
c_2 &= -\pi a_h b^2 \\
c_3 &= 2\pi(1-\Psi_1-\Psi_2) \\
c_4 &= \pi b(1+(1-2a_h)(1-\Psi_1-\Psi_2)) \\
c_5 &= \frac{2\pi}{b}(\epsilon_1\Psi_1+\epsilon_2\Psi_2) \\
c_6 &= 2\pi((1-\Psi_1-\Psi_2)+(\frac{1}{2}-a_h)(\epsilon_1\Psi_1+\epsilon_2\Psi_2)) \\
c_7 &= 2\pi\epsilon_1\Psi_1(1-\epsilon_1(1-\frac{1}{2}-a_h)) \\
c_8 &= 2\pi\epsilon_2\Psi_2(1-\epsilon_2(\frac{1}{2}-a_h)) \\
c_9 &= -2\pi\epsilon_1^2\Psi_1 \\
c_{10} &= -2\pi\epsilon_2^2\Psi_2 \\
c_{11} &= \epsilon_1\Psi_1 2T_{10}-\epsilon_1^2\Psi_1 T_{11} \\
c_{12} &= \epsilon_2\Psi_2 2T_{10}-\epsilon_2^2\Psi_2 T_{11} \\
c_{13} &= 2\pi\epsilon_3\Psi_3 \\
c_{14} &= 2\pi\epsilon_4\Psi_4 \\
c_{15} &= c_\delta \qquad c_{16} = bc_{\delta'} \qquad c_{17} = b^2 c_{\delta''}
\end{aligned}
\tag{A.88}
$$

$$
\begin{aligned}
d_1 &= \frac{\pi}{2} a_h b \\
d_2 &= -\frac{1}{2}(a_h^2 + \frac{1}{8}) b^2 \\
d_3 &= \pi(\frac{1}{2} + a_h)(1 - \Psi_1 - \Psi_2) \\
d_4 &= \frac{\pi}{6}(\frac{1}{2} - a_h)((\frac{1}{2} + a_h)(1 - \Psi_1 - \Psi_2) - \frac{1}{2}) \\
d_5 &= \frac{\pi}{6}(\frac{1}{2} + a_h)(\epsilon_1 \Psi_1 + \epsilon_2 \Psi_2) \\
d_6 &= \pi(\frac{1}{2} + a_h)((1 - \Psi_1 - \Psi_2) + (\frac{1}{2} - a_h)((\epsilon_1 \Psi_1 + \epsilon_2 \Psi_2))) \\
d_7 &= \pi(\frac{1}{2} + a_h)(\epsilon_1 \Psi_1 (1 - \epsilon_1 (\frac{1}{2} - a_h))) \\
d_8 &= \pi(\frac{1}{2} + a_h)(\epsilon_2 \Psi_2 (1 - \epsilon_2 (\frac{1}{2} - a_h))) \\
d_9 &= -\pi(\frac{1}{2} + a_h)\epsilon_1^2 \Psi_1 \\
d_{10} &= -\pi(\frac{1}{2} + a_h)\epsilon_2^2 \Psi_2 \\
d_{11} &= (\frac{1}{2} + a_h)(T_{10}\epsilon_1 \Psi_1 - \frac{T_{11}}{2}\epsilon_1^2 \Psi_1) \\
d_{12} &= (\frac{1}{2} + a_h)(T_{10}\epsilon_2 \Psi_2 - \frac{T_{11}}{2}\epsilon_2^2 \Psi_2) \\
d_{13} &= \pi(\frac{1}{2} + a_h)\epsilon_3 \Psi_3 \qquad d_{14} = \pi(\frac{1}{2} + a_h)\epsilon_4 \Psi_4 \\
d_{15} &= d_\delta \qquad d_{16} = b d_{\delta'} \qquad d_{17} = b^2 d_{\delta''}
\end{aligned}
\tag{A.89}
$$

Following Eq. (A.85) $\ddot{\boldsymbol{x}}_s$, $\dot{\boldsymbol{x}}_s$ and $\boldsymbol{x}_s$ are written

$$
\ddot{\boldsymbol{x}}_s^A = \begin{Bmatrix} \boldsymbol{P}_a \\ ad_{a1}^j + ar_{a1} \\ 0 \\ 0 \end{Bmatrix}, \dot{\boldsymbol{x}}_s^A = \begin{Bmatrix} \boldsymbol{P}_v \\ ad_{v1}^j + ar_{v1} \\ 0 \\ 0 \end{Bmatrix}, \boldsymbol{x}_s^A = \begin{Bmatrix} \boldsymbol{P}_d \\ ad_{d1}^j + ar_{d1} \\ 0 \\ 0 \end{Bmatrix} \tag{A.90}
$$

As seen from Eq. (A.90) in the coupled rigid–body structural dynamics the total angle of attack is the sum of the rigid–body rotation and the local torsion of the deformed aerofoil section across the wing. Note that the aerodynamic forces are nonlinear due to the reason that the effective freestream speed is a nonlinear function of the rigid–body rotations and as a result the elements that consist the aerodynamic mass, damping, and stiffness matrices are nonlinear. Although, for reasonable small rigid–body rotations a linearisation should give the exact same solution as the fully nonlinear case. Important contributions arise also from the augmented unsteady aerodynamic forces which for each deformable aerofoil section are given by

$$
\dot{\boldsymbol{w}}_f = \boldsymbol{A}_{fs}^A \boldsymbol{x}_s^A + \boldsymbol{A}_{ff} \boldsymbol{w}_f + \boldsymbol{A}_{fc} \boldsymbol{u}_c + \boldsymbol{A}_{fg} \boldsymbol{u}_d \tag{A.91}
$$

The expressions given in Eq. (A.85) and (A.91) are formulated based on a vector of structural and rigid body degrees–of–freedom defined in the aerodynamic reference frame A. Matrix $\boldsymbol{A}_{fs}$ has dimension (8×6), matrix $\boldsymbol{A}_{ff}$ has dimension (8×8), matrix $\boldsymbol{A}_{fc}$ has dimension (8×3) and matrix $\boldsymbol{A}_{fg}$ has a dimension (8×3) for the three possible gust components in x, y, z. The non–zero components of those matrices are.

$$\begin{array}{cccc}
\boldsymbol{A}^A_{fs16} = \frac{U_{eff}}{b}, & \boldsymbol{A}^A_{fs26} = \frac{U_{eff}}{b}, & \boldsymbol{A}^A_{fs32} = \frac{U_{eff}}{b^2}, & \boldsymbol{A}^A_{fs41} = \frac{U_{eff}}{b^2} \\
\boldsymbol{A}_{ff11} = -\frac{\epsilon_1 U_{eff}}{b}, & \boldsymbol{A}_{ff22} = -\frac{\epsilon_2 U_{eff}}{b}, & \boldsymbol{A}_{ff33} = -\frac{\epsilon_1 U_{eff}}{b^2}, & \boldsymbol{A}_{ff44} = -\frac{\epsilon_2 U_{eff}}{b^2} \\
\boldsymbol{A}_{ff55} = -\frac{\epsilon_1 U_{eff}}{b}, & \boldsymbol{A}_{ff66} = -\frac{\epsilon_2 U_{eff}}{b}, & \boldsymbol{A}_{ff77} = -\frac{\epsilon_3 U_{eff}}{b^2}, & \boldsymbol{A}_{ff88} = -\frac{\epsilon_4 U_{eff}}{b^2} \\
\boldsymbol{A}_{fc51} = \frac{U_{eff}}{b}, & \boldsymbol{A}_{fc61} = \frac{U_{eff}}{b}, & \boldsymbol{A}_{fg71} = \frac{U_{eff}}{b}, & \boldsymbol{A}_{fg81} = \frac{U_{eff}}{b}
\end{array}$$

In order to form the global system of equations of motion, a coordinate transformation has to be performed to transfer the structural degrees–of–freedom in the beam reference frame. This is accomplished by the transformation

$$\boldsymbol{x}^A_s = \boldsymbol{R}\boldsymbol{x}^B_s = \boldsymbol{R}\boldsymbol{x}_s \tag{A.92}$$

where subscript B indicates the beam reference frame. The transformation matrix for a deformed cantilever beam is given by $\boldsymbol{R}_c$

$$\boldsymbol{R}_c = \begin{bmatrix}
0 & 0 & 1 & 0 & 0 & 0 \\
-cos\,(ad_{1d}) & -sin\,(ad_{1d}) & 0 & 0 & 0 & 0 \\
sin\,(ad_{1d}) & -cos\,(ad_{1d}) & 0 & 0 & 0 & 0 \\
0 & 0 & 0 & 0 & 0 & 1 \\
0 & 0 & 0 & -cos\,(ad_{1d}) & -sin\,(ad_{1d}) & 0 \\
0 & 0 & 0 & sin\,(ad_{1d}) & -cos\,(ad_{1d}) & 0
\end{bmatrix} \tag{A.93}$$

If Eq. (A.92) is substituted in Eq. (A.85) yields the aerodynamic forces in the beam reference frame

$$\boldsymbol{F}^B_S = \boldsymbol{M}^B_{\boldsymbol{f}}\ddot{\boldsymbol{x}}^B_s + \boldsymbol{C}^B_{\boldsymbol{f}}\dot{\boldsymbol{x}}^B_s + \boldsymbol{K}^B_{\boldsymbol{f}}\boldsymbol{x}^B_s + \boldsymbol{A}^B_{sf}\boldsymbol{w}_f + \boldsymbol{A}^B_{sc}\boldsymbol{u}_c \tag{A.94}$$

The transformed matrices are defined in an equivalent way as

$$\boldsymbol{M}^B_{\boldsymbol{f}} = \boldsymbol{R}^T_c\boldsymbol{M}^A_{\boldsymbol{f}}\boldsymbol{R}_c \tag{A.95}$$
$$\boldsymbol{C}^B_{\boldsymbol{f}} = \boldsymbol{R}^T_c\boldsymbol{C}^A_{\boldsymbol{f}}\boldsymbol{R}_c \tag{A.96}$$
$$\boldsymbol{K}^B_{\boldsymbol{f}} = \boldsymbol{R}^T_c\boldsymbol{K}^A_{\boldsymbol{f}}\boldsymbol{R}_c \tag{A.97}$$
$$\boldsymbol{A}^B_{sf} = \boldsymbol{R}^T_c\boldsymbol{A}^A_{sf}\boldsymbol{R}_c \tag{A.98}$$
$$\boldsymbol{A}^B_{sc} = \boldsymbol{R}^T_c\boldsymbol{A}^A_{sc} \tag{A.99}$$
$$\tag{A.100}$$

Similarly Eq. (A.91) becomes

$$\dot{\boldsymbol{w}}_f \;=\; \boldsymbol{A}^B_{fs}\boldsymbol{x}^B_s \;+\; \boldsymbol{A}_{ff}\boldsymbol{w}_f \;+\; \boldsymbol{A}_{fc}\boldsymbol{u}_c \;+\; \boldsymbol{A}_{\boldsymbol{fg}}\boldsymbol{u}_d \tag{A.101}$$

where $\boldsymbol{A}^B_{fs} \;=\; \boldsymbol{A}^A_{\boldsymbol{fs}}\boldsymbol{R}_c$. In this way the global equations of motion can be re–written as

$$\begin{bmatrix} \boldsymbol{M}_{SS} & \boldsymbol{M}_{SR} \\ \boldsymbol{M}^T_{SR} & \boldsymbol{M}_{RR} \end{bmatrix} \begin{Bmatrix} \ddot{\boldsymbol{w}}_s \\ \ddot{\boldsymbol{w}}_r \end{Bmatrix} + \begin{bmatrix} \boldsymbol{C}_{SS} & \boldsymbol{C}_{SR} \\ \boldsymbol{C}_{RS} & \boldsymbol{C}_{RR} \end{bmatrix} \begin{Bmatrix} \dot{\boldsymbol{w}}_s \\ \dot{\boldsymbol{w}}_r \end{Bmatrix} + \begin{bmatrix} \boldsymbol{K}_{SS} & 0 \\ \boldsymbol{K}_{RS} & 0 \end{bmatrix} \begin{Bmatrix} \boldsymbol{w}_s \\ \boldsymbol{w}_r \end{Bmatrix} = \begin{Bmatrix} \boldsymbol{F}_S \\ \boldsymbol{F}_R \end{Bmatrix}$$

The previous equation is also coupled with the quaternions that are used to determine the orientation of the beam reference frame, and the augmented aerodynamic states which are expressed as a first–order ODE. A new state vecor is defined such as

$$\boldsymbol{q} \;=\; \left\{\boldsymbol{w}^T_s, \boldsymbol{w}^T_r\right\}^T \tag{A.102}$$

The equations of motion with the quaternions and the augmented aerodynamic states are expressed as

$$\boldsymbol{M}\ddot{\boldsymbol{q}} + \boldsymbol{C}\dot{\boldsymbol{q}} + \boldsymbol{K}\boldsymbol{q} = \begin{pmatrix} \boldsymbol{F}_S \\ \boldsymbol{F}_R \end{pmatrix} \tag{A.103}$$

$$\dot{\zeta}_i \;+\; \boldsymbol{C}_{QR}\left[\boldsymbol{w}_r\right]\dot{\boldsymbol{w}}_r \;+\; \boldsymbol{C}_{QQ}\left[\boldsymbol{\zeta_i}\right]\boldsymbol{\zeta_i} \;=\; 0 \tag{A.104}$$

$$\dot{\boldsymbol{w}}_f \;=\; \boldsymbol{A}^B_{fs}\boldsymbol{x}^B_s \;+\; \boldsymbol{A}_{ff}\boldsymbol{w}_f \;+\; \boldsymbol{A}_{fc}\boldsymbol{u}_c \;+\; \boldsymbol{A}_{\boldsymbol{fg}}\boldsymbol{u}_d \tag{A.105}$$

The forces on the right hand side of Eq. (A.103) are nonlinear and can be linearised to update the total mass, stiffness and damping matrices on the left hand side in order to recast the system as a first–order ODE. The linearised tangent matrix can be used for the Nonlinear Newmark β iteration scheme and the prediction of the nonlinear aerodynamic forces at the current timestep.

The linearisation is done analytically and thus the nonlinear expressions are written as

$$\boldsymbol{F}_{SL} \;=\; \boldsymbol{M}_{\boldsymbol{f}}\ddot{\boldsymbol{q}} \;+\; \boldsymbol{C}_{\boldsymbol{f}}\dot{\boldsymbol{q}} \;+\; \boldsymbol{K}_{\boldsymbol{f}}\boldsymbol{q} \;+\; \boldsymbol{A}_{sf}\boldsymbol{w}_f \;+\; \boldsymbol{A}_{sc}\boldsymbol{u}_c \tag{A.106}$$

$$\boldsymbol{F}_{RL} \;=\; \boldsymbol{M}_{\boldsymbol{r}}\ddot{\boldsymbol{q}} \;+\; \boldsymbol{C}_{\boldsymbol{r}}\dot{\boldsymbol{q}} \;+\; \boldsymbol{K}_{\boldsymbol{r}}\boldsymbol{q} \;+\; \boldsymbol{A}_{rf}\boldsymbol{w}_f \;+\; \boldsymbol{A}_{rc}\boldsymbol{u}_c \tag{A.107}$$

$$\dot{\boldsymbol{w}}_f \;=\; \boldsymbol{A}_{fs}\boldsymbol{q} \;+\; \boldsymbol{A}_{ff}\boldsymbol{w}_f \;+\; \boldsymbol{A}_{fc}\boldsymbol{u}_c \;+\; \boldsymbol{A}_{fg}\boldsymbol{u}_d \tag{A.108}$$

In this way the nonlinear system can be fully linearised and one can assemble the total coupled mass, damping and stiffness matrix as

$$\boldsymbol{M}_T \;=\; \boldsymbol{M} \;-\; \boldsymbol{M}_f \;-\; \boldsymbol{M}_r \tag{A.109}$$

$$\boldsymbol{C}_T \;=\; \boldsymbol{C} \;-\; \boldsymbol{C}_f \;-\; \boldsymbol{C}_r \tag{A.110}$$

$$\boldsymbol{K}_T \;=\; \boldsymbol{K} \;-\; \boldsymbol{K}_f \;-\; \boldsymbol{K}_r \tag{A.111}$$

The coupled equations become

$$\boldsymbol{M}_T\ddot{\boldsymbol{q}} + \boldsymbol{C}_T\dot{\boldsymbol{q}} + \boldsymbol{K}_T\boldsymbol{q} = \boldsymbol{A}_{sf}\boldsymbol{w}_f + \boldsymbol{A}_{sc}\boldsymbol{u}_c + \boldsymbol{A}_{rf}\boldsymbol{w}_f + \boldsymbol{A}_{rc}\boldsymbol{u}_c \tag{A.112}$$

$$\dot{\zeta}_i + \boldsymbol{C}_{QR}\dot{\boldsymbol{w}}_r + \boldsymbol{C}_{QQ}\boldsymbol{\zeta_i} = 0 \tag{A.113}$$

$$\dot{\boldsymbol{w}}_f = \boldsymbol{A}_{fs}\boldsymbol{q} + \boldsymbol{A}_{ff}\boldsymbol{w}_f + \boldsymbol{A}_{fc}\boldsymbol{u}_c + \boldsymbol{A}_{fg}\boldsymbol{u}_d \tag{A.114}$$

By inverting the coupled mass matrix and multiplying both sides of Eq. (A.112) yields the final linearised second–order ODE flight dynamics equations.

$$\ddot{\boldsymbol{q}} = -\boldsymbol{M}_T^{-1}\boldsymbol{C}_T\dot{\boldsymbol{q}} - \boldsymbol{M}_T^{-1}\boldsymbol{K}_T\boldsymbol{q} + \boldsymbol{M}_T^{-1}\boldsymbol{A}_{sf}\boldsymbol{w}_f + \boldsymbol{M}_T^{-1}\boldsymbol{A}_{rf}\boldsymbol{w}_f + \boldsymbol{M}_T^{-1}\boldsymbol{A}_{sc}\boldsymbol{u}_c + \boldsymbol{M}_T^{-1}\boldsymbol{A}_{rc}\boldsymbol{u}_c \tag{A.115}$$

$$\dot{\zeta}_i = -\boldsymbol{C}_{QR}\dot{\boldsymbol{w}}_r - \boldsymbol{C}_{QQ}\boldsymbol{\zeta_i} \tag{A.116}$$

$$\dot{\boldsymbol{w}}_f = \boldsymbol{A}_{fs}\boldsymbol{q} + \boldsymbol{A}_{ff}\boldsymbol{w}_f + \boldsymbol{A}_{fc}\boldsymbol{u}_c + \boldsymbol{A}_{fg}\boldsymbol{u}_d \tag{A.117}$$

A new state vector is defined such as $\boldsymbol{x}_{new} = (\boldsymbol{q}, \dot{\boldsymbol{q}}, \zeta_i, \boldsymbol{w}_f)$. Then by taking the derivative of the new state vector and using the above equations which are coupled, the system is recast as a first–order ODE as follows

$$\begin{Bmatrix} \boldsymbol{q} \\ \dot{\boldsymbol{q}} \\ \dot{\zeta}_i \\ \dot{w}_f \end{Bmatrix} = \begin{bmatrix} 0 & I & 0 & 0 \\ -\boldsymbol{M}_T^{-1}\boldsymbol{K}_T & -\boldsymbol{M}_T^{-1}\boldsymbol{C}_T & 0 & \boldsymbol{M}_T^{-1}\boldsymbol{A}_{sf} + \boldsymbol{M}_T^{-1}\boldsymbol{A}_{rf} \\ 0 & -\boldsymbol{C}_{QR} & -\boldsymbol{C}_{QQ} & 0 \\ \boldsymbol{A}_{fs} & 0 & 0 & \boldsymbol{A}_{fs} \end{bmatrix} \begin{Bmatrix} \boldsymbol{q} \\ \dot{\boldsymbol{q}} \\ \zeta_i \\ \boldsymbol{w}_f \end{Bmatrix} + \begin{bmatrix} 0 \\ \boldsymbol{M}_T^{-1}\boldsymbol{A}_{sc} + \boldsymbol{M}_T^{-1}\boldsymbol{A}_{rc} \\ 0 \\ \boldsymbol{A}_{fs} \end{bmatrix} \boldsymbol{u}_c + \begin{Bmatrix} 0 \\ 0 \\ 0 \\ \boldsymbol{A}_{fg} \end{Bmatrix} \boldsymbol{u}_d$$

The solution of the eigenvalue problem of the above equation provides insight on the stability of the nonlinear system at the equilibrium point the linearisation was performed and can be used to construct the basis for the free–flying nonlinear model order reduction.